WIDE-ANGLE SEISMIC REFLECTION STUDIES OF THE ELBERTON GRANITE AND CAROLINA TERRANE, SOUTHERN APPALACHIANS, NORTHEAST GEORGIA

by

MOHAMED OMRAN MOHAMED KHALIFA

(Under the Direction of Robert B. Hawman)

ABSTRACT

The first part of the study uses wide-angle seismic reflections to investigate the tectonic relationship between the Elberton granite and Appalachian thrusting and to image the base of the granite. Field experiments were designed to take advantage of the increase in reflection coefficients near the critical angle to image relatively subtle contrasts in the acoustic impedance between the Elberton and underlying gneisses. Shot gathers show strong first arrivals and high amplitude events arriving shortly after the direct P wave that are interpreted as post-critical reflections from a "layered" complex at depths of 3 to 4 (possibly 2-4) km. Possible interpretations of the layering include migmatitic rocks, mafic cumulates, or a mylonitic shear zone at the base of the granite. The migrated sections show southeast-dipping features that span a depth of 5-10 km. The transition from horizontal to dipping reflections beneath the Elberton granite supports the hypothesis that the granite is a tabular body. A high-amplitude, multicyclic event at ~ 11 km is interpreted as the master decollement. The second part of the study involves migration of wide-angle data collected along the axis of the East Coast gravity high within the Carolina Terrane. The study compares the reflection response of the crust to COCORP-style vertical profiling and wide-angle profiling. The two data sets differ in dominant frequency and therefore are sensitive to different scales of layering. Depths of some migrated events match the depths of prominent reflection packages previously

interpreted as the master decollement and Modoc zone. The migrated wide-angle sections also show prominent sub-horizontal events at 30 km that do not appear in the COCORP sections. If basement rocks here do indeed represent rifted continental crust as proposed by earlier workers, then the reflectors could be mafic sills. In this study, very high-amplitude events interpreted as near-critical reflections from the Moho appear at projected vertical two-way times that are slightly greater (11.6-11.9 s) than two-way times for Moho reflections in the COCORP sections (11 s). Overall, the elevated reflection coefficients at wide angles have proved quite useful for imaging subtle constrasts in acoustic impedance otherwise missed by near-vertical recording.

INDEX WORDS: Elberton Granite, Inner Piedmont, Wide-angle, Dimension-stone blasts, COCORP, Master decollement, Carolina Terrane, Moho, Kiokee Belt, Charlotte Belt.

WIDE-ANGLE SEISMIC REFLECTION STUDIES OF THE ELBERTON GRANITE AND CAROLINA TERRANE, SOUTHERN APPALACHIANS, NORTHEAST GEORGIA

by

MOHAMED OMRAN MOHAMED KHALIFA

B.S. Assiut University, Egypt, 1986

M.S. Assiut University, Egypt, 1993

A Dissertation Submitted to the Graduate Faculty of The University of Georgia in Partial Fulfillment of the Requirements for the Degree

DOCTOR OF PHILOSOPHY

ATHENS, GEORGIA

2002

WIDE-ANGLE SEISMIC REFLECTION STUDIES OF THE ELBERTON GRANITE AND CAROLINA TERRANE, SOUTHERN APPALACHIANS, NORTHEAST GEORGIA

by

MOHAMED OMRAN MOHAMED KHALIFA

Approved:

Major Professor: Dr. Robert B. Hawman

Committee: Dr. James A. Whitney
Dr. Samuel E. Swanson
Dr. Michael F. Roden
Dr. Sally E. Walker

Electronic Version Approved:

Gordhan L. Patel
Dean of the Graduate School
The University of Georgia
August 2002

DEDICATION

In The Memory of My Beloved Mother

To My Dear Father

To My Wife

To My Brothers and Sisters

To My Children Ahmed, Abdel Rahman,

Maryam, and Eman

ACKNOWLEDGEMENTS

Praise be to ALLAH, the Almighty, who by His infinite mercy enabled me to finish this work. I am pleased to acknowledge my debt to my parents. Deep thanks to my major professor Dr. Robert B. Hawman for his guidance, help, and support. I would like to thank my committee members, Dr. James Whitney, Dr. Samuel Swanson, Dr. Michael Roden, Dr. Sally Walker, and Dr. Ervan Garrison for their support and encouragement. I am thankful for the cooperation of the Quarry personnel. Special thanks to Mr. Vince Fernandez at Blue Ribbon Quarries, Inc., Mr. James Boyd at Boyd Granite Company, Mr. John Dye and Mr. John Oldham at Dye Granite, Inc., Mr. James Adams and Anthony Adams at Gold Eagle Quarries, Inc., and Mr. Rusty Adams and Mr. Mark Adams at Star Granite Company, Inc. Thanks to Jeff Clippard for his field help and computer support. This research was supported in part by NSF grant # EAR0124249 (P.I. Dr. Hawman). I thank the government of my country, Egypt, for offering me a scholarship and giving me the chance to study in USA. Thanks to the Department of Geology at the university of Georgia for the financial support through two grants from "Watts-Wheeler research and travel fund". I thank Hisham Ahmed, my dear friend, for his help and encouragement. I extend my thanks to my brothers and sisters and their families. Deep thanks to my wife and my kids (Ahmed, Abdel Rahman, Maryam, and Eman). Thanks to our friend, Ms. Karen Hamrick, for her warm feelings toward my family during my stay in the United States. Finally I would like to thank anyone who offered me any kind of help along my way to finish my dissertation.

TABLE OF CONTENTS

Page

LIST OF FIGURES

Page

CHAPTER 1

INTRODUCTION

Elberton Granite Study

The tectonic history of the Elberton granite is very important in understanding the geological history of the Inner Piedmont and consequently the evolution of the southern Appalachian thrusting system. The Elberton granite is nearly concordant with the strike of enveloping rocks, suggesting a strong geologic relationship between the granite, enclosing rocks, and thrust faults. However, the emplacement time of the granite with respect to the thrusting and the nature of the granite itself (whether it is allochthonous or a rooted body) are poorly constrained by conventional seismic data. Competing models for the Elberton granite include a rooted body extending to depths greater than 8 km, a tabular intrusion, and the upper portion of a large pluton decapitated by thrust faulting (Jurdy and Phinney, 1983)

In COCORP (Cook et al., 1979) and ADCOH (Coruh et al., 1987) seismic reflection profiles, strong continuous reflections interpreted to be from the sole thrust and platform sediments beneath the Blue Ridge and the northwest flank of the Inner Piedmont give way to weaker, more scattered reflections beneath the Elberton granite (Inner Piedmont) and the Carolina Terrane.

When compared to the COCORP work, the current study is local, mainly focused on the Elberton granite and the surrounding rocks. The recording parameters for the wide-angle study were chosen to optimize coverage of the top 12 km of the crust,

especially for the uppermost 2-4 km where reflections were poorly imaged in the COCORP sections. The wide-angle technique employed for this study takes advantage of the increase in reflection coefficients with incidence angle (Braile and Chiang, 1986) to image relatively subtle contrasts in acoustic impedance between rock units of similar composition.

The principal goals of this study were to image the base of the Elberton granite and underlying units, to take advantage of the relative seismic transparency of the Elberton granite to study the nature of the master decollement in the transition zone between the Inner Piedmont and Carolina Terrane, and finally, to place constraints on the fine-scale geologic structure of major reflectors by comparing the seismic response of the Elberton granite and other features at near-vertical angles (COCORP studies) and wide-angles (this study).

Carolina Terrane Study

The southern Appalachians have been crossed by several near-vertical seismic profiles. Consortium for Continental Reflection Profiling (COCORP) lines imaged most of the upper crust but were less successful in imaging deeper structures (Hawman, 1996).

The study presented here is a continuation of the work begun by Hawman (1996). In that study, dense recording arrays and timed quarry blasts were used to model the crustal velocity structure of the East Coast gravity high. The experiments were also designed to improve the detectability of the Moho and other major discontinuities that were not well imaged in previous COCORP profiles by taking advantage of large reflection coefficients at near-critical incidence angles. The main objective of the quarry-

blast experiments was to place constraints on crustal structures responsible for the steep gravity gradient and regional gravity high.

The present study involves full-wavefield migration of all reflections to obtain a higher-resolution image of the crust along the profile. The study uses a subset of 16 blasts at quarries near the southwest end of the original profile. Specific targets for the present study include the master decollement, structure within the Kiokee and Charlotte Belt allochthons and underlying basement, and the Moho. The ultimate goal of this work is a unified interpretation of the COCORP and wide-angle migrated images based on the velocity model of Hawman (1996), keeping in mind the differences in reflectivity of the crust for near-vertical, short-wavelength signals and wide-angle, long-wavelength signals.

CHAPTER 2

WIDE-ANGLE SEISMIC REFLECTION STUDIES OF THE ELBERTON GRANITE, SOUTHERN APPALACHIANS, USING SHORT-APERTURE ARRAYS AND INSTANTANEOUS BLASTS AT DIMENSION-STONE QUARRIES[1]

[1] Khalifa, M. O., R. B. Hawman. To be submitted to *Geophysics.*

ABSTRACT

The study uses wide-angle seismic reflections to investigate the tectonic relationship between the Elberton granite and Appalachian thrusting. The principal goal was to image the base of the granite. Field experiments were designed to take advantage of the increase in reflection coefficients near the critical angle to image relatively subtle contrasts in the acoustic impedance between the Elberton and underlying gneisses. Shot-receiver offsets were chosen to avoid interference with shear waves. A total of 9 timed, instantaneous dimension-stone quarry blasts were recorded at distances from 7.77 to 14.91 km. The receiver spacings were chosen tight, 50 m, to avoid spatial aliasing. Recording apertures for each blast were roughly 1 km, giving a total coverage of about 8-9 km. Shot gathers show strong first arrivals and high amplitude events arriving shortly after the direct P wave that are interpreted as post-critical reflections from a "layered" complex at migrated depths of 3 to 4 (possibly 2-4) km. These events are interpreted as reflections from layering near the base of the Elberton granite. Possible interpretations of the layering include migmatitic rocks with alternating layers of different densities (acidic and mafic), mafic cumulates, or a mylonitic shear zone at the base of the granite associated with late Alleghanian compression. Although the wide-angle recordings give an incomplete image of the subsurface and further recording is recommended, they are considered the first successful attempt to image the base of the Elberton granite. The migrated sections also show southeast-dipping features that span a depth of 5-10 km and which correlate with previously reported southeast-dipping features from COCORP work. The transition from horizontal to dipping reflections beneath the Elberton granite supports the hypothesis that the granite is a tabular body that does not extend deeper than

4 km. A high-amplitude, well-resolved, multicyclic event at ~ 11 km is interpreted as the master decollement. This event loses considerable strength in COCORP sections as one travels southeastward from the Brevard Zone. The wide-angle results constrain the depth of this feature beneath the southeast flank of the Inner Piedmont and show that is layered, with a thickness of roughly 500 m.

INDEX WORDS: Elberton Granite, Inner Piedmont, Wide-angle, Dimension-stone blasts, COCORP, Master decollement.

Introduction

The Elberton granite is intruded in the Inner Piedmont belt of the southern Appalachians in northeast Georgia. The Inner Piedmont, which represents a zone of high grade, migmatitic gneisses, extends from Virginia to Alabama. The Inner Piedmont has been subdivided into a high-grade core and to lower-grade flanks (Griffin, 1971; Hatcher, 1972). The tectonic history of the Elberton granite is very important in understanding the geological history of the Inner Piedmont and consequently the evolution of the southern Appalachian thrusting system. The Elberton granite is nearly concordant with the strike of enveloping rocks, suggesting a strong geologic relationship between the granite, enclosing rocks, and thrust faults. However, the emplacement time of the granite with respect to the thrusting and the nature of the granite itself (whether it is allochthonous or a rooted body) are poorly constrained by conventional seismic data. Competing models for the Elberton granite include a rooted body extending to depths greater than 8 km, a tabular intrusion, and the upper portion of a large pluton decapitated by thrust faulting (Jurdy and Phinney, 1983; Figure 2.6).

A related question involves the volume of rock involved in late Alleghanian thrusting. Although Middle to Late Paleozoic thrusting of Valley and Ridge and Blue Ridge rocks over relatively undeformed platform sediments of the North American craton is now well established by several conventional seismic reflection profiles (Cook et al., 1979), the style and extent of thrusting beneath the outboard terranes of the crystalline core (the Inner Piedmont and Carolina terrane) remain controversial. In COCORP (Cook et al., 1979) and ADCOH (Coruh et al., 1987) seismic reflection profiles, strong continuous reflections interpreted to be from the sole thrust and platform sediments

beneath the Blue Ridge and the northwest flank of the Inner Piedmont give way to weaker, more scattered reflections beneath the Elberton granite (Inner Piedmont) and the Carolina terrane. It is not clear whether the sole thrust steps down into basement rock and terminates beneath the northwest flank of the Carolina terrane in a zone of southeast-dipping reflections possibly marking the root zone for the Blue Ridge/Inner Piedmont nappes (Iverson and Smithson, 1982), or whether the sole thrust and associated platform sediments continue southeast beneath the Carolina terrane and the Coastal plain, indicating a Blue Ridge/Inner Piedmont root zone somewhere beneath the continental shelf (Cook et al., 1979; Harris and Bayer, 1979).

Goals of Study

The principal aim of this study was to determine the relationship between the Elberton granite and Late Alleghanian thrusting by placing constraints on the geometry of the granite body and the nature of its contacts with surrounding rocks. In contrast with earlier seismic profiling conducted by COCORP, the wide-angle experiments described here take advantage of the increase in reflection coefficients near the critical angle to image relatively subtle contrasts in acoustic impedance between rock units of similar composition.

Specifically, the goals of the experiments were:

1. To image the base of the Elberton granite and underlying units.
2. To take advantage of the relative seismic transparency of the Elberton granite to study the nature of the master decollement in the transition zone between the Inner Piedmont and Carolina Terrane, and

3. To place constraints on the fine-scale geologic structure of major reflectors by comparing the seismic response of the Elberton granite and other features at near-vertical angles (old COCORP studies) and wide-angles (this study).

Geological Setting

The Elberton granite is an undeformed body located in the Inner Piedmont province of northeastern Georgia (Figure 2.1). The Inner Piedmont is composed of polydeformed meta-sedimentary and metavolcanic rocks, many highly aluminous in composition. The Elberton granite is an elongated intrusion about 60 km long and 7-10 km wide trending NE-SW. It cuts across both the Inner Piedmont flank (IPF) and the Inner Piedmont core (IPC) (Griffin, 1978) and is located between two major faults: The Middleton–Lowndesville shear zone to the southeast and the Hartwell extension of the Towaliga fault to the northwest (Griffin, 1971). The Middleton-Lowndesville zone represents a major boundary in the area of study as it separates mafic Charlotte belt rocks (maximum metamorphism grade upper amphibolite) from the schists and sillimanite-grade gneisses of the Inner Piedmont (Stormer et al., 1980). The two fault zones converge toward the Elberton area (Higgins, 1971; Griffin, 1971).

Petrographically, the Elberton intrusion is fine-grained and homogenous in composition and there are no significant lithologic variations within the body (Ellwood et al., 1980; Hess, 1979; Rozen; 1978.) This has led to the interpretation of the Elberton as a single intrusion as opposed to a composite body (Stormer et al., 1980). The Elberton granite pluton is characterized in general by a slight increase in grain size toward the core and by the presence of abundant, partially assimilated xenoliths. Contacts with the surrounding rocks are sub-horizontal (Dallmeyer et al., 1981; Whitney et al., 1980.) It has

been proposed that the Elberton granite originated from anatexis of metavolcanic rocks at depths of about 18-20 km with intrusion at depths of 12 to 15 km (Stormer et al., 1980).

Geochronology

A number of attempts (Ellwood et al., 1980; Dallmeyer et al., 1981) have been made to constrain the age of late Paleozoic thrusting in the southern Appalachians by dating unmetamorphosed plutons. The Elberton granite, intruded near the southwest flank of the Inner Piedmont, has figured prominently in these studies because it is the only pluton crossed by COCORP seismic lines (Cook et al., 1979). Unfortunately, these attempts have been frustrated by the poor quality of seismic images beneath the pluton (see next section).

Recent geochronological studies suggest an age of 320 ± 20 m.y. based on U/Pb zircon dating (Ross and Bickford, 1980 in Stormer et al., 1980). Grunenfelder and Silver (1958) suggested an older age (450-490 m.y.) based on $^{238}U/^{206}Pb$, $^{235}U/^{207}Pb$, and $^{207}Pb/^{206}Pb$ ages from Elberton granite zircons. According to Dallmeyer (1978) and Ellwood et al. (1980), however, these ages appear to be inconsistent with the structural relationships and uplift history of the Piedmont. Dallmeyer (1978) and Ellwood et al. (1980) believe that these ages are older than the crystallization age of Elberton granite and suggest that many of the Elberton zircons did not recrystallize at the magmatic temperatures of the Elberton. A Rb-Sr whole rock isochron reported from low oxygen isotopic values revealed an age of 350 ± 11 m.y. (Ellwood et al., 1980), however samples from quarries contain xenoliths that give older age of 376 ± 45 m.y.with higher initial Sr^{87}/Sr^{86} of 0.7054 (Ellwood et al., 1980). A combined Rb/Sr biotite and whole rock age is younger (~ 250 m.y.) and similar to K-Ar and Ar^{40}/Ar^{39} ages but younger than Ar^{39}/Ar^{40} ages on

hornblende (Fairbairn et al., 1960; Dallmeyer et al., 1981). These results suggested that the Elberton granite cooled slowly for about 100 m.y. but did not continue cooling below the blocking temperature of biotite (300-350^{o}) (Allard and Whitney, 1994).

Previous Geophysical Work

Gravity

The regional Bouguer gravity over the southern Appalachian orogen is characterized by a steep gravity gradient that separates a prominent gravity low to the northwest and a prominent gravity high to the southeast (Figure 2.4). This gradient has been interpreted as a result of a combination of the effects of crustal thickening to the northwest, near-surface mafic rocks to the southeast, and additional density variations in the mid-crust (Long, 1979).

Based on gravity modeling studies, Long (1979) suggested that continental crustal rocks in Georgia and south Carolina extend to depths of 10 – 15 km in the Inner Piedmont and to 20 km in the Carolina Terrane. Studies conducted by Dainty and Frazier (1984) show that the gravity anomaly generated by the Elberton granite is very small, suggesting that this intrusion could be very thin or that there is no appreciable density contrast with surrounding rocks. In his modeling study of the Bouguer gravity anomalies over and near the intrusions, Frazier (1982) reported a maximum Bouguer gravity anomaly of 0.3 mGal associated with the Elberton granite. The lack of density contrast between the Elberton granite and the surrounding rocks supports the idea that the Elberton granite originated through anatexis of rocks in the vicinity of the granite (Dainty and Frazier, 1984).

Heat Flow

A linear relationship between surface heat flow and radioactivity for the crystalline rocks of the southern Appalachians including the Elberton and other 300 m.y. granites has been noted by Costain and Glover, 1980 (cited in Jurdy and Phinney, 1983). Costain and Glover (1980) suggested a uniform depth distribution for radioactive heat sources, which implies that the granite bodies extend to a common depth of 8 km.

Paleomagnetism

The Elberton granite has a magnetic foliation that dips 30^{o} to the southeast (Figure 2.2) (Ellwood and Whitney, 1980; Ellwood, 1980; Ellwood et al., 1980). Magnetic data indicate that the granitic magma may have been emplaced in the southeastern and south-central parts of the body and then flowed to the northeast and southwest due to plastic deformation. The data indicate that the entire pluton was rotated about a non-plunging N-NE trending axis to the southeast by 30^{o}-35^{o} (Ellwood et al., 1980; Ellwood, 1980; Ellwood and Whitney, 1980.) Ellwood et al. (1980) reported a Late Devonian – Early Mississippian paleomagnetic age of approximately 350 m. y. The position of the Elberton granite within a hinge block separating Inner Piedmont (Dallmeyer, 1978) from the relatively stable Charlotte-Slate belts suggests a slight rotation about the horizontal, NE-SW, axis. This consistency leads to the suggestion that any large scale thrusting involving Piedmont probably predates the emplacement of the Elberton intrusion (Ellwood, 1980).

Previous Seismic Reflection Work

Between 1978 and 1980, the Consortium for Continental Reflection Profiling (COCORP) recorded seismic reflection data along several lines in Georgia and Tennessee (Figure 2.3). The Elberton Granite was the only major pluton to be crossed by the

COCORP seismic lines (Cook et al., 1983). One of the most distinctive features observed in the seismic sections was a band of strong, continuous, muticyclic reflections extending from Tennessee (TWT: 1 s; depth: 3-4 km) southeastward beneath most of the Inner Piedmont (TWT: ~3 s; depth: 10 km). Nearly all workers (Cook et al., 1979; Iverson and Smithson, 1982) have interpreted these events as reflections from a sequence of relatively undeformed, late Precambrian/lower Paleozoic platform sediments overthrust by crystalline rocks of the Inner Piedmont and Blue Ridge.

However, the interpretation of prominent eastward-dipping reflections along the northwest flank of the Charlotte belt, just southeast of the Elberton granite, has been more controversial. Cook et al. (1979) suggested that these events and a band of less continuous, nearly horizontal events (TWT: 2 s; depth: 6 km) beneath the Carolina Terrane represent more overthrust platform sedimentary rocks. Iverson and Smithson (1982) argued that the dipping reflections mark the root zone of the master decollement, and associated the less continuous horizontal reflections with mylonites and layered volcanics.The poorer continuity was also attributed in part to poorer coupling of seismic sources and to scattering of seismic energy by the numerous granitic intrusions and diabase dikes. Figure 2.4 shows a crustal cross section along COCORP Georgia line 1 where the master decollement lies within an antiformal warp reaching the base of the Elberton granite. Phinney and Roy-Chowdhurry (1989) combined coherency filtered CDP (common depth point) stacks for COCORP lines 1, 5, and 8 into a single model. They interpreted these southeast–dipping features as the western flank of an open syncline that is located under the Charlotte Belt and which forms an eastward extension of the main detachment.

According to the interpretation of Cook et al. (1979; 1983), the Elberton granite was transported within enveloping rocks of the Inner Piedmont during the Alleghanian orogeny by several hundred km to the northwest. The interpretation of Iverson and Smithson (1982) involves almost no movement of the Elberton over this master decollement but does not rule out the possibility that part of the Elberton was truncated and transported along thrust faults at shallower depths.

COCORP data directly over the Elberton granite have been difficult to interpret because the COCORP experiments were designed to optimize signal quality for the lower crust and uppermost mantle. Jurdy and Phinney (1983) reprocessed data from COCORP Georgia line 1 in an attempt to improve subsurface images of the Elberton granite. In the common-depth-point (CDP) section, the Elberton granite was seismically transparent and at about 3 s TWT (depth: 9 km) there were some indications of horizontal reflectors, which they interpreted as the Valley and Ridge sediments beneath the crystalline thrust sheet (Figure 2.5). Migrated sections (Jurdy and Phinney, 1983) revealed improvement in the continuity of the reflections beneath the granite, which suggested that the Valley and Ridge equivalent reflectors were not disturbed. The migrated sections imaged reflections from 10-12 km (3- 4 s TWT) but they were not able to do so within the upper 2-4 km.

Unfortunately, neither the migrated nor the reprocessed CDP sections were able to resolve the shape of the body. On the migrated sections there are numerous reflectors at depths between 4 and 10 km. These reflectors are similar to those in the area of non-granitic rocks. This made it difficult to decide if these reflectors are related to the Elberton granite. The upper 3 km (1 s TWT) of the crust were poorly imaged because of interfering shear waves. Muting of the S-waves resulted in complete elimination of

reflections present at 2 km and partial elimination of reflections to ~ 6 km. To resolve structure in the top 3-4 km, Jurdy and Phinney (1983) tried surgical muting (elimination) of the early, large-amplitude and low velocity arrivals by bandpass filtering prior to CDP stacking. This approach allowed the recovery of some reflectors between 0.5 and 1 s (1.5-3 km) (Figure 2.7a). Another approach that suppressed interfering arrivals by applying apparent-velocity filters to CDP gathers before CDP stacking shows non-continuous reflectors at a two-way travel time of 1 s (Figure 2.7b).

Recording Strategy

When compared to the COCORP work, the current study is local, mainly focused on the Elberton granite and the surrounding rocks. The recording parameters for the wide-angle study were chosen to optimize coverage of the top 12 km of the crust, especially for the uppermost 2-4 km where reflections were poorly imaged in the COCORP sections. The wide-angle technique employed for this study takes advantage of the increase in reflection coefficients with incidence angle (Braile and Chiang, 1986) to image relatively subtle contrasts in acoustic impedance between rock units of similar composition.

The table below compares recording parameters for the COCORP and wide-angle experiments.

	Current work Smaller deployments "point soundings"	COCORP work (Georgia line 1)*
- S-R range	7-15 km	469 - 6834 m
- Geophone	4.5 Hz (3-component)	7.5 Hz (single component)
- Geophone spacing	50 -100 m	67.1 m
- Recorder	twenty PRS-4	96-channelMDS-10
- Sample rate	5 ms	8 ms
- seismic source	Instantaneous quarry blasts	5 Vibrators
- line length	0.5-1 km/deployment total : ~8-9 km	185.9 km

* Source (Gremell and Cook (1985); Kaufman (1979).)

The geometry of the experiment was based on the optimum-offset method (Hunter and Pullan, 1989) that was guided by the calculation of travel time curves (Figure 2.8). The main goal of these calculations was to avoid interference of reflections from the target interfaces with direct S waves and surface waves. For example, to record reflections from a depth of 3 km without interference from direct shear waves and surface waves, the offset must be greater than 4.5 km. To avoid contamination of reflections from greater depth (10 km), the offsets should be greater than 14.5 km.

The experiment consisted of 9 deployments (Figure 2.9) distributed over a wide area that provided "point soundings" at critical distances and a variety of raypath azimuths. The critical distances are the minimum distances from the source at which the

first critical (total) reflection can be recorded. The source-receiver distances were chosen to record post-critical reflections from interfaces at depths between 2 and 12 km. The recording was carried out using closely spaced recorders (50-100 m) to avoid spatial aliasing (Hawman, 1996; Hawman et al., 1990). Blasts were recorded using 20 PRS-4 recorders with three-component 4.5 Hz geophones. Shot-receiver offsets ranged from 7-15 km. Seismic sources were instantaneous blasts at dimension-stone quarries. Two types of instantaneous blasts were recorded: "line shots", which consist of vertical holes, and "lifting shots", which consist of both vertical and horizontal holes (Khalifa et al., 2001a,b, and c). Both are designed to detach large blocks intact. We recorded one lifting shot and 8 line shots. The lifting shot and 3 of the line shots yielded usable signals.

The recording strategy (Hawman, 1996) involved programming the PRS-4 systems to wake for recording every fifteen minutes for a 30-second duration and that is repeated for duration of 6 hours. This was done due to the limitation of the PRS's memory (1 MB). Blasts were timed with one or two PRS-4 systems deployed at the quarry at a distance of roughly 100-200 m from the shot. Arrangements were made with the quarry staff to fire the blasts within the first few seconds of the 15-minute mark using digital watches that were synchronized to WWV. The fieldwork was carried out during Summer 2000.

Processing

Processing steps for the shot gathers are summarized in the flow chart (Figure 2.10).

Trace editing and bandpass filters

Along with the removal of individual dead and noisy traces, large portions of the shot gathers were edited where background noise dominated the seismograms. Amplitude spectra for the shot gathers were studied to discern noise from signal. Amplitude spectra show signal energy at frequencies as high as 45-50 Hz (Figure 2.11). Bandpass filtering was applied to suppress coherent and incoherent noise. The filters were designed to attenuate surface waves and enhance higher frequencies (P waves). Optimum filter bandpass settings varied for each gather. For some blasts, the optimum filter settings varied for subsets of traces, so the gathers were subdivided and filtered with different bandpass settings. Notch filters were also applied to eliminate noise at 60 Hz (the power line frequency, which was consistent in almost all shots) and other narrow-band noise generated by local industry. Filtering removed much of the noise.

Deconvolution

Predictive deconvolution (Robinson and Treitel, 1980; Yilmaz, 1987) was applied to improve the resolution of the seismic data by compressing the source wavelet. Deconvolution enhanced the signal to noise ratio for most of the shots (Figures 2.12 - 2.14). The effect of predictive deconvolution on amplitude spectra is shown in Figure 2.13. An example of deconvolution using spectral whitening (Yilmaz, 1987) is shown in Figure 2.15.

Velocity Reduction and Statics

The shot gathers were plotted with a reduction velocity of 5.8 km/s (the apparent velocity of direct P waves) to help identify disruption of first arrivals and other coherent events by static shifts (variations in travel time caused by topography and lateral variations in near-surface seismic velocity). In this study, non-surface-consistent static corrections were applied to enhance the coherency of first breaks and/or other prominent arrivals (Hawman et al., 2000). Cross-correlation was used to find static shifts for traces in each velocity-reduced gather. The choice of reduction velocity depends on the target arrival used for the static correction; reflections will be characterized by apparent velocities greater than 5.8 km/s. Static corrections improved the coherence of reflections (Figures 2.13 and 2.15). The raw and final shot gathers after applying static correction are shown in Figures 2.17, 2.22, 2.27, and 2.32.

Slant Stacking and Coherency Filtering

The static-corrected shot gathers then were slant stacked to provide objective measures of apparent velocity for coherent arrivals. Slant stacking represents the transformation of data from x (distance) and T (2-way travel time) to ρ (ray parameter or inverse apparent velocity) and travel time for the average offset of the array. This process is a linear wave field transformation that decomposes the wave field into its plane-wave components (Phinney et al., 1981); this allows the identification of various types of arrival on the basis of apparent velocity (Hawman et al., 1990; Hawman and Phinney, 1992). Slant stacking also suppresses noise. For random noise, the improvement in signal level is proportional to $n^{1/2}$, where n is the number of traces in the shot gather. Slant

stacks are computed by summing amplitudes along lines of constant slope (p) and intercept time:

$$\Psi(\rho,\tau) = \sum_{i=1}^{n} \Phi(x_i, \tau + \rho x_i)$$

where ψ is the slant stack, Φ is the input record section, τ is the intercept time, and ρ is the ray parameter (s/km).

For the stacks computed here, the intercept time corresponds to the travel time to the center of the recording array. In general, the ray parameter for reflections recorded at a given distance from a shot will decrease (the apparent velocity will increase) with increasing depth to the reflectors. Ray parameters for P-SV converted reflections are distributed along a roughly parallel band at larger times and ray parameters. Slant stacks before and after applying static corrections of all migrated shot gathers are presented in Figures 2.18, 2.23, 2.28, and 2.33. The slant stacks computed for shot gathers with statics corrections show improved focusing and coherence.

The semblance of the slant stack was also computed. Semblance is a coherency measure defined as the energy ratio for normalized input to output:

$$S(\tau,\rho) = \frac{\sum_{k=-m}^{m} [\sum_{i=1}^{n} \Phi(x_i, \tau + k\Delta\tau + \rho x_i)]^2}{n \sum_{k=-m}^{m} \sum_{i=1}^{n} \Phi^2(x_i, \tau + k\Delta\tau + \rho x_i)}$$

(Douze and Laster, 1979), where n is the number of traces, τ is the intercept time, ρ is the ray parameter (s/km) and m is the number of samples in a time gate centered about the

sample of interest. Semblance is not sensitive to amplitude differences between different coherent arrivals in a gather but is affected by amplitude variations along a given arrival (the beam). Therefore the traces were normalized by their rms values prior to stacking. Statistical properties of the semblance measure are discussed by Douze and Laster (1979). Semblance of all shot gathers before and after applying static correction are presented in Figures 2.19, 2.24, 2.29, and 2.34.

The semblance was used to derive a coherency filter to isolate the most reliable portions of the slant stack prior to migration. The semblance was first smoothed in the frequency domain by high-cut filtering (Stoffa et al., 1981). Then a coherency filter was constructed by assigning zeros for all samples in the smoothed semblance with values less than the chosen threshold and value of 1 for the remaining samples. The slant stack then was multiplied by this filter. Raising the threshold value results in more focused events in the slant stack. The smoothed semblances of all gathers after applying static correction are presented in Figures 2.20, 2.25, 2.30, and 2.35.

Migration

The coherency filtered slant stacks were used as an input to the migration process, which is based on the method explained by Hawman and Phinney (1992). Migration of coherency-filtered slant stacks minimized the spatial extent of "smiles" generated by conventional migration. I used a migration algorithm (Hawman, in preparation) which is an extension of the approach described by Hawman and Phinney (1992) (Figure 2.38).

This algorithm maps samples in travel-time/ray-parameter space into dipping segments in the subsurface image. The widths of residual "smiles" are determined by the beam widths of the recording arrays. The actual length of reflecting interfaces should be

approximately half the width of the recording array. The smearing or "smiles" seen in the migrated images represent confidence regions; the width of the smiles is determined by the degree of smearing (uncertainty in ray parameter) in the slant stack, which in turn is controlled by the beam-width of the recording array. The array beam-width is the ability of the array to resolve events with different ray parameter (inverse apparent velocity). It is determined by the length of the recording array and the frequency content of the signal (longer arrays and higher frequencies allow smaller differences in ray parameter to be resolved).

The velocity model used for migration (Figure 2.37) consists of 6 layers and was determined based, in part, on the geometry of the experiment where the top layer (0.5 km) velocity was calculated from the travel time of the direct P wave arrival and the rest of the 15 km based on the averaged velocities for P wave derived in previous laboratory measurements carried out at room temperature and confining pressures up to 10 kbar for similar rock units (Birch, 1960).

Description of the Migrated Sections

The data set consists of a relatively small number of blasts recorded with small-aperture (1 km) arrays. Therefore the migrated sections do not represent a complete image of the subsurface structure between each blast and array. In addition to the smearing described above, the reflector distributions for these partial images are strongly controlled by the sparse recording geometries (Hawman et al., 2001).

Blue Ribbon (line B) migrated section

Figure 2.39a shows migrated sections generated for a range of coherency filter settings. The section described here belongs to the slant stack that was coherency filtered

using a cutoff semblance value of 0.45. The distance range of the recording was 14.01-14.90 km. Ray paths for this blast are almost parallel to the direction of the maximum dip of the rocks. This section contains a series of events with a maximum depth of 11.0 km s (3.65 s TWT) (Figure 2.39). At depths between 10 and 11 km, a series of events with gentle apparent dip (0-7 degrees toward the southeast) occur with a relatively good horizontal resolution of 2 km (km 8 to km 10). At 9.4 km (3.1 s) there is an event with very gentle apparent dip and relatively poor horizontal resolution of about 4 km (km 5.6 to km 9.6). Above this event is a series of southeast dipping events (0-5 to 8-20 degrees) at depths of 6.5 to 9.5 km. Another sub-horizontal event lies above this at a depth of 6 km (2.0 s) with an apparent dip of 0-8 degrees to the southeast. The shallowest events occur as a package at depths between 3 and 4 km; within this package, horizontal resolution improves with depth. The part of this package that is characterized by the highest amplitude has an apparent dip of 0-11 degrees to the northwest. Migrated sections produced from slant stacks with higher threshold settings are more focused (Figure 2.39 b-c). These sections though do not contain all events.

Dye Granite (line C) migrated section

The section described here (Figure 2.40a) was generated from the slant stack that was coherency filtered using a cutoff semblance value of 0.46. The distance range of this recording was 11.53-12.48 km. This recording is parallel to COCORP Line1 (Figure 2.9), at an angle to the regional dip. The migrated section is dominated by horizontal to sub-horizontal, well focused events except for two steeply dipping events at the NNW end of the section. The deepest event occurs at 6.7 km (2.2 s TWT). The event has a resolution width of about 2.8 km (km 6.4 to km 9.2) and shows a mostly horizontal appearance

(apparent dip: 0 – 6 degrees to the NNW). Immediately above is another event which is horizontal and well resolved. This event has a resolution width of 2.2 km (km 5.5 to km 7.7). At a depth of 6 km, a slightly dipping event with better horizontal resolution is observed (apparent dip: 0-5 degrees NNW). Two similar events are observed at 5.2 (1.76 s) and 4 km (1.365 s) depth. They are both sub-horizontal with resolution widths of 2 km. A shallower and better resolved horizontal event (km 6 to km 7.2) is observed at a depth of 3.25 km (1.12 s). The shallowest event is observed at a depth of 1.5 km (0.53 s) with less than 4 degrees apparent dip toward the SSE. Other migrated coherency filtered slant stacks from this blast are presented in Figure 2.40 b-d. As mentioned above, increasing the threshold value for the slant stack yields a more focused image, but some events may be entirely eliminated.

Boyd 3 (line F) migrated section

The section described here (Figure 2.41a) was generated from the slant stack that was coherency filtered with a cutoff semblance value of 0.45. The distance range for this recording was 13.09-14.18 km. The ray paths for this recording are almost perpendicular to the ray paths for the Blue Ribbon recording. The deepest event is observed at 8.5 km (2.84 s TWT) and is well resolved (resolution width: 0.8 km; km 6.4 to km 7.2). At a depth of 8.0 km (2.68 s), a short event with an apparent dip of 12 degrees to the SE is observed. A multicyclic event appears at 7.8 km (2.6 s) with a poorer resolution width of 3.6 km (from km 6 to km 9.6). At a depth of 6.6 km (2.23 s), a well-resolved south-dipping event is observed. A horizontal, multicyclic event appears at depths between 4.7 and 5 km (1.6-1.7 s). Horizontal resolution for this event is relatively poor (4 km). The shallowest complex of events consists of two lower events that dip gently toward the

south; the top event is sub-horizontal. Other migrated coherency filtered slant stacks from this blast are presented in Figure 2.41 b-d.

Boyd 2 (line A) migrated section

The section described here (Figure 2.42a) was generated from the filtered slant stack that was coherency filtered with a cutoff semblance value of 0.45. The distance range of this recording was 7.77-9.02 km. Only the portion of the gather recorded at offsets between 7.77 and 8.2 km is shown here. The deepest observed event (depth: 5.5 km (1.86 s TWT)) is flat and well resolved. One kilometer above, at 4.5 km, another event is observed with similar horizontal resolution and an apparent dip of 10 degrees toward the west. A poorly resolved but mostly flat event is observed at 3.8 km (1.3 s TWT). Apparent dips range from zero to 15^{o} to the west. An east-dipping event is observed at a depth of 2.7 km (0.93) with an apparent dip of 15 degrees. The shallowest events appear at depths of about 2 and 2.2 km. Both are sub-horizontal, with large resolution widths. Other migrated coherency filtered slant stacks from this blast are presented in Figure 2.42 b, c.

Interpretation

All previous seismic work on the Elberton granite used near-vertical reflections. This is the first time that the Elberton granite has been examined using a wide-angle experiment. Because it takes advantage of increases in reflection coefficients with incidence angle, the wide-angle reflection technique can image relatively subtle contrasts in acoustic impedance. However, because of the limited number of sources and receivers used for this study, the migrated sections discussed above represent only partial images of the subsurface. The subset of features illuminated by the experiments is controlled by the

distribution of blasts and recording arrays as well as by the geologic structure (Hawman et al., 2001). As additional sources and arrays are deployed along these profiles (see "Suggestions for Future Work"), the images will become more complete.

Events in the top 4 km

Migrated sections in the current study contain features that appear to be consistent and others that appear in one section and not in others. The wide-angle migrated sections show shallower events that have not been observed in previous work. At about 3 km, there are events that are noticed in the Blue Ribbon, Dye, and Boyd 3 migrated sections (Figures 2.39 - 2.41). These events appear either in a package of reflections as in the Blue Ribbon migrated section that started at 3 km and extended to 4 km of depth (1-1.37 s TWT), or as single events that appear at 3.2 and 4 km (1.1-1.37 s TWT) in the Dye Granite migrated section, at 2.5 and 4.5 km (0.87 – 1.5 s TWT) in the Boyd Granite 3 migrated section, and at 2 and 3.8 km (0.7 and 1.3 s TWT) in the Boyd Granite 2 migrated section. The Elberton granite is thinner in the migrated section of Boyd granite 2 (2km) which could be explained from the outcrop (Figure 2.9) as a separated thin remnant of a larger body. Taken together, a picture emerges of a layered complex beginning at 2-3 km depth and bottoming out at roughly 4 km. This feature is similar to layering found near the base of other granitic batholiths (Lynn et al., 1981) and could be interpreted as layering near the base of the Elberton granite.

Lynn and others (1981) proposed four interpretations for subhorizontal reflections associated with the base of batholithic bodies. The first interpretation is that the granitic magma is underplated by basaltic magma; this is consistent with the "continued injection of hot basaltic magmas to keep some silicic magma systems hot", and "the common

occurrence of basalt along with silicic extrusives". A second explanation is related to melting of crustal rocks by mantle basalts which yields cumulate layers of mafic composition. Contrasts in acoustic impedance between these layers and overlying rocks would cause reflections near the base of the batholiths. Reflections due to rocks of migmatitic composition with alternating layers of minerals with different densities (acidic and mafic) represent the third interpretation. The last explanation attributes subhorizontal reflections to tectonic contacts, either thrust fault contacts between the base of the intrusion and layered sediments, or mylonitic shear zones of finite thickness. Reflection from a sequence of thin layers can greatly increase reflection amplitudes through constructive interference. The effect depends on the scale of layering, the layer velocities, the angle of incidence, and the frequency content of the signal (Fountain et al., 1984; Braile and Chiang, 1986). Within shear zones, fine-scale layering coupled with contrasts in the degree of anisotropy between adjacent layers (weak anisotropy within feldspar-rich layers; strong transverse anisotropy with the slow velocioty oriented vertically within mica-rich layers) enhances reflectivity (Fountain et al., 1984). Anastomozing layering/structure within such a shear zone beneath the Elberton Granite could help to explain the variations in apparent dips and thicknesses of the shallow layered complexes seen in the wide-angle migrated sections. The absence of reflections above 2 km is consistent with an intrusive body that is seismically transparent.

Events between 4 and 10 km

Directly beneath the layered complex, the wide-angle migrated sections show a relatively reflection-free zone, followed by gently dipping reflections at roughly 6 km. These events have gentle NNW apparent dips (0 - 5^{o}) in the Dye granite migrated section

and a gentle SE apparent dip (0 – 8^{o}) in the Blue Ribbon migrated section. Similar events also appear in the Boyd granite 3 migrated section but at 6.6 km with gentle apparent dip toward the south. The Blue Ribbon migrated section (Figure 2.39) is unique in displaying southeast-dipping events that span a depth of 6-10.5 km. These events are well correlated with the southeast-dipping events in COCORP line 1 (Figures 2.5 and 2.43). The COCORP line shows apparent dips ranging from 15^{o} (Jurdy and Phinney, 1983) to about 20^{o} (Iverson and Smithson, 1983). None of these events appear in the sections reprocessed by Phinney and Roy-Chowdhury (1989) except for a hint of the southeast dipping arrivals after 3 seconds (Figure 2.44). This study shows a range of apparent dip for these arrivals between 8-20 degrees to the SE. Interestingly, these events are parallel to the southeast projection of the Towaliga-Hartwell fault zone.

The southeast-dipping reflections are not observed in migrated images for the other blasts; two of the blasts (Boyd Granite 3 and Dye Granite) were recorded along raypaths at appreciable angles to the dip direction and the third was recorded at smaller offsets where shear waves interfered with reflections arriving from depths greater than 5 km.

Events at depths greater than 10 km

The Blue Ribbon blast produced the only migrated section that shows an event at 11 km; for the other blasts, this event may have been obscured by interfering shear waves. Reprocessed COCORP sections over the Elberton (Iverson and Smithson, 1983; Jurdy and Phinney, 1983) show weaker, sporadic arrivals at two-way travel times consistent with the 11-km event. The event in the wide-angle migrated section is multisyclic, subhorizontal, relatively high in amplitude, and well resolved. Reflections

with similar characteristics in profiles across other crystalline terranes have been interpreted as mylonitic shear zones (Smithson et al., 1979; Hurich et al., 1985). We interpret this event as a package of reflections from the master decollement. As noted earlier, this event loses considerable strength in COCORP sections as one travels southeastward from the Brevard Zone. The wide-angle results constrain the depth of this feature beneath the southeast flank of the Inner Piedmont and show that it is layered. However, questions regarding the composition of rocks within the fault zone (whether they are mylonites or relatively undeformed platform sedimentary rocks) remain unresolved. A high-resolution analysis of seismic wave velocities within this zone based on additional wide-angle data would help resolve this issue.

Suggestions for Future Work

Taking advantage of dimension-stone quarries as inexpensive seismic source offered a good chance to test their capabilities for imaging crystalline rocks. Based on the limited number of blasts recorded, "lifting shots" are recommended; the signal/noise ratio in the Blue Ribbon shot gather is much higher than the other recordings in which we used the "line shots" as a seismic source. Due to operation conditions at the dimension-stone quarries, the blasts are not available on a daily basis and are subject to last-minute changes due to weather conditions and production delays.

I recommend continued recording with short aperture arrays along different azimuths. Some of these arrays should overlap COCORP lines 1 and 5 which would allow a direct comparison of normal-incidence and wide-angle reflections.

A longer, reversed, wide-angle profile placed parallel to regional strike, could be used for constructing a velocity model for the Inner Piedmont beneath the Elberton granite to a depth of 12 km.

Regarding the seismic source, using another source such as vibroseis will help in two ways: A better coupling within the crystalline rocks will be achieved, and the flexibility in placing the arrays will not be restricted to a specific direction.

More complete wide-angle coverage would allow estimation of velocities which would be especially important for determining the nature of multicyclic reflections at the base of the Elberton granite.

Conclusions

1. Instantaneous blasts fired at dimension-stone quarries generate usable seismic signals (frequency range: (4 –50 Hz) to distances of at least 15 km. Based on the limited number of blasts recorded, it appears that "lifting shots" produce stronger signals than "line shots".

2. High-amplitude, multicyclic events arriving shortly after the direct P wave are interpreted as post-critical reflections from a layered complex at depths of 2 to 4 km. The events at 2 km are among the shallowest yet detected for the Elberton granite and the layered complex resembles reflection packages observed beneath other granitic plutons. Apparent dips are small (0-10 degrees to the southeast). Possible interpretations for the layered complex include:

    a. A shear zone at the base of the granite, associated with late Alleghanian compression. Mylonitic shear zones are characterized by preferred orientation of

minerals and consequently different seismic velocities from surrounding unmylonitized rocks which explain why these zones are highly reflective.

b. Compositional layering within the intrusive body itself, as originally emplaced. The multicyclic reflections may be generated by basaltic intrusions, indicating that the granitic magma was underplated by basaltic magma. Alternatively, the layering may be due to the melting reaction of mantle basalts to the crustal rocks, yielding cumulate layers of mafic composition. Compositional layering also could be related to the presence of migmatitic rocks with alternating layers of minerals with different densities (acidic and mafic).

3. Other prominent features in the migrated image include:

   a. Subhorizontal reflections at a depth of roughly 6 km.

   b. A zone of reflections at depths between 5 and 10 km, with apparent dips ranging from 8^{o} to 20^{o} to the southeast. These reflections are similar to reflections seen in reprocessed COCORP Georgia line 1 and may be associated in part with the subsurface projection of the Towaliga-Hartwell fault zone.

   c. A high amplitude, multicyclic, gently SE-dipping reflection at a depth of roughly 11 km that possibly marks the southeastward extension of the master decollement to the southeast flank of the Inner Piedmont. This 500-m thick package could consist of undeformed platform sedimentary rocks or a mylonitic shear zone.

4. Improvement of the results in the upper 2-4 km has been achieved using the wide-angle technique where the reflections were poor in the COCORP work. The improvement resulted from:

a. The geometry of the experiments which employed the optimum offset method in recording to avoid the interference of the shear waves.

b. The use of the wide-angle technique itself which took advantage of the increase in reflection coefficients near the critical angle to image relatively subtle contrasts in acoustic impedance between rock units of similar composition.

References

Allard, G. O., and J. A. Whitney, Geology of the Inner Piedmont, Carolina Terrane, and Modoc Zone in Northeast Georgia, *Georgia DNR, Environmental division, Georgia Geol. Surv., Project report 20,* 36p, 1994.

Birch, F., The velocity of compressional waves in rocks to 10 kilobars, 1, *J. Geophys. Res*., *65*, 1083-1102, 1960.

Braile, L. W., and C. S. Chiang, The continental Mohorovicic discontinuity: Results from near-vertical and wide-angle seismic reflection studies, *Geodynamic series, Am. Geophys. Union, 13*, 257-272, 1986.

Cook, F. A., L. D. Brown, S. Kaufman, and J. E. Oliver, The COCORP seismic reflection traverse across the Southern Appalachians, *AAPG Studies in Geology*, No. 14, Tulsa, OK, 61 p., 1983.

Cook, F. A., D. S. Albaugh, L. D. Brown, S. Kaufman, J. E. Oliver, and R. D. Hatcher, Thin skinned tectonics in the crystalline southern Appalachian: COCORP seismic reflection profiling of the Blue Ridge and Piedmont, *Geology, 7*, 563-567, 1979.

Coruh, C. J., K. Costain, R. D. Hatcher, T. L. Pratt, R. T. Williams, and R. A. Phinney, Results from regional vibroseis profiling: Appalachian ultra-deep core hole site study, *Geophys. J. R. Astron. Soc., 89*, 147-157, 1987

Costain, J. D., and L. Glover, III, Heat flow in granites, Implications for crustal structure in the Appalachians, in the Caledonides in the USA, edited by W. R. Wones, 215-220, *Dept. Geol. Sci., Va. Polytech. Inst. and State Univ., Blacksburg, VA.,* 1980.

Dainty, A. M., and J. E. Frazier, Bouguer gravity in northeastern Georgia: A buried suture, a surface suture, and granites, *Geol. Soc. Am. Bull., 95*, 1168-1175, 1984.

Dallmeyer, R. D., $^{40}Ar/^{39}Ar$ incremental release ages of hornblende and biotite across the Georgia Inner Piedmont: Their bearing on Late Paleozoic-Early Mesozoic tectonothermal history, *Am. J. Sci.*, *278*, 124-149, 1978.

Dallmeyer, R. D., J. R. Hess, and J. A. Whitney, Post-magmatic cooling of the Elberton Granite: Bearing on the late Paleozoic tectonothermal history of the Georgia Inner Piedmont, *J. Geology*, *89*, 585 – 600, 1981.

Dallmeyer, R. D., Late Paleozoic thermal evolution of crystalline terranes within portions of the U.S. Appalachian orogen, *The Geology of North America,* F2, The Appalachian-Ouachita in the United States, *Geol. Soc. Am,* 417–444, 1989.

Douze, E. J., and S. J. Laster, Statistics of semblance, *Geophysics*, 44, 1999-2003, 1979.

Ellwood, B. B., Magnetization of the Elberton Granite*: in* Stormer, J. C., and Whitney, J. A., Geological, Geochemical, and Geophysical Studies of the Elberton , Eastern Georgia, *Atlanta, Ga, Dept. Natural Res. Guide book 19*, 80-97, 1980

Ellwood, B. B., J. A. Whitney, D. B. Wenner, D. Mose, and Amerigian, Age, Paleomagnetism, and tectonic significance of the Elberton granite, northeast Georgia Piedmont, *J. Geophys. Res.*, *85*, 6521– 6533, 1980.

Ellwood, B. B., and J. A. Whitney, Magnetic Fabric of the Elberton Granite, Northeast Georgia, *J. Geophys. Res*., *85*, 1481 - 1486, 1980.

Fairbairn, H. W., W. H. Pinson, P. M. Hurley, and R. F Cormier, A comparison of the ages of coexisting biotite and muscovite in some Paleozoic granite rocks, *Geochimica et Cosmochimica Acta, l9*, 7-9, 1960.

Fountain, D. M., Hurich, C. A., and Smithson, S. B., Seismic reflectivity of mylonite zones in the crust, *Geology*, *12*,195-198, 1984.

Frazier, J. E, Analysis of Bouguer gravity anomalies in the region surrounding the Elberton granite and Danburg granites in east-central Georgia, (*M.S. Thesis*), Atlanta, Georgia, Georgia Institute of Technology, 149p., 1982..

Gremell, P. E., and F. A. Cook, Shear waves (?) on COCORP southern Appalachian reflection data, *J. Geophys. Res.*, *90*, 11, 367 - 11, 373, 1985.

Griffin, V. S., Detailed analysis of tectonic levels in the Appalachian Piedmont, *Geol. Rundschau, 67,* 180-201, 1978.

Griffin, V. S., The Inner Piedmont of the southern crystalline Appalachians, *Geol. Soc. Am. Bull., 82, 1885-1898,* 1971.

Grunenfelder, M., and L. T. Silver, Radioactive age-dating and its petrological implications for some Georgia granites (abstract), *Geol. Soc. Am. Bull., 69*, p. 1574, 1958.

Harris, L. D., and K. C. Bayer, Sequential development of the Appalachian orogen above a master decollement – A hypothesis, *Geology, 7*, 568-572, 1979.

Hatcher, R. D., Developmental model for for the southern Applachians, *Geol. Soc. Am. Bull.*, 83, 2735-2760, 1972.

Hawman, R. B., Wide-angle, three-component seismic reflection profiling of the crust along the East Coast Gravity High, southern Appalachian, using quarry b lasts*, J. Geophys. Res., 101*, 13,933-13,945, 1996.

Hawman, R. B., R. H. Colburn, D. A. Walker, and S. B. Smithon, Processing and inversion of refractionand wide-angle reflection data from the 1986 Nevada Passcal Experiment , *J. Geophys. Res., 95*, 4657-4691, 1990.

Hawman, R. B., and R. A. Phinney, Structure of the crust and upper mantle beneath the Great Valley and Allegheny Plateau of Eastern Pennsylvania: 2.Gravity modeling and migration of wide-angle reflection data, *J. Geophys. Res.*, 97, 393-415, 1992.

Hawman, R. B., M. C. Chapman, C. A. Powell, and J. E. Clippard, and H. O. Ahmed, Wide-angle reflection profiling with quarry blasts in the Eastern Tennessee seismic zone, *Seismol. Res. Lett*, *72*, 108-122, 2001.

Hawman, R. B., Prosser, C. L., and Clippard, J. E., Shallow seismic reflection profiling over the Brevard Zone, South Carolina, *Geophysics, 65*, 1388-1401, 2000.

Hess, J. R., Geochemistry of the Elberton Granite and the geology of the Elberton west quadrangle, Georgia, *M. S. Thesis, University of Georgia*, 193 p., 1979.

Higgins, M. W., in Rozen (1978), Cataclastic rocks: *U. S. Geol. Survey Prof. Paper* 687, 97 p., 1971.

Hunter, J. A., and Pullan, S. E., Optimum offset shallow reflection technique, *Proceedings of the Symp. On the application of geophysics to engineering and environmental problems, Soc. Eng. & Mineral Exploration Geophysicits*, *2*,143-174, 1989.

Hurich, C. A., S. B. Smithson, D. M. Fountain, and M. C. Humphreys, Seismic evidence of mylonite reflectivity and deep structure in the Kettle dome metamorphic core complex, Washington, *Geology, 13*, 577-580, 1985.

Iverson, W. P., and S. B. Smithson, Master decollement root zone beneath the southern Appalachians and crustal balance, *Geology*, *10*, 241 - 245, 1982.

Iverson, W. P., and S. B. Smithson, Reprocessing and reinterpretation of COCORP southern Appalachian profiles, *Earth and Planetary Science Lett., 62,* 75 - 90, 1983.

Jurdy, D. M., and R. A. Phinney, Seismic imaging of the Elberton granite, Inner Piedmont, Georgia, using COCORP southern Appalachian data, *J. Geophys. Res., 88*, 5865-5873, 1983.

Kaufman, S., COCORP southern Appalachian data, *Geophysics, 44,* 1598 - 1599, 1979.

Khalifa, M. O., J. A. Kucinskis, and R. B. Hawman, 2001a, Wide-angle reflection studies of the Elberton Granite and surrounding Inner piedmont, northeast Georgia, *Geol. Soc. Am., Southeastern Section, Raleigh, North Carolina,* April 5, 2001.

Khalifa, M. O., J. A. Kucinskis, J. E. Clippard, and R. B. Hawman, 2001b, Wide-angle reflection profiling of the Elberton granite and deep structure of the Inner Piedmont, Southern Appalachians, using instantaneous and ripple-fired quarry blasts, *EOS Trans. Am. Geophys. Union, 82, 20, Spring Meeting Suppl., Abstract S52A-10*, 2001.

Khalifa, M. O., J. A. Kucinskis, J. E. Clippard, and R. B. Hawman, 2001c, Short-aperture array studies of crustal structure in the southern Appalachians using instantaneous and delay-fired quarry blasts, *Seismol. Soc. America, Eastern Section, Annual Meeting,* 2001.

Long, L., The Carolina Slate belt – Evidence of a continental rift zone, Geology, *7,* 180-184, 1979

Lynn, H. B., L. D. Hale, and G. A. Thompson, Seismic reflections from the basal contacts of batholiths, *J. Geophys. Res.,* 86, *11*, 10633 -10638, 1981.

Phinney, R. A., and K. Roy-Chowdhury, Reflection seismic studies of crustal structure in the Eastern United States, *Memoir, Geol. Soc. Am.,172*, 613-653, 1989.

Phinney, R. A., K . Roy-Chowdhury, and L. N. Frazier, Transformation and analysis of record sections, *J. Geophys. Res, 86*, 359-377, 1981.

Robinson, E.A. and S. Treitel, 1980; Geophysical Signal Analysis, *Prentice-Hall, Englewood Cliffs NJ*, 466 p, 1980.

Ross, C. R., and M. E. Bickford, The U-Pb age of zircons from the Elberton granite, Piedmont of Georgia: *in* Stormer, J. C., and J. W. Whitney, Geological, Geochemical, and Geophysical Studies of the Elberton Batholith, Eastern Georgia: Atlanta, Georgia *Dept. Natural Res. Guide Book 19*, 52-62, 1980.

Rozen, R. W., The Geology of the Elberton East quadrangle, Georgia, *M.S. Thesis, Athens, University of Georgia*, 110 p., 1978.

Smithson, S. B., J. A. Brewer, S. Kauffmann, J. E. Oliver, and C. A. Hurich, Structure of the Laramide Wide River uplift, Wyoming, from COCORP deep reflection data and from gravity data, *J. Geophys. Res., 84*, 5955-5972, 1979.

Stormer, J. C., J. A. Whitney, and J. R. Hess, Petrology and geochemistry of the Elberton Granite, *in* Geological, Geochemical, and Geophysical Studies of the Elberton , Eastern Georgia, *Atlanta, Ga, Dept. Natural Res. Guide Book 19*, 10-30, 1980.

Stoffa, P. L., P. Buhl, J. B. Diebold, and F. Wenzel, Direct mapping of seismic data to the domain of intercept time and ray parameter: A plane wave decomposition, *Geophysics, 46*, 255-267, 1981.

Whitney, J. A. and J. R. Hess, Geochronology and coolin history of the Elberton granite, *in* Geological, Geochemical, and Geophysical Studies of the Elberton, Eastern Georgia, *Atlanta, Ga, Dept. Natural Res. Guide Book 19,* 63-79, 1980.

Whitney, J. A. D. E. Wells, and R. W. Rozen, Structural and tectonic setting of the Elberton , Eastern Georgia Piedmont, *in* Geological, Geochemical, and Geophysical Studies of the Elberton , Eastern Georgia, *Atlanta, Ga, Dept. Natural Res. Guide Book 19*, 1-10, 1980.

Yilmaz, O., Seismic data processing, Society of exploration geophysicists (SEG), 526 p., 1987.

Figure 2.1: Regional geologic map showing the position of the Elberton granite with respect to the surrounding lithologic units (After Dallmyer, 1989).

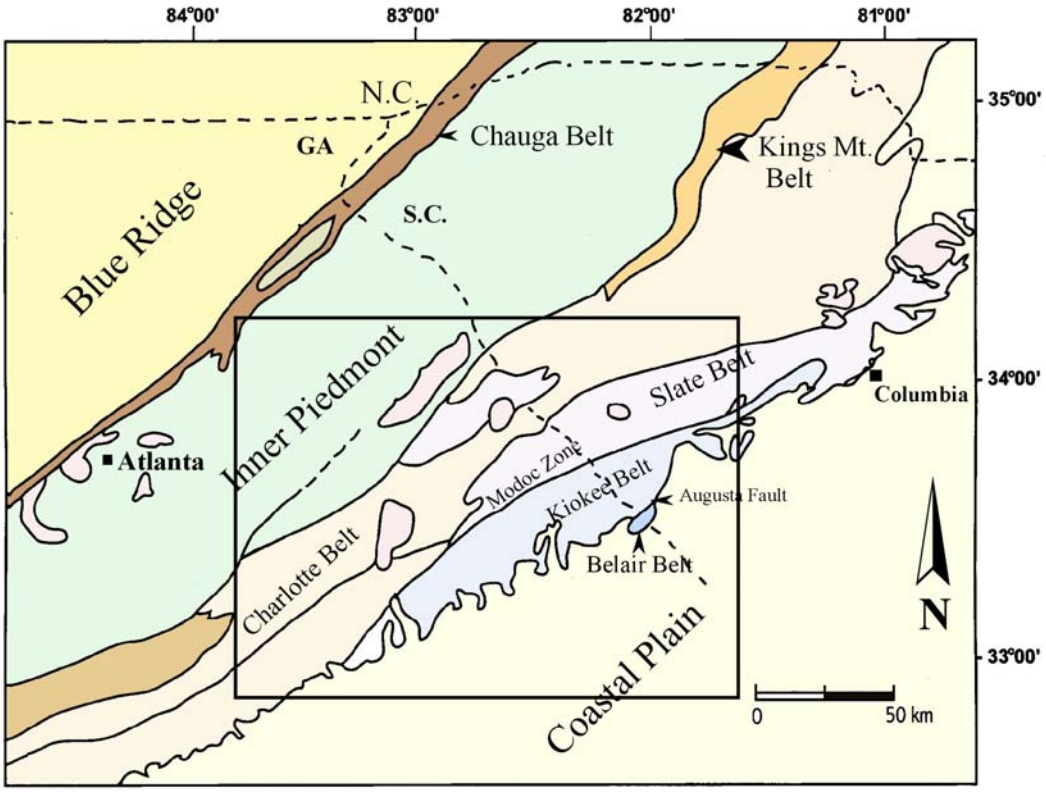
84°00'
83°00'
82°00'
81°00'
35°00'
34°00'
33°00'
N.C.
GA
S.C.
Chauga Belt
Kings Mt. Belt
Blue Ridge
Inner Piedmont
Slate Belt
Columbia
Atlanta
Modoc Zone
Kiokee Belt
Augusta Fault
Belair Belt
Charlotte Belt
Coastal Plain
N
0
50 km

(Figure 2.1)

Figure 2.2: Map showing magnetic foliation within the Elberton granite batholith. Inset (upper left corner) shows the location of the study area. (After Ellwood, 1980).

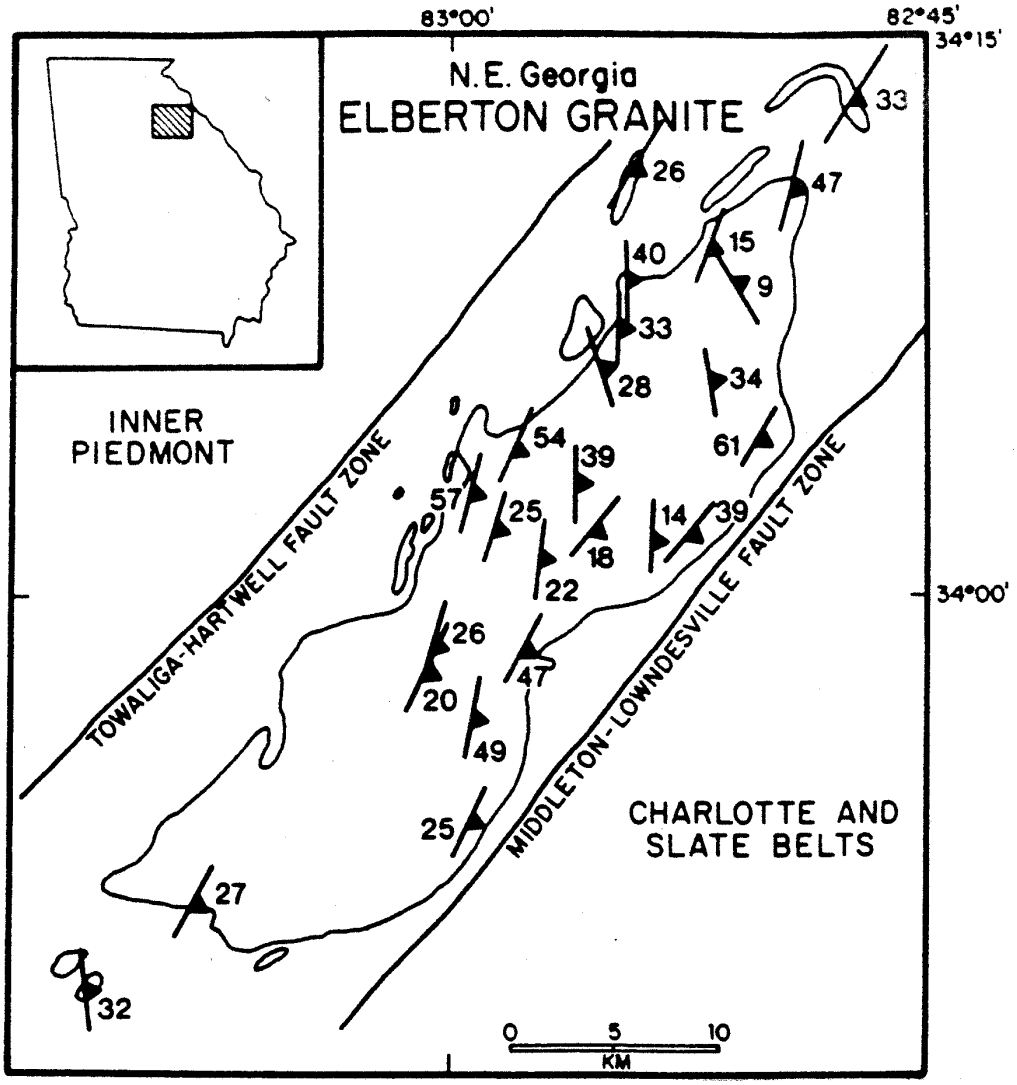
83°00'
82°45'
34°15'
34°00'
N.E. Georgia
ELBERTON GRANITE
INNER
PIEDMONT
TOWALIGA-HARTWELL FAULT ZONE
MIDDLETON-LOWNDESVILLE FAULT ZONE
CHARLOTTE AND
SLATE BELTS
33
26
47
40
15
9
33
28
34
54
39
61
57
25
18
14
39
22
26
47
20
49
25
27
32
0
5
10
KM

(Figure 2.2)

Figure 2.3: Maps showing the locations of COCORP lines. (a) map from Iverson and Smithson (1983). (b) and (c) are maps from Jurdy and Phinney (1983).

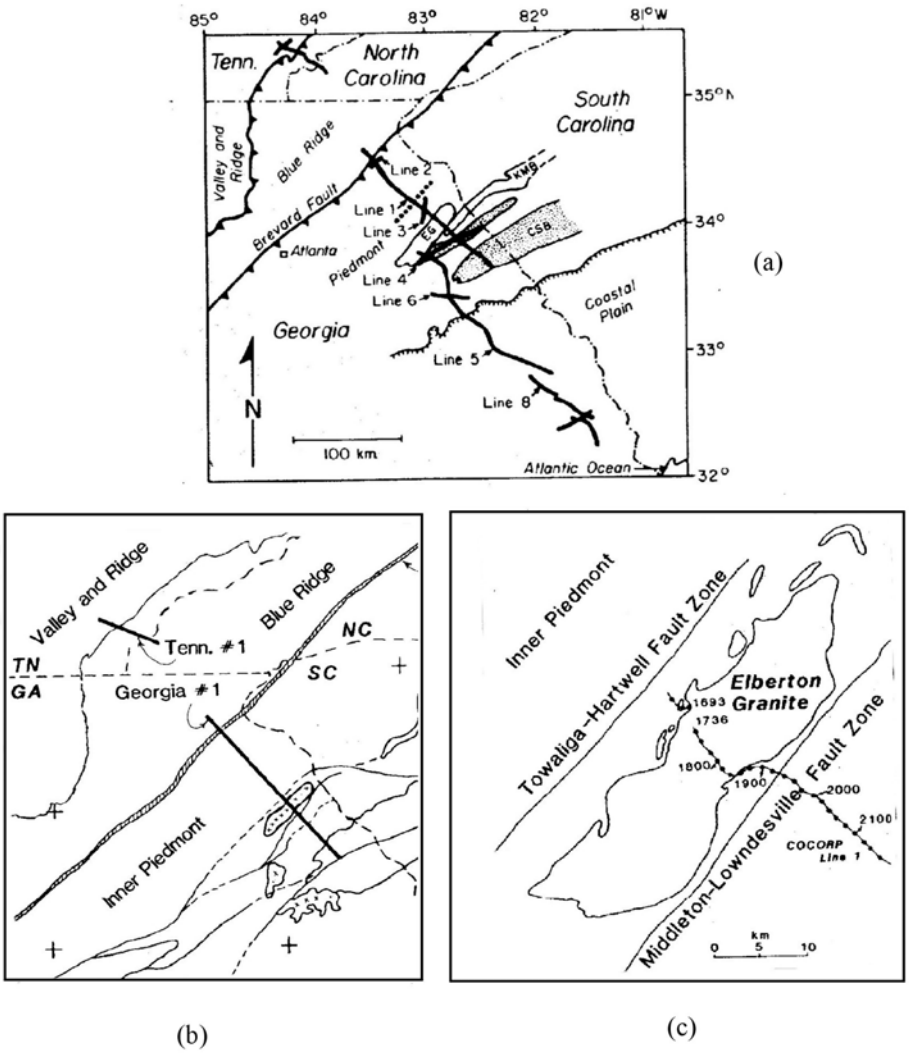
85°
84°
83°
82°
81°W
Tenn.
North Carolina
South Carolina
35°N
Valley and Ridge
Blue Ridge
Brevard Fault
Atlanta
Piedmont
Line 1
Line 2
Line 3
Line 4
Line 5
Line 6
Line 8
EG
KMG
CSB
Coastal Plain
Georgia
34°
33°
32°
N
100 km
Atlantic Ocean
(a)
Valley and Ridge
Blue Ridge
Tenn. #1
NC
TN
GA
Georgia #1
SC
Inner Piedmont
(b)
Inner Piedmont
Towaliga-Hartwell Fault Zone
Elberton Granite
1693
1736
1800
1900
2000
2100
COCORP Line 1
Middleton-Lowndesville Fault Zone
km
0
5
10
(c)

(Figure 2.3)

Figure 2.4: Crustal cross section along COCORP Georgia line 1 (Figure 2.3) showing the assumed master decollement and its relation to the granitic intrusions. "EG" is the Elberton granite. Bottom shows Bouguer gravity anomaly profile for the same area. (After Iverson and Smithson, 1982).

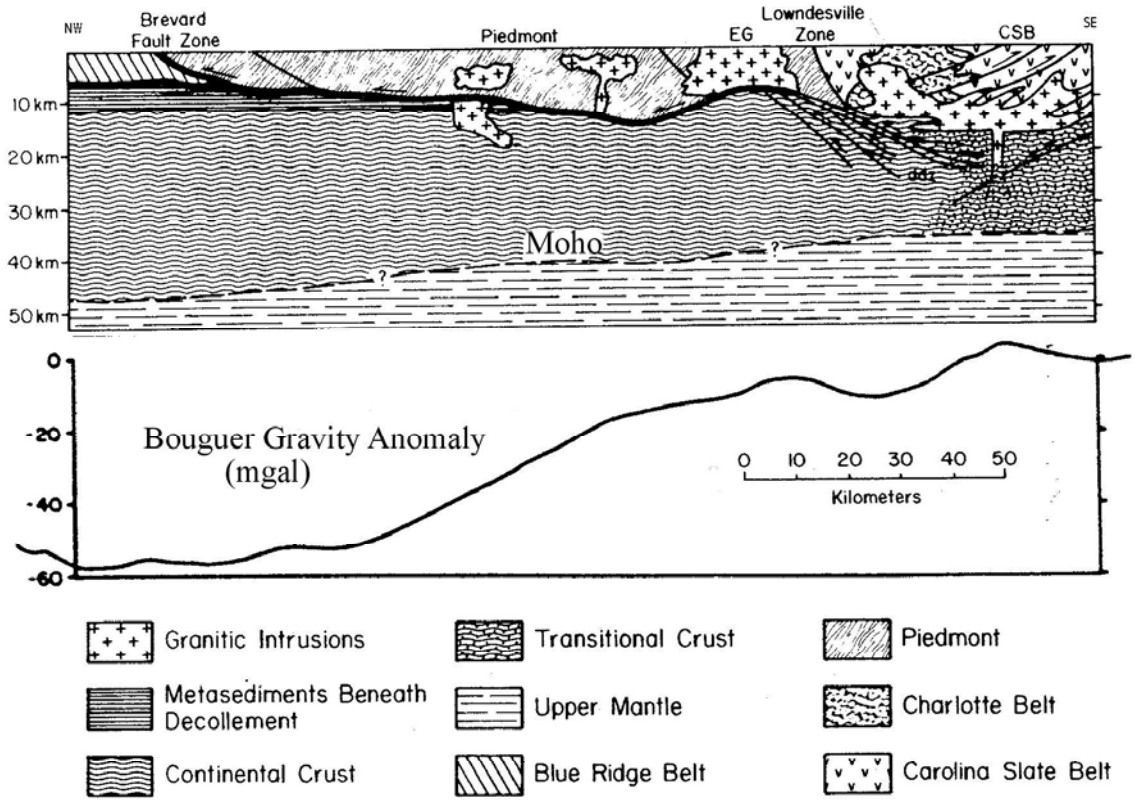
NW
Brevard
Fault Zone
Piedmont
EG
Lowndesville
Zone
CSB
SE
10 km
20 km
30 km
40 km
50 km
Moho
0
-20
-40
-60
Bouguer Gravity Anomaly
(mgal)
0 10 20 30 40 50
Kilometers
Granitic Intrusions
Transitional Crust
Piedmont
Metasediments Beneath
Decollement
Upper Mantle
Charlotte Belt
Continental Crust
Blue Ridge Belt
Carolina Slate Belt

(Figure 2.4)

Figure 2.5: Portion of CDP section from Georgia COCORP line 1 covering the eastern part of the Elberton granite. To the east, small arrows show dipping reflections at ~ 10- 12 km whereas in the upper 3 km it is difficult to recognize any features. (After Jurdy and Phinney, 1983.)

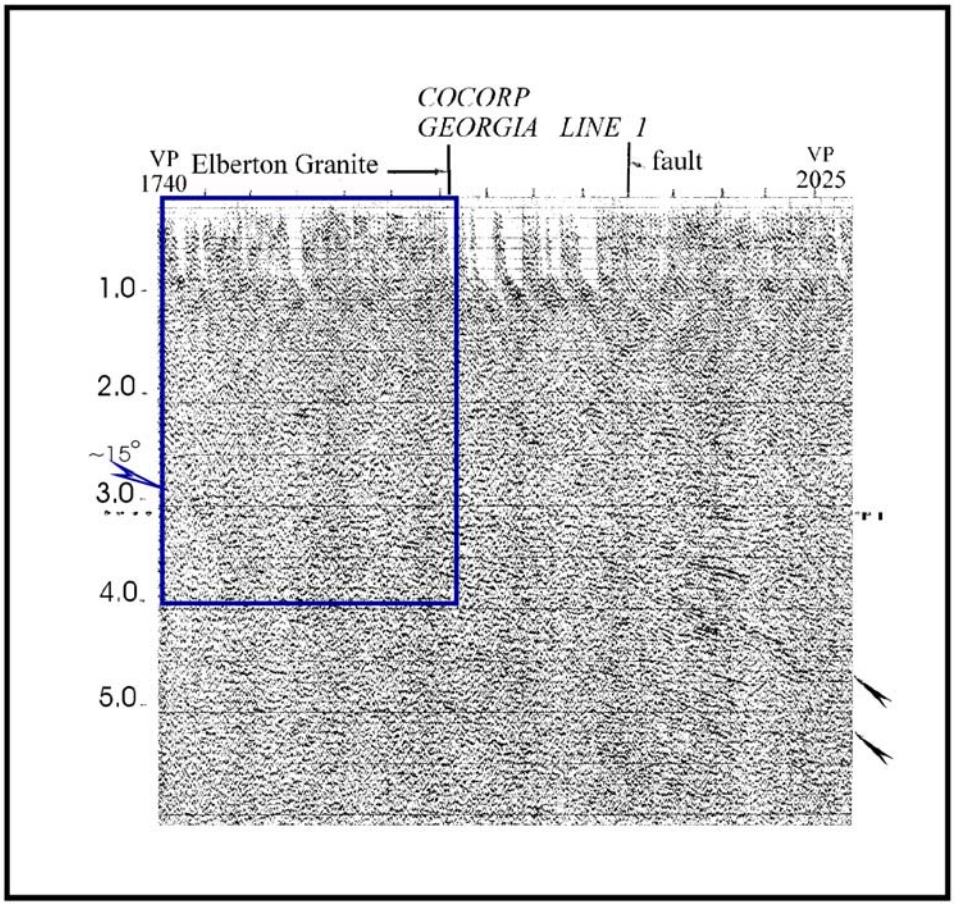
COCORP
GEORGIA LINE 1
VP
1740
Elberton Granite
fault
VP
2025
1.0
2.0
~15°
3.0
4.0
5.0

(Figure 2.5)

Figure 2.6: Alternate models for the relationship between the emplacement of the Elberton granite and Appalachian thrusting (Jurdy and Phinney, 1983). (a) indicates post-thrust emplacement where the laminated reflections are completely disturbed. (b) and (c) syn- and pre-thrust emplacement respectively show the situation where the Elberton granite intrusion does not disturb the deeper reflections as its timing of emplacement is earlier than the thrusting.

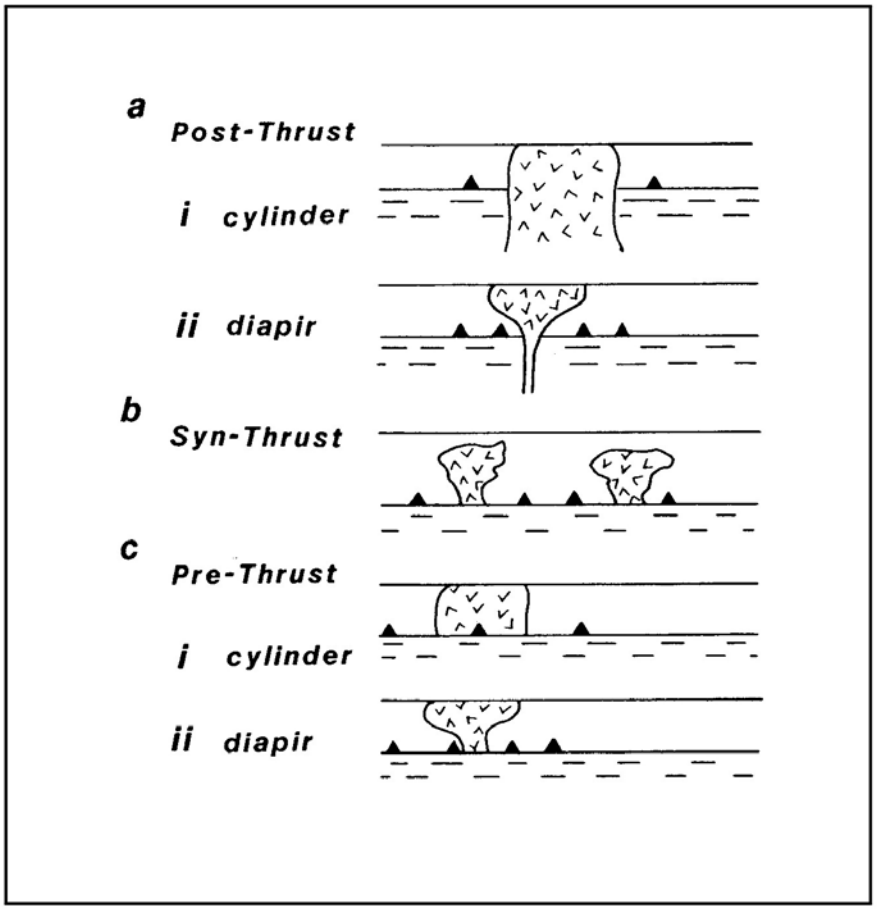
a
Post-Thrust
i cylinder
ii diapir
b
Syn-Thrust
c
Pre-Thrust
i cylinder
ii diapir

(Figure 2.6)

Figure 2.7: CDP –stacked section of COCORP line 1 after (a) smoothing and keeping only a frequency range of 12-30 Hz; some reflectors between 0.5 and 1 s (1.5-3 km) were observed, and (b) apparent velocity filtering of CDP gathers, which shows the CDP filtered section after smoothing and keeping only a frequency range of 12-30 Hz (after Jurdy and Phinney, 1983).

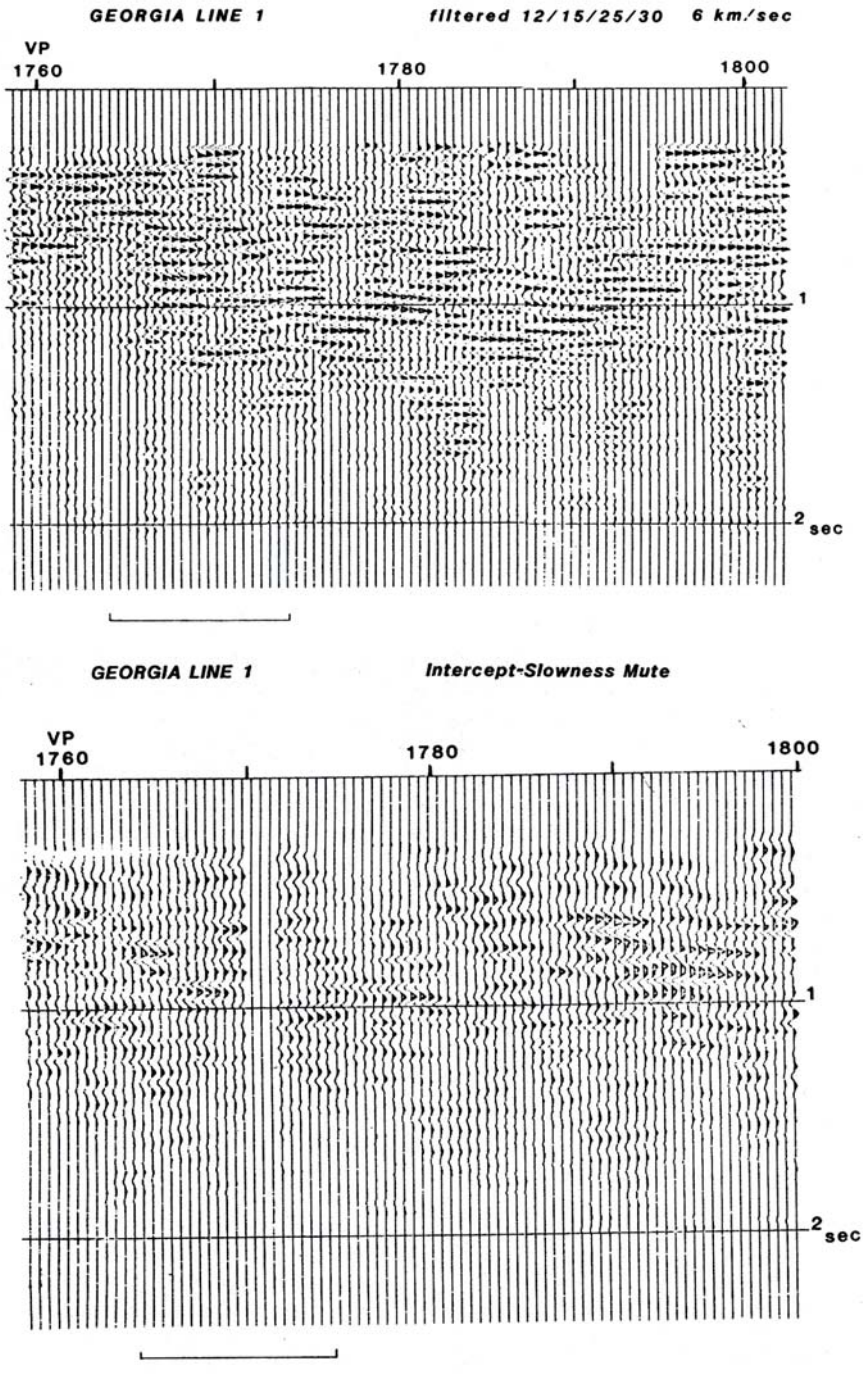
GEORGIA LINE 1
filtered 12/15/25/30 6 km./sec
VP
1760
1780
1800
1
2 sec
GEORGIA LINE 1
Intercept-Slowness Mute
VP
1760
1780
1800
1
2 sec

(Figure 2.7)

Figure 2.8: Diagram showing the expected travel –time curves for direct P waves and S waves and reflections from various interfaces at different depths (3000 m and 10000 m represent the base of the granite and the master decollement respectively).To record reflections from a depth of 3 km interface without interference from direct shear waves and surface waves, the offset must be greater than 4.5 km. To avoid contamination of reflections from greater depth (10 km), the offsets should be greater than 14.5 km.

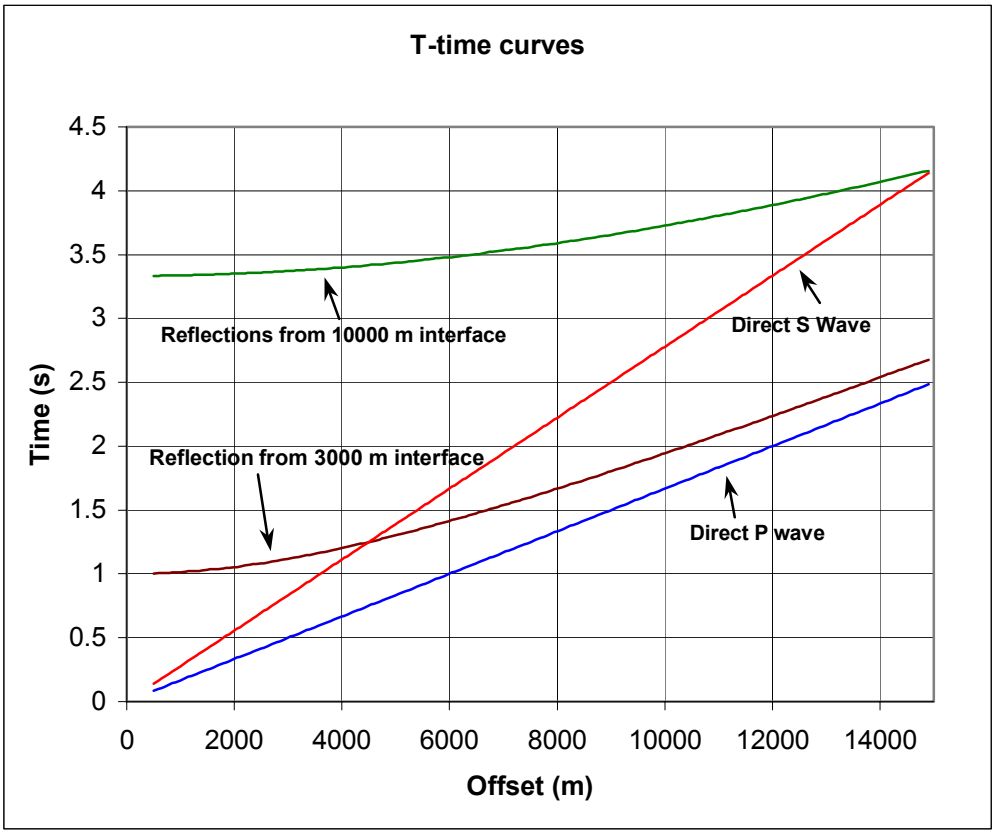
T-time curves
Time (s)
Offset (m)
Reflections from 10000 m interface
Direct S Wave
Reflection from 3000 m interface
Direct P wave
0
0.5
1
1.5
2
2.5
3
3.5
4
4.5
0
2000
4000
6000
8000
10000
12000
14000

(Figure 2.8)

Figure 2.9: Map of the Elberton granite (after Jurdy and Phinney, 1983) showing the locations of quarries, recording sites, and ray paths for the recorded shots. The granite is flanked by the Towaliga-Hartwell fault and the Middleton-Lowndesville fault. Map in the upper left corner shows the location of the study area in Georgia. The solid red line with black dots represents COCORP Line 1. Nine blasts were recorded. The four used shots are: Two from Boyd granite quarry (arrays A and F), 1 from Dye granite quarry (array C), 1 from Blue Ribbon quarry (array B). The blasts that did not produce usable signals are: Three from Star granite quarry with unusable signals (not shown), 1 from Gold Eagle quarry, and 1 from Boyd granite (not shown).

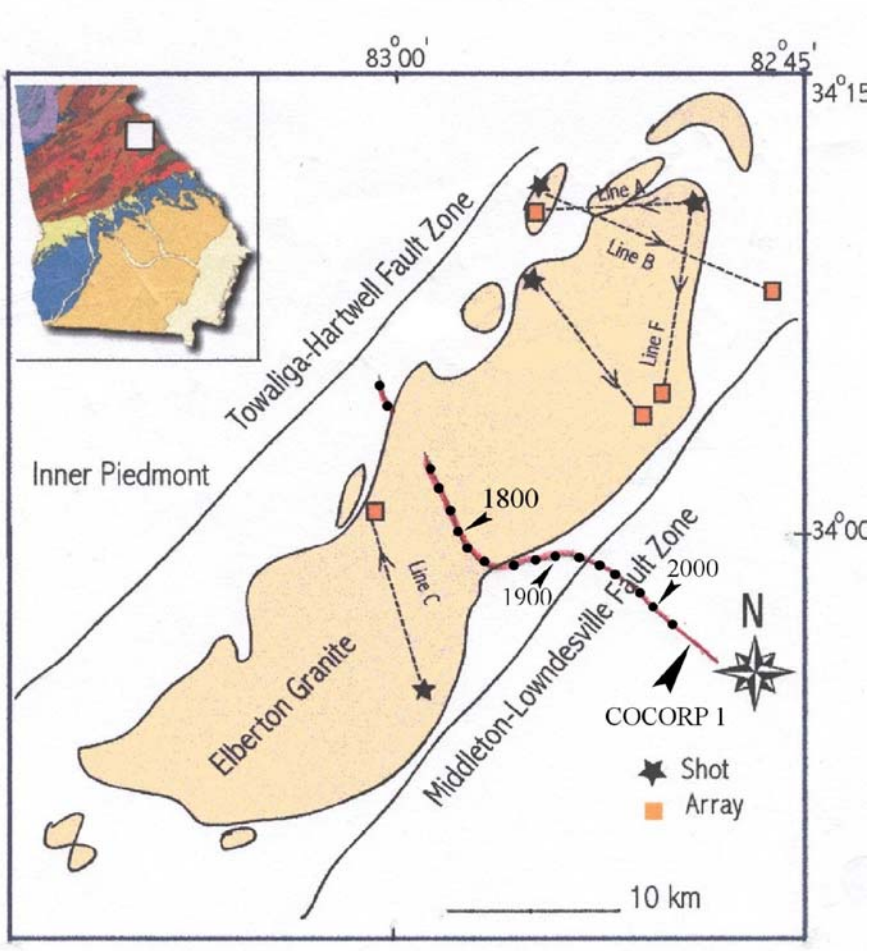
83°00'
82°45'
34°15
34°00
Towaliga-Hartwell Fault Zone
Inner Piedmont
Line A
Line B
Line F
Line C
1800
1900
2000
Elberton Granite
Middleton-Lowndesville Fault Zone
N
COCORP 1
Shot
Array
10 km

(Figure 2.9)

Figure 2.10: Flow chart showing a summary of seismic data processing steps carried out on the shot gathers.

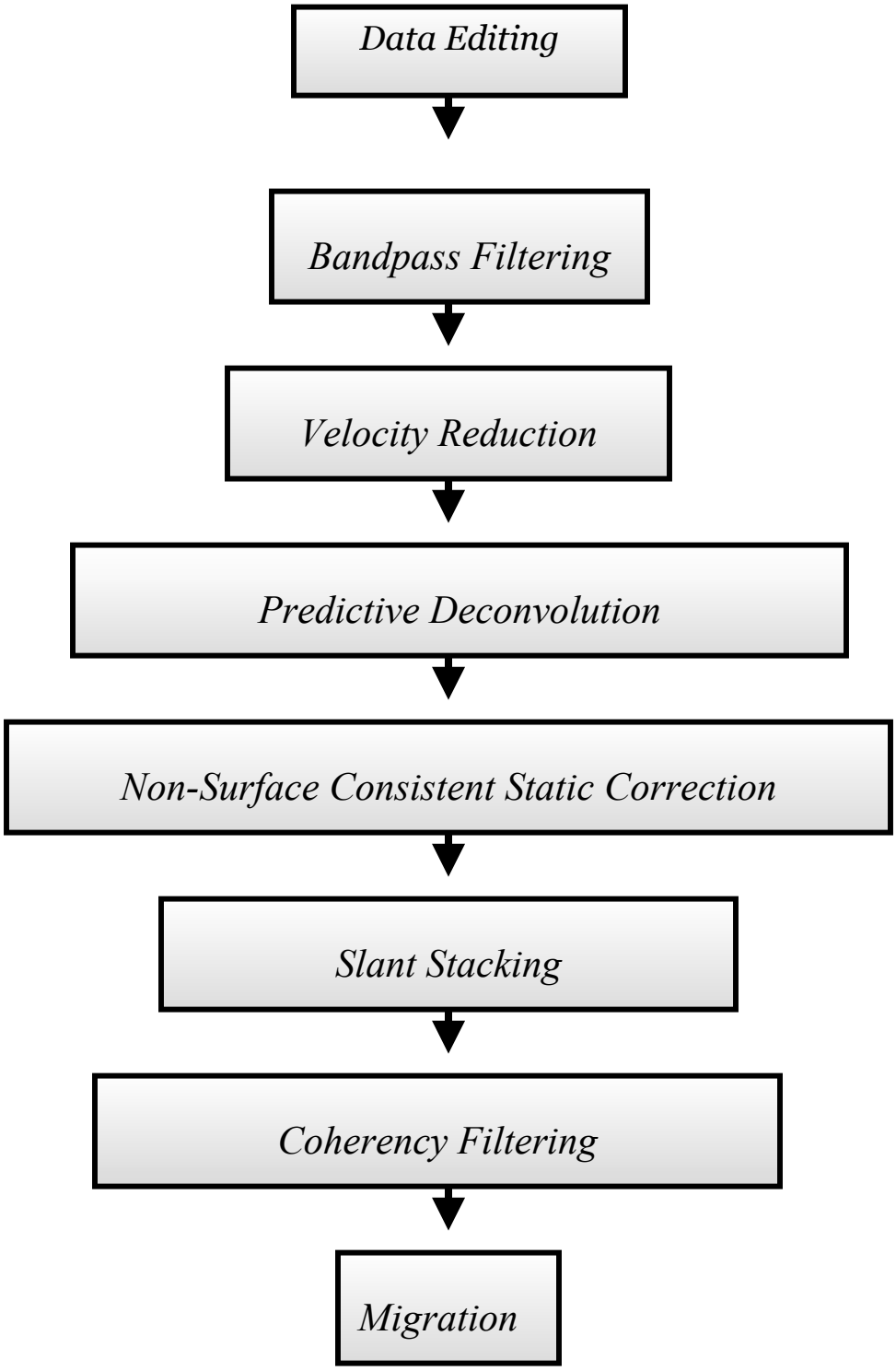
Data Editing
Bandpass Filtering
Velocity Reduction
Predictive Deconvolution
Non-Surface Consistent Static Correction
Slant Stacking
Coherency Filtering
Migration

(Figure 2.10)

Figure 2.11: Amplitude spectra of four shot gathers used in this study, after deleting noisy traces. The amplitude spectra show signal energy as high as 45-50 Hz. Amplitude spectra shown are for (a) Array B, the Blue Ribbon shot (14.01-14.91 km), (b) Array F, the Boyd Granite 3 shot (13.09-14.18 km), (c) Array C, the Dye Granite shot (11.53-12.48 km), and (d) Array A, the Boyd Granite 2 shot (7.77-9.02 km).

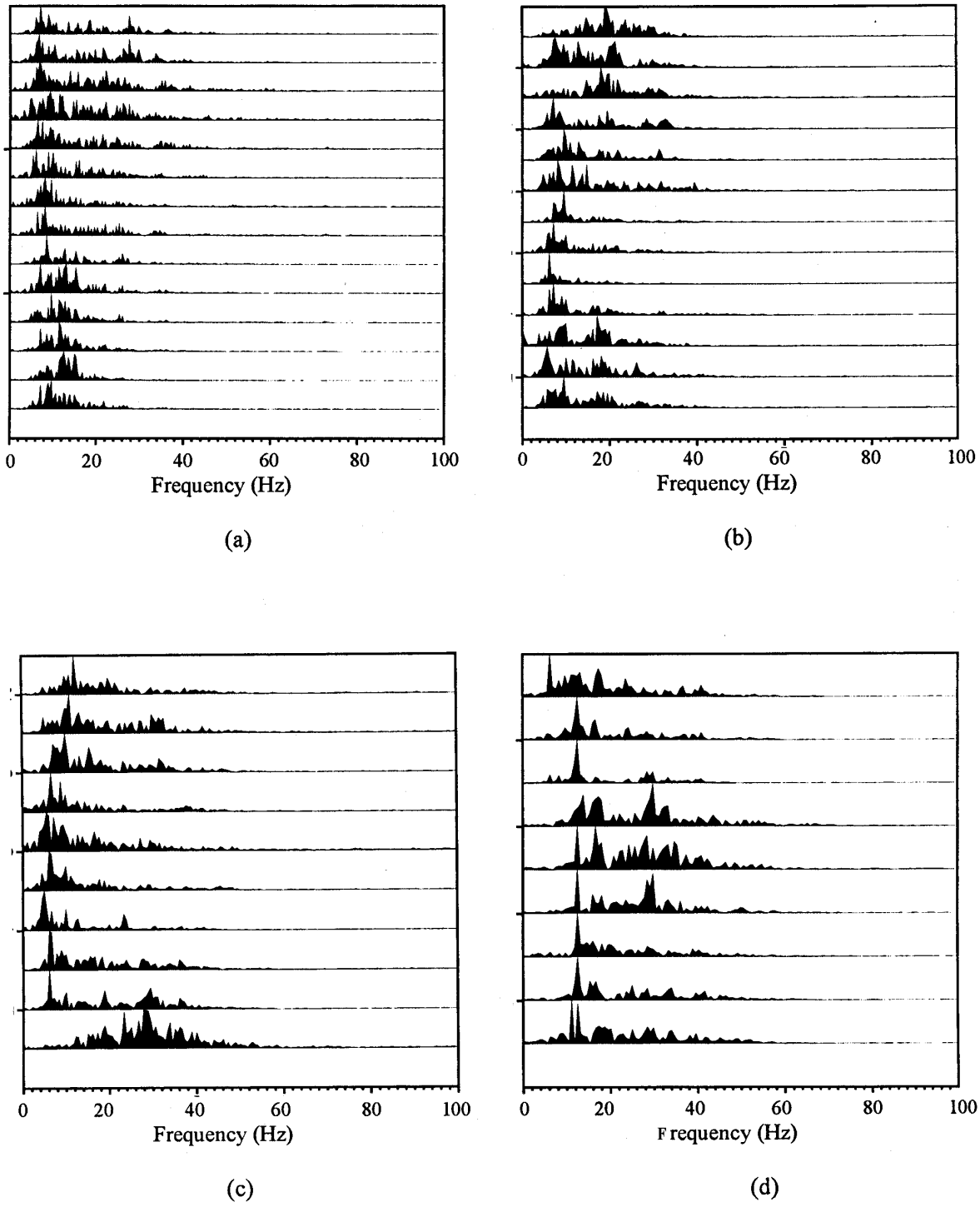

(Figure 2.11)

Figure 2.12: Predictive deconvolution (Robinson and Treitel, 1980; Yilmaz, 1987) applied to an unfiltered velocity-reduced gather of Dye granite recording line (filter setting 20, 25, 60, 70 Hz). (a) Pre-whitening of 0.01 was used. Broader bandpass improved phase coherence shown in (b) after deconvolution. Arrows mark events that were difficult to recognize before deconvolution. The predictive lag (α) was one sample (spiking deconvolution).

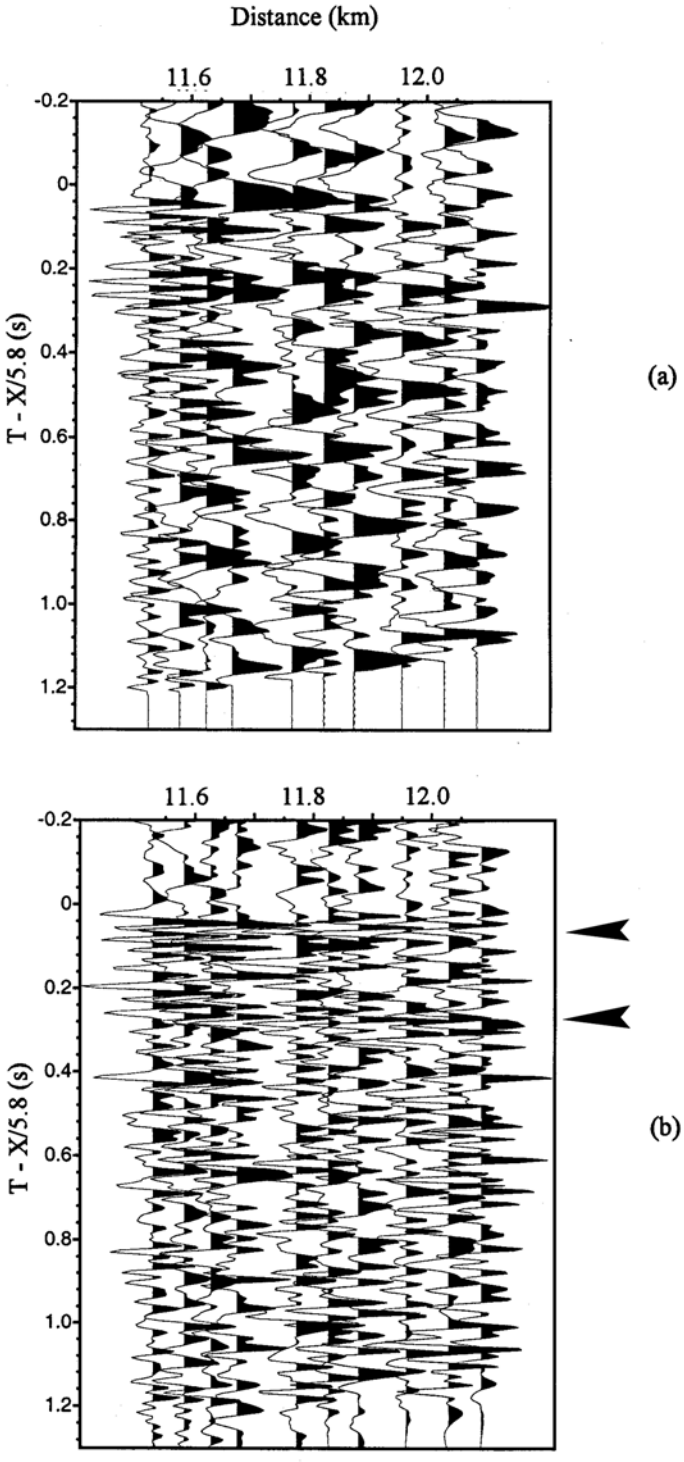
Distance (km)
11.6
11.8
12.0
-0.2
0
0.2
0.4
0.6
0.8
1.0
1.2
T - X/5.8 (s)
(a)
11.6
11.8
12.0
-0.2
0
0.2
0.4
0.6
0.8
1.0
1.2
T - X/5.8 (s)
(b)

(Figure 2.12)

Figure 2.13: Amplitude spectrum of Dye Granite shot gather (line C) (a) before and (b) after the predictive deconvolution. Pre-whitening of 0.01 was used. The prediction lag (α) was one sample (spiking deconvolution).

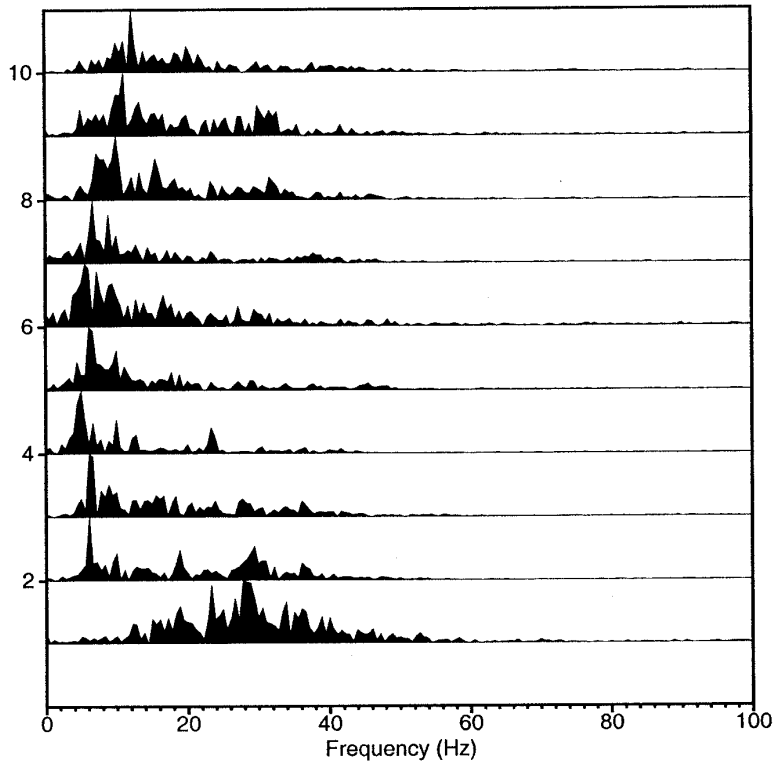

(a)

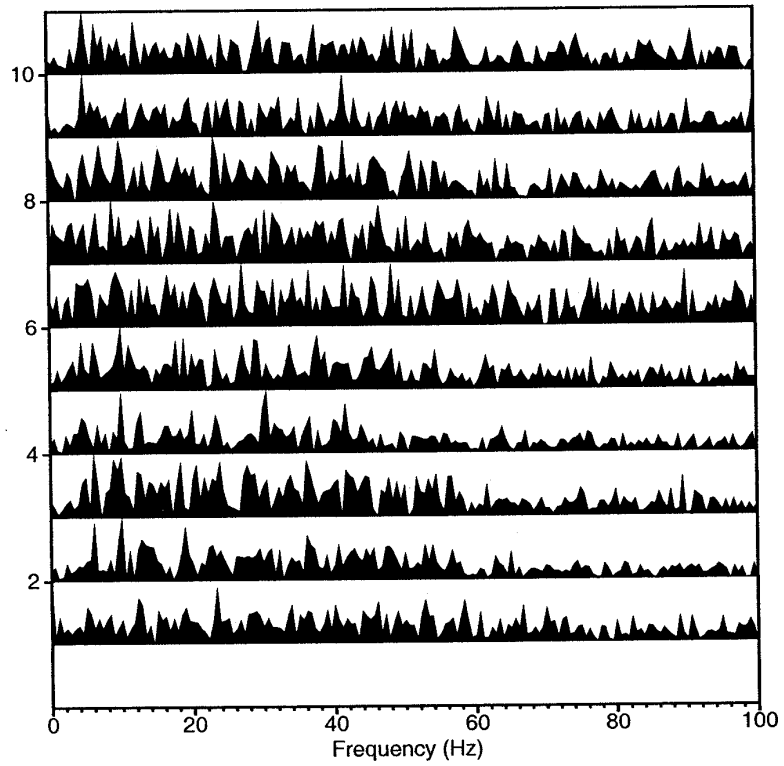

(b)

(Figure 2.13)

Figure 2.14: Example showing the improvement achieved after applying both static correction and predictive deconvolution to the shot gather for Array A. Deconvolution helps sharpen the signal and static corrections improve phase coherence. P indicates the direct p wave and E points to a reflection at a depth of roughly 2 km. Filter setting is 15,25,45,60 Hz.

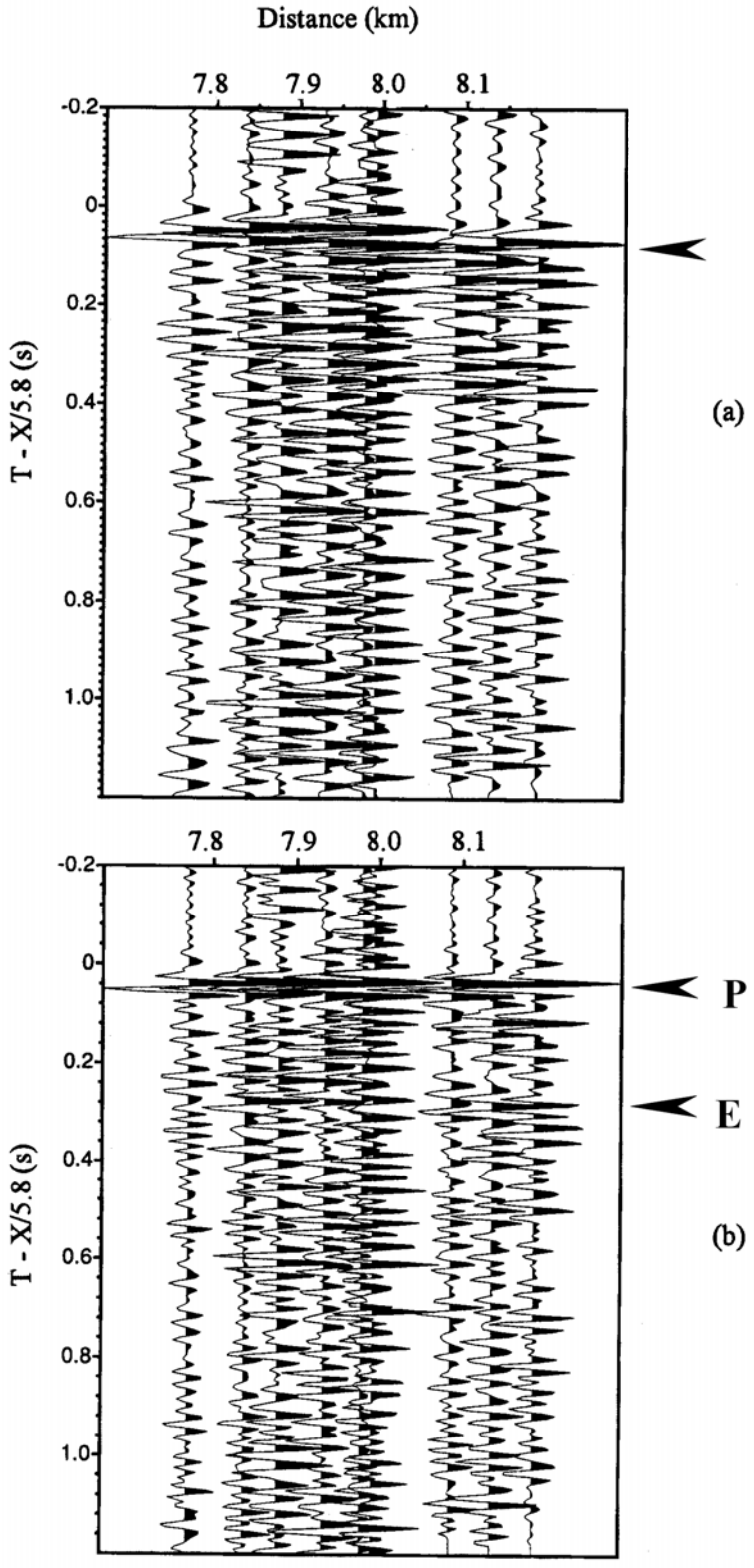

(Figure 2.14)

Figure 2.15: Example of deconvolution by spectral whitening applied to the shot gather for Array B (15, 26, 44, 55 Hz) with pre-whitening values of 0.01 (b), 0.05 (c), and 0.1 (d). (a) shows the shot gather without whitening.

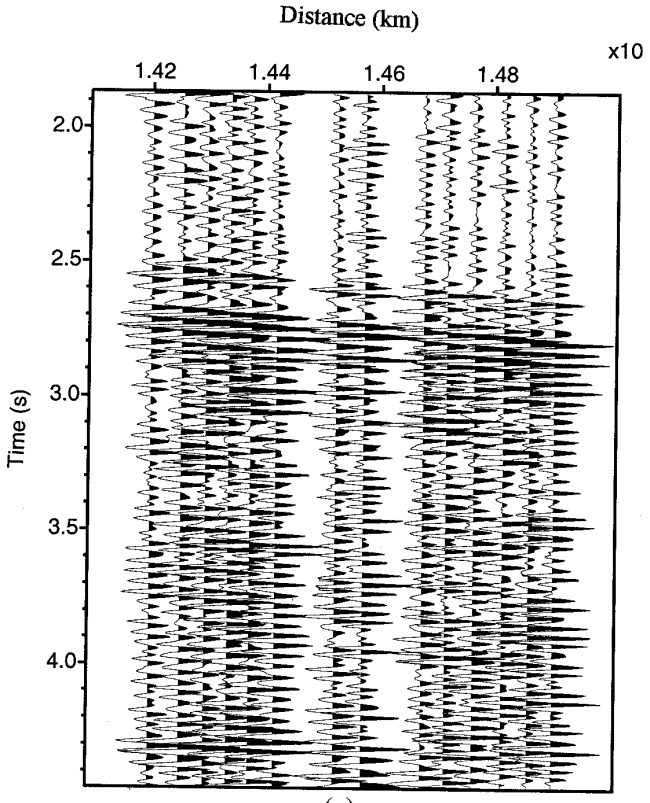

(a)

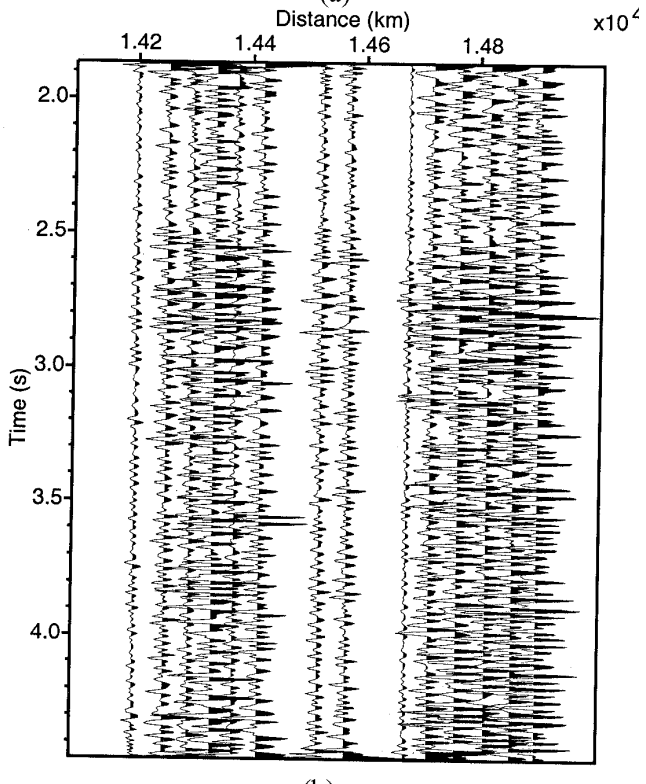

(b)

(Figure 2.15)

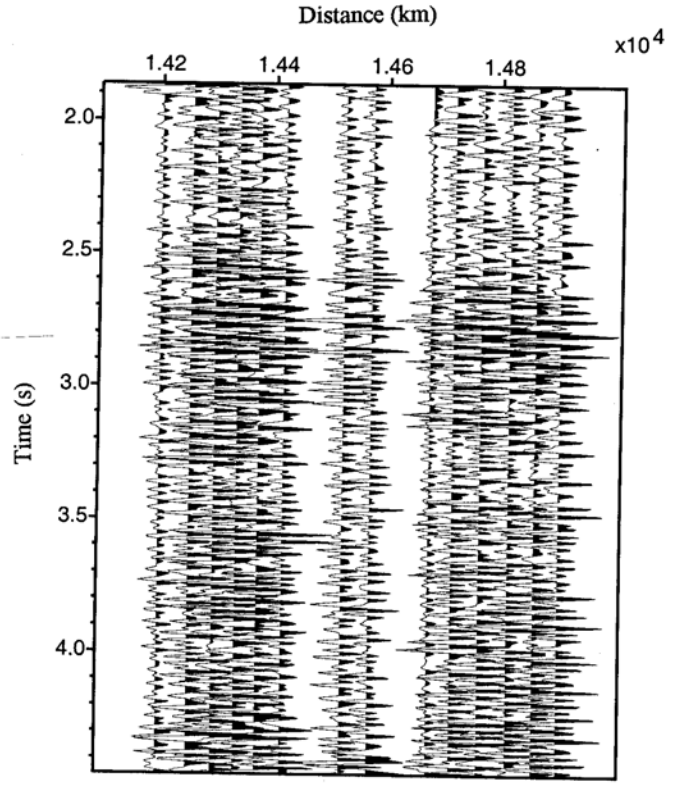

(c)

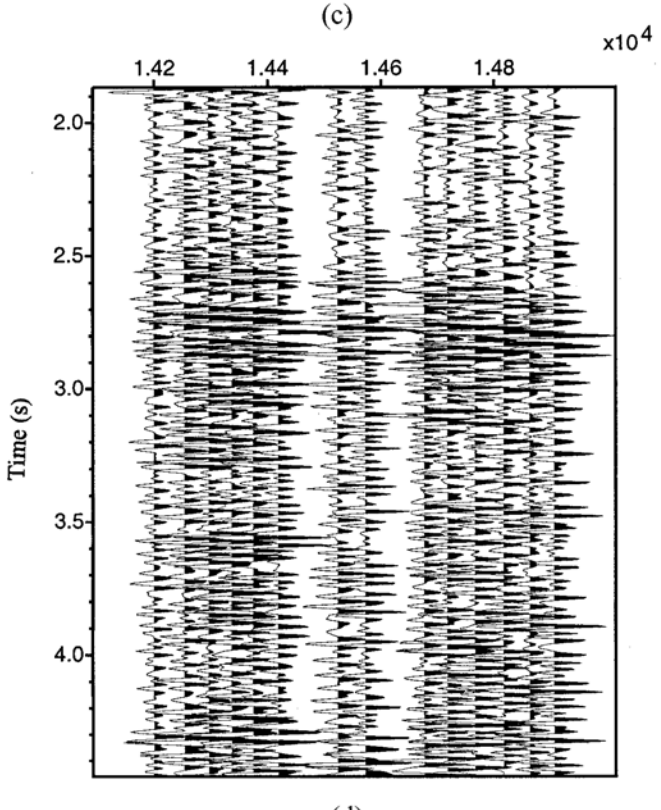

(d)

(Figure 2.15)

Figure 2.16: Velocity reduced gather of line B (a) before and (b) after applying static corrections. Note the enhancement of phase coherence for the first arrival and the large-amplitude event interpreted as a post-critical reflection (arrow). P is the direct P wave and E is the proposed base of the granite. Removal of statics has also removed the moveout, therefore distorting the apparent velocities. This was corrected prior to migrating the slant stacks.

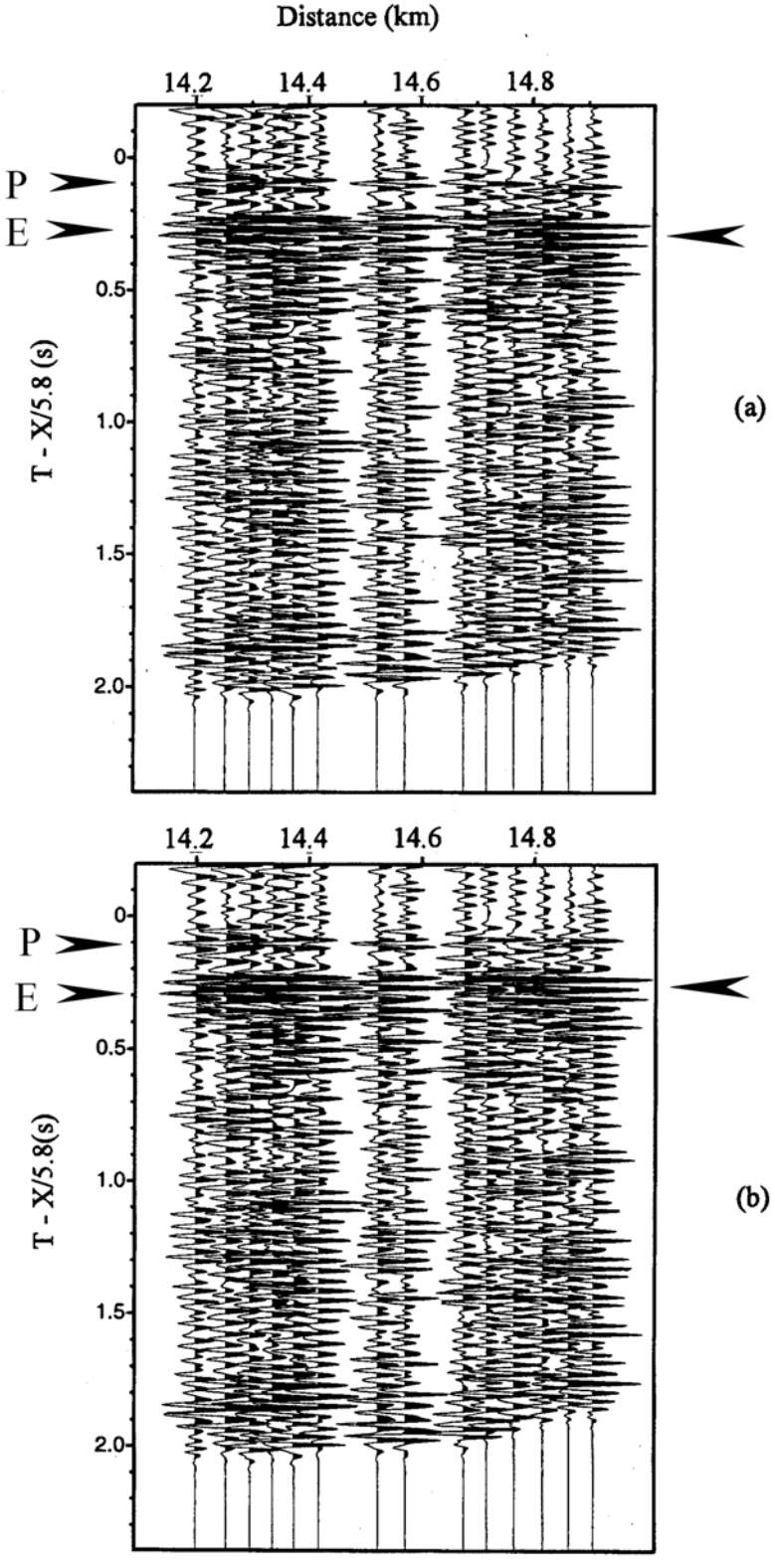
Distance (km)
14.2
14.4
14.6
14.8
P
E
0
0.5
1.0
1.5
2.0
T - X/5.8 (s)
(a)
14.2
14.4
14.6
14.8
P
E
0
0.5
1.0
1.5
2.0
T - X/5.8(s)
(b)

(Figure 2.16)

Figure 2.17: The raw (a) and final (b) shot gather for Array B (Blue Ribbon). The raw shot gather shows contamination by traffic noise in the near traces. Processing for the final shot gather include trace editing, bandpass filtering, and static corrections.

Bandpass: 15, 26, 44, 55 Hz

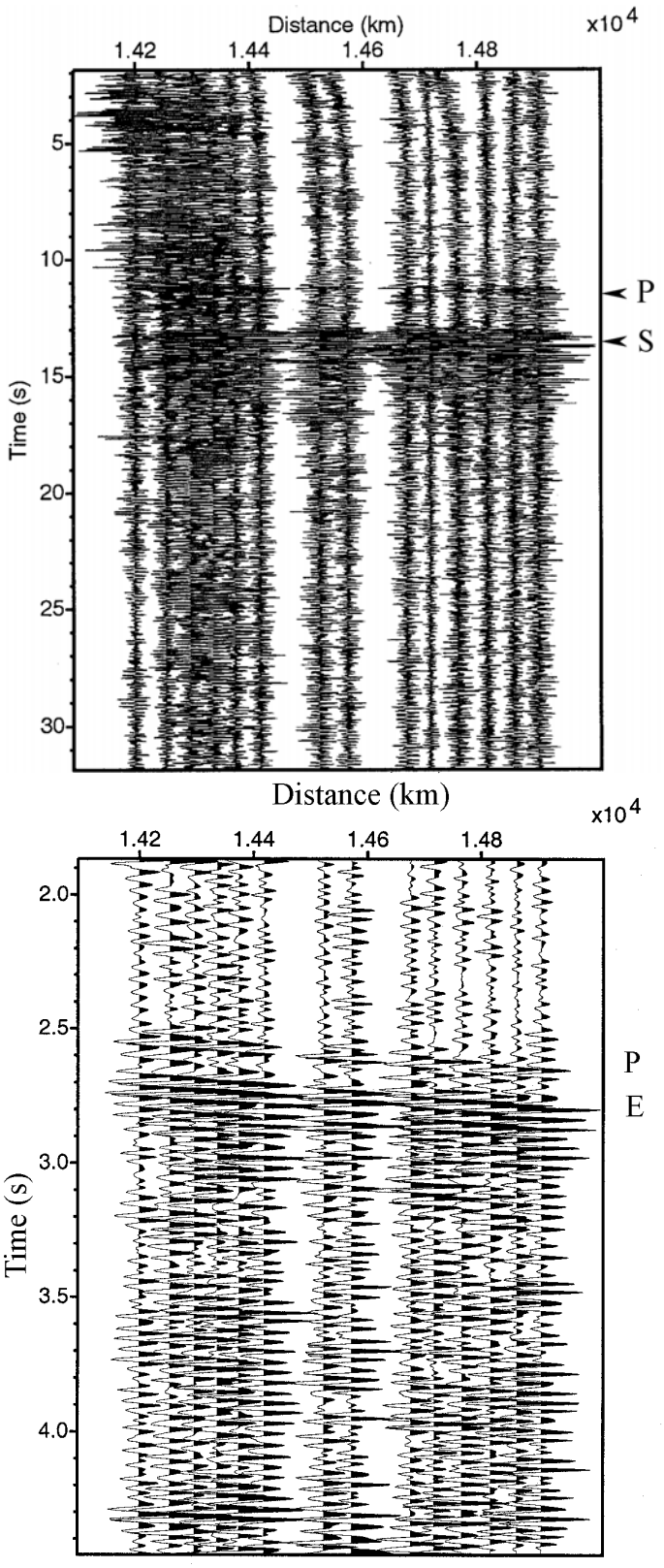
Distance (km)
x10^4
1.42
1.44
1.46
1.48
5
10
15
20
25
30
Time (s)
P
S
Distance (km)
x10^4
1.42
1.44
1.46
1.48
2.0
2.5
3.0
3.5
4.0
Time (s)
P
E

(Figure 2.17)

Figure 2.18: Slant stack of the Blue Ribbon shot gather (Array B). Time axes for the slant stack represents the travel time for the center offset trace. Prior to stacking, shot gather traces were filtered with a zero-phase, bandpass filter (15, 26, 44, and 55 Hz) and normalized by their rms amplitudes. “E” refers to events interpreted as the base of the granite and “M” refers to an event interpreted as the master decollement. The slant stack is shown (a) before applying the static correction and (b) after. In this shot, using 5.8 km/s as the reduced velocity distorted the apparent velocity, therefore the static-corrected slant stack was shifted back by 0.034 s/km before the migration process. The stack here is shown before applying this final shift.

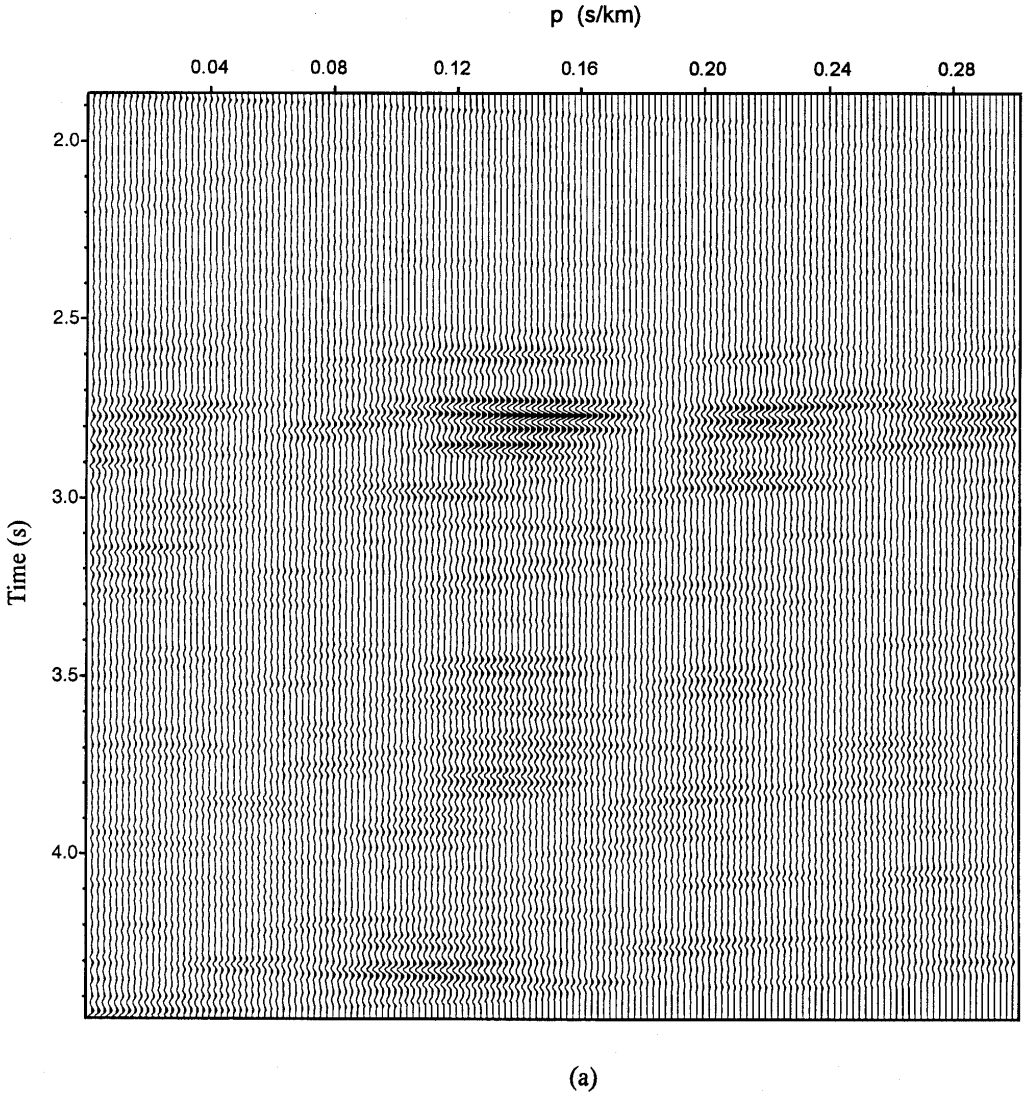

(a)

(Figure 2.18)

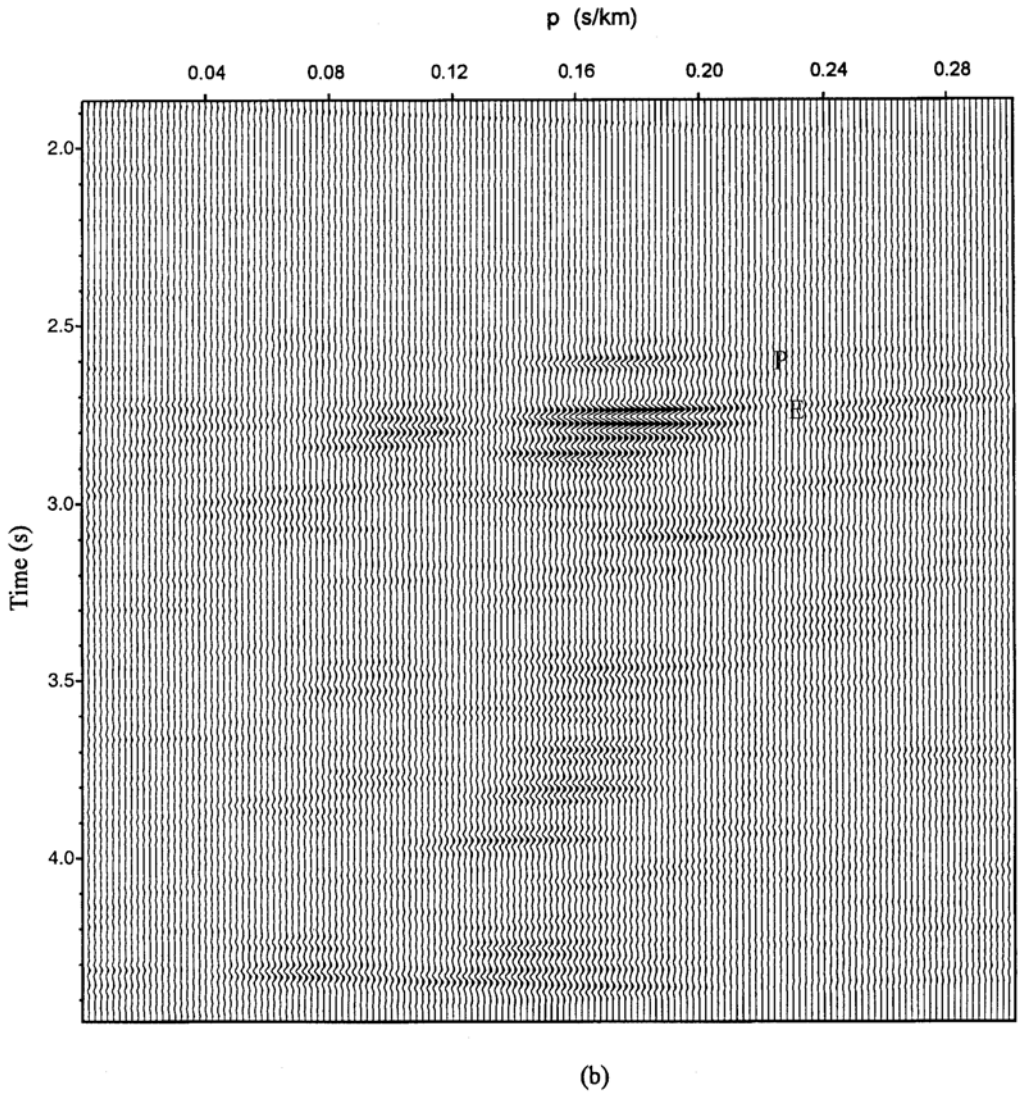

(Figure 2.18)

Figure 2.19: Semblance of the slant stack of shot gather for the Blue Ribbon (Array B). The bandpass filter frequencies of the shot gather are 15,26,44,55 Hz. The semblance is shown (a) before and (b) after applying static corrections. The concentration of the seismic energy is very clear after applying the static correction. The enhancement is indicated by more focused events after static corrections but they are shifted toward a higher ray parameter due to using 5.8 km/s as a reduction velocity for lining up the first arrivals. This distortion was corrected before the migration by shifting back the arrivals by 0.034 s/km (ray parameter). The section here is shown before applying this final shift. The direct P wave shows an average ray parameter (p) of about 0.18. Coherent arrivals with ray parameters less than 0.18 s/km are interpreted as P-wave reflections. Arrivals with ray parameters greater than 0.18 s/km are interpreted as P-SV converted waves.

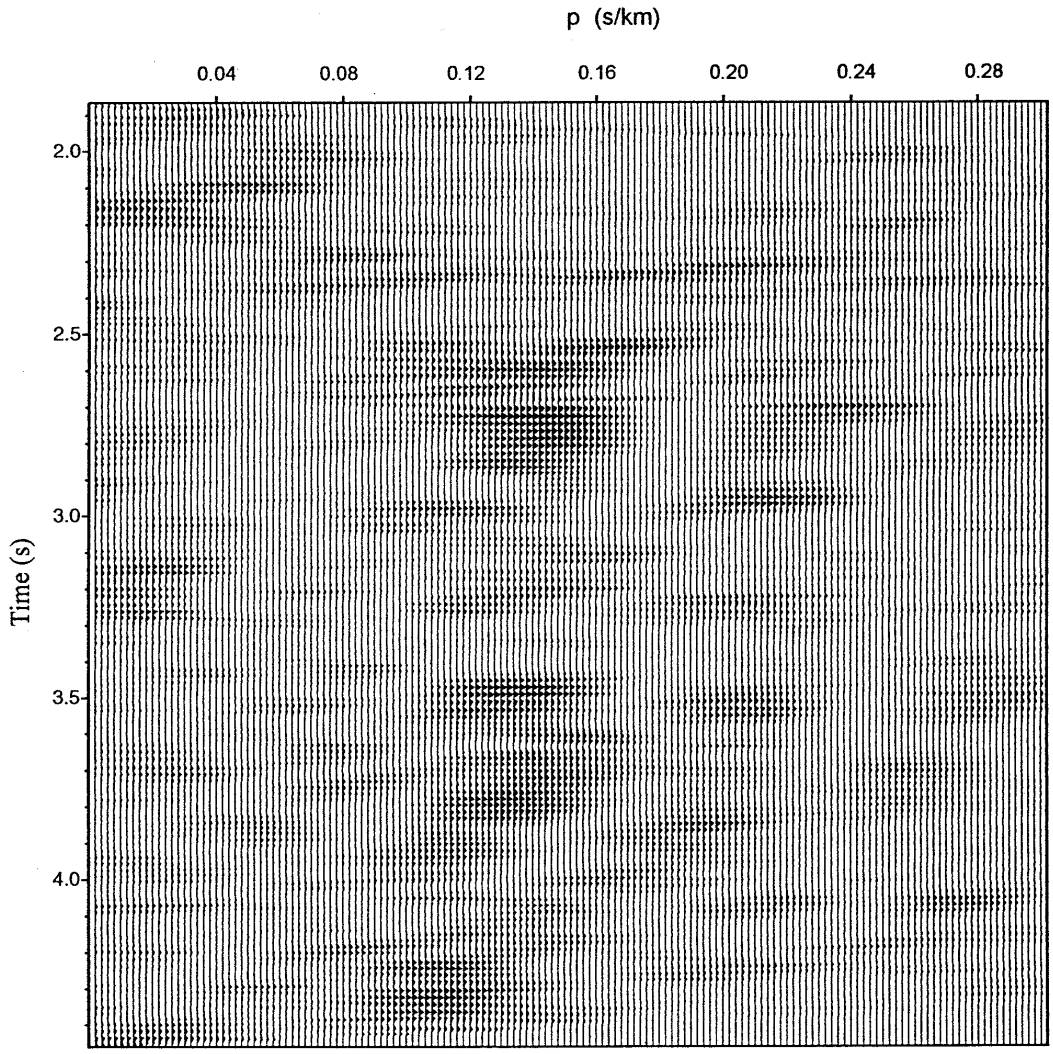

(a)

(Figure 2.19)

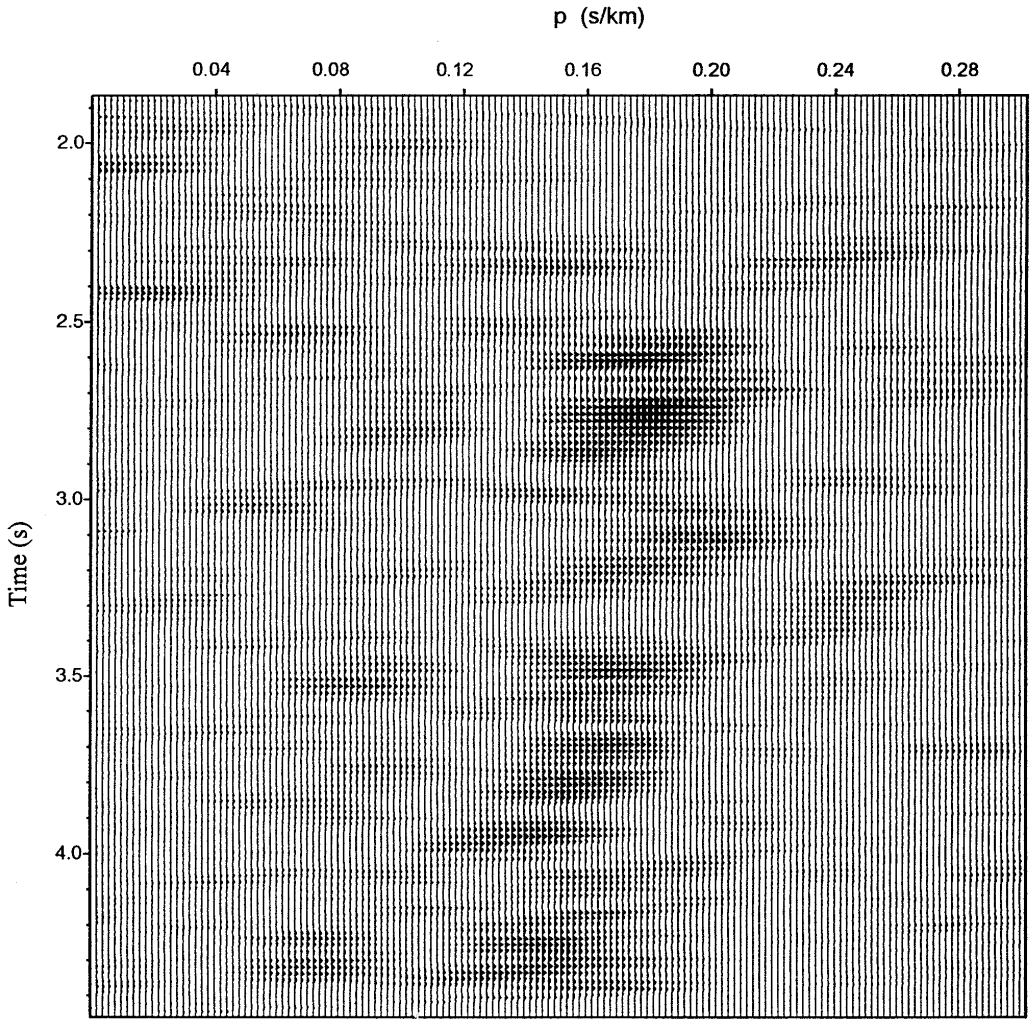

(b)

(Figure 2.19)

Figure 2.20: Smoothed semblance for the Blue Ribbon shot (recording line B). In this shot, using 5.8 km/s as the reduced velocity distorted the apparent velocity, therefore the static-corrected slant stack was shifted back by 0.034 s/km just before the migration process. The semblance here is shown before applying this final shift. The smoothed semblance is shown after static correction.

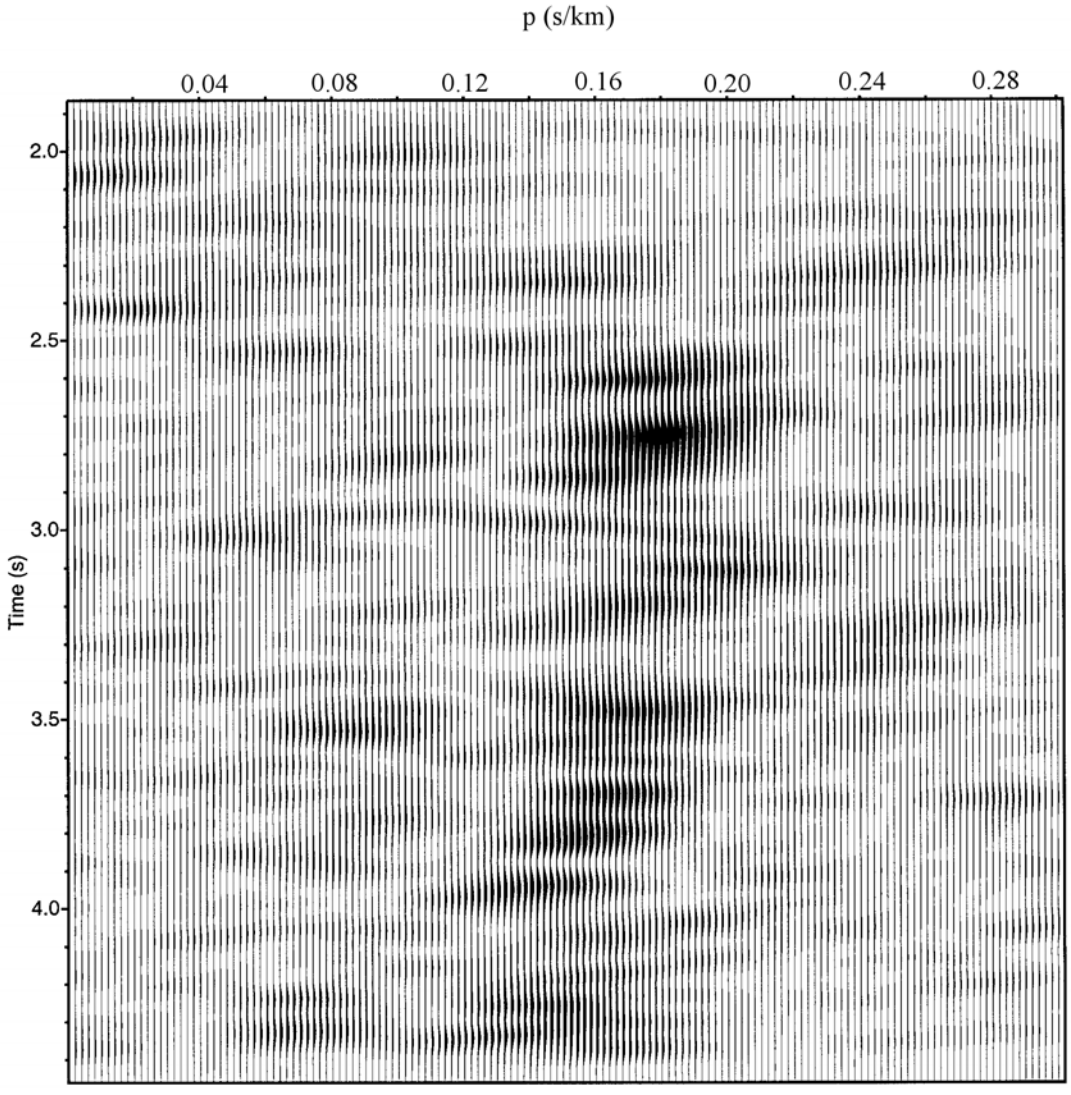

(Figure 2.20)

Figure 2.21: Coherency filtered slant stacks that were migrated for the Blue Ribbon shot (recording line B). After smoothing the unfiltered semblance (Figure 2.19a) of the slant stack, a coherency filter was constructed by assigning zeros for all samples in the smoothed semblance with values less than the chosen threshold and value of 1 for the remaining samples. This suppresses incoherent noise. P-SV indicates events interpreted as converted P to SV waves; generally they are characterized by larger ray parameter than that of the direct P-wave. E marks the possible base of the Elberton granite. M indicates the event interpreted as a reflection from the master decollement. (a) show the coherency filtered slant stack for a threshold value of 0.45, (b,c, and d) represent the same operation with higher threshold values (0.5,0.55 and 0.6 respectively). Raising the threshold value yields more focused events for migration. As mentioned before, these slant stacks were shifted back by 0.034 s/km before migration. The plotted slant stacks are shown before the shift.

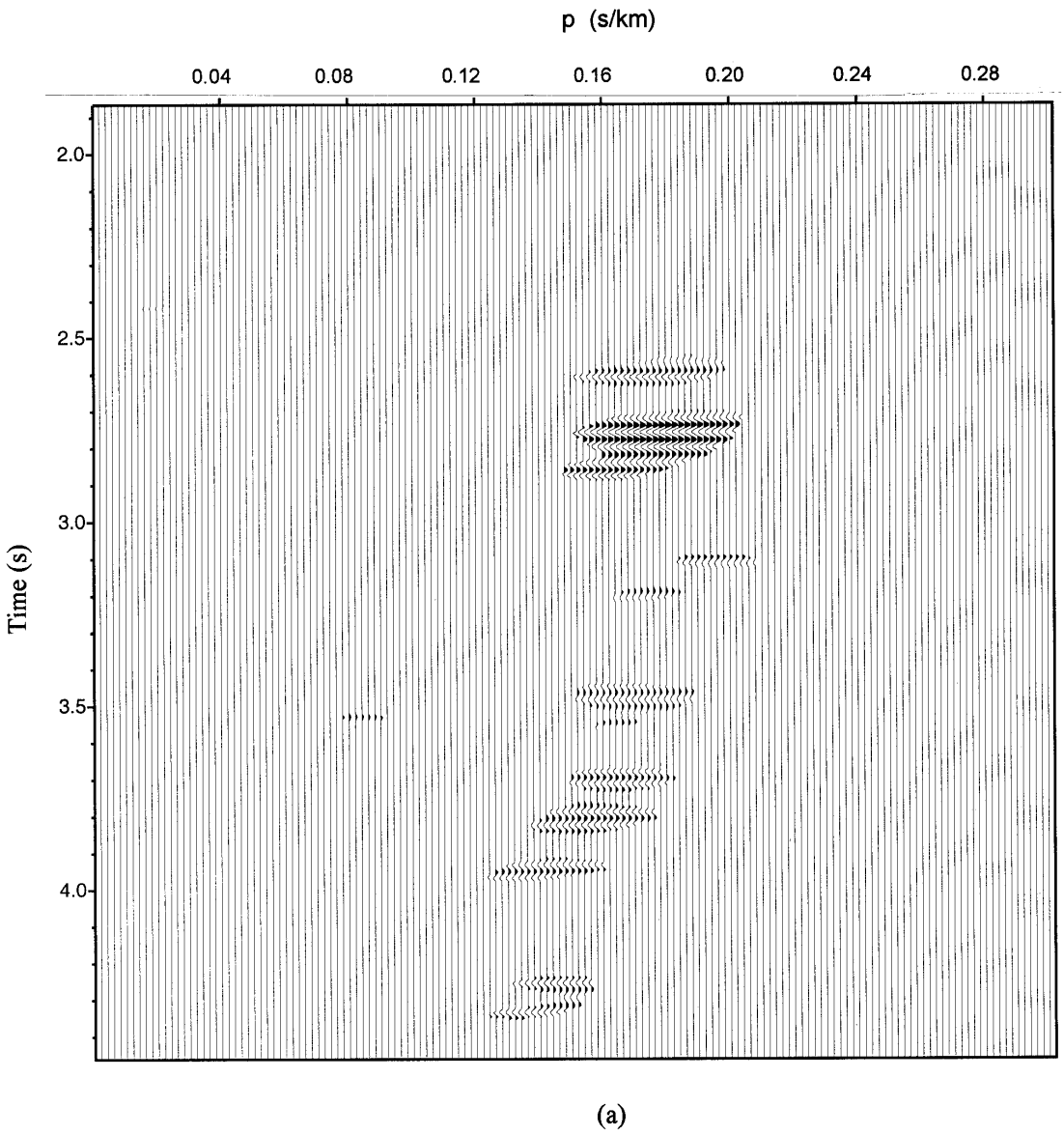

(a)

(Figure 2.21)

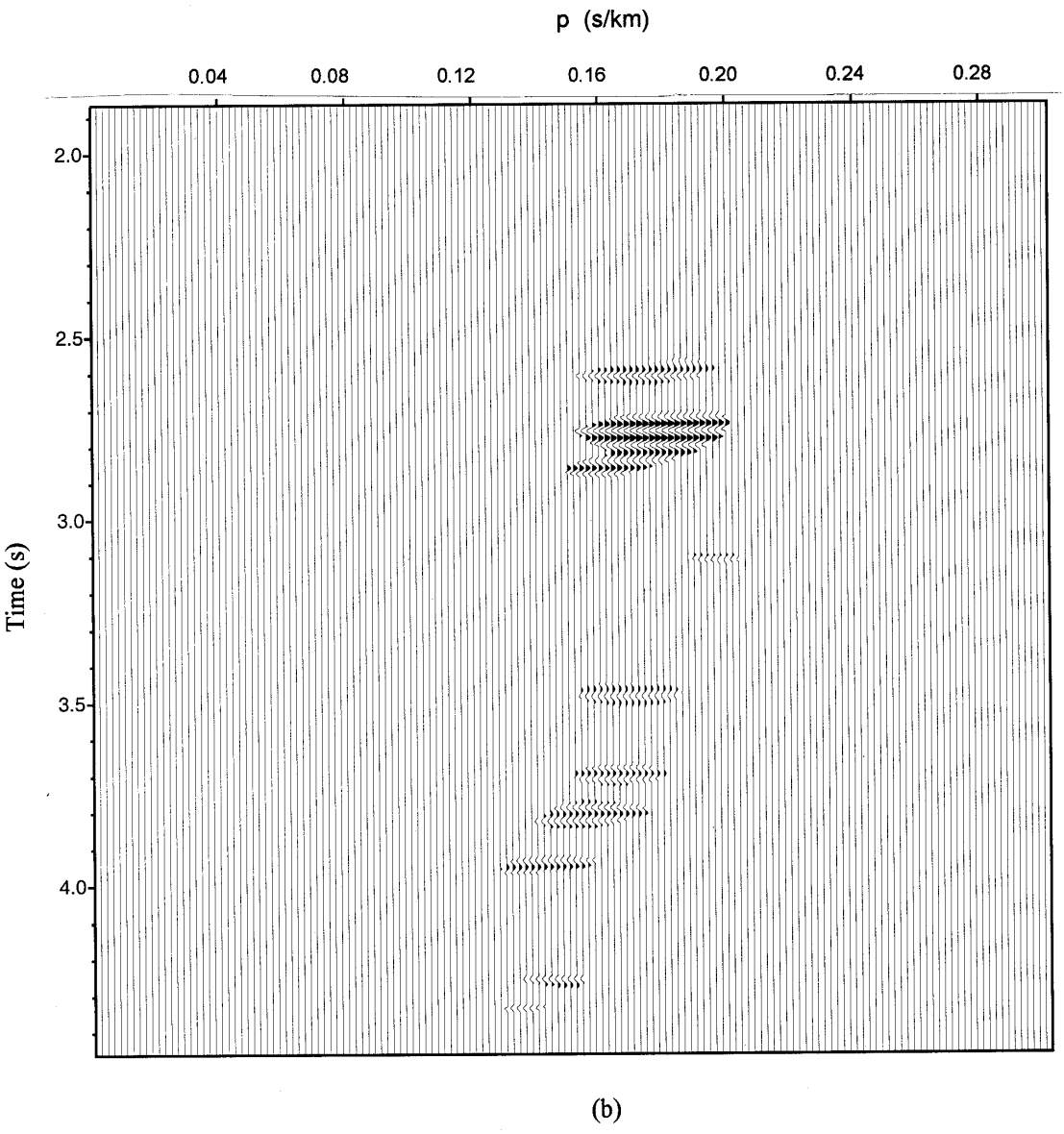

(b)

(Figure 2.21)

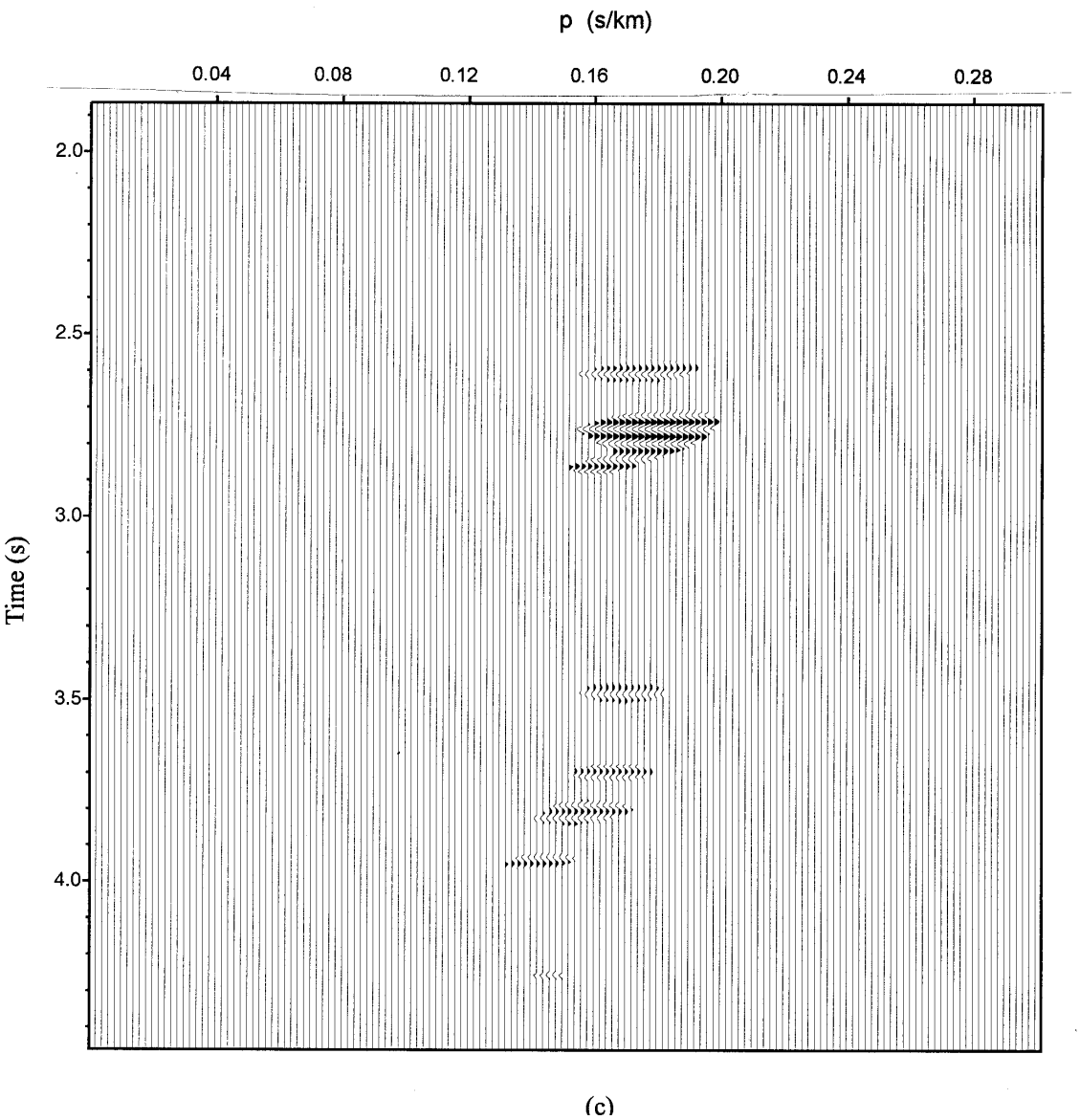

(Figure 2.21)

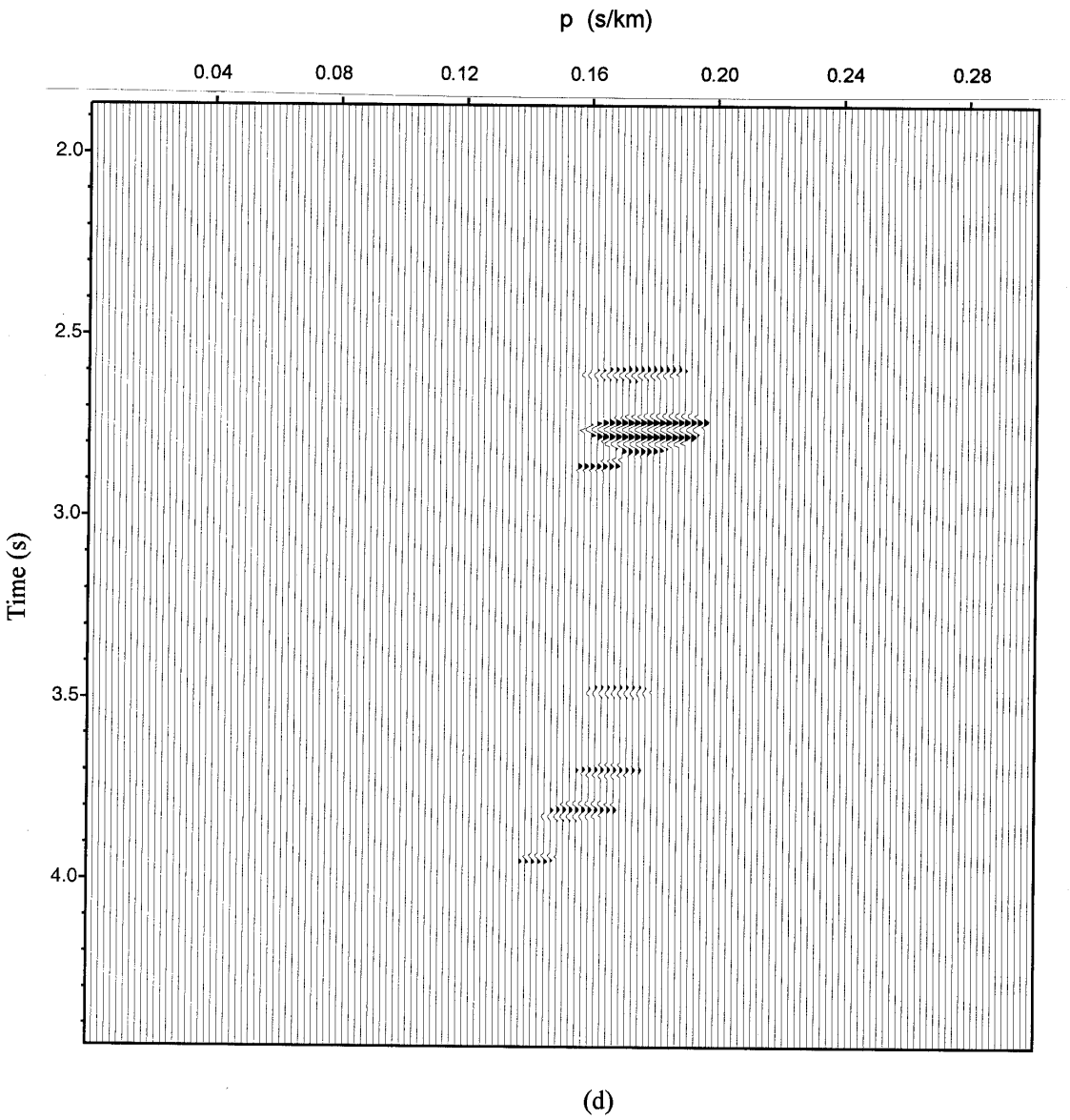

(d)

(Figure 2.21)

Figure 2.22: The raw (a) and final (b) shot gather for Array C (Dye Granite). Processing for the final shot gather included trace editing, bandpass filtering, deconvolution, and static corrections.

Bandpass: 20,25,60,70 Hz

The distance range was 11.53-12.48 km.

deconvolution prewhitening=0.01

prediction lag (α) = 1 sample (spiking deconvolution).

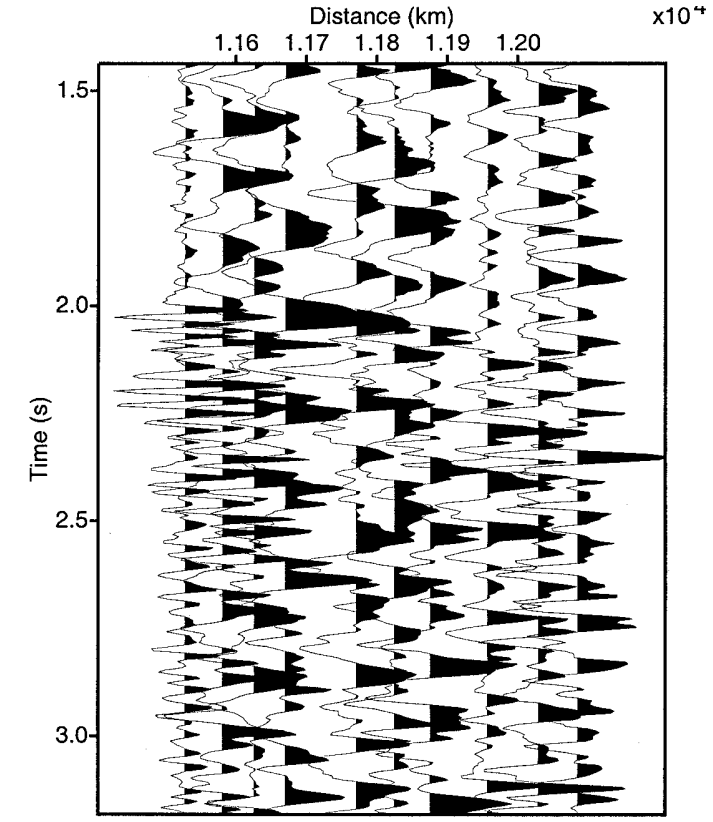

(a)

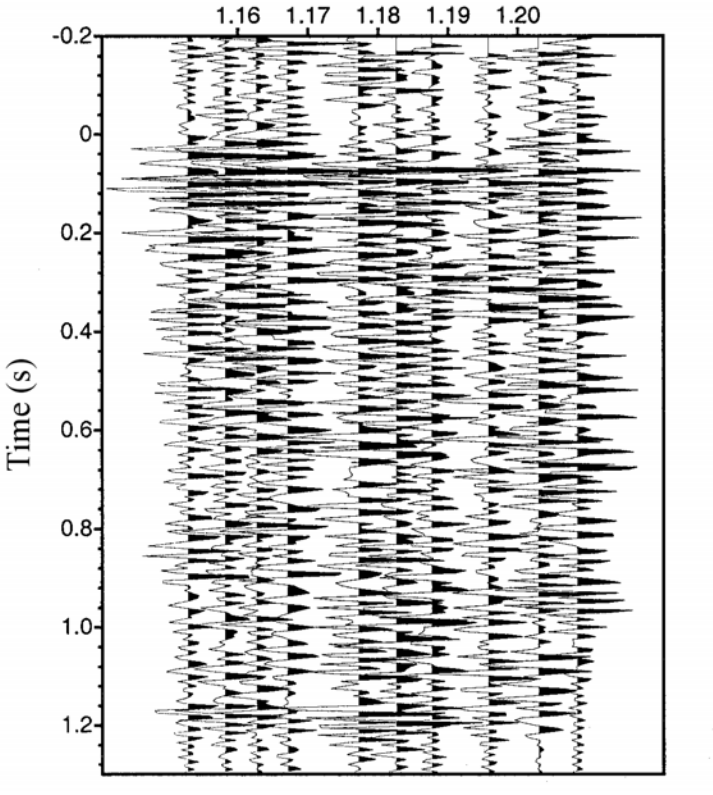

(b)

(Figure 2.22)

Figure 2.23: Slant stack of the Dye Granite shot gather (Array C). Time axis for the slant stacks represents the travel times for the center offset trace. Prior to stacking, shot gather traces were bandpass filtered with a zero-phase filter (20, 25, 60,and 70 Hz) and normalized by their rms amplitudes. “E” refers to the events interpreted as the base of the granite. The slant stack is shown (a) before applying static corrections and (b) after. Static corrections result in significant improvement in focusing and coherency of arrivals. “P” refers to the direct P wave.

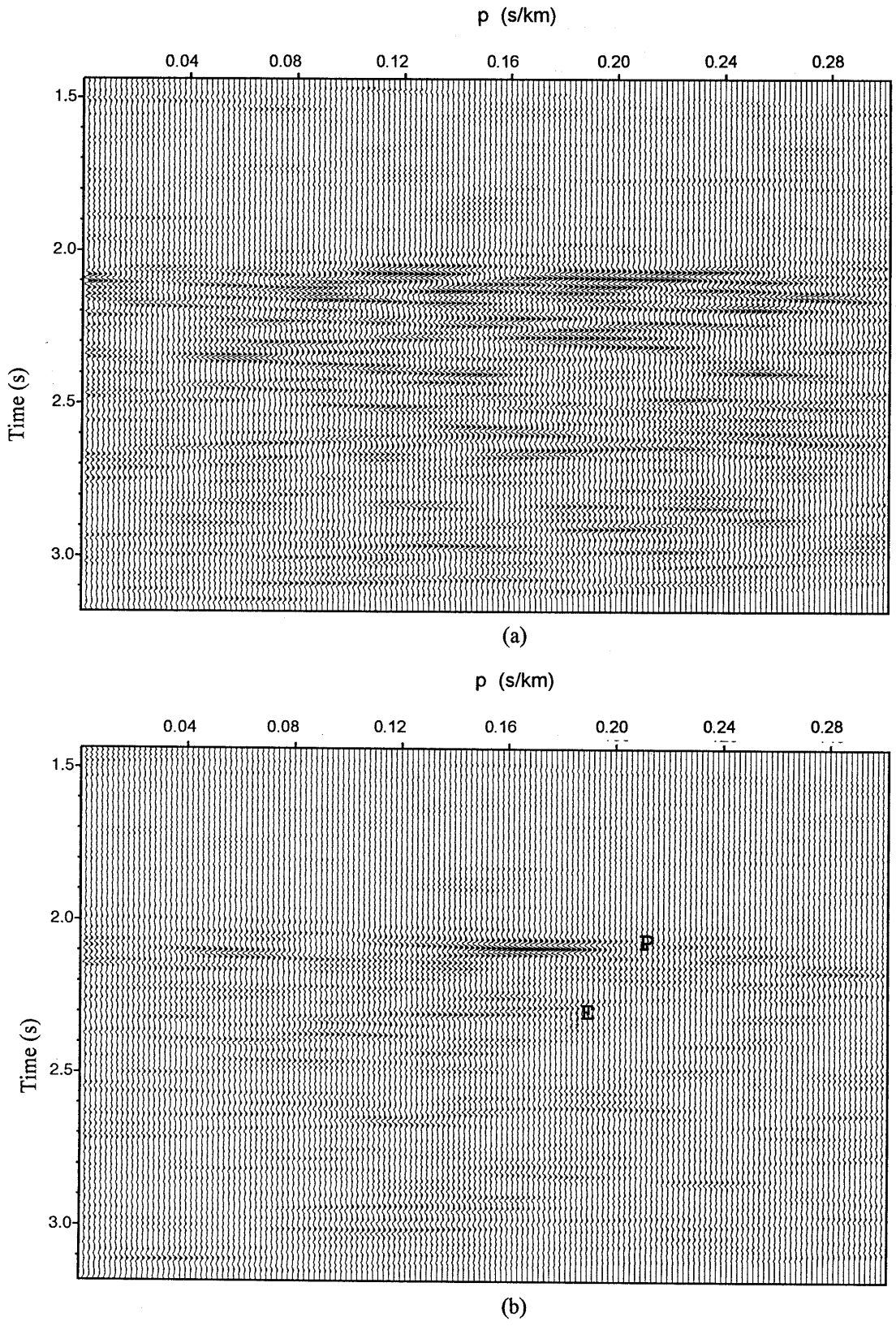
p (s/km)
0.04
0.08
0.12
0.16
0.20
0.24
0.28
1.5
2.0
2.5
3.0
Time (s)
(a)
p (s/km)
0.04
0.08
0.12
0.16
0.20
0.24
0.28
1.5
2.0
2.5
3.0
Time (s)
P
E
(b)

(Figure 2.23)

Figure 2.24: Semblance of the slant stack for Dye Granite (Array C). The filter frequencies of the shot gather are 20, 25, 60, 70 Hz. The semblance is shown (a) before and (b) after applying static corrections. The direct P wave shows an average ray parameter (p) of about 0.18 s/km. As noted earlier, static corrections enhance the phase coherence of reflections.

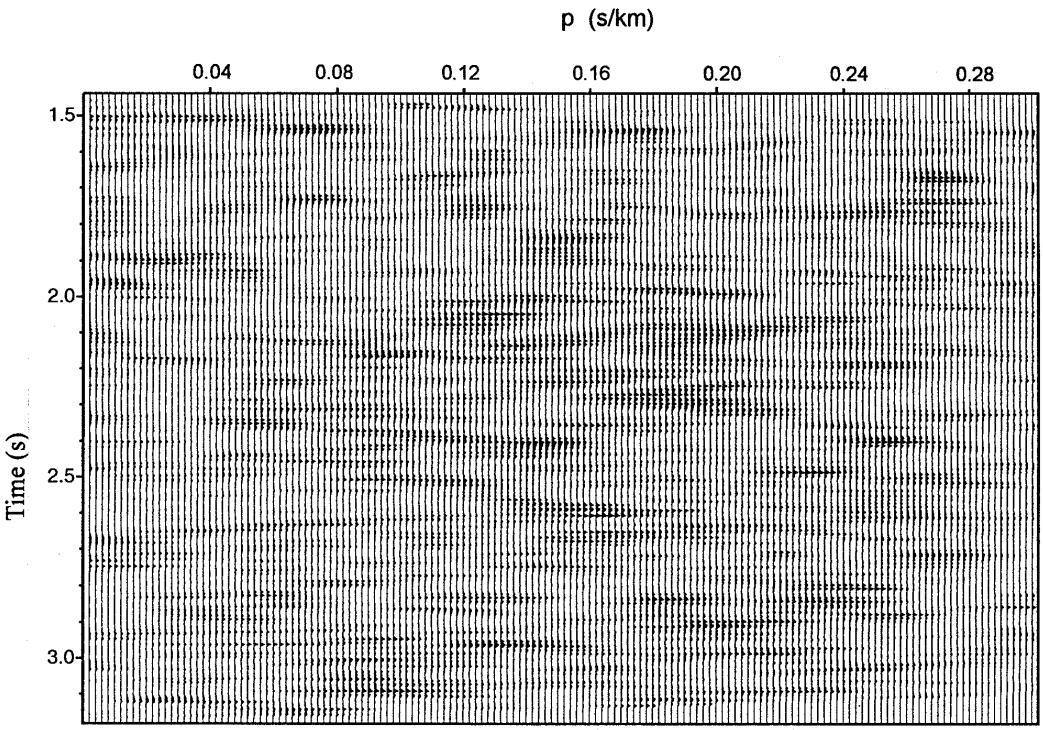

(a)

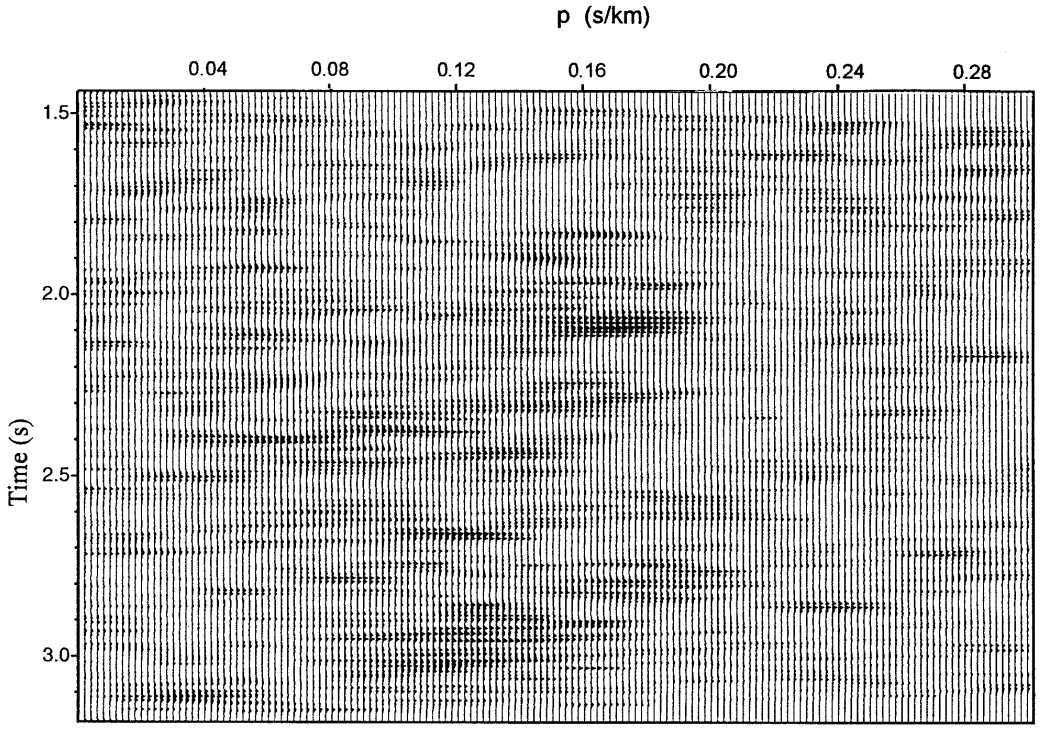

(b)

(Figure 2.24)

Figure 2.25: Smoothed semblance for the Dye Granite shot gather (Array C). It is shown after static correction.

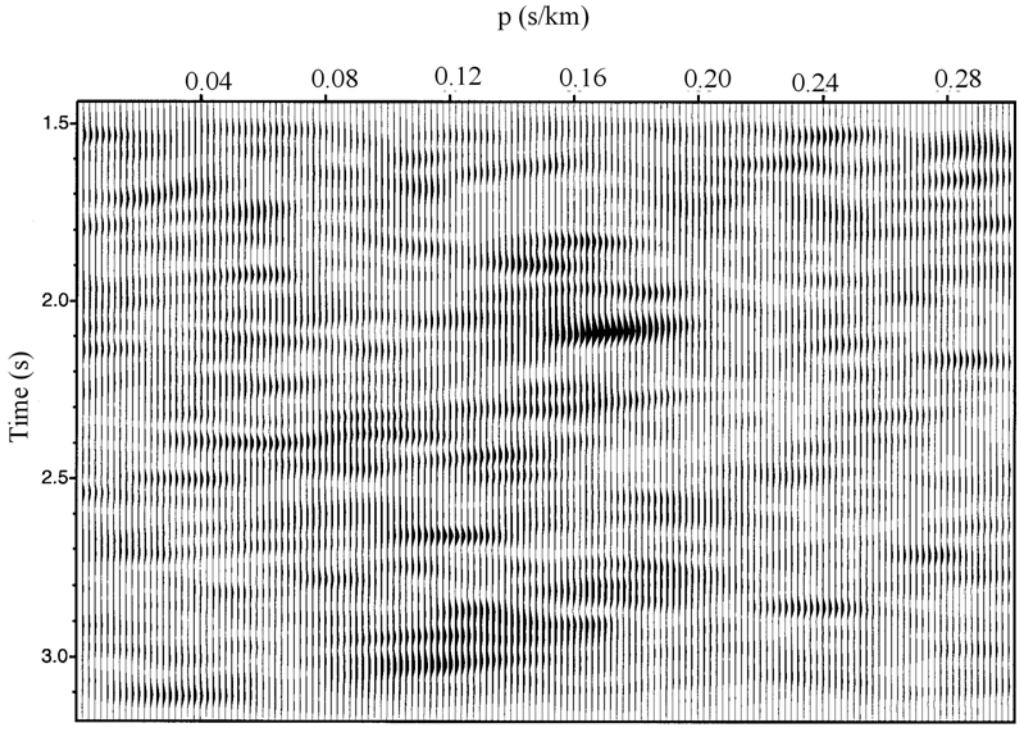

(Figure 2.25)

Figure 2.26: Coherency filtered slant stacks that were migrated for the Dye Granite shot gather (Array C). After smoothing the unfiltered semblance (Figure 2.24a) of the slant stack, a coherency filter was constructed by assigning zeros for all samples in the smoothed semblance with values less than the chosen threshold and value of 1 for the remaining samples. This suppresses the incoherent noise. P-SV indicates events interpreted as converted P to SV waves. E points to the possible base of the Elberton granite. (a) shows the coherency filtered slant stack for a threshold value 0.46, (b, c, and d) represent the same operation with higher threshold values (0.47,0.5 and 0.55 respectively). Raising the threshold yields more focused events for migration.

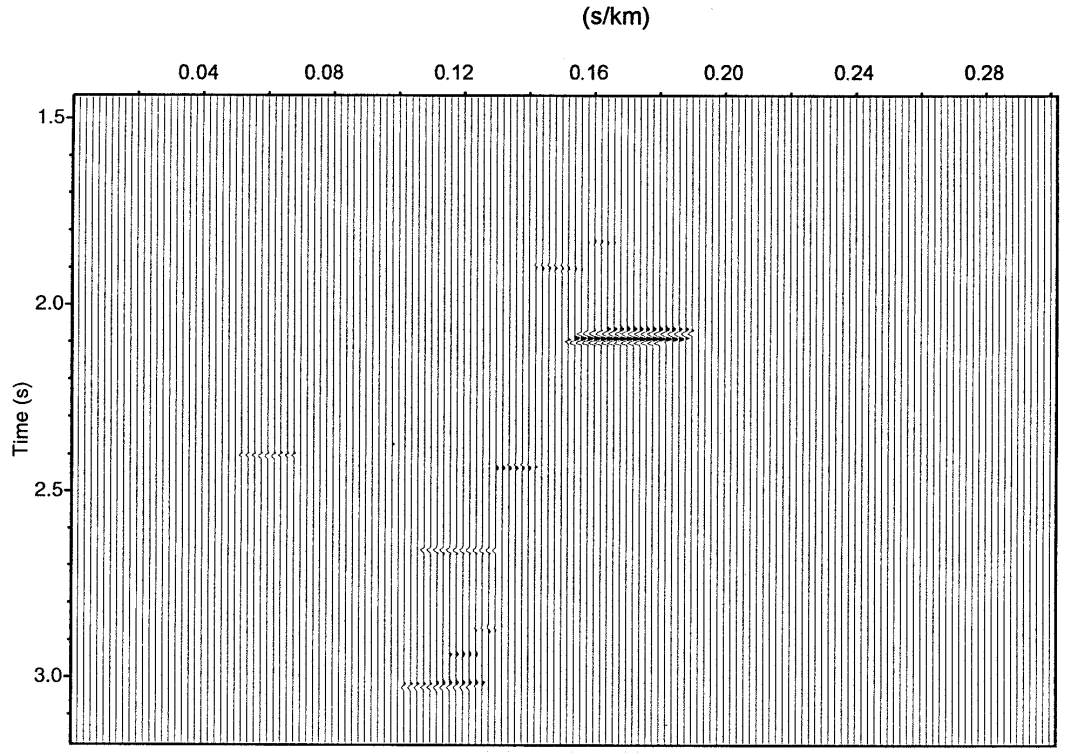

(c)

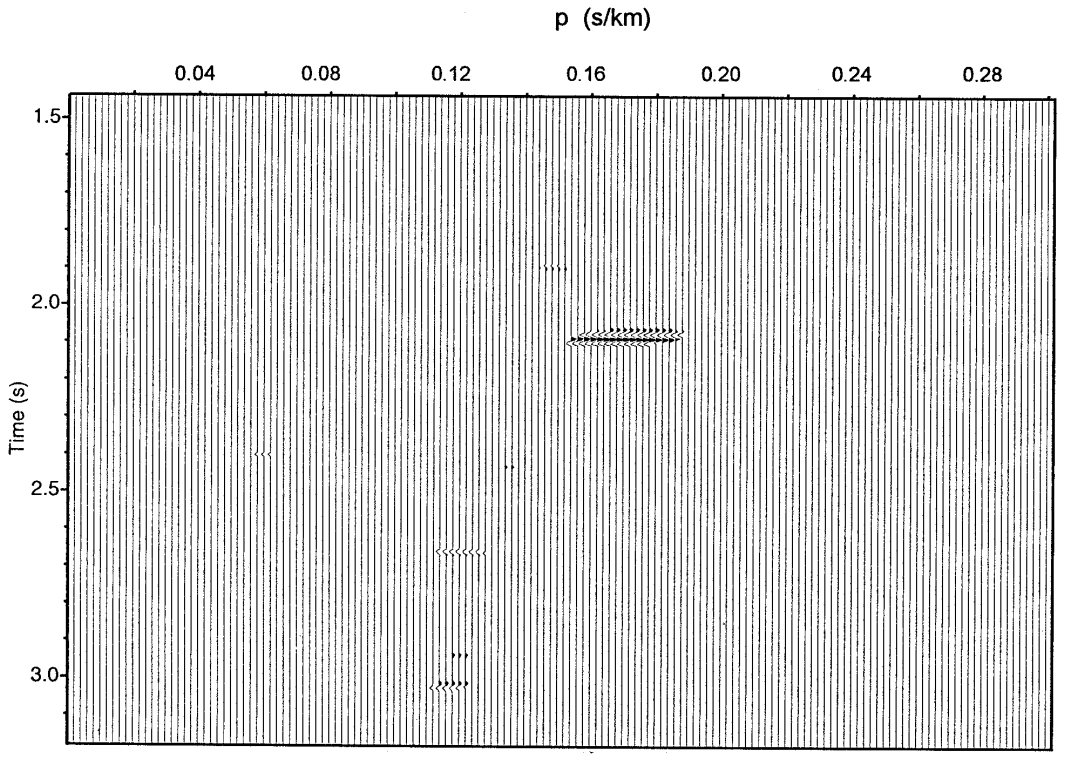

(d)

(Figure 2.26)

Figure 2.27: The raw (a) and final (b) shot gather for Array F (Boyd Granite 3). The distance range for this gather was 13.09-14.18 km. Processing for the final shot gather includes trace editing, bandpass filtering, deconvolution, and static corrections

Bandpass: 13,19,33,45 Hz

Prewhitening=0.01

prediction lag (α) = 1 sample (spiking deconvolution).

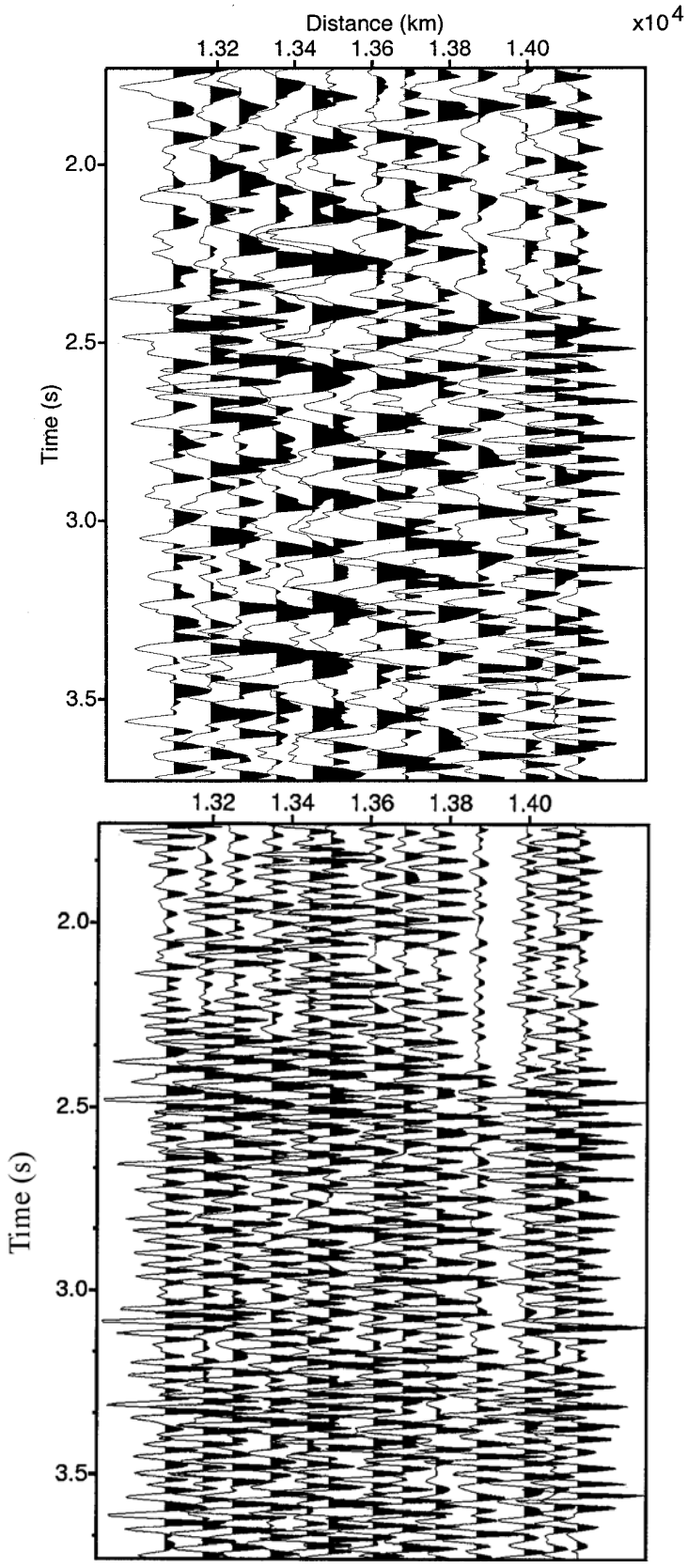
Distance (km)
x10^4
1.32
1.34
1.36
1.38
1.40
2.0
2.5
3.0
3.5
Time (s)
1.32
1.34
1.36
1.38
1.40
2.0
2.5
3.0
3.5
Time (s)

(Figure 2.27)

Figure 2.28: Slant stack of the Boyd Granite 3 shot gather, array F, (a) before static correction and (b) after. Time axes for the slant stacks represent the travel times for the center offset trace. Prior to stacking, shot gather traces were filtered with a zero-phase, bandpass filter (13, 19, 33, and 45 Hz) and normalized by their rms amplitudes. “E” refers to the events interpreted as the base of the granite. The slant stack is shown (a) before applying the static corrections and (b) after. In this shot, using 5.8 km/s as the reduced velocity distorts the apparent velocity. Therefore the static-corrected slant stack was shifted back by 0.030 s/km (ray parameter) right before the migration process to correct for the bias. The stack here is shown before applying this final shift.

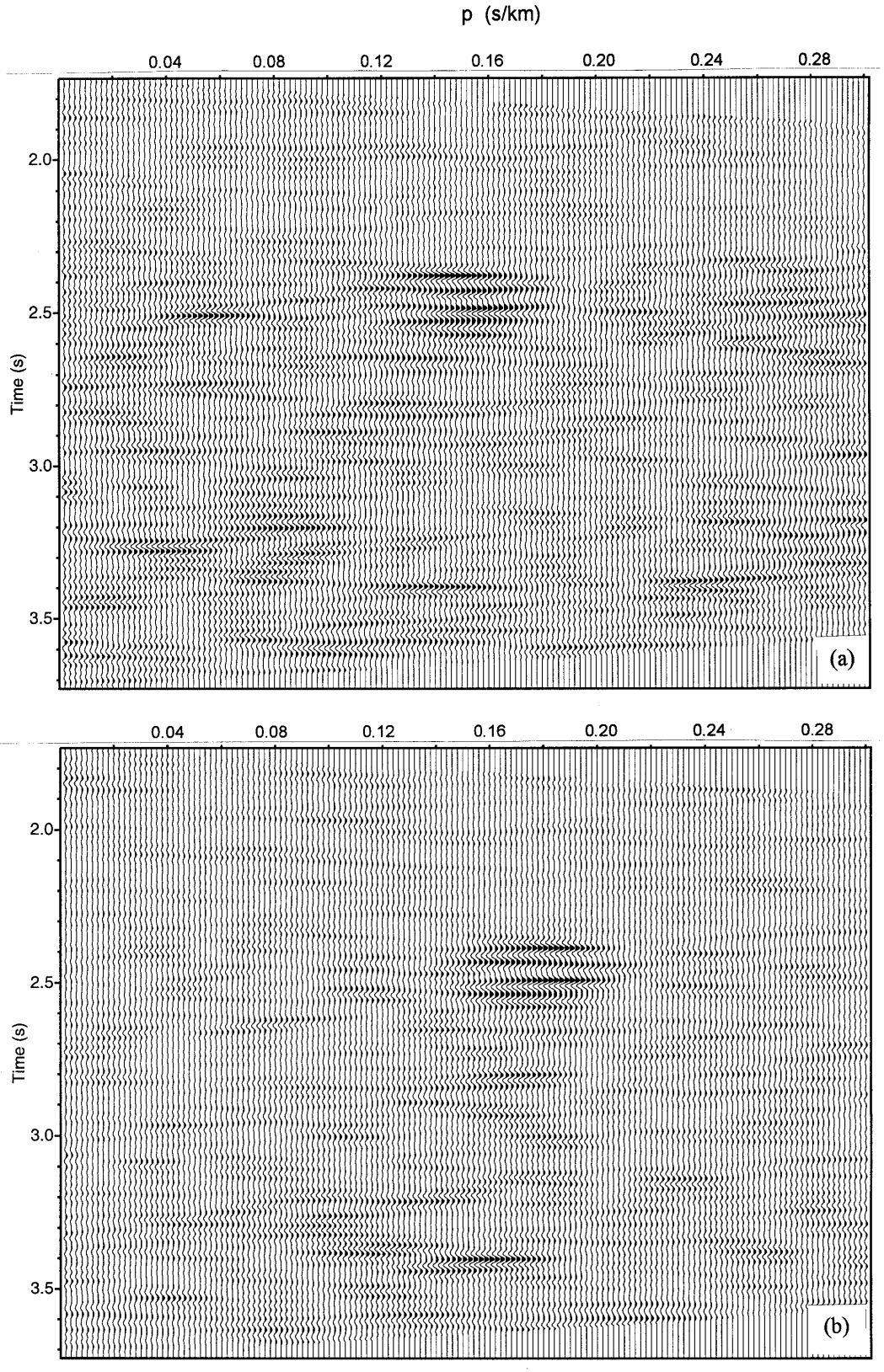

(Figure 2.28)

Figure 2.29: Semblance of the slant stack of the shot gather for Boyd Granite 3 (Array F). The bandpass filter frequencies of the shot gather are 13,19,33,45 Hz. The semblance is shown before (a) and after (b) applying static corrections. The concentration of the seismic energy is very clear after applying static corrections. The enhancement is indicated by more focused events after static corrections but they are shifted toward a higher ray parameter due to using 5.8 km/s as a reduced velocity for lining up the first arrivals. This distortion is corrected for before the migration by shifting back the arrivals by 0.030 s/km (ray parameter). The semblance here is shown before applying this final shift.

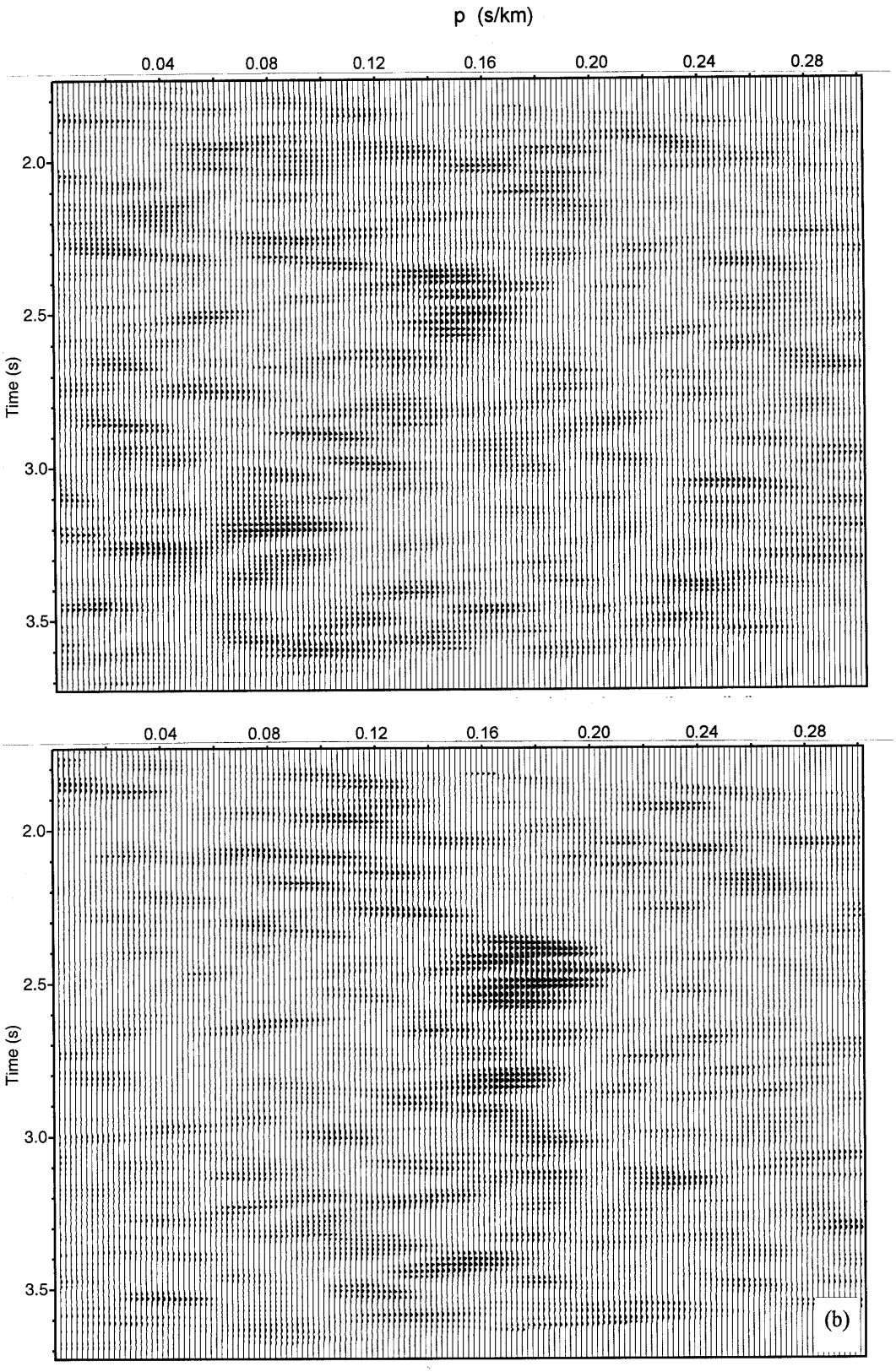

(Figure 2.29)

Figure 2.30: Smoothed semblance for the Boyd granite 3 shot Gather (Array F). It is shown after static correction. The semblance was shifted toward a higher ray parameter due to using 5.8 km/s as a reduced velocity for lining up the first arrivals. This distortion is corrected for before the migration by shifting back the arrivals by 0.030 s/km (ray parameter). The semblance here is shown before applying this final shift.

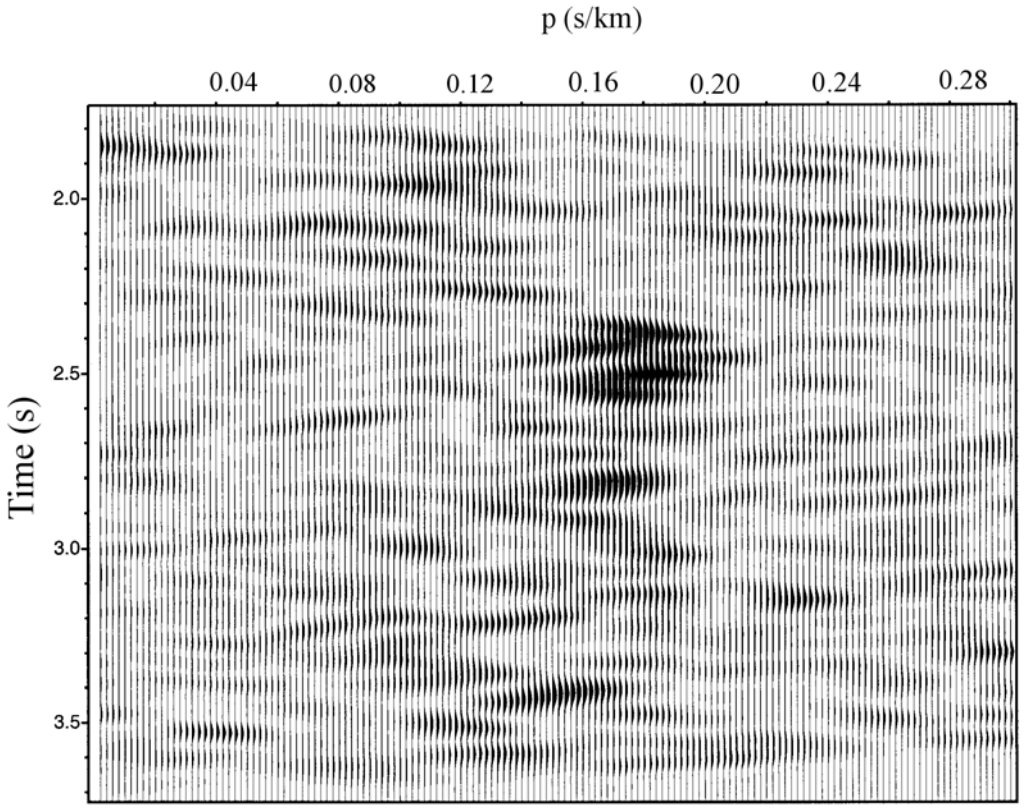

(Figure 2.30)

Figure 2.31: Coherency filtered slant stacks that were migrated for the Boyd Granite 3 shot gather (Array F). After smoothing the unfiltered semblance (Figure 2.29a) of the slant stack by high cut filter, a coherency filter was constructed by assigning zeros for all samples in the smoothed semblance with values less than the chosen threshold and value of 1 for the remaining samples. This suppresses the incoherent noise. P-SV indicates arrivals interpreted as converted P to SV waves. E marks the possible base of the Elberton granite. (a) shows the coherency filtered slant stack for a threshold value of 0.45, (b, c, and d) represent the same operation with higher threshold values (0.5,0.55 and 0.6 respectively) Raising the threshold yields more focused events for migration. The higher ray parameter distortion is corrected for before the migration by shifting back the arrivals by 0.030 s/km (ray parameter). The stacks here are shown before applying this final shift.

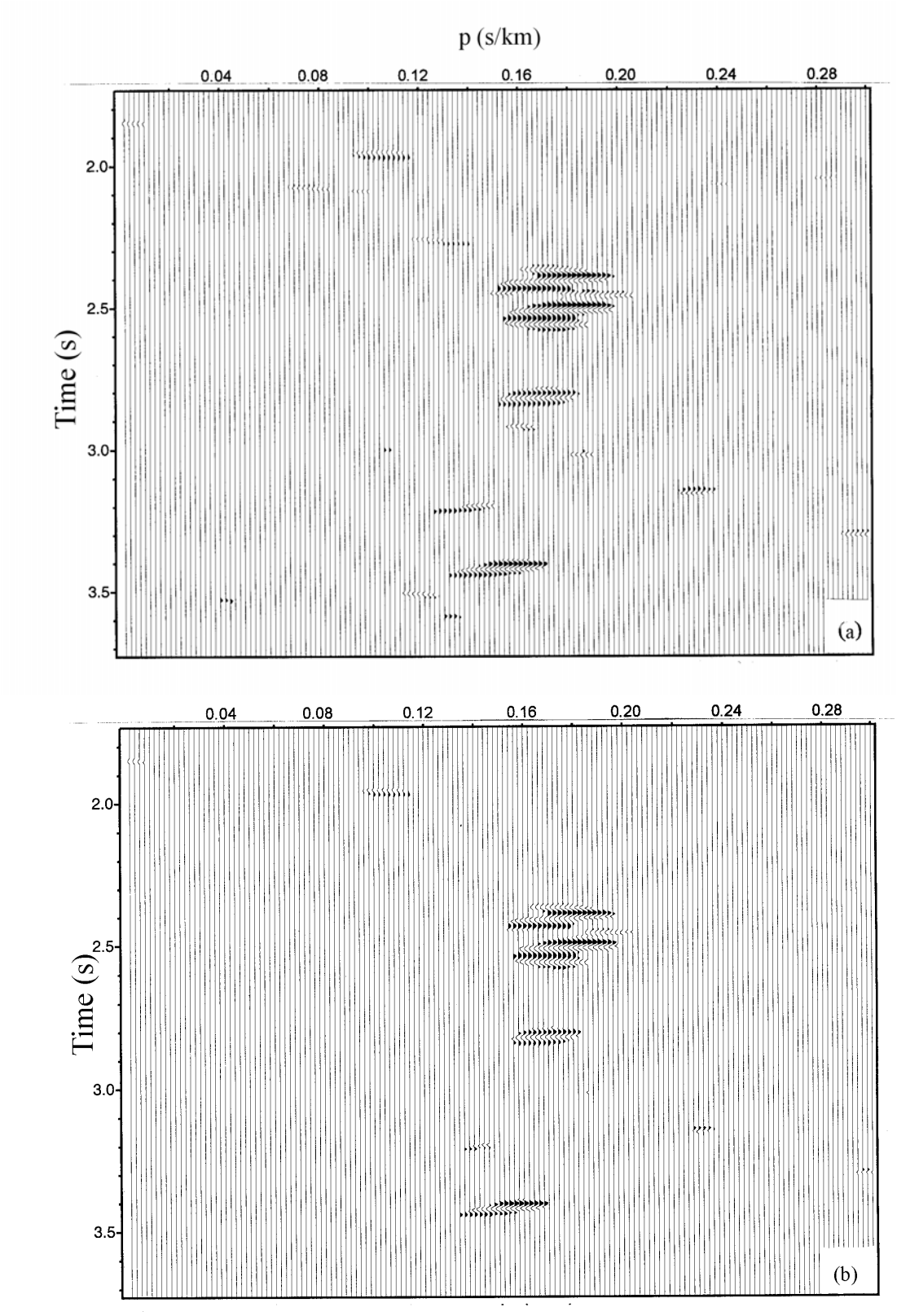

(Figure 2.31)

Figure 2.32: The raw (a) and final (b) shot gather for Array A (Boyd Granite 2). Distance range was 7.77-8.2 km. Processing steps for the final gather include trace editing bandpass filtering, deconvolution, and statics corrections

Bandpass: 15,25,45,60 Hz

Deconvolution pre-whitening=0.01.

prediction lag (α) = 1 sample (spiking deconvolution).

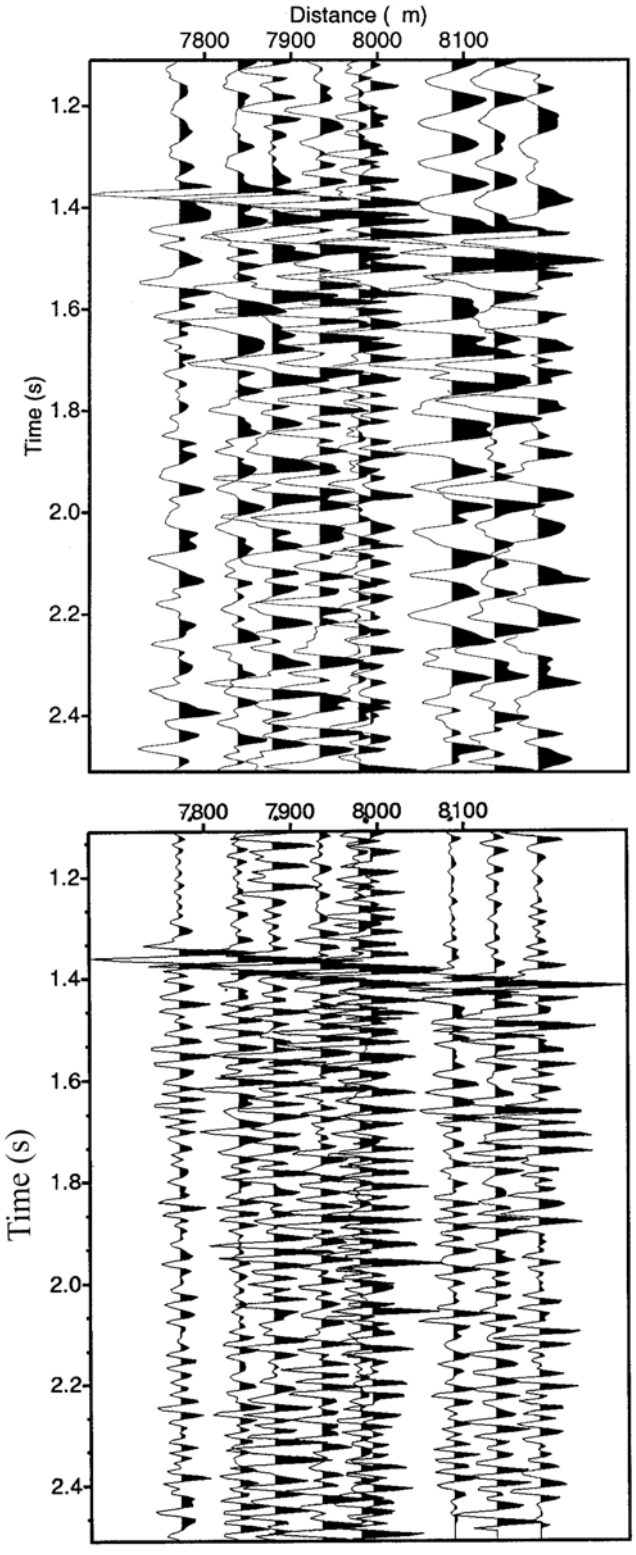
Distance (m)
7800
7900
8000
8100
1.2
1.4
1.6
1.8
2.0
2.2
2.4
Time (s)
7800
7900
8000
8100
1.2
1.4
1.6
1.8
2.0
2.2
2.4
Time (s)

(Figure 2.32)

Figure 2.33: Slant stack of the Boyd Granite 2 shot gather (Array A). Time axis for the slant stacks represents the travel times for the center offset trace. Shot gather traces were filtered with a zero-phase, bandpass filter (15, 25, 45, and 60 Hz) and normalized by their rms amplitudes. The slant stack is shown (a) before applying static corrections and (b) after. Static corrections improve the phase coherence of reflections. “P” refers to the direct P wave and “E” to an event interpreted as a reflection from the base of the granite.

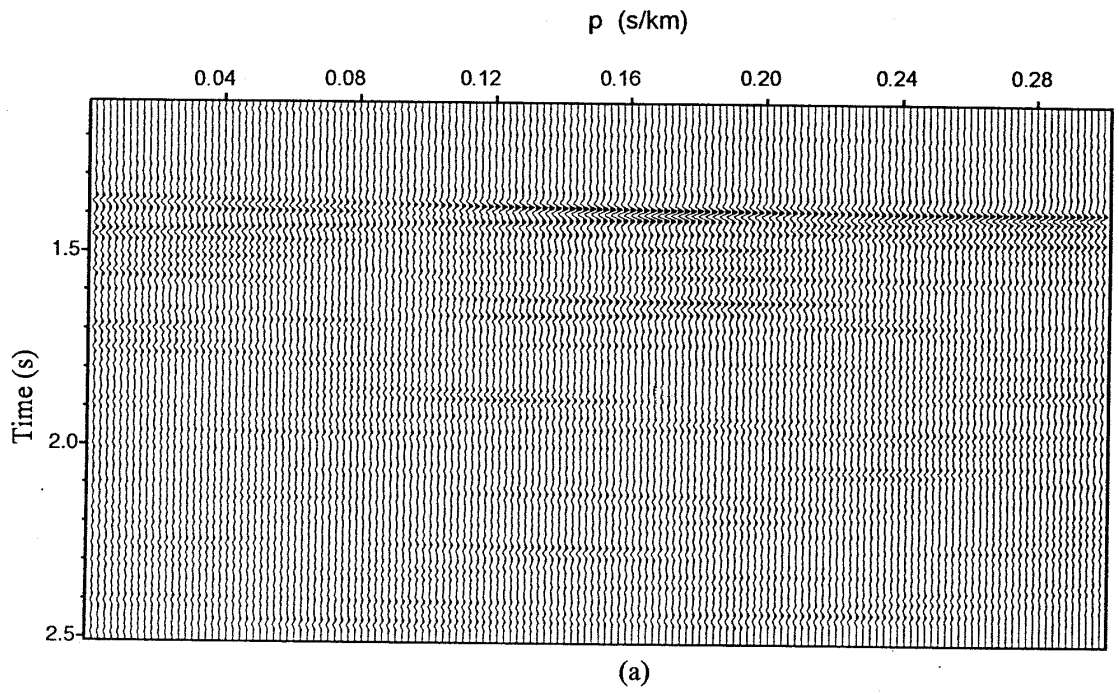

(a)

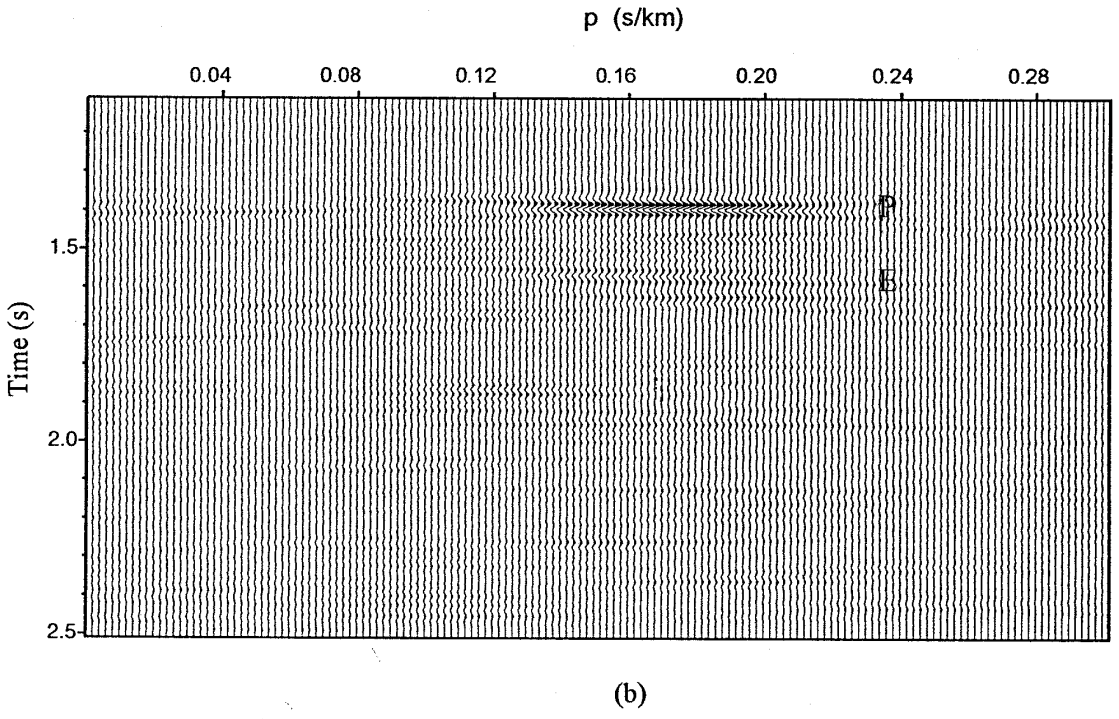

(b)

(Figure 2.33)

Figure 2.34: Semblance of the slant stack of the shot gather for Boyd Granite 2 (Array F). The filter frequencies of the shot gather are 15, 25, 45, 60 Hz. The semblance is shown before (a) and after (b) applying the static correction. The concentration of the seismic energy is very clear after applying the static correction.

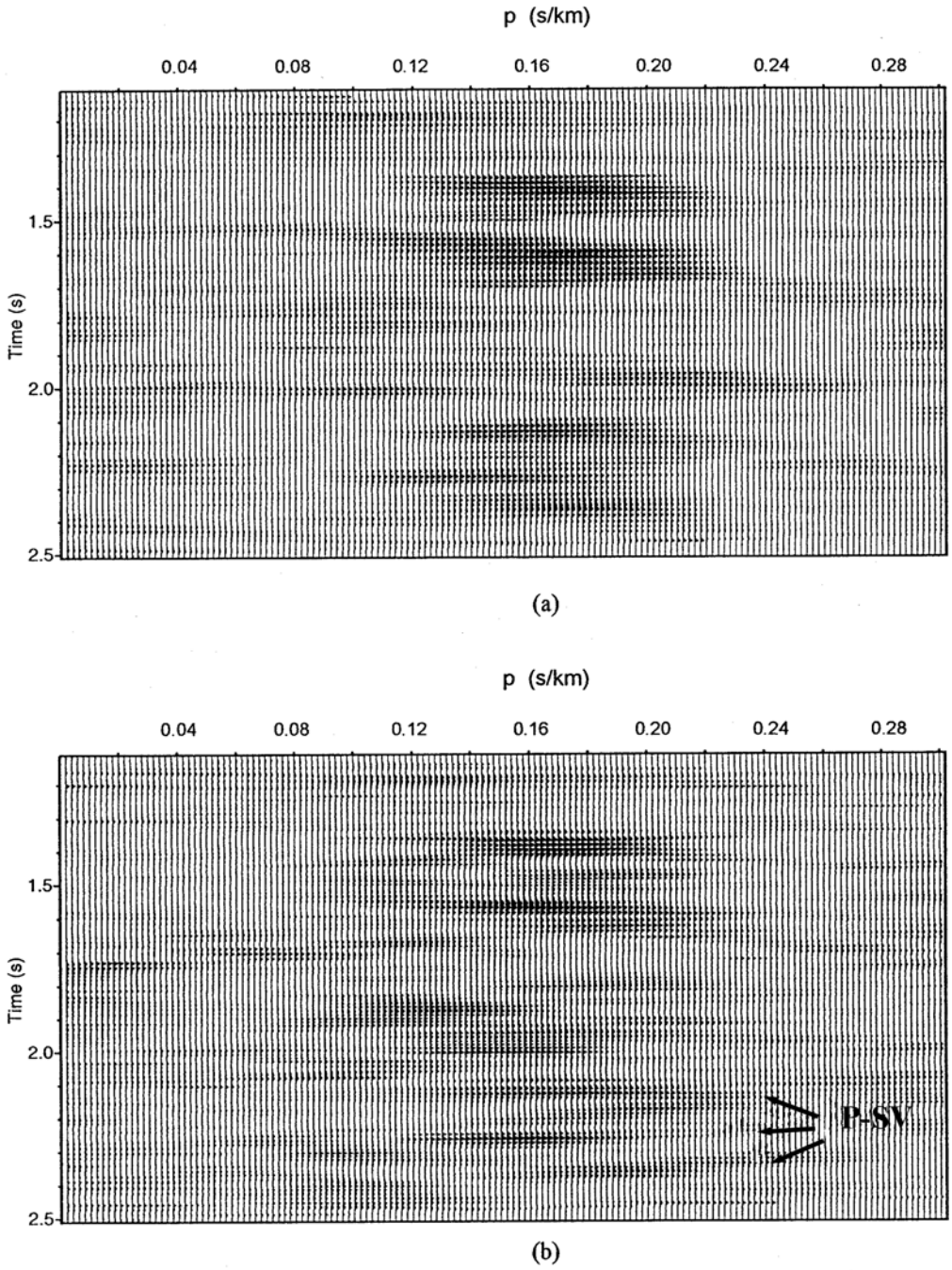
p (s/km)
0.04
0.08
0.12
0.16
0.20
0.24
0.28
Time (s)
1.5
2.0
2.5
(a)
p (s/km)
0.04
0.08
0.12
0.16
0.20
0.24
0.28
Time (s)
1.5
2.0
2.5
P-SV
(b)

(Figure 2.34)

Figure 2.35: Smoothed semblance for the Boyd Granite 2 shot gather (Array A). It is shown after static corrections.

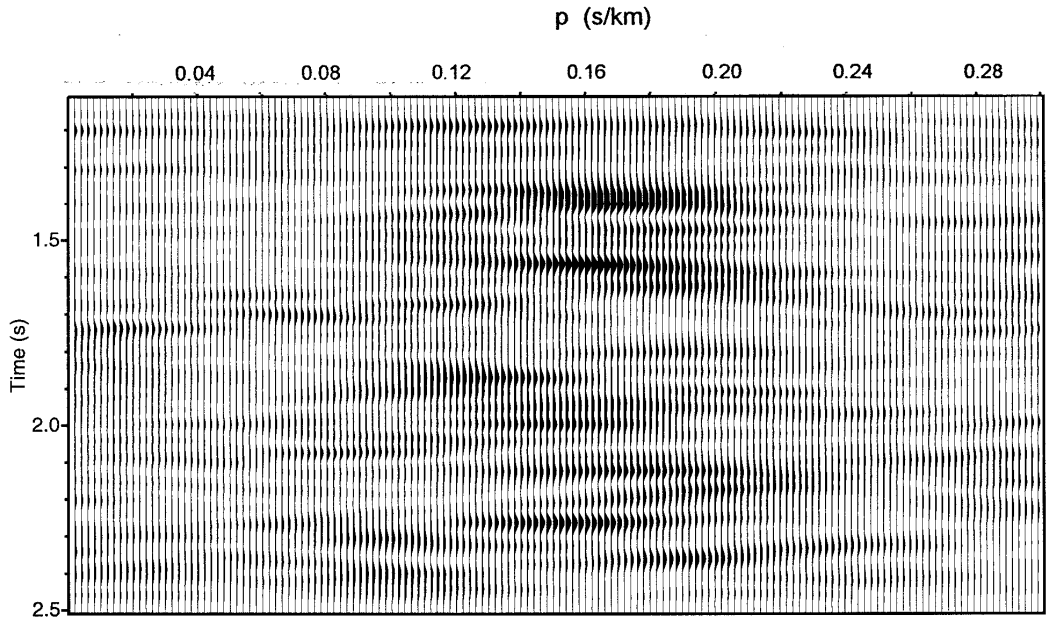

(Figure 2.35)

Figure 2.36: Coherency filtered slant stacks that were migrated for the Boyd Granite 2 shot gather (Array A). After smoothing the unfiltered semblance (Figure 2.34a) of the slant stack by high cut filter, a coherency filter was constructed by assigning zeros for all samples in the smoothed semblance with values less than the chosen threshold and value of 1 for the remaining samples. This suppresses incoherent noise. P-SV indicates events interpreted as converted P to SV waves. “E” marks the possible base of the Elberton granite. (a) shows the coherency filtered slant stack for a threshold value 0.45, (b and c) represent the same operation with higher threshold values (0.5 and 0.6 respectively).

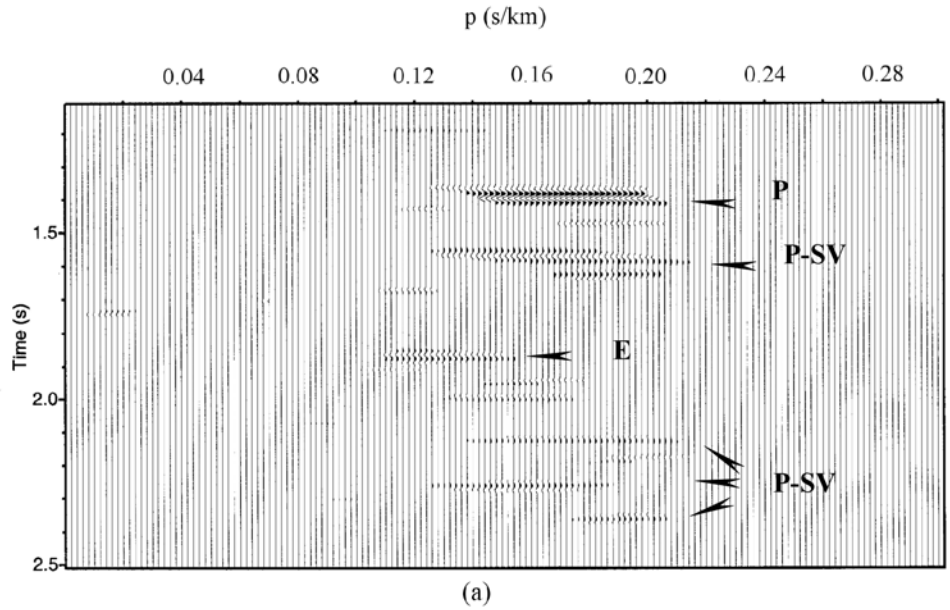

(a)

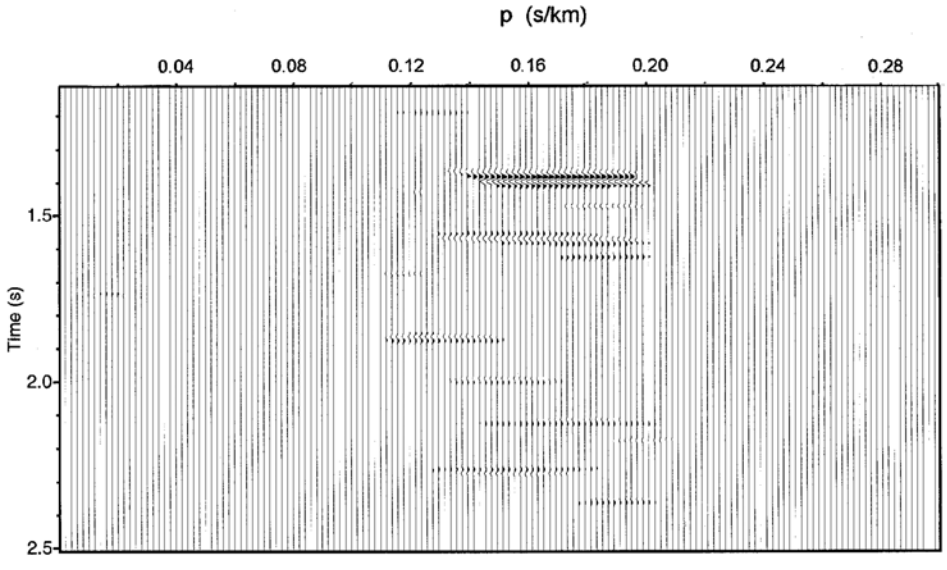

(b)

(Figure 2.36)

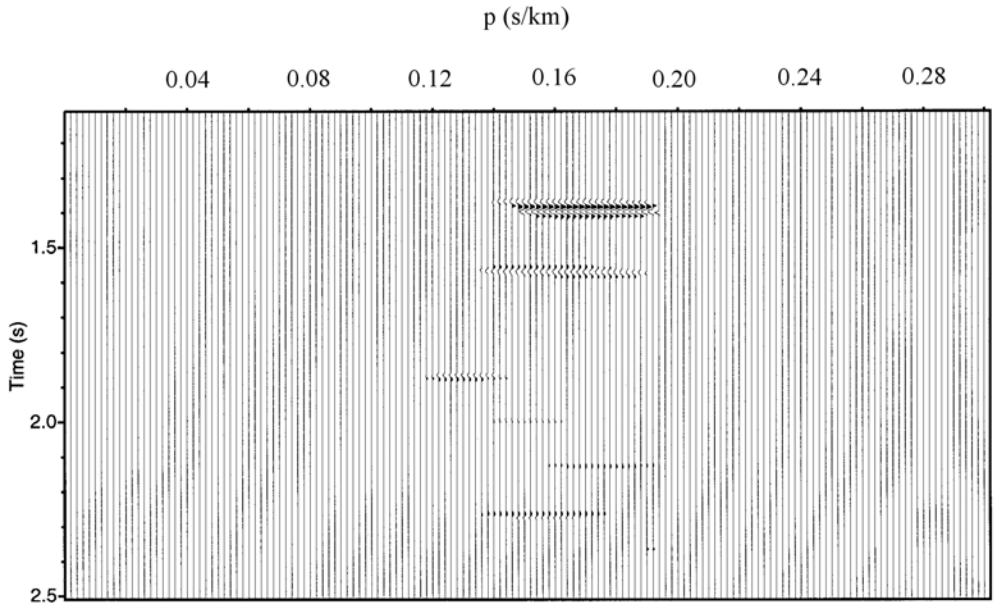

(c)

(Figure 2.36)

Figure 2.37: The velocity-depth model used for all shots as an input to the migration process. The model consists of 6 layers. The minimum velocity used was 5.5 km/s and the maximum was 6.2 km/s. The top layer velocity was determined from the travel time of the direct P wave. Velocities for the other layers were based on the averaged velocities for P wave derived in previous laboratory measurements carried out at room temperature and confining pressures up to 10 kbar for similar rock units (Birch, 1960).

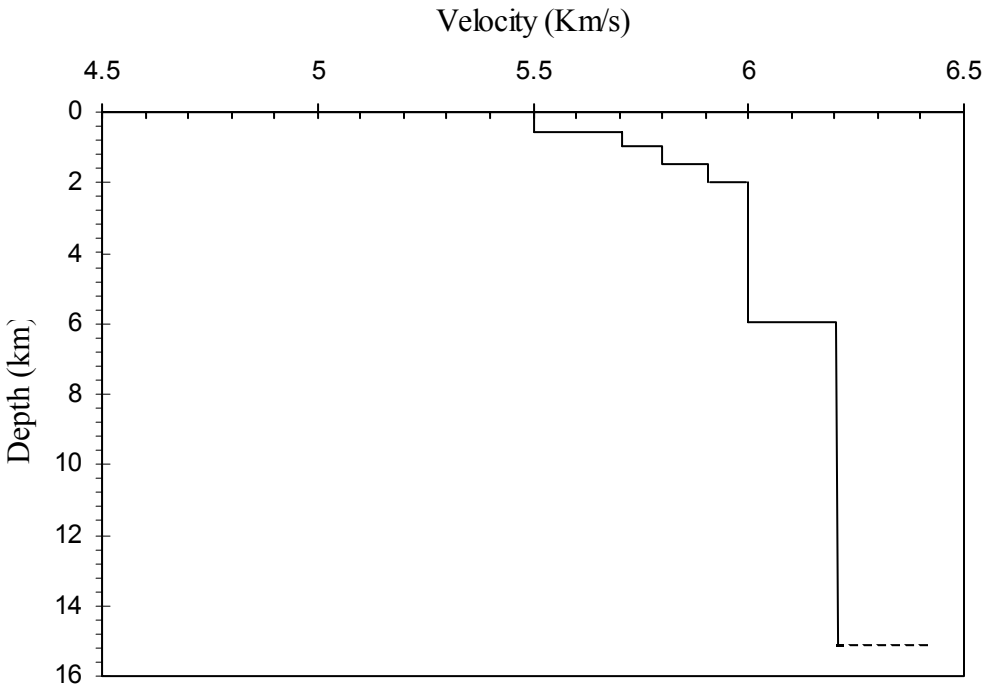

(Figure 2.37)

Figure 2.38: Diagram showing the procedure for migrating wide-angle reflections (after Hawman and Phinney, 1992). “The migration algorithm involves downward continuing the up-going ray with observed ray parameter p_o until it intersects a down-going ray that gives a total two-way travel time which matches the observed travel time. First we find the point of intersection of the upcoming ray detected at the recording spread with rays traveling downward from the source. Because of refraction, not all down-going rays will intersect the up-going ray.”(p.399)

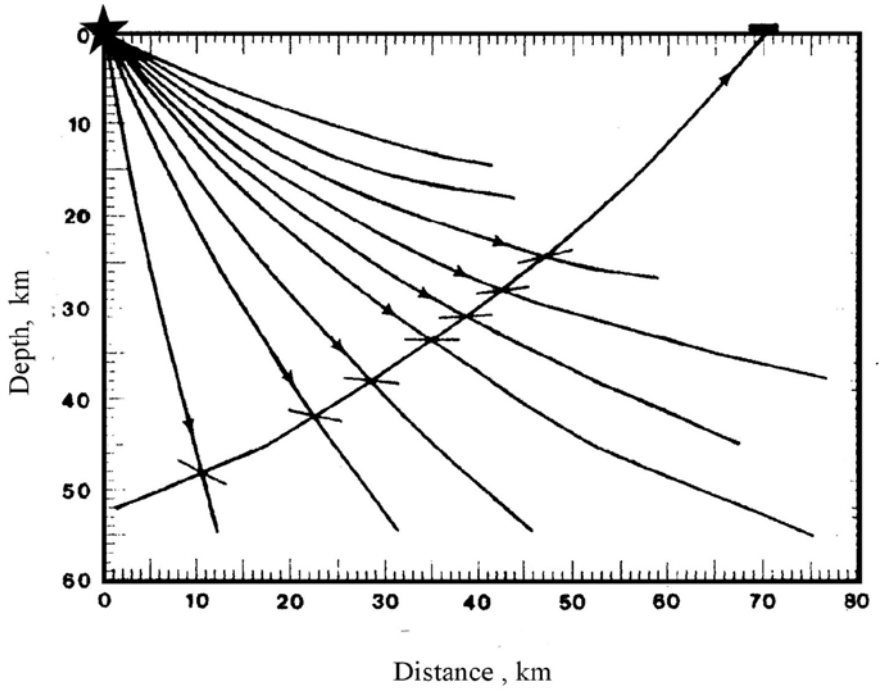

(Figure 2.38)

Figure 2.39: Migrated section of the Blue Ribbon (Array B) coherency-filtered slant stacks. Bandpass filter (15,26,44,55 Hz). (a) shows the migrated section that belongs to the slant stack that was coherency filtered using a cutoff semblance value of 0.45. (b, c, and d) represent the migrated section with higher cutoff semblance values (0.5, 0.55, and 0.6). "E" refers to package of reflections interpreted as the base of the Elberton granite, "M" to the master decollement, and P-SV to converted P to S waves.

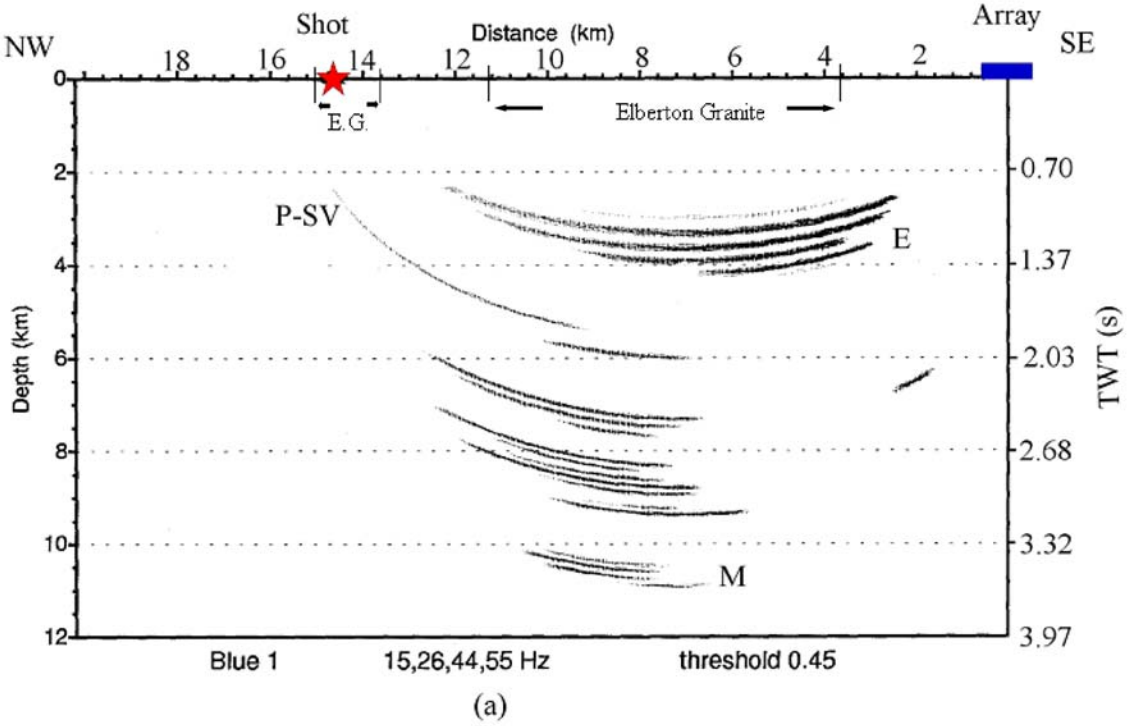

(a)

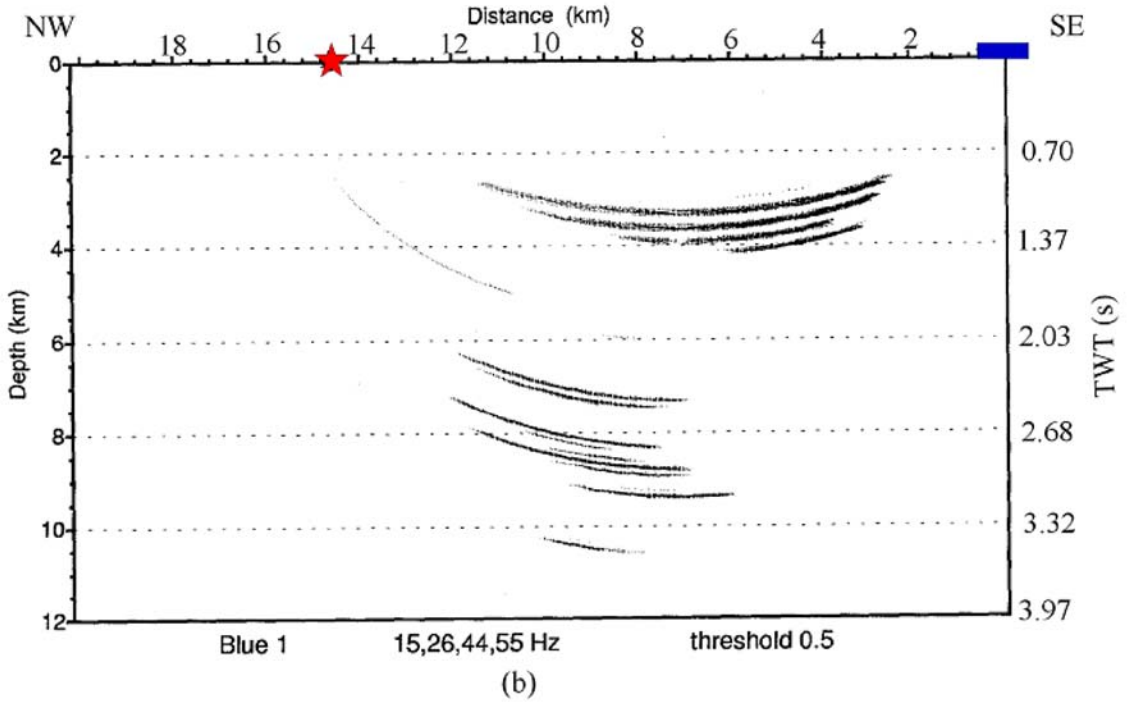

(b)

(Figure 2.39)

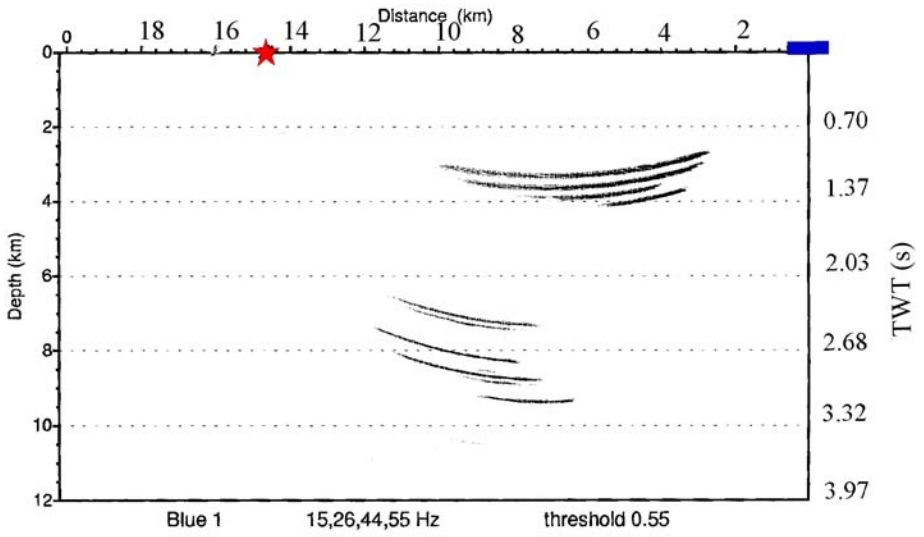

(c)

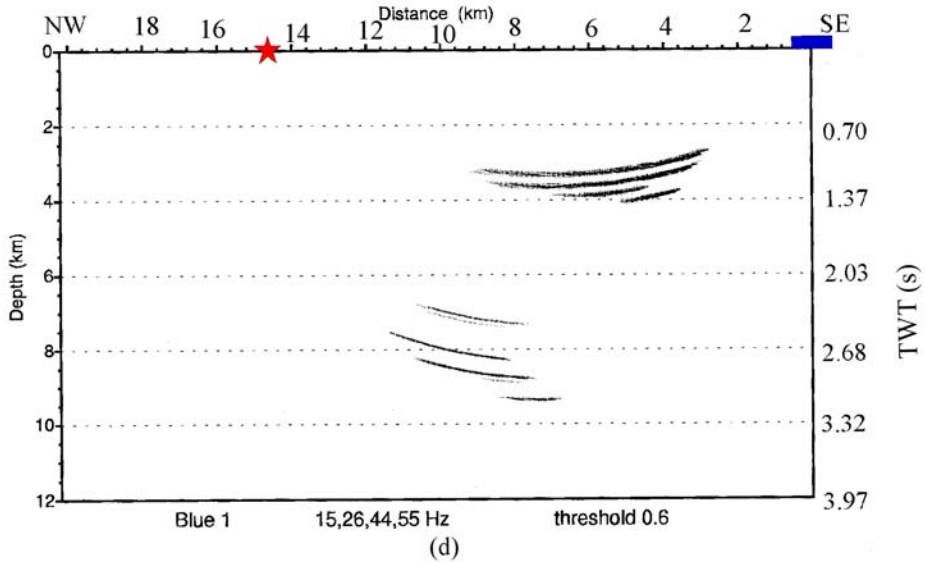

(d)

(Figure 2.39)

Figure 2.40: Migrated section of the Dye Granite (Array C) coherency-filtered slant stacks. Bandpass filter (20, 25, 60, 70 Hz). (a) shows the migrated section of the coherency filtered slant stack using a cutoff semblance value of 0.46. (b, c, and d) represent the migrated section with higher cutoff semblance values (0.47,0.5, and 0.55). "E" is interpreted as the bottom of a layered complex at the base of the Elberton granite. In (a) the horizontal reflection just above it may mark the top of this complex.

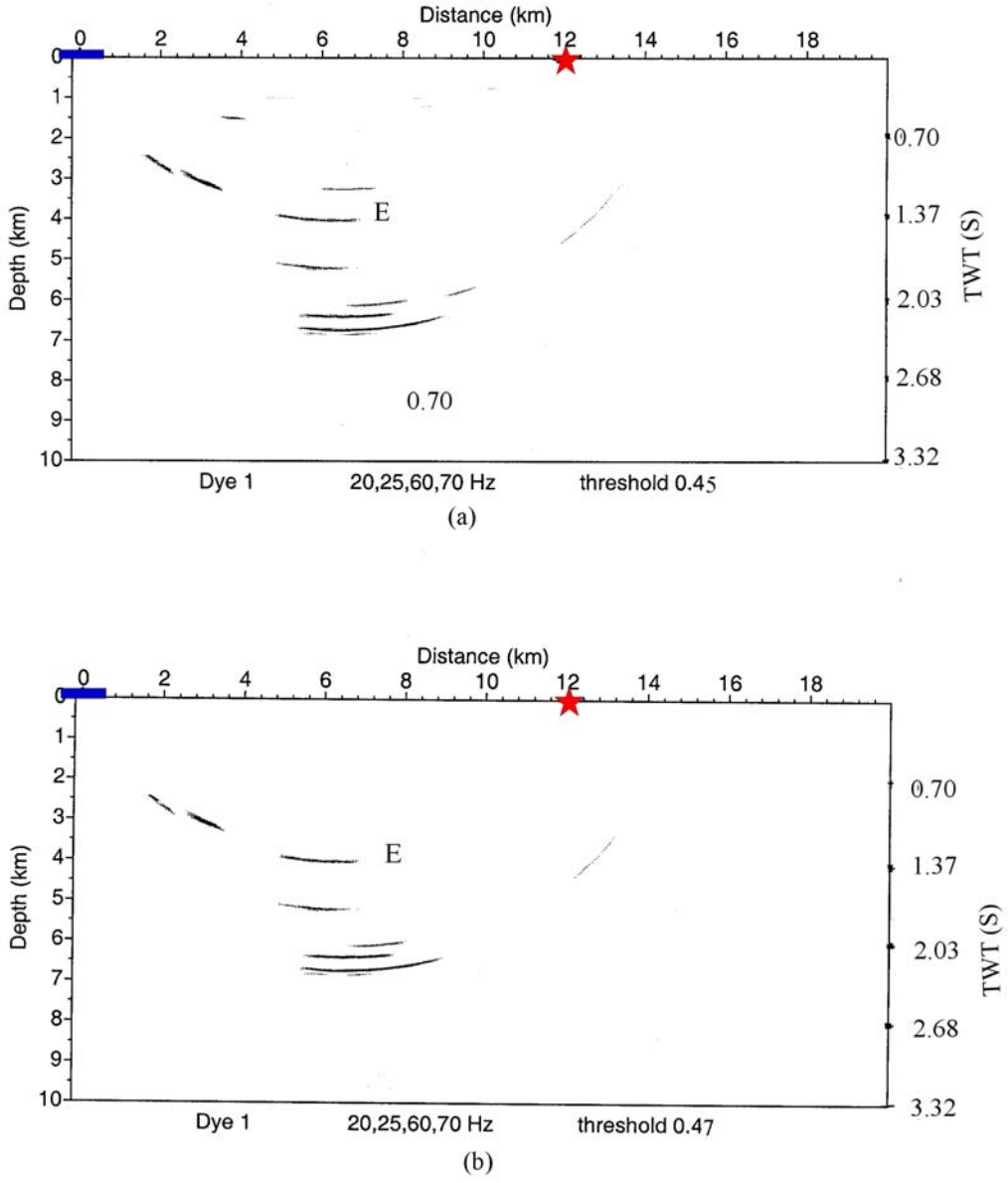
Distance (km)
0 2 4 6 8 10 12 14 16 18
Depth (km)
0 1 2 3 4 5 6 7 8 9 10
E
0.70
0.70 1.37 2.03 2.68 3.32
TWT (S)
Dye 1
20,25,60,70 Hz
threshold 0.45
(a)
Distance (km)
0 2 4 6 8 10 12 14 16 18
Depth (km)
0 1 2 3 4 5 6 7 8 9 10
E
0.70 1.37 2.03 2.68 3.32
TWT (S)
Dye 1
20,25,60,70 Hz
threshold 0.47
(b)

(Figure 2.40)

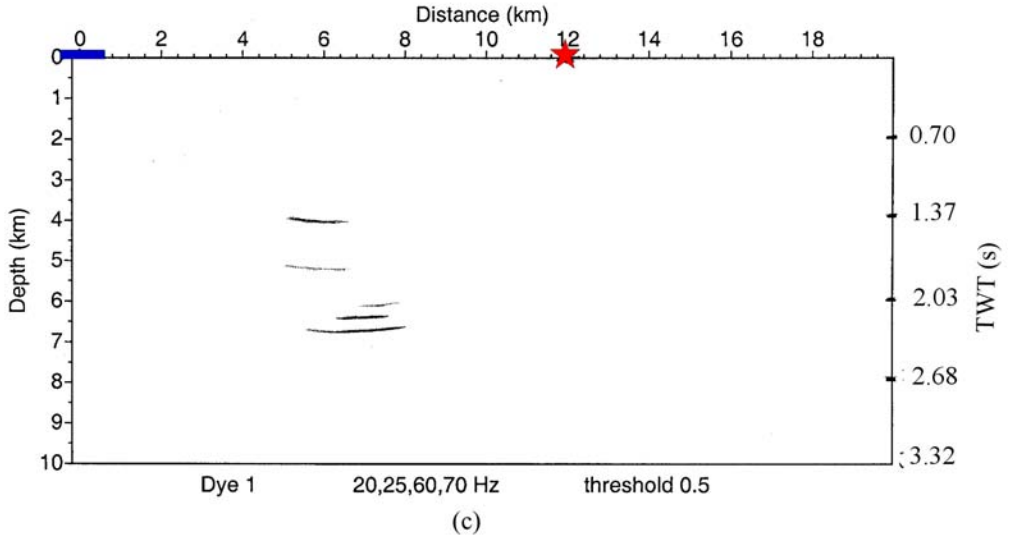

(c)

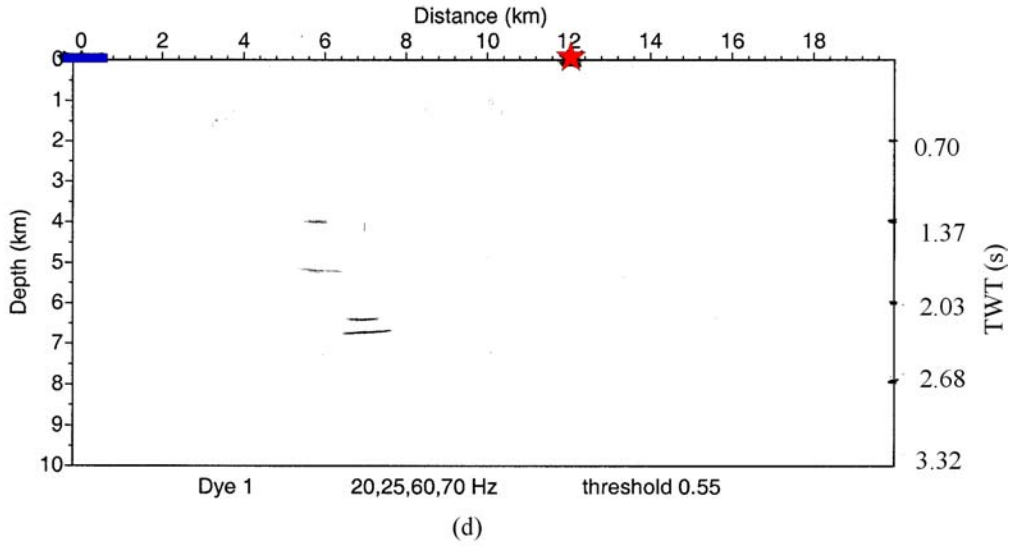

(d)

(Figure 2.40)

Figure 2.41: Migrated section of the Boyd Granite 3 (Array F) coherency-filtered slant stacks. Bandpass filter (13,1 9, 33, 45 Hz). (a) shows the migrated section of the coherency filtered slant stack using a cutoff semblance value of 0.45. (b, c, and d) represent the migrated section with higher cutoff semblance values (0.5,0.55, and 0.6). “E” refers to the top and bottom of a package of reflections interpreted as the base of the Elberton granite.

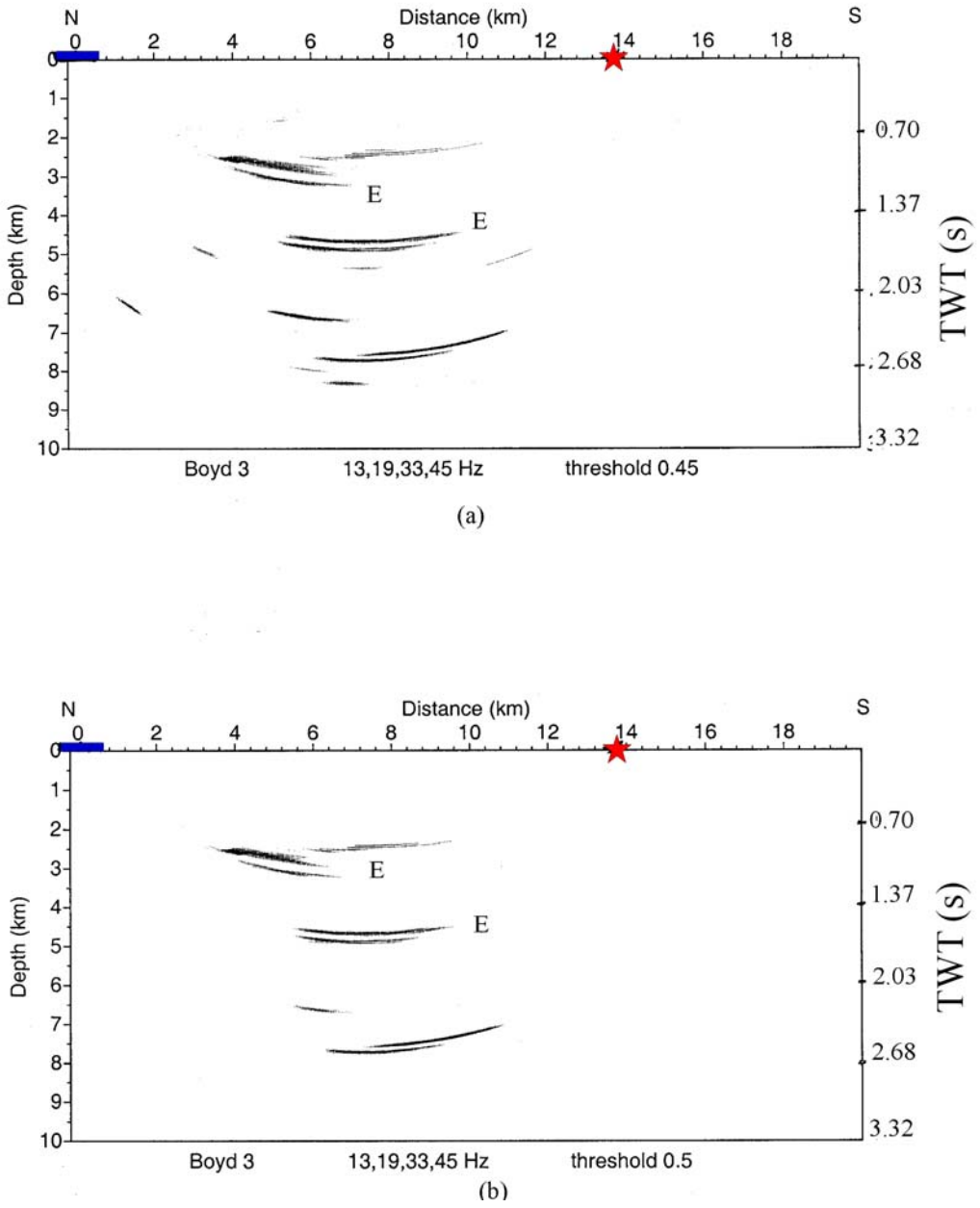
N
Distance (km)
S
0 2 4 6 8 10 12 14 16 18
Depth (km)
0 1 2 3 4 5 6 7 8 9 10
E
E
0.70
1.37
2.03
2.68
3.32
TWT (s)
Boyd 3
13,19,33,45 Hz
threshold 0.45
(a)
N
Distance (km)
S
0 2 4 6 8 10 12 14 16 18
Depth (km)
0 1 2 3 4 5 6 7 8 9 10
E
E
0.70
1.37
2.03
2.68
3.32
TWT (s)
Boyd 3
13,19,33,45 Hz
threshold 0.5
(b)

(Figure 2.41)

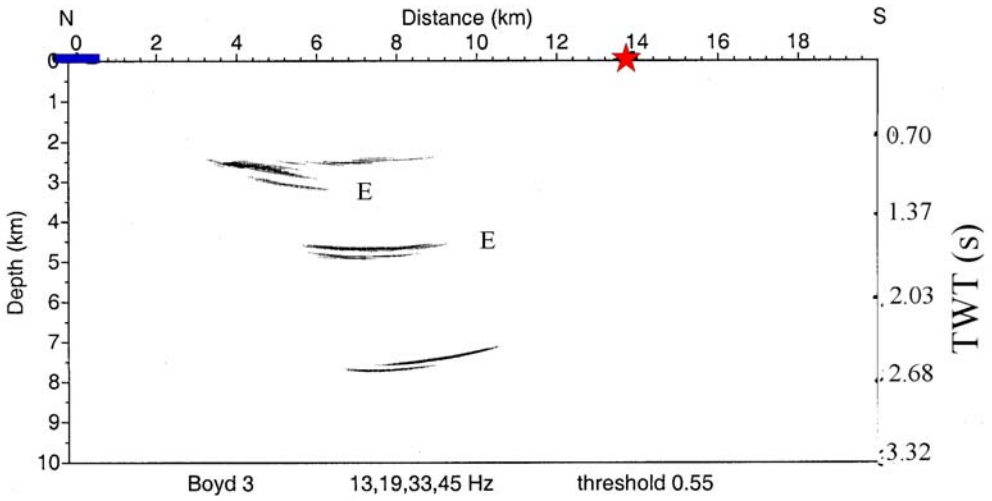

(c)

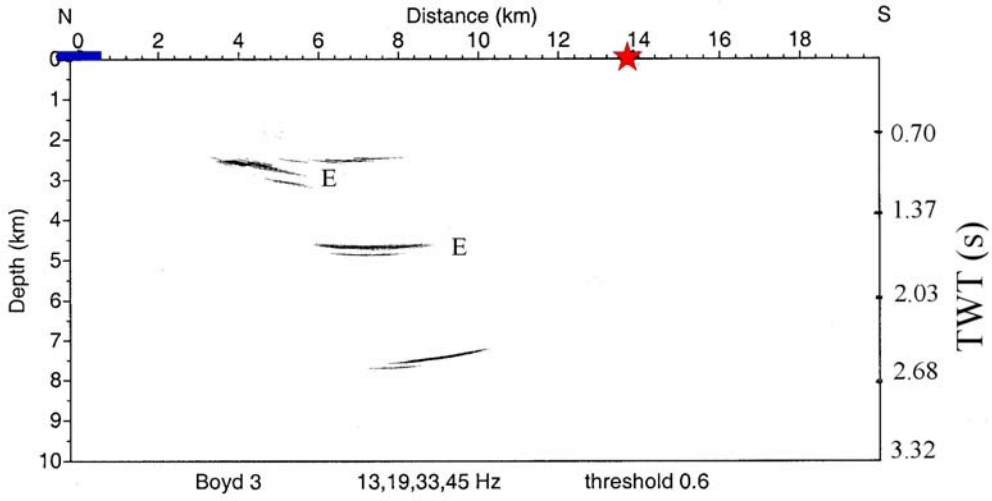

(d)

(Figure 2.41)

Figure 2.42: Migrated section of the Boyd Granite 2 (Array A) coherency-filtered slant stacks. Bandpass filter (15, 25, 45, 60 Hz). (a) shows the migrated section of the coherency filtered slant stack using a cutoff semblance value of 0.45. (b and c) represent the migrated section with higher cutoff semblance values (0.5 and 0.6). "E" refers to an event interpreted as a reflection from near the base of the Elberton granite. The Elberton granite is thinner here (2 km) which could be explained from the outcrop (Figure 2.8) as a separated thin remnant of a larger body.

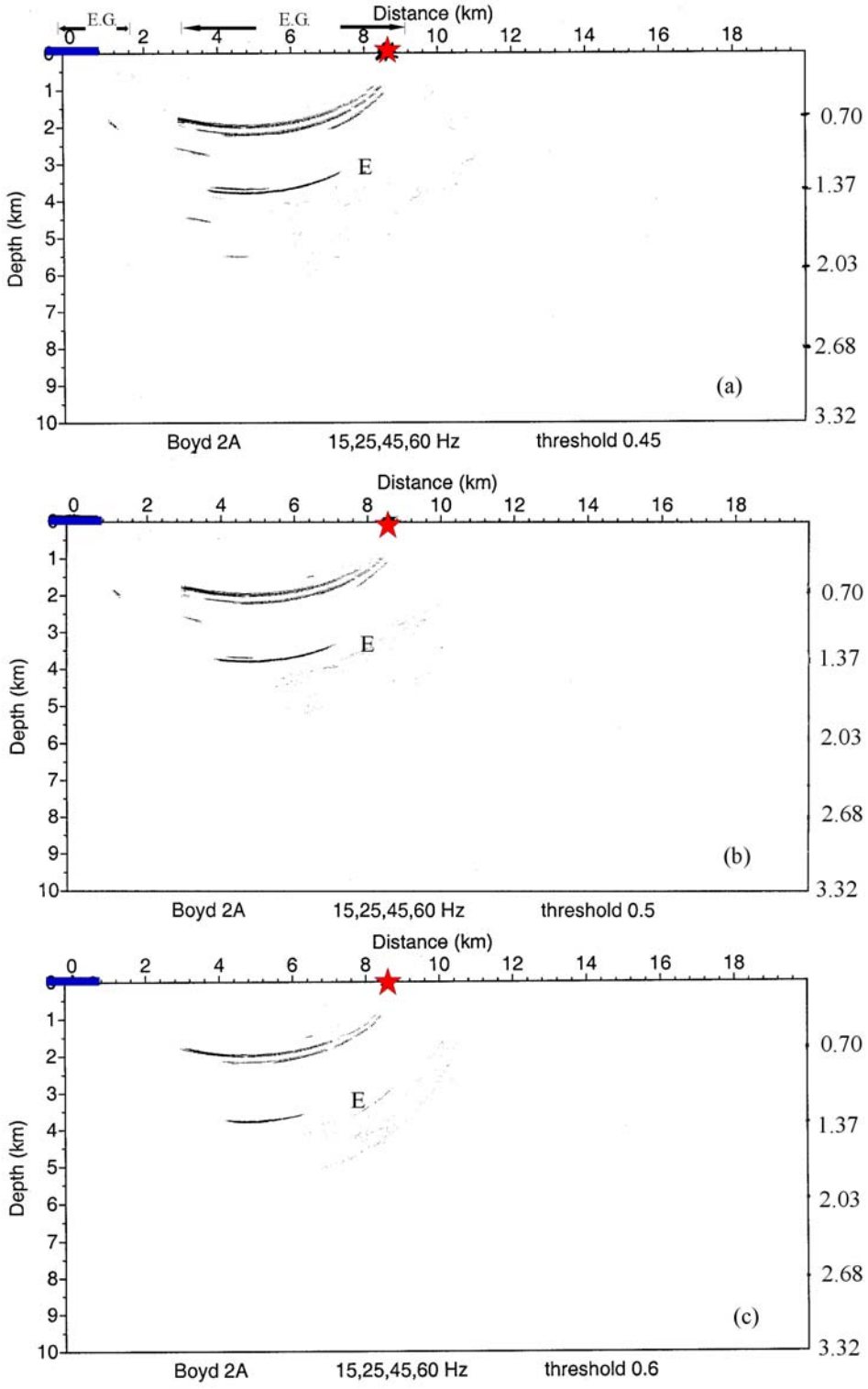
E.G.
E.G.
Distance (km)
0 2 4 6 8 10 12 14 16 18
Depth (km)
0 1 2 3 4 5 6 7 8 9 10
E
0.70
1.37
2.03
2.68
3.32
(a)
Boyd 2A 15,25,45,60 Hz threshold 0.45
Distance (km)
0 2 4 6 8 10 12 14 16 18
Depth (km)
0 1 2 3 4 5 6 7 8 9 10
E
0.70
1.37
2.03
2.68
3.32
(b)
Boyd 2A 15,25,45,60 Hz threshold 0.5
Distance (km)
0 2 4 6 8 10 12 14 16 18
Depth (km)
0 1 2 3 4 5 6 7 8 9 10
E
0.70
1.37
2.03
2.68
3.32
(c)
Boyd 2A 15,25,45,60 Hz threshold 0.6

(Figure 2.42)

Figure 2.43: Reprocessed COCORP Georgia Line 1 showing the important boundaries. Small box on the upper left corner shows the southeast-dipping features underneath the Elberton granite. (After Iverson and Smithson, 1983)

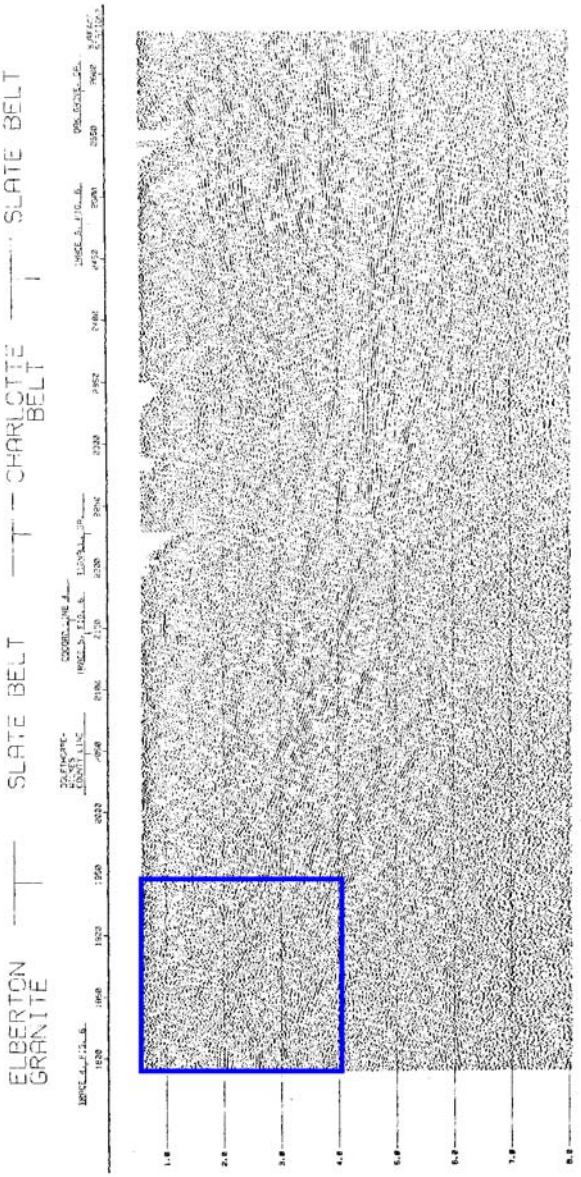

(Figure 2.43)

Figure 2.44: COCORP Georgia line 1, coherency filtered and migrated at 4.5 km/s by Phinney and Chowdhury (1989). The solid lines are the interpretative lines. The Small Box on the upper left corner shows the section beneath the Elberton granite with no reflections.

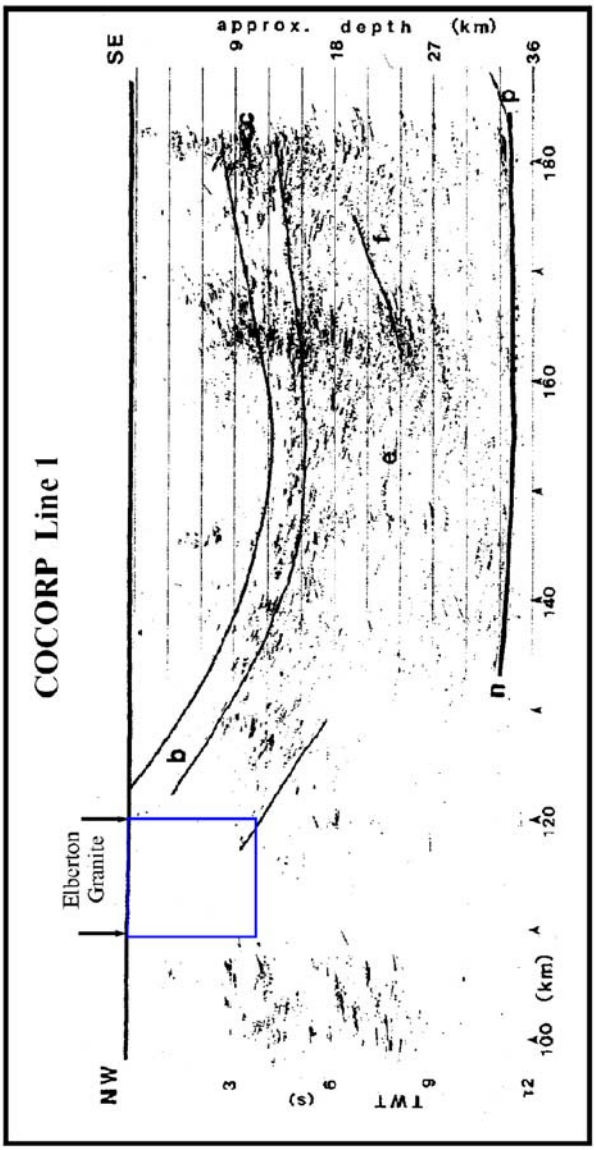
COCORP Line 1
SE
NW
approx. depth (km)
9
18
27
36
b
c
e
f
n
p
Elberton Granite
100
120
140
160
180
(km)
3
6
9
12
(s)
TWT

(Figure 2.44)

Figure 2.45: Modified crustal cross section along COCORP Georgia line 1 (after Iverson and Smithson ,1983) showing the assumed master decollement and its relation to the granitic intrusions. “EG” is the Elberton granite. Note the depth to the base of the Elberton granite (4 km) and the southeast-dipping reflection underneath the granite (could be associated to the Towaliga-Hartwell fault ?). Also note the reflections near the base of the granite (migmatites ? or shear zone).

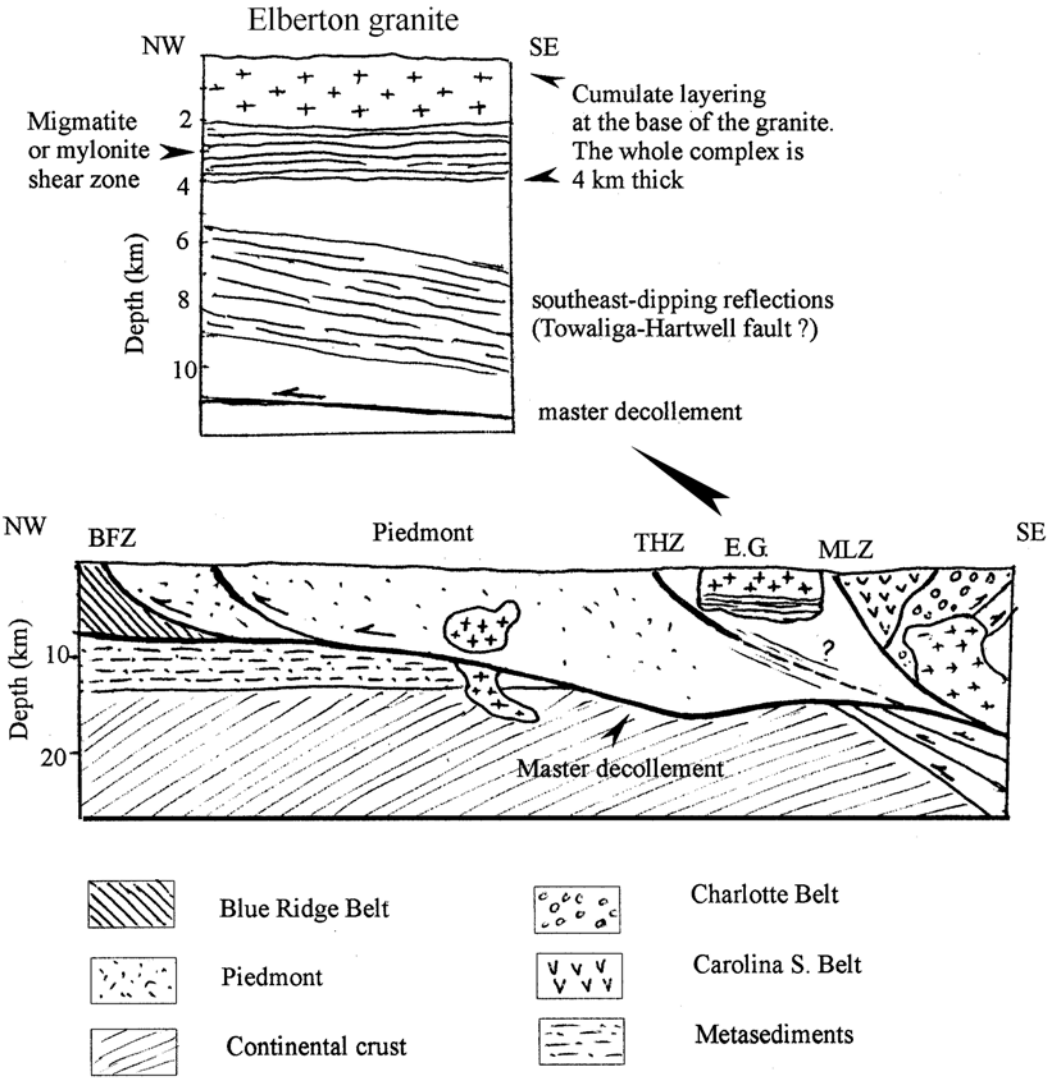
Elberton granite
NW
SE
Migmatite
or mylonite
shear zone
Cumulate layering
at the base of the granite.
The whole complex is
4 km thick
Depth (km)
2
4
6
8
10
southeast-dipping reflections
(Towaliga-Hartwell fault ?)
master decollement
NW
BFZ
Piedmont
THZ
E.G.
MLZ
SE
Depth (km)
10
20
?
Master decollement
Blue Ridge Belt
Piedmont
Continental crust
Charlotte Belt
Carolina S. Belt
Metasediments

(Figure 2.45)

CHAPTER 3

IMAGING OF THE CRUST BENEATH THE CAROLINA TERRANE USING WIDE-ANGLE SEISMIC REFLECTIONS GENERATED BY DELAY-FIRED QUARRY BLASTS[1]

[1] Khalifa, M. O., and R. B. Hawman. To be submitted to *Journal of Geophysical Research.*

ABSTRACT

Wide-angle data, previously inverted for velocity structure of the crust beneath the Carolina Terrane, is now used to image major tectonic elements. The recording lines were placed along the axis of the regional East Coast gravity high, within high-grade rocks of the Kiokee and Charlotte Belts, and crossed previously conducted COCORP lines 1 and 5. Besides imaging the Carolina allochthon and underlying basement structures, the current study compares the reflection response of the crust to COCORP-style vertical profiling and wide-angle profiling. The two data sets differ in dominant frequency and therefore are sensitive to different scales of layering. Static-corrected shot gathers were slant stacked and migrated. Depths of some migrated events match the depths of prominent reflection packages observed on COCORP lines 1 and 5, especially for the shallower portions of the profile. Matching events include features interpreted by previous workers as the Modoc fault zone, and the base of the Carolina Terrane. In contrast with the largely reflection-free zone beneath the Carolina Terrane allochthon seen in COCORP sections, however, the migrated wide-angle sections show a prominent sub-horizontal event at 30 km. The amplitudes of wide-angle reflections generated by these interfaces might be enhanced by longer-wavelength tuning effects, as well as by increased reflection coefficients near the critical angle. If basement rocks here do indeed represent rifted continental crust as proposed by earlier workers, then the reflectors could be mafic sills. In this study, very high-amplitude events interpreted as near-critical reflections from the Moho appear at projected vertical two-way times that are slightly greater (11.6-11.9 s) than two-way times for events interpreted as Moho reflections in the COCORP sections (11 s). This represents a depth difference of 2-3 km and is consistent

with the response expected for a thinly layered zone at the crust-mantle transition. Overall, the elevated reflection coefficients at wide angles have proved quite useful for imaging subtle constrasts in acoustic impedance otherwise missed by near-vertical recording. Taken together, the different length-scales imaged by the higher-frequency COCORP and lower-frequency wide-angle reflection data provide complementary information on the structure of the crust for this portion of the southern Appalachians.

INDEX WORDS: Wide-angle, Carolina Terrane, Moho, Kiokee Belt, Charlotte Belt, Moho, COCORP

Introduction

The southern Appalachians have been crossed by several near-vertical seismic profiles. Consortium for Continental Reflection Profiling (COCORP) lines imaged most of the upper crust but were less successful in imaging deeper structures (Cook et al., 1979). In 1987 a higher resolution seismic study, the Appalachian Ultradeep Core Hole Project (ADCOH), covered the Inner Piedmont, The Brevard Fault Zone and the Eastern Blue Ridge. The results of that study suggested that the Blue Ridge crystalline thrust sheet is relatively thin and that a sequence of imbricated lower Paleozoic shelf strata 4-5 km thick lies beneath the Blue Ridge (Coruh et al., 1987).

The study presented here is a continuation of the work begun by Hawman (1996). In that study, dense recording arrays and timed quarry blasts were used to model the crustal velocity structure of the East Coast gravity high. The experiments were also designed to improve the detectability of the Moho and other major discontinuities that were not well imaged in previous COCORP profiles by taking advantage of large reflection coefficients at near-critical incidence angles. The main objective of the quarry-blast experiments was to place constraints on crustal structures responsible for the steep gravity gradient and regional gravity high.

Source-receiver raypaths for those experiments were concentrated in high-grade rocks of the Kiokee and Charlotte Belts, along the axis of the gravity high. The profile was strategically placed to tie Georgia COCORP lines 1 and 5; the profile crosses line 5 and ends close to line 1 (Figures 3.1 and 3.2). The velocity models and Vp/Vs ratios discussed by Hawman (1996) were obtained by inversion of travel times for direct arrivals, Moho reflections, and one prominent intracrustal reflection. In contrast, the

analysis carried out for the present study involves full-wavefield migration of *all* reflections to obtain a higher-resolution image of the crust along the profile. The present study uses a subset of 16 blasts at quarries near the southwest end of the original profile. Specific targets for the present study include the master decollement, structure within the Kiokee and Charlotte Belt allochthons and underlying basement, and the Moho. The ultimate goal of this work is a unified interpretation of the COCORP and wide-angle migrated images based on the velocity model of Hawman (1996), keeping in mind the differences in reflectivity of the crust for near-vertical, short-wavelength signals and wide-angle, long-wavelength signals.

Regional Ggeology and Tectonics

Ray paths for most of the recorded blasts lie in the Kiokee Belt; the rest of the lines either fall entirely in the Charlotte Belt, or partly in the Slate Belt (Figure 3.1). The recorded lines are superimposed on the East Coast gravity high (Figure 3.2). The Carolina Terrane is composed of four geologic/tectonic belts, the Charlotte, the Carolina Slate, the Belair, and the Kiokee Belts.

The Charlotte Belt:

The Charlotte Belt represents a zone of extensive felsic and mafic intrusives, which lies southeast of the Kings Mountain belt in the Carolinas and within Carolina slate belt rocks in east Georgia (Secor et al., 1986a). Rock units include granites, granite gneisses, schists, gabbros, and metagabbros. A complicated sequence of intrusions is suggested for the Charlotte Belt rocks; plutonism occurred sporadically throughout most of the Paleozoic and ended around 270 ma (Secor, 1986a). The original rocks of the belt may have been volcanic and volcanic derivatives, which were later metamorphosed and

today are found as granitic gneisses (Allard and Whitney, 1994). Peak metamorphism is upper amphibolite and fabric is similar in many respects to the Inner Piedmont rocks (Whitney et al., 1980).

The Carolina Slate Belt:

The dominantly volcanic rocks of the Carolina slate belt extend from 50 km north of the Virginia-North Carolina line to 100 km into Georgia. Rock units include both felsic and mafic tuffs, eruptive breccias, volcanic flows, mudstones, argillites, and graywackes. Age of the later sequence is believed to be middle Cambrian based on the presence of trilobite remains in stream rubble (Maher, et al., 1981). Metamorphism is generally low grade. On a regional scale, the Carolina slate belt has been interpreted to be a synclinorium (Hatcher, 1972) exhibiting both broad and tight folding. Igneous intrusives of varied ages and compositions are found but they are not as widespread as in the Charlotte belt. It is unknown whether metamorphic grade simply increases laterally from the Carolina slate belt to the Charlotte belt (Secor, 1986a), or the two are separated by a fault contact.

The Kiokee Belt:

The Kiokee Belt of Georgia and South Carolina is bordered to the north by the Modoc fault zone and to the south by the Coastal Plain. The Kiokee Belt is separated from the Carolina Slate Belt by the Modoc fault zone and is covered to the southeast by Coastal Plain sediments (Secor et al., 1986a). This province is thought to comprise an Alleghanian metamorphic complex. Metamorphic grade reaches upper amphibolite facies (Secor et al., 1986a). Lithologies include biotite-granite gneiss, metaquartzite, amphibolite, granite, metagranite, mafic and ultramafic plutonic rocks and

metasedimentary and, possibly, metavolcanic rocks. Metamorphic grade reaches amphibolite facies. Structurally, the Kiokee belt rocks form an anticline which is overlain by Carolina Slate belt rocks in the stratigraphic section. The ages of these rocks are poorly constrained but are believed to be late Precambrian-early Paleozoic (Secor et al., 1986a).

The Belair Belt:

The Belair Belt lithologies are found in a relatively small region along the Savannah River near Augusta, Georgia. The Augusta fault is a structural divide between the Kiokee and the Belair belts. Rock units in the Belair belt include a wide variety of sedimentary and volcanic rocks which have undergone greenschist facies metamorphism (Secor et al., 1986a). Allard and Whitney (1994) inferred an age of late Pre-Cambrian-early Paleozoic, similar to the age of Kiokee belt units. The Kiokee Belt and the Belair Belt may be the respective equivalents of the Charlotte and Carolina Slate Belts (Secor et al., 1986a).

Inner Piedmont

The rocks in the Inner Piedmont are megacrystic microcline gneiss interlayered with biotite schists and gneisses. Minor lithologies include amphibolite and calcsilicate granofels and gneisses (Allard and Whitney, 1994; Griffin, 1971). Compared to the Carolina Terrane, the Inner Piedmont has undergone more deformation in the form of recumbent folds that are overturned to the northwest; and the rocks of the Inner Piedmont are of upper amphibolite grade of metamorphism.

Plate Tectonic Setting

Three main deformational events controlled the tectonic history of the southern Appalachians: the Taconic orogeny, the Acadian orogeny, and the Alleghanian orogeny (Hatcher, 1989). The Taconic orogeny involved northwestward thrusting of the Inner Piedmont onto North America and ductile deformation along the Middleton-Lowndesville shear zone (Dallmeyer et al., 1986; Secor et al., 1986b). The Acadian orogeny was characterized by large-scale recumbent folding, reactivation of Taconic thrust faults, and finally intrusion of the Elberton and Stone Mountain granites (Secor et al., 1986a). The Alleghanian orogeny was responsible for folding and thrust faulting of the Blue Ridge, Inner Piedmont and Carolina Terrane and for the metamorphism in the Kiokee Belt (Hatcher, 1989; Secor, 1986a). The Carolina Terrane has been interpreted as an island arc. The Inner Piedmont has been subdivided into a high-grade core and to lower-grade flanks (Griffin, 1971; Hatcher, 1972). It is separated from the Eastern Blue Ridge by the Brevard zone and from the Charlotte Belt, to the southeast, by the narrow Kings Mountain Belt. This province comprises medium and high grade schists and gneisses that have been multiply deformed (Secor, 1986a; Hatcher, 1989). The Taconic orogeny is thought to be the first major compressive event caused by one stage of the closing of the Iapetus ocean. The Middle Devonian Acadian orogeny of the northern Appalachian and Piedmont provinces was another compressional event during closing of the Iapetus Ocean (Hatcher, 1989). The Iapetus Ocean finally closed with the continental collision of North America and Africa during the late Paleozoic Alleghanian orogeny. The Alleghanian orogeny lasted from the Late Mississippian until the Late Permian (340 to 250 Ma) (Hatcher, 1989).

Previous Geophysical Work

Regional Gravity

A steep, NE-trending gravity gradient located between a broad Bouguer gravity low to the northwest and positive anomalies (The East Coast Gravity High) to the southeast is shown in Figure 3.2. Long (1979) compiled and interpreted the gravity data covering the southern Appalachians in Georgia, South Carolina, and North Carolina. The gravity gradient extends from Alabama to New York. In the southern Appalachians, the gravity gradient separates the gravity lows on the northwest that are occupied by the Inner Piedmont, Blue Ridge, and Appalachian Fold and Thrust belt from positive anomalies of the Carolina Terrane to the southeast. The broad gravity low may be due to over-compensation of mountain topography while the southeast positive anomalies may be due in part to higher density mafic rock in the crust (Long, 1979; Hutchinson et al., 1983; Hawman, 1996). The steep gravity gradient has also been interpreted to mark the southeast extent of Grenville basement (Hutchinson et al., 1983). Small, circular gravity anomalies along the crest of the gravity high have been correlated with granitic plutons (Long and Dainty, 1985).

Results from conventional reflection profiling

On the basis of COCORP reflection studies, Cook et al. (1979) interpreted a band of strong, continuous reflections as the master sole thrust that extends from the Valley and Ridge at 6 km depth to the Coastal Plain at about 15 km depth. Iverson and Smithson (1982) and Cook and others (1981) defined the edge of the early Paleozoic North American continental shelf by the termination of this strong reflector beneath the Inner Piedmont. Previous workers have different opinions on the extension of the main

detachment to the southeast. One interpretation shows the detachment extending beneath the Coastal Plain with a root zone beneath the continental shelf (Cook et al., 1979; Harris and Bayer, 1979). Other workers suggested a root zone at the contact between the Inner Piedmont and the Carolina Terrane which was interpreted as a deep-seated suture between the basement and a continental fragment (Iverson and Smithson, 1982). Williams and Hatcher (1983) suggested that the basement beneath the Carolina Terrane is exotic to North America while Phinney and Roy-Chowdhury (1989) suggested that it is rifted Grenville (North American) crust.

Phinney and Roy-Chowdhury (1989) reprocessed COCORP lines 1, 5 and 8 (Figures 3.25-3.27). The CMP stacks were coherency filtered and migrated, and travel times were converted to depths using an underestimated average velocity of 6.0 km/s. The study revealed a sub-horizontal, open syncline beneath the Charlotte Belt with a thickness of 3-8 km. Beneath the syncline, they observed a zone marked "e/E" which is bounded on the east by a west-dipping wedge/pillow-like reflection "f/F". This reflection roots at a depth of 20 km. The surface projection of the west limb of the syncline coincides with the Middleton-Lowndesville cataclastic zone. (In Figures 3.25-3.27, upper and lower case letters refer to the same features on COCORP line 1 and the composite of lines 5 and 8 respectively). In COCORP line 5, at a depth of approximately 8-10 km, the west limb is horizontal to sub-horizontal. Phinney and Roy-Chowdhury (1989) proposed that the rocks in the Kiokee Belt and Charlotte Belt are stacks of thrust sheets that overlie a thinned and rifted Grenville crust. They traced the southeastward extension of the main detachment along path B-C-D (Figure 3.27). Beneath the Charlotte Belt, the depth to the detachment is roughly 10 km; ultimately it roots near the Moho about 130 km to the

southeast (Figure 3.27). Phinney and Roy-Chowrdhury (1989) considered the Middleton-Lowndesville Cataclastic zone as a late splay of the main detachment. A pre-Ordovician basement underneath the main thrust (beginning at a depth of 12 - 15 km beneath the Kiokee Belt) that extends southeastward to km 140 on line 5-8 (Figure 3.26) was interpreted by Phinney and Roy-Chowdhury (1989) as Grenville basement. They credited the late Pre-Cambrian rifting with the presence of a partially rifted North American basement. This places the eastern edge of the north American craton 100 km to the southeast of the position suggested by earlier workers (Iverson and Smithson, 1982; Cook et a., 1981).

Interpretations of higher-resolution seismic profiles obtained for the Appalachian Ultradeep Core Hole (ADCOH) project indicate that the Blue Ridge crystalline thrust sheet is only 2-3 km thick and underlain by 4-5 km of lower Paleozoic shelf strata (Coruh et al., 1987).

Refraction/Wide-Angle Reflection Profiles

Early refraction experiments in the study area did not render useful velocity models due to the large receiver spacings and the use of earthquakes and untimed blasts as seismic sources. A review of results for these early experiments can be found in Hawman (1996). Hawman (1996) used dense recording arrays and timed quarry blasts to model the crustal velocity structure of the gravity high. The experiments were also designed to improve the detectability of the Moho and other major discontinuities that were not well imaged in previous COCORP profiles by taking advantage of large reflection coeffiecients at near-critical incidence angles. The main objective of the

quarry-blast experiments was to place constraints on crustal structures responsible for the steep gravity gradient and regional gravity high.

The study revealed higher P wave velocities of the crust than those assumed by earlier workers and consequently a new estimate of crustal thickness was obtained. Average crustal P wave velocities were found to be 6.5-6.6 km/s. Average crustal thickness estimated based on an accurate velocity analysis was 37-39 km. Low Vp/Vs ratios obtained from direct P and S waves and P and S reflections from the Moho suggested that the high velocities are associated with rocks of high metamorphic grade and intermediate, not mafic average composition. Prominent reflections indicated a discontinuity at a depth of 24-26 km, and the Moho at 37-39 km.

Details of the Wide-Angle Reflection Experiment

The experiments discussed by Hawman (1996) were carried out from 1992 to 1993. Thirty-nine timed quarry blasts were recorded; average charge size was roughly 400 kg explosive / delay. The recording was carried out using twenty seismic recorders with three-component, 4.5-Hz geophones. Geophone spacing was roughly 330 meters. The spatial geometry of recorders and sources provided overlapping and reversed coverage over a profile roughly 180 km long. Raypaths were concentrated in high-grade rocks of the Kiokee and Charlotte Belts, along the axis of the gravity high. Recording along strike minimized lateral variations in geologic structure and seismic velocity and allowed more complete sampling of the gravity high. The profile was strategically placed to tie Georgia COCORP lines 1 and 5; the profile crosses line 5 and ends just southwest of line 1 (Figure 3.2).

The velocity models and Vp/Vs ratios discussed by Hawman (1996) were obtained by inversion of travel times for direct arrivals, Moho reflections, and one prominent intracrustal reflection. The analysis carried out for the present study involved full-wavefield migration of *all* reflections to obtain a higher-resolution image of the crust along the profile. Of the 39 blasts collected in the original field experiments, 16 were used for the present study. These blasts were at two quarries near the southwest end of the profile, just north of Macon, Georgia: the Hitchcock quarry operated by Southern Aggregates Company and the Ruby quarry operated by Martin Marietta Aggregates. Of particular interest were the master decollement, structure within the Kiokee and Charlotte Belt allochthons and underlying basement, and the Moho. The ultimate goal of this work was a unified interpretation of the COCORP and wide-angle migrated images based on the velocity model of Hawman (1996), keeping in mind the differences in reflectivity of the crust for near-vertical, short-wavelength signals and wide-angle, long-wavelength signals.

Processing

Migrated sections were generated from coherency filtered slant stacks. Preliminary processing carried out by Hawman (1996; in preparation) included trace editing, frequency filtering (highcut filtering using a linear ramp from 10 to 15 Hz), deconvolution using non-standard techniques for removing the effects of extended seismic source wavelets generated by ripple firing (Hawman et al., 2001; Hawman, in prep.), correction for elevation statics, and correction for residual statics.

Slant Stacking and Coherency Filtering

The deconvolved, static-corrected shot gathers were slant stacked to provide objective measures of apparent velocity for coherent arrivals. Figure 3.3 shows examples of slant stacking and coherency filtering for Hitchcock blast # 1.

Slant stacking represents the transformation of data from x (distance) and T (2-way travel time) to ρ (ray parameter or inverse apparent velocity) and travel time for the average offset of the array. This process is a linear wave field transformation that decomposes the wave field into its plane-wave components (Phinney et al., 1981); this allows the identification of various types of arrival on the basis of apparent velocity (Hawman et al., 1990; Hawman and Phinney, 1992). Slant stacking also suppresses noise; for random noise, the improvement in signal level is proportional to $n^{1/2}$, where n is the number of traces in the shot gather.

Slant stacks are computed by summing amplitudes along lines of constant slope (p) and intercept time:

$$\Psi(\rho,\tau) = \sum_{i=1}^{n} \Phi(x_i, \tau + \rho x_i)$$

where ψ is the slant stack, Φ is the input record section, τ is the intercept time, and ρ is the ray parameter (s/km). For the stacks computed here, the intercept time corresponds to the travel time to the center of the recording array. In general, the ray parameters for reflections recorded at a given distance from a shot will decrease (the apparent velocity will increase) with increasing depth to the reflectors. Ray parameters for P-SV converted reflections are distributed along a roughly parallel band at larger times and ray parameters.

The semblance of the slant stack was also computed (Figure 3.3b). Semblance is a coherency measure defined as the energy ratio for normalized input to output:

$$S(\tau,\rho)=\frac{\sum_{k=-m}^{m}\left[\sum_{i=1}^{n}\Phi(x_i,\tau+k\Delta\tau+\rho x_i)\right]^2}{n\sum_{k=-m}^{m}\sum_{i=1}^{n}\Phi^2(x_i,\tau+k\Delta\tau+\rho x_i)}$$

(Douze and Laster, 1979), where n is the number of traces, τ is the intercept time, ρ is the ray parameter (s/km), and m is the number of samples in a time gate centered about the sample of interest.

Semblance is not sensitive to amplitude differences between different coherent arrivals in a gather but is affected by amplitude variations along a given arrival (the beam). Therefore the traces were normalized by their rms values prior to stacking. Statistical properties of the semblance measure are discussed by Douze and Laster (1979).

The semblance was used to derive a coherency filter to isolate the most reliable portions of the slant stack prior to migration. The semblance was first smoothed in the frequency domain by high-cut filtering (Stoffa et al., 1981). Then a coherency filter was constructed by assigning zeros for all samples in the smoothed semblance with values less than the chosen threshold and a value of 1 for the remaining samples. The slant stack then was multiplied by this filter. Raising the threshold value results in more focused events in the stack. Figure 3.3e-j shows the stacks after being coherency filtered using sequentially higher values of threshold, the higher the threshold value the more focused

the events. Figures 3.4-3.19 show the static-corrected gather, semblance, slant stack, and coherency filtered slant stacks for all recordings from the Southern Aggregates Hitchcock quarry and Martin Marietta Ruby quarry blasts.

Migration

The coherency filtered slant stacks were used as an input to the migration process. Migration of coherency-filtered slant stacks minimized the spatial extent of "smiles" generated by conventional migration. I used a migration algorithm (Hawman, in preparation) which is an extension of the approach described by Hawman and Phinney (1992). "The migration algorithm involves downward continuing the up-going ray with observed ray parameter p_o until it intersects a down-going ray that gives a total two-way travel time which matches the observed travel time. First we find the point of intersection of the upcoming ray detected at the recording spread with rays traveling downward from the source. Because of refraction, not all down-going rays will intersect the up-going ray."(p.399)

This algorithm maps samples in travel-time/ray-parameter space into dipping segments in the subsurface image. The widths of residual "smiles" are determined by the beam widths of the recording arrays. The actual length of reflecting interfaces will be approximately half the width of the recording array. The smearing or "smiles" seen in the migrated images represent confidence regions; the width of the smiles ("resolution width") is determined by the degree of smearing (uncertainty in ray parameter) in the slant stack, which in turn is controlled by the beam-width of the recording array. The array beam-width is the ability of the array to resolve events with different ray parameter (inverse apparent velocity). It is determined by the length of the recording array and the

frequency content of the signal (longer arrays and higher frequencies allow smaller differences in ray parameter to be resolved).

The velocity model used for migration was based on model A from Hawman (1996). The linear velocity gradients in this model were converted to layers of constant velocity; layer thicknesses were 0.1 km in the top kilometer and 1 km for the rest of the crust. The datum elevation used for the migration was 145 m, the average elevation for the recording arrays. Velocities for reductions of the travel times to the datum were 5 km/s (a value appropriate for fractured bedrock) at the blast sites and 2 km/s (a value appropriate for a mixture of soil and saprolite) at the arrays.

After evaluating the individual migrated section from each blast (Figs. 20 and 22), each migrated section was normalized by its maximum amplitude to preserve relative amplitudes in the composite migrated sections for each quarry (Figs 21 and 23). The migrated image preserves the relative strengths of recorded reflections; these are controlled in part by variations in reflection coefficients with angle of incidence.

The composite of migrated sections that were recorded at the Hitchcock and Ruby quarries were individually evaluated and added together after determining the exact distance between the two shots to form the final composite (Figure 3.24).

Descriptions of the Migrated Sections

Due to limitations in instruments, the field geometry employed short arrays. Therefore these migrated sections do not represent complete images of the subsurface structure between the blasts and the arrays. The reflector distributions for these partial images are strongly controlled by the sparse recording geometries (Hawman et al., 2001).

To facilitate comparison with COCORP sections, normal two-way times (TWT) were computed from the velocity model used to migrate the data. This velocity model was also used to generate a new depth scale for the COCORP section reprocessed by Phinney and Roy-Chowdhury (1989) for comparison with their original depth scale (Figures 3.25 and 3.26).

The Hitchcock Quarry Migrated Sections:

Descriptions of individual sections:

Hitchcock1:

The average offset of the recording is 109.1 km. The total array length is 4.8 km. This section contains near-horizontal events (Figure 3.20 a). The deepest event, at 38 km (11.6 s TWT), is well resolved. A shallower horizontal event is observed at 29 km (9.0 s TWT). A suite of gently dipping events (apparent dip 0-10 degrees to the NE) is observed between 30-34 km (9.3 -10.4 s TWT). The shallowest events occur at 22 km (6.97 s TWT). One is poorly resolved with an apparent dip of 0-10 degrees, NE; the other is better resolved, with dips in the opposing direction (apparent dip 0-10 degrees, SW).

Hitchcock2:

The average offset of the recording is 88.65 km. The total array length is 5.9 km. The deepest event in the section is at 33 km (10.2 s TWT) with an apparent dip of 5^{o}, SW (Figure 3.20 b). More steeply dipping events (apparent dip of 30^{o}, SW) are observed at 24 and 19 km (7.6 and 6.1 s TWT), respectively. A package of events is observed at depths between 10 and 15 km (3.2–4.8 s TWT). The deepest part of the package is nearly horizontal with a resolution width of 31 km (km: 23 to km: 54) and an apparent dip of 5^{o} to the NE.

Hitchcock3:

The average offset of the recording is 118.3 km. The total array length is 6.7 km (Figure 3.20 c). High-amplitude events with small apparent dips are observed at 39 km (11.9 s TWT) and 36 km (11.1 s TWT). A strong horizontal, multicyclic event is observed at 30 km (9.3 s TWT). The shallowest event has an apparent dip of 5 ^{o} to the NE, and occurs at 28 km (8.7 s TWT). Resolution widths in the section range from 12 to 30 km.

Hitchcock4:

The average offset of the recording is 76.29 km, with a total array length of 4.6 km (Figure 3.20 d). A dipping event (apparent dip: 15 ^{o} to the NE) is observed at 33 km (10.2 s TWT). An event with an apparent dip in the opposite direction is observed at 27 km (8.4 s TWT) (15^{o} to the SW). An event with an apparent dip of 27^{o} to the NE is observed at 17 km (5.4 s TWT). The shallowest event (11 km; 3.57 s TWT) has an apparent dip of 5 ^{o} to the NE. Overall, the reflectors are well resolved: resolution widths range between 4 and 18 km.

Hitchcock5:

The average offset of the recording is 81.75 km, with a total array length of 5.7 km (Figure 3.20 e). Two well resolved events of different dips are observed 32 km (9.9 s TWT) (apparent dips 10 ^{o} and 7 ^{o} to the NE). The shallowest event (17 km; 5.4 s TWT) has a range of apparent dip of 0 to 20 ^{o} to the NE and a resolution width of 24 km.

Hitchcock6:

The average offset of the recording is 51.8 km, with a total array length of 7 km (Figure 3.20 f). The deepest event is horizontal at 34 km (10.4 s TWT). An event with an

apparent dip of 20° to the NE is observed at 23 km (7.2 s TWT). A single event dipping in the opposite direction (apparent dip of 17° to the SW) is observed at 17 km (5.4 s TWT). An event with an apparent dip of 20° to the NE is observed at 11 km (3.5 s TWT). All of these events are resolved (resolution widths 4-9 km). Multicyclic events with larger resolution widths and apparent dips of 13° to the NE are observed between 6 and 8 km (1.98 and 2.62 s TWT).

Hitchcock8A:

The average offset of the recording is 54.2 km (Figure 3.20 g). The total array length is only 2 km. Lateral resolution of the reflectors is good, however, because of the wide bandwidth of the signals. In this section the events are rather shallow; all but one of the events dip to the southwest. The two events at 18 km (5.7 s TWT) have apparent dips of 20° and 15°. The shallowest event occurs at 11 km (3.6 s TWT) with an apparent dip between 5° and 10° to the SW.

Hitchcock8B:

The average offset of the recording is 58.3 km. The total array length is 2.8 km (Figure 3.20 h). The deepest event occurs at 29 km (9.0 s TWT), and is horizontal. Between 18 and 28 km (5.8 – 8.7 s TWT) three events are observed with apparent dips of roughly 20° to the NE and resolution widths of ~15 km. The shallowest event is horizontal at 19 km (6.06 s TWT).

Hitchcock9:

The average offset of the recording is 134.05 km. The total array length is 9.3 km (Figure 3.20 i). A horizontal event is observed at 40 km (12.0 s TWT). A much stronger event occurs at 37 km (11.36 s TWT) with an apparent dip of 10° to the SW. At 22 km

(6.9 s TWT), a weak event with an apparent dip of 14 ^{o} to the SW is observed. Horizontal resolution of these reflectors is excellent.

Hitchcock10:

The average offset of the recording is 66.09 km. The total array length is 8 km (Figure 3.20 j). The deepest event occurs at 37 km (11.3 s TWT), with an apparent dip between 0 and 5^{o} to the SW. A horizontal event is observed at 32 km (9.9 s TWT). An event with an apparent dip of 5 to 12 ^{o} to the SW appears at 29 km (9.0 s TWT). At 27 km (8.2 s TWT) there is an event with an apparent dip between 0 and 8^{o} to the NE. Resolution widths for these events range from 4–8 km. An event at 13 km (4.2 s TWT) has an apparent dip of 0-10 ^{o} to the NE. The apparent horizontal resolution for a shallow suite of events between 9 and 10 km (2.94 and 3.26 s TWT) is poorer, perhaps because of destructive interference of some frequencies by the layered structure.

Description of the Composite Section for the Hitchcock Blasts:

The composite migrated section for the Hitchcock blasts (Figure 3.21) contains many distinct events. Events are observed at depths as shallow as 5 km (1.6 s TWT) and as deep as 39 km (11.9 s TWT). In the shallow part of the composite section, a clustering of events is observed between 5-14 km (1.6 – 4.5 s TWT). Some of these shallow events are horizontal to sub-horizontal, with stronger clustering over depths of 6-8 km (1.9 – 2.6 s TWT). A second set of roughly horizontal events is observed at depths between 18 and 20 km (5.7– 6.3 s TWT). A third clustering of events is observed between 29 and 30 km (9.0 – 9.3 s TWT). The events are sub-horizontal. The deepest events in the section show up strongly at the depth range of 35-39 km (10.7 – 11.9 s TWT). Most of these events are also sub-horizontal.

The Ruby Quarry Migrated Sections

Description of individual sections:

Ruby1:

The average offset of the recording is 24.5 km. The total array length is 7 km, which together with the high-frequency signals yields good horizontal resolution (Figure 3.22 a). The events in this section are clustered in the shallow southwesterly corner of the section. The deepest event appears at 16 km (5.1 s TWT). Just above it (depth: 12.5 km; TWT: 4s) is another event with an apparent dip of 5-10 ^{o} to the NE. Two high-amplitude events (apparent dip 0-15 ^{o} to the NE) appear at 7 and 7.5 km. The shallowest event, at 5 km (1.65 s TWT), is subhorizontal.

Ruby2A:

The average offset of the recording is 96.5 km (Figure 3.22 b). The total array length is only 2.1 km; this accounts for the poor lateral resolution of reflections (resolution width: 23-26 km). The section contains a group of horizontal events at depths between 25 and 29 km (7.8 – 9.0 s TWT).

Ruby2B:

The average offset of the recording is 104.4 km (Figure 3.22 c). The total array length is 1.3 km; again the small array aperture results in poor horizontal resolution. A single dipping event is observed at 25 km (7.8 s TWT) with an apparent dip of 0-5 ^{o} to the SW.

Ruby3:

The average offset of the recording is 62.8 km (Figure 3.22 d). The total array length is 5.4 km. The deepest event is well resolved at 38 km (11.0 s TWT), and is horizontal. An event with an apparent dip of 0-10^{o} to the NE is observed at 34 km (10.4 s TWT). There is a single, well-resolved horizontal event at 30 km (9.3 s TWT). At 27 km (8.4 s TWT), an event is observed with an apparent dip of 5-13 ^{o} to the NE. A clustering of events (apparent dips 0 to 15 ^{o} to the NE) occurs between 16 and 19 km (5.1 - 6.0 s); resolution widths for this depth range vary between 8 and 16 km.

Ruby4:

The average offset of the recording is 79.1 km (Figure 3.22 e). The total array length is 6.7 km. Two horizontal events are observed at 35-33.5 km (10.7 and 10.2 s TWT). Another horizontal event is observed at 17 km (5.4 s TWT). A suite of events with apparent dips of 5 to 15^{o} to the NE is observed at depths between 18 and 25 km (5.8– 7.8 s TWT). Another suite of better resolved events occurs over the same depth range with apparent dips to the SW. The shallowest event (depth: 14 km; 4.5 s TWT) is sub-horizontal (apparent dip of 0-5 ^{o} to the NE).

Ruby5B:

The average offset of the recording is 49.9 km (Figure 3.22 f). The total array length is 2.7 km. The deepest event at 33 km (10.2 s TWT) dips 18 ^{o} to the SW. Another event (apparent dip: 18^{o} to the NE) is observed at 25 km (7.8 s TWT). A SW dipping event (5-15 ^{o}) is observed at 20 km (6.3 s TWT). The shallowest two events are observed at 12.5 km (3.8 s TWT) with an apparent dip of 5-15 ^{o} to the NE, and at 11 km (3.5 s TWT) with an apparent dip of 0-10 ^{o} to the NE. Resolution widths vary from 4 to 24 km.

Ruby6:

The average offset of the recording is 73.5 km (Figure 3.22 g). The total array length is 6 km. The section contains a number of horizontal events. The deepest event is at 10.49 s TWT (34 km), followed by consecutive events at 30,28,23,21,18,13,10, and 6 km (9.3, 8.7, 7.2, 6.6, 6.0, 4.2, 3.2, and 1.9 s TWT). This section contains remarkable sub-horizontal multicyclic events at 22-24 km (7.0 –7.6 s TWT) and at 12-13 km (3.9 – 4.2 s TWT).

Description: Composite Section for the Ruby Blasts:

In the Ruby composite migrated section (Figure 3.23), events are observed at depths between 4 km (0.3 s TWT) and 38 km (11.6 s TWT).

In the shallow part of the section, a distinct clustering is readily visible between 6 and 8 km (1.9–2.6 s TWT) with small apparent dips to the NE. A second set of horizontal events is observed between 12 and 14 km (3.8– 4.5 s TWT). A strong multicyclic package of gently dipping events (apparent dips 0 to 7 ^{o} to the NE) is observed between 18 and 22 km (5.7 – 6.9 s). A fourth clustering of horizontal events is observed at 29-30 km (9.0 – 9.3 s TWT). A weak set of horizontal events is observed at 32 km (9.9 s TWT). In the deeper part, horizontal events are observed at 39 km (11.9 s TWT).

Comparison of the two composites of Hitchcock and Ruby blasts shows good agreement in depth and dip of the events. We have to keep in mind that blasts from the Ruby quarry were recorded at smaller distances than those at the Hitchcock quarry. Also, the Ruby quarry yielded fewer blasts. The number and distribution of events on each of these composites are controlled by the number of blasts recorded in each and by the length of the offsets. Events cluster at similar locations for the two composites. The Ruby

composite section shows fewer deep events because the offset coverage is not as great. On the other hand, the smaller source-receiver offsets available for the Ruby composite allow better imaging of shallow structure. Examples include the event at 4 km depth, which is not shown in the Hitchcock composite section.

Composite Migration Section of Hitchcock and Ruby Blasts

In the composite migrated section for the Hitchcock and Ruby blasts (Figure 3.24 b), the Hitchcock shot location represents the westernmost point in the section. Three kilometers east of Hitchcock is the location of the Ruby shot points. The actual distance between the two shot points was 3.25 km. The line connecting the two shot locations has a bearing of N 70^{o} E, compared with a bearing of N 48^{o} E for the composite line of Hitchcock blasts. After projection, the Ruby quarry falls 3 km away from the Hitchcock quarry on the composite line.

Most of the events are concentrated near the western edge of the composite section. This can be explained by the concentration of midpoints that were hit by the rays between shots and each array. The central part of the section also contains a number of deeper events. The easternmost part of the section is noticeably devoid of shallow events. This gap in subsurface coverage will be at least partially filled after migration of additional data for blasts at the Martin Marietta Warrenton and Camak quarries.

In the deeper part of the section (35-40 km; 10.7–12.2 s TWT), continuous, mostly horizontal events can be correlated over a distance of ~ 72 km (km 36 to km 108). The western part of the deep section contains multiple, well resolved events for small-offset recordings, while in the eastern part, the resolution widths increases because of the loss of high frequencies with increasing distance from the quarries. Strong, horizontal

events also occur at depths between 25 and 33 km (7.8 - 10.2 s TWT), and are fairly continuous for ~ 66 km (km 24 to km 88).

Compared to the deeper part of the sections (> 25 km; >7.8 s TWT), the shallow parts reveal a denser and more clustered distribution of events that range from horizontal to gently dipping toward the northeast. The events range in depth from 17-23 km (5.4 – 7.2 s TWT), and occur in localized clusters (km 20 to km 76).

A sequence of horizontal events at depths between 10.5 and 14 km (3.2 – 4.5 s TWT) is piecewise continuous over a distance of roughly 45 km (km10 to km56). The shallowest group of events ranges in depth from 4 to 9 km (1.3–2.9 s TWT), and is correlated over a distance of about 55 km (km 4 to km 59).

The section also contains "reflection-free" zones. These zones follow the general dip of the events to the NE, most noticeably over the depth ranger 13-16 km, 22-25 km, and (in the eastern half of the section) 30-38 km. The section contains some other steeply dipping events that do not coincide with the general trend of other events in depth or apparent dip. These could be diffractions caused by scattering from complex structures such as igneous intrusions (plutons and dikes) and tight folds. These events are most numerous at depths between 10 and 24 km.

Discussion of the Results:

Geologic interpretation

The composite section (Figure 3.24) contains strong events at depths of about 38-40 km (11.6–11.9 s TWT) that correlate over a distance of roughly 72 km (km 36 to km 108). In the original shot gathers (Figures 3.3-3.19), these reflections are characterized by high relative amplitudes; at distances greater than 100 km, these are the strongest events

in the shot gathers (Hawman, 1996). Based on their relative amplitude and apparent velocity, we interpret these events as near-critical reflections from the Moho.

A gently dipping event that occurs at 24-30 km (7.6 – 9.3 s TWT) can be traced over a distance of ~ 75 km, (km10 to km85). This event is suggested to be reflections from within the basement. Another gently dipping event (~ 7 degrees, NE), at depths between 16 and 20.5 km (5.1-6.5 s TWT), can be correlated for roughly 65 km (km10 to km75); I suggest that this event represents a major shear zone, perhaps the base of the master decollement. Yet another gently dipping event (~ 5 deg, NE), extends from 12-16 km (3.9 – 5.1 s TWT), and can be correlated over a distance of roughly 45 km (km 10 to km 55); this event is suggested to be the top of the master decollement. This suggests that the whole 4 km thick package represents the master decollement in this area. At the intersection of our line with the reprocessed COCORP line 5 by Phinney and Roy-Chowdhury (1989), the main detachment shows a thickness of about 4.5 km (9.5-14 km). The shallowest event in the section is sub-horizontal, occurs at 7km (2.3 s TWT), and can be correlated (with large gaps) over a distance of 35 km (km 5 to km 40); the TWT of this event is in agreement with previous interpretations of COCORP data for the Modoc Fracture Zone (MFZ). This event is recorded by Ruby blast number 6 (Figure 3.19). Another shallow event (5 km) shown in the migrated section for the Ruby1 blast (Figure 3.13), northwest of the MFZ, correlates with "Boundary C" in Phinney and Roy-Chowdhruy (1989) interpretation (Figure 3.26). In the composite interpretation of COCORP Georgia line 1,5, and 8 (Figure 3.27), "BCD" represents the SE extension of the detachment, "G-H" correlates at the surface with the Modoc fracture zone (MFZ), and "J-K" in the same manner correlates with the Augusta fault.

In the interpretation of Phinney and Roy-Chowdhury (1989) COCORP line 5, a sequence of reflections interpreted as the Modoc fracture zone (MFZ) appears at 2 s TWT (Figure 3.26); similarly, in the current migrated section a strong reflection appears at 1.97 s TWT (Figure 3.28). In COCORP line 5 (Figure 3.26) at the intersection point with our profile, the authors proposed a 1.6 s TWT thickness for the allochthon (3.2 - 4.8 s TWT) (~6 km). In our section, a similar series of reflectors appears to have a thickness of 2.1 s TWT near the shot (3.9 – 6.0 s TWT) (~ 7 km).

In contrast with the reprocessed section of Phinney and Roy-Chowdhury (1989), which shows few events between the base of the Carolina Terrane allochthon and the Moho, our line shows a strong event at 9.3 s TWT (30 km).

Regarding the tectonic movement along the sole thrust, our line was positioned along the strike and thus was able to image the less studied plunge in the Kiokee belt. The top of the master decollement zone that plunges ~5 degrees to the NE and extends for ~45 km, while the base plunges ~7 degrees to the NE and extends for ~75 km. Both the top and the bottom of the master decollement zone show a gradual decrease in dip from SW to NE and nearly flatten out at their NE borders. This implies that the Kiokee plunges to the northeast.

Comparison of Results for Wide-Angle and COCORP Experiments

Most of the differences in the COCORP and wide-angle results can be explained by the differences in frequency content for the two data sets. The frequency content is determined by the nature of the seismic source and by preferential loss of higher frequencies through an elastic attenuation and scattering. Because of the greater physical dimensions of quarry blast sources and the much greater amount of energy released, the

energy generated by quarry blasts extends well below the nominal 8-40 Hz range of the Vibroseis sweep used for COCORP work. For ripple-fired quarry blasts, the delays between holes also tend to attenuate higher frequencies by destructive interference (Hawman et al., 2001). For instantaneous blasts used at dimension-stone quarries, these higher frequencies are preserved (Khalifa et al., 2001b). The dominant frequency range actually recorded in COCORP signals begins at frequencies somewhat higher than 8 Hz because of imperfect ground coupling of the vibrator plate (Richard Williams, personal communication, 2002).

The features imaged in the COCORP and wide-angle migrated sections are most similar at shallow depths, where the overlap in frequency content of the two data sets is the greatest. For targets at greater depths, the wide-angle data experience greater attenuation of higher frequencies because of the increased source-receiver offsets used to image deeper structure.

Reflection amplitudes for both data sets will be greatly enhanced by "tuning", the constructive interference generated by layered sequences of alternating high and low velocity (Fountain et al., 1984; Yilmaz, 1987). The degree of amplification is a function of layer thicknesses, layer velocities, frequency of the signal, and angle of incidence. For vertical incidence, tuning is optimized for signals with wavelengths roughly four times the dominant layer thickness. Thus for a quarry-blast signal with dominant frequencies between 5 and 10 Hz, the strongest reflections will be generated for layering with thicknesses on the order of 640 - 1280 m, while for a COCORP signal with dominant frequencies between 15 and 40 Hz, the strongest reflections will be seen for layering with thicknesses on the order of 160 - 427 m. For greater angles of incidence, the scale of

layering seen by the wide-angle signals will be somewhat different but still greater than that detected by COCORP signals.

The higher-frequency signals generated by vibrator sources are especially effective for imaging mylonitic shear zones (Fountain et al., 1984; Hurich et al., 1985; Smithson et al., 1979). These may be transparent to longer-wavelength quarry blast signals (especially at wide angles) if the shear zone is thin compared with the dominant signal wavelength and if it is bounded above and below by rock masses of similar composition (Braile and Chiang, 1986).

In this study, very high-amplitude events interpreted as near-critical reflections from the Moho appear at projected vertical two-way times that are slightly greater (11.6-11.9 s) than two-way times for events interpreted as Moho reflections in the COCORP sections (11 s). This represents a depth difference of 2-3 km and is consistent with the response expected for a thinly layered zone at the crust-mantle transition; higher-frequency, normally-incident energy will return a multicyclic reflection from within this zone, while lower-frequency, wide-angle energy will not "see" this relatively thin sequence but rather will penetrate through it and undergo reflection from within the uppermost mantle (Braile and Chiang, 1986).

Likewise, there may be features that reflect low-frequency signals but are transparent to higher-frequency signals. Examples include velocity gradient zones ("second-order discontinuities" across which there is no break in seismic wave velocity) that separate two thick layers of different velocity. This type of velocity transition will reflect longer-wavelength signals because the latter will not "see" the gradient zone, only the contrast in velocities above and below it (Braile and Chiang, 1986). Another example

involves layering at course scales that does not produce tuning at higher frequencies and therefore does not show up with appreciable amplitude in COCORP-style experiments.

The amplitudes of wide-angle reflections generated by these interfaces might be enhanced by longer-wavelength tuning effects, as well as by increased reflection coefficients near the critical angle.

We suggest the latter explanation for the wide-angle reflections that migrate to depths of 30 km beneath the study area. If basement rocks here do indeed represent rifted continental crust as proposed by Phinney and Roy-Chowdhury (1989), then the reflectors could be mafic sills. These would increase the average density of the lower crust beneath the Carolina Terrane and thus help to explain the steepness of the gravity gradient, as proposed by Hawman (1996).

Further Work

Migration of gathers for twenty-three additional blasts from other quarries (Hawman, 1996) recorded in the reversed direction will help fill gaps in subsurface coverage. Migration of S-wave reflections for all blasts will image S-wave reflectivity and will provide independent constraints on the detailed structure of the crust.

Conclusions

Wide-angle reflections generated by quarry blasts and recorded along the axis of the East Coast Gravity High within the Charlotte and Kiokee Belts have been used to image several interesting structures within the crust:

1. Several features in the upper 12 km are similar to those observed in overlapping portions of reprocessed COCORP data (Lines 1 and 5). Examples of these features are the Modoc fault zone and the master decollement. In the

migrated sections, these features show a multicyclic character indicating a mylonitic nature. The migrated sections show that the interpreted top of the master decollement zone plunges ~5 degrees to the NE and extends for ~45 km, while the base plunges ~7 degrees to the NE and extends for ~75 km. Both the top and the bottom of the master decollement zone show a gradual decrease in dip from SW to NE and nearly flatten out at their NE borders. This implies that the Kiokee plunges to the northeast.

2. Strong events at depths of 38-40 km show piecewise continuity over a distance of roughly 72 km. Based on their relative amplitude and apparent velocity, we interpret these events as near-critical and post-critical reflections from the Moho. Corresponding normal-incidence reflection times (11.6 - 11.9 s) computed using the velocity model of Hawman (1996) are slightly greater than times observed for reflection packages interpreted as Moho in the COCORP lines. The difference is attributed to differences in wavelength of incident energy. The depth difference is consistent with the response expected for a thinly layered zone at the crust-mantle transition; higher-frequency, normally-incident energy will return a multicyclic reflection from within this zone, while lower-frequency, wide-angle energy will not "see" this relatively thin sequence but rather will penetrate through it and undergo reflection from within the uppermost mantle (Braile and Chiang, 1986).

3. The wide-angle sections show strong reflections at roughly 30 km that do not appear in the COCORP profiles. These reflections are interpreted as evidence for layering at course scales that does not produce tuning at higher frequencies

and therefore does not show up with appreciable amplitude in COCORP-style experiments. The amplitudes of wide-angle reflections generated by these interfaces might be enhanced by increased reflection coefficients near the critical angle. If basement rocks here do indeed represent rifted continental crust as proposed by Phinney and Roy-Chowdhury (1989), then the reflectors could be mafic sills. These would increase the average density of the lower crust beneath the Carolina Terrane and thus help to explain the steepness of the gravity gradient, as proposed by Hawman (1996).

Overall, the elevated reflection coefficients at wide angles have proved quite useful for imaging subtle constrasts in acoustic impedance otherwise missed by near-vertical recording. Taken together, the different length-scales imaged by the higher-frequency COCORP and lower-frequency wide-angle reflection data provide complementary information on the structure of the crust for this portion of the southern Appalachians.

References

Allard, G. O., and J. A. Whitney, Geology of the Inner Piedmont, Carolina Terrane, and Modoc Zone in Northeast Georgia, *Georgia DNR, Environmental division, Georgia Geol. Surv., Project report 20,* 36p, 1994.

Braile, L. W., and C. S. Chiang, The continental Mohorovicic discontinuity: Results from near-vertical and wide-angle seismic reflection studies, *Geodynamic series, Am. Geophys. Union, 13*, 257-272, 1986.

Chreistensen, N. I., and D. M. Fountain, Constitution of the lower continental crust based on experimental studies of seismic velocities in granulite, *Geol. Soc. Am. Bull., 86,* 227-236, 1975.

Cook, F. A., L. D. Brown, S. Kaufman, J. E. Oliver, and T. A. Peterson, COCORP seismic profiling of the southern Appalachian orogen beneath the Coastal Plain of Georgia: *Geol. Soc. Am. Bull., 92,* 738-748, 1981.

Cook, F. A., D. S. Albaugh, L. D. Brown, S. Kaufman, J. E. Oliver, and R. D. Hatcher, Thin skinned tectonics in the crystalline southern Appalachian: COCORP seismic reflection profiling of the Blue Ridge and Piedmont, *Geology*, 7, 563-567, 1979.

Coruh, C., J. K. Costain, R. D. Hatcher, T. L. Pratt, R. T. Williams, and R. A. Phinney, Results from regional vibroseis profiling: Appalachian ultra-deep core hole site study, *Geophys. J. R. Astron. Soc., 89*, 147-157, 1987.

Dallmeyer, R. D., Late Paleozoic thermal evolution of crystalline terranes within portions of the U.S. Appalachian orogen, *The Geology of North America,* F2, The Appalachian-Ouachita in the United States, *Geol. Soc. Am,* 417–444, 1989.

Dallmeyer, R. D., Wright, J. E., Secor, D. T., Jr., and Snoke, A. W., Character of the Alleghanian orogeny in the southern Appalachians: Part II. Geochronological constraints on the tectonothermal evolution of the eastern Piedmont in South Carolina: *Geol. Soc. Am. Bull., 97*, 1329-1344, 1986

Douze, E. J., and S. J. Laster, Statistics of semblance, *Geophysics*, *44*, 1999-2003, 1979.

Fountain, D. M., Hurich, C. A., and Smithson, S. B., Seismic reflectivity of mylonite zones in the crust, *Geology, 12*, 195-198, 1984.

Griffin, V. S., The Inner Piedmont Belt of the southern crystalline Appalachians, *Geol. Soc. Am. Bull., 82,* 1885-1898, 1971.

Harris, L. D., and K. C. Payer, Sequential development of the Appalachian orogen above a master decollement – A hypothesis, Geology, 7, 568-572, 1979.

Hatcher, R. D., Developmental model for for the southern Applachians, *Geol. Soc. Am. Bull*., 83, 2735-2760, 1972.

Hatcher, R. D., Tectonic synthesis of the U.S. Appalachians in the Appalachian-Ouachita Orogen in the United States, Geol. of N. Am., vol. F-2, edited by R.D. Hatcher, W. A. Thomas, and G. W. Viele, 511-535, *Geol. Soc. Of Am., Boulder, Colorado*, 1989.

Hawman, R. B., Wide-angle, three-component seismic reflection profiling of the crust along the East Coast Gravity High, southern Appalachian, using quarry blasts*, J. Geophys. Res., 101*, 13,933 - 13,945, 1996.

Hawman, R. B., R. H. Colburn, D. A. Walker, and S. B. Smithson, Processing and inversion of refractionand wide-angle reflection data from the 1986 Nevada Passcal Experiment , *J. Geophys. Res., 95,* 4657-4691, 1990.

Hawman, R. B., M. C. Chapman, C. A. Powell, and J. E. Clippard, and H. O. Ahmed, Wide-angle reflection profiling with quarry blasts in the Eastern Tennessee seismic zone, *Seismol. Res. Lett*, *72*, 108-122, 2001.

Hawman, R. B., and R. A. Phinney, Structure of the crust and upper mantle beneath the Great Valley and Allegheny Plateau of Eastern Pennsylvania: 2.Gravity modeling and migration of wide-angle reflection data, *J. Geophys. Res.*, *97*, 393-415, 1992.

Hurich, C. A., S. B. Smithson, D. M. Fountain, and M. C. Humphreys, Seismic evidence of mylonite reflectivity and deep structure in the Kettle dome metamorphic core complex, Washington, *Geology, 13*, 577-580, 1985.

Hutchinson, D. R., G. A. Grow, and K. D. Klitgord, Crustal structure beneath the southern Appalachians: Nonuniquness of gravity modeling, *Geology, 11,* 611-615, 1983.

Iverson, W. P., and S. B. Smithson, Master decollement root zone beneath the southern Appalachians and crustal balance, *Geology*, 10, 241 - 245, 1982.

Khalifa, M. O., J. A. Kucinskis, J. E. Clippard, and R. B. Hawman, 2001b, Wide-angle reflection profiling of the Elberton granite and deep structure of the Inner Piedmont, Southern Appalachians, using instantaneous and ripple-fired quarry blasts, *EOS Trans. Am. Geophys. Union, 82, 20, Spring Meeting Suppl., Abstract S52A-10*, 2001.

Long, L. T., and A. M. Dainty, Studies of gravity anomalies in Georgia and adjacent areas of the southeastern United States, in *The Utility of the Regional Gravity and Magnetic Anomaly Maps*, edited by W. J. Hinze, pp. 308-319, Soc. of Explor. Geophys., Tulsa, Okla., 1985.

Long, L. E., J. L. Kulb, and F. D. Eckelmann, Chronology of major metamorphic events in the southeastern United States, *Am. J. Sci*., *257*, 585 – 603, 1959.

Long, L., The Carolina Slate belt - Evidence of a continental rift zone, *Geology, 7,* 180-184*,* 1979

Maher, H. D., Palmer, A. R., Secor, D. T., and Snoke, A. W., New Trilobite locality in the Piedmont of South Carolina and its regional implications, *Geology, 9*, 34-36, 1981.

Phinney, R. A., and K. Roy-Chowdhury, Reflection seismic studies of crustal structure in the Eastern United States, *Memoir, Geol. Soc. Am.,172*, 613-653, 1989.

Phinney, R. A., K . Roy-Chowdhury, and L. N. Frazier, Transformation and analysis of record sections, *J. Geophys. Res, 86*, 359-377, 1981.

Secor, D. T., A. W. Snoke, K. W. Bramlett, O. B. Costello, and O. B. Kimbrell, Charater of the Alleghanian orogeny in the southern Appalachians, I, Alleghanian

deformation in the eastern Piedmont of South Carolina, *Geol Soc Am. Bull., 97*, 1319-1328, 1986a.

Secor, D. T., A. W. Snoke, A. W., and Dallmeyer, R. D., Charater of the Alleghanian orogeny in the southern Appalachians: Part III Regional tectonic relashionships: *Geol. Soc. Am. Bull.,* 79, 1345-1353, 1986b.

Smithson, S. B., J. A. Brewer, S. Kauffmann, J. E. Oliver, and C. A. Hurich, Structure of the Laramide Wide River uplift, Wyoming, from COCORP deep reflection data and from gravity data, *J. Geophys. Res., 84*, 5955-5972, 1979.

Society of exploration Geophysicists, Gravity anomaly map of the United States, Tulsa, Okla., 1982.

Stoffa, P. L., P. Buhl, J. B. Diebold, and F. Wenzel, Direct mapping of seismic data to the domain of intercept time and ray parameter: A plane wave decomposition, *Geophysics, 46*, 255-267, 1981.

Whitney, J. A. D. E. Wells, and R. W. Rozen, Structural and tectonic setting of the Elberton , Eastern Georgia Piedmont, *in* Geological, Geochemical, and Geophysical Studies of the Elberton , Eastern Georgia, *Atlanta, Ga, Dept. Natural Res. Guide Book 19*, 1-10, 1980.

Whitney, J. A., T. A. Paris, R. H. Carpenter, and M. E. Hartley, Volcanic evolution of the southern Slate Belt of Georgia and South Carolina: A primitive oceanic island arc, *J. Geol., 86*, 173-192, 1978.

Williams, H., and R. D. Hatcher, Appalachian suspect terranes, in Contribution to the Teconics and Geophysics of Mountain Chains, edited by R. D. Hatcher, H. Williams, and I. Zietz, *Mem. Geol. Soc. Am., 158*, 33-53, 1983.

Yilmaz, O., Seismic data processing, Society of exploration geophysicists (SEG), 526 p., 1987.

Figure 3.1: Geologic map of the study area showing ray paths for Southern Aggregates Hitchcock and Martin Marietta Ruby quarry blasts. The map shows the geologic belts of the area (after Dallmeyer, 1989). Stars and bars indicate shots and array locations, respectively. E.G indicates Elberton granite. Other pink bodies represent granitic intrusions.

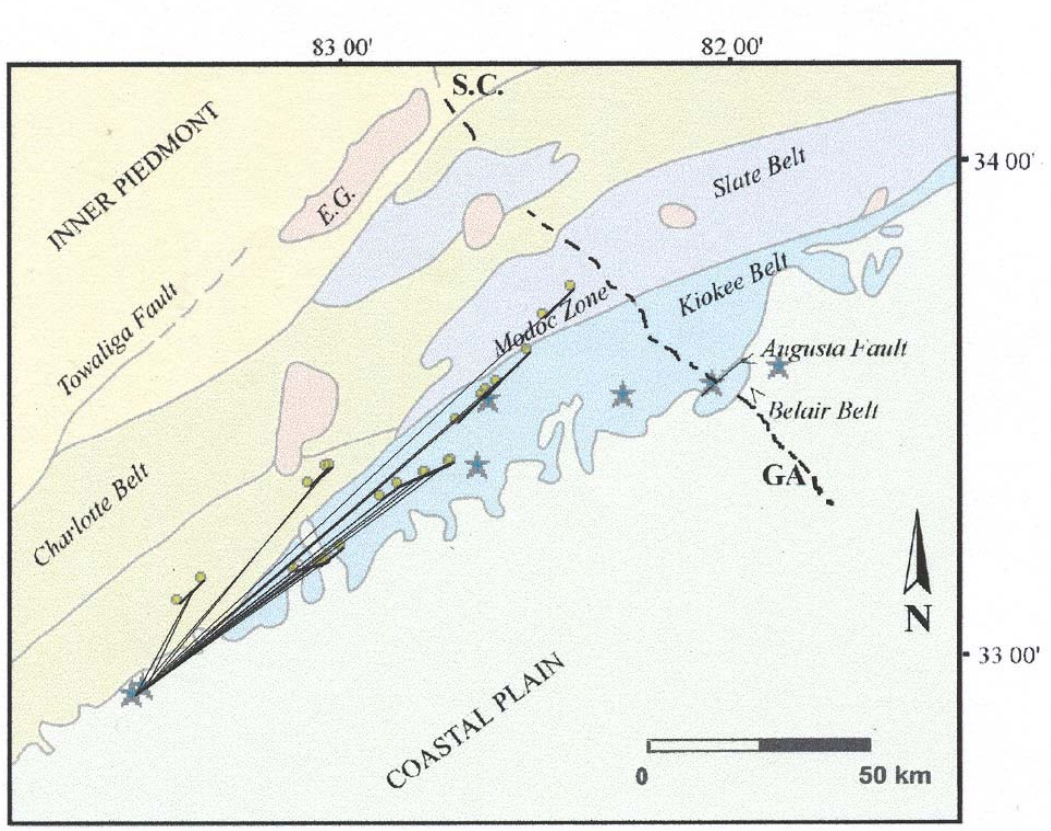
83.00'
82.00'
S.C.
INNER PIEDMONT
E.G.
Slate Belt
34 00'
Towaliga Fault
Kiokee Belt
Modoc Zone
Augusta Fault
Belair Belt
GA
Charlotte Belt
N
33 00'
COASTAL PLAIN
0
50 km

(Figure 3.1)

Figure 3.2: Gravity anomaly map (after Society of Exploration Geophysicists, 1982) of the study area showing the seismic recorded lines running along the East Coast Gravity High. The dashed line is the (-25MGal) contour that marks the maximum gradient between gravity lows and highs. Solid lines (C1 and C5) represent the COCORP lines 1 and 5 respectively.

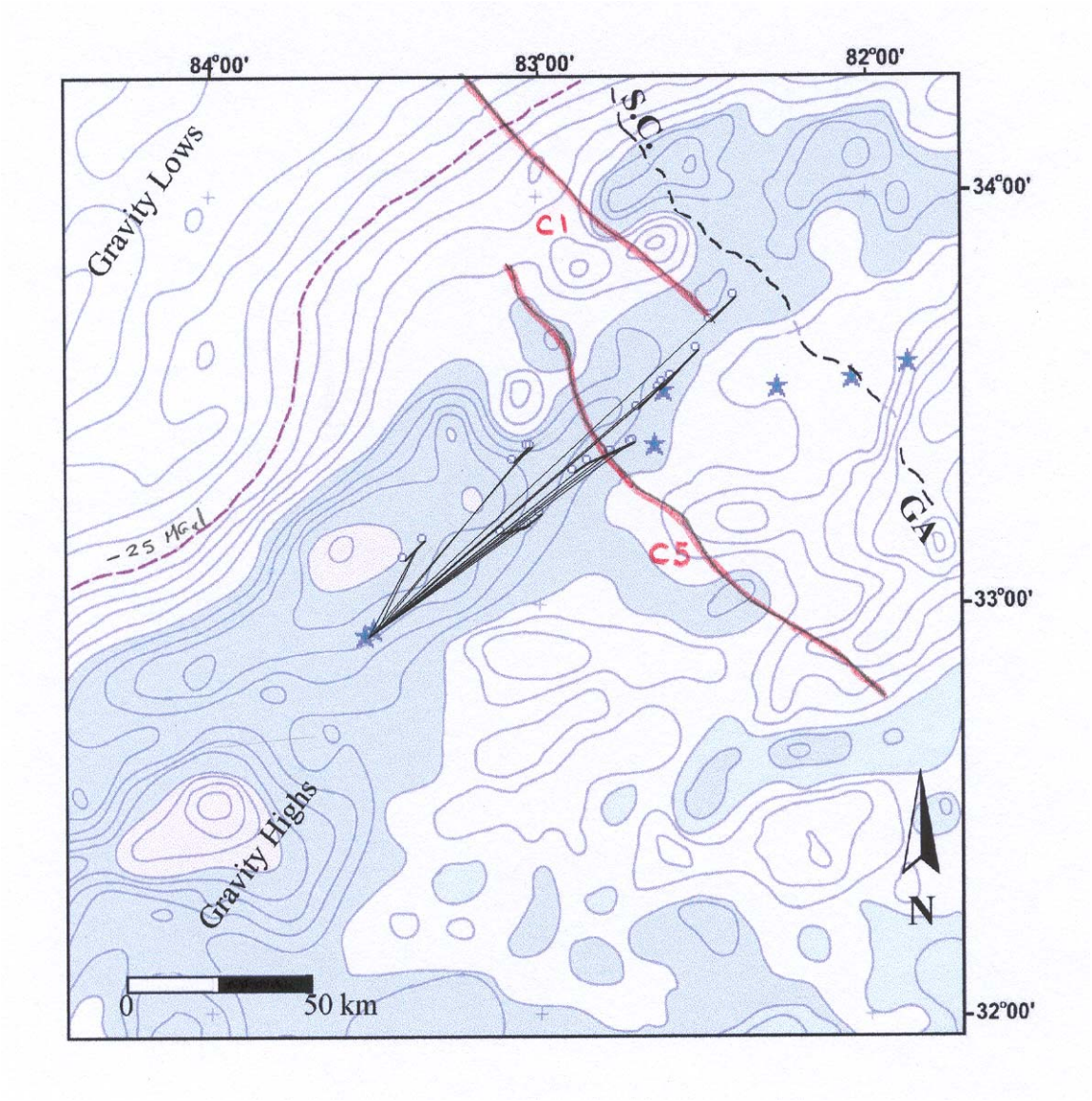
84°00'
83°00'
82°00'
34°00'
33°00'
32°00'
Gravity Lows
Gravity Highs
-25 MGal
C1
C5
GA
N
0
50 km

(Figure 3.2)

Figure 3.3a: Static-corrected, deconvolved shot gather of Hitchcock blast #1, vertical component. The distance range was 106.7-111.5 km. The gather was high-cut filtered using a filter with a linear cutoff of 10-15 Hz. The horizontal axis represents the distance in km from the shot while the vertical axis represents the reduced time starting at -1.0 s. Velocity reduction was applied using 6.0 km/s. The gather has been static-corrected using a reduction velocity of 6.5 km/s to flatten the target arrival.

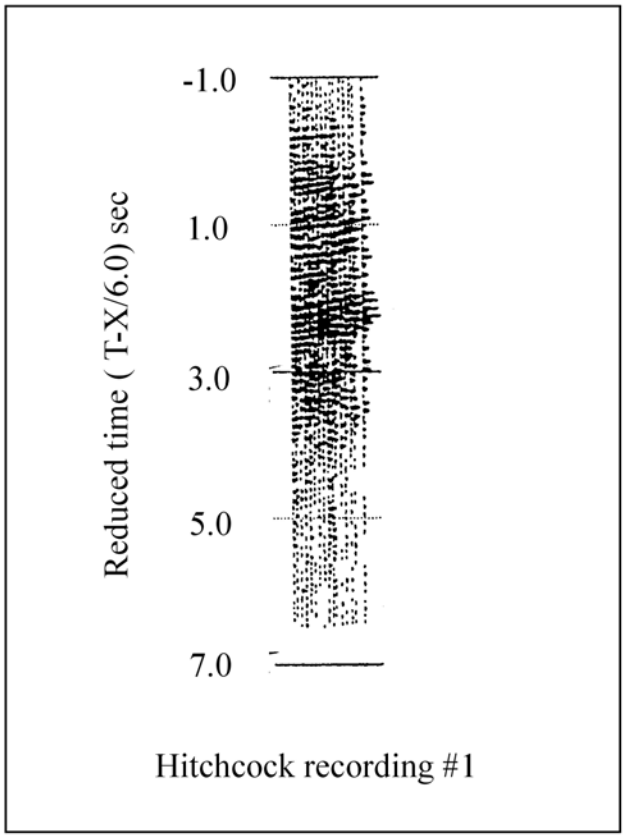

(Figure 3.3a)

Figure 3.3b: Semblance of the slant stack of Hitchcock recording 1. Direct P wave shows an average ray parameter (p) of about 0.14 to 0.17 s/km. Coherent arrivals with ray parameter less than 0.17 are interpreted as P-wave reflections. Arrivals with ray parameter greater than 0.17 s/km are interpreted as P-SV converted waves. Time axis indicates the TWT time to the center of the array. Ray parameters range from 0.17 s/km for shallow reflections to 0.10 s/km for deep reflections. PmP marks reflections interpreted as reflections from the Moho.

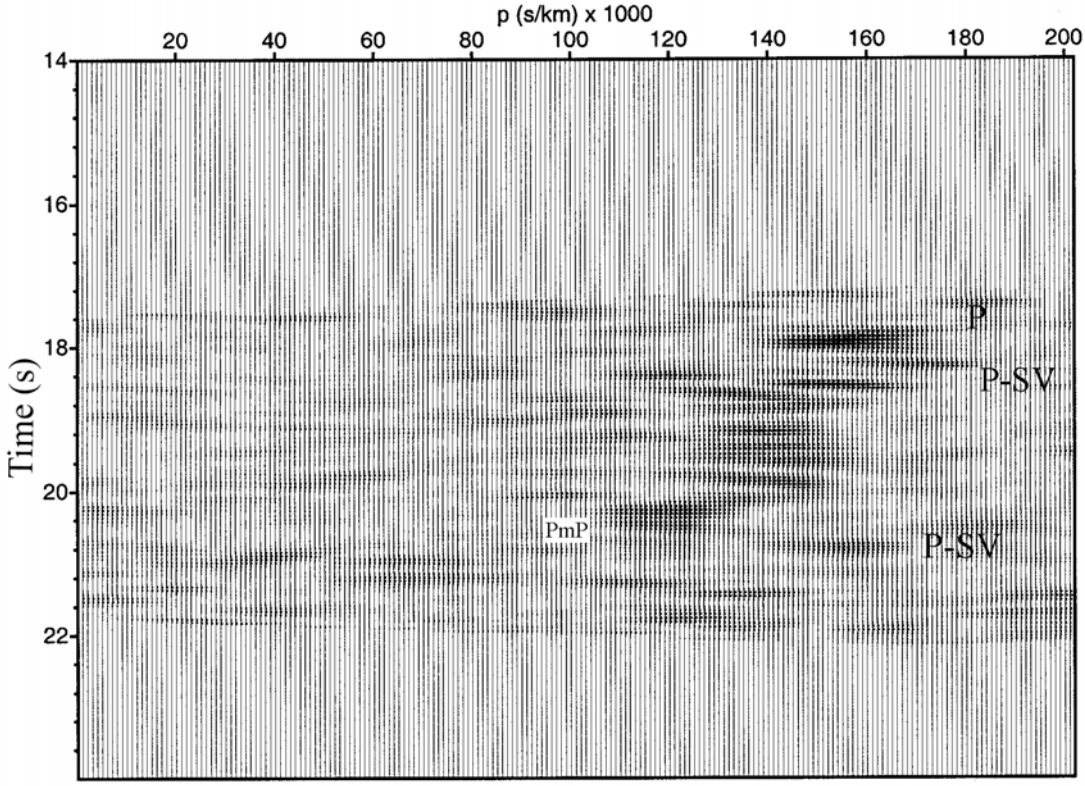
p (s/km) x 1000
20
40
60
80
100
120
140
160
180
200
14
16
18
20
22
Time (s)
P
P-SV
PmP
P-SV

(Figure 3.3b)

Figure 3.3c: Slant stack of Hitchcock recording 1 vertical component. Time axis for the slant stack represents the travel times for the center offset trace.

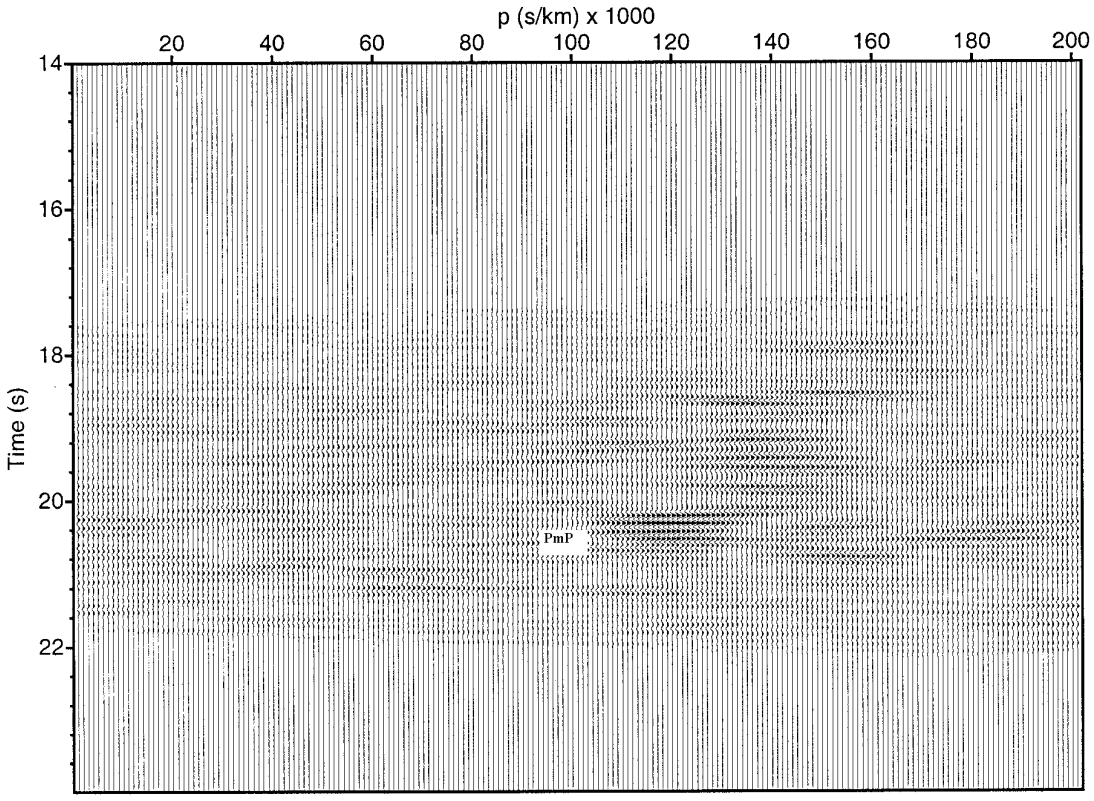
p (s/km) x 1000
20
40
60
80
100
120
140
160
180
200
14
16
18
20
22
Time (s)
PmP

(Figure 3.3c)

Figure 3.3d: Smoothed semblance of Hitchcock recording 1.

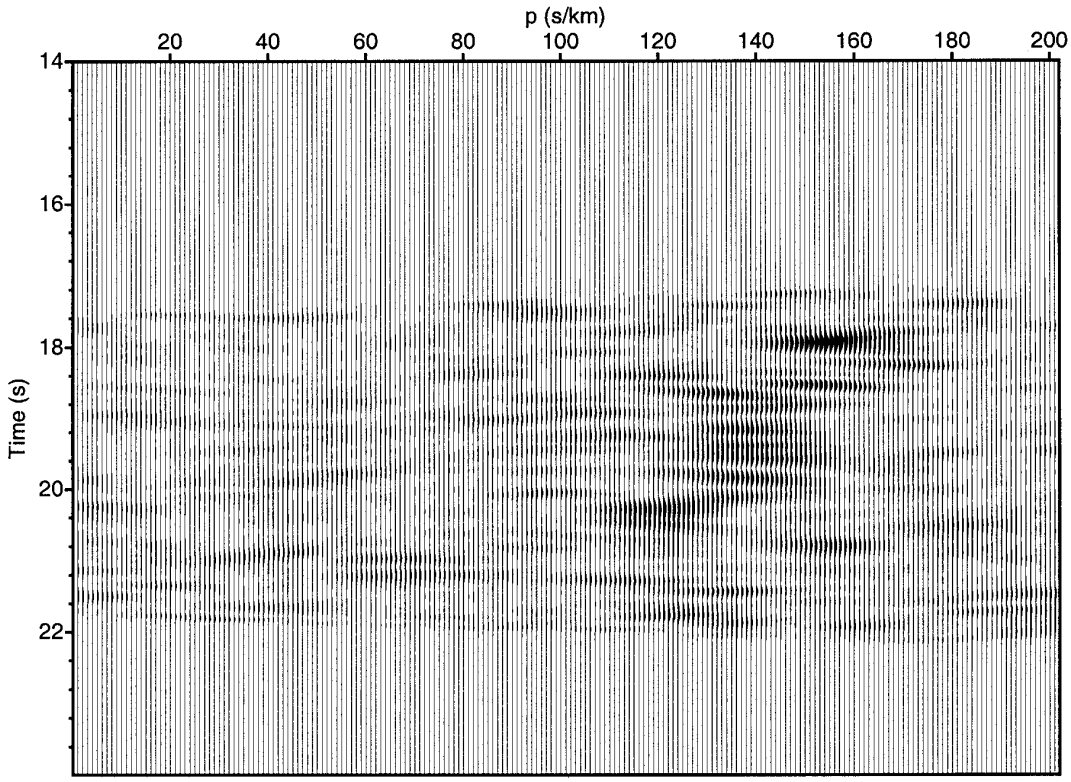

(Figure 3.3d)

Figure 3.3: (e-j) Series of coherency filtered slant stacks of Hitchcock recording 1. After smoothing the unfiltered semblance of the slant stack by high cut filtering (using a linear ramp from 10 to 15 Hz). All samples with values that are less than the given threshold are zeroed out. This suppresses incoherent noise. As the threshold value is raised the events become more focused; eventually, some events are completely lost. The Figure 3.shows a series of threshold settings that begins with e. 0.4 threshold, f. 0.45, g. 0.5, h. 0.55, i. 0.6, and j. 0.7. A threshold setting of 0.55 was used prior to migration.

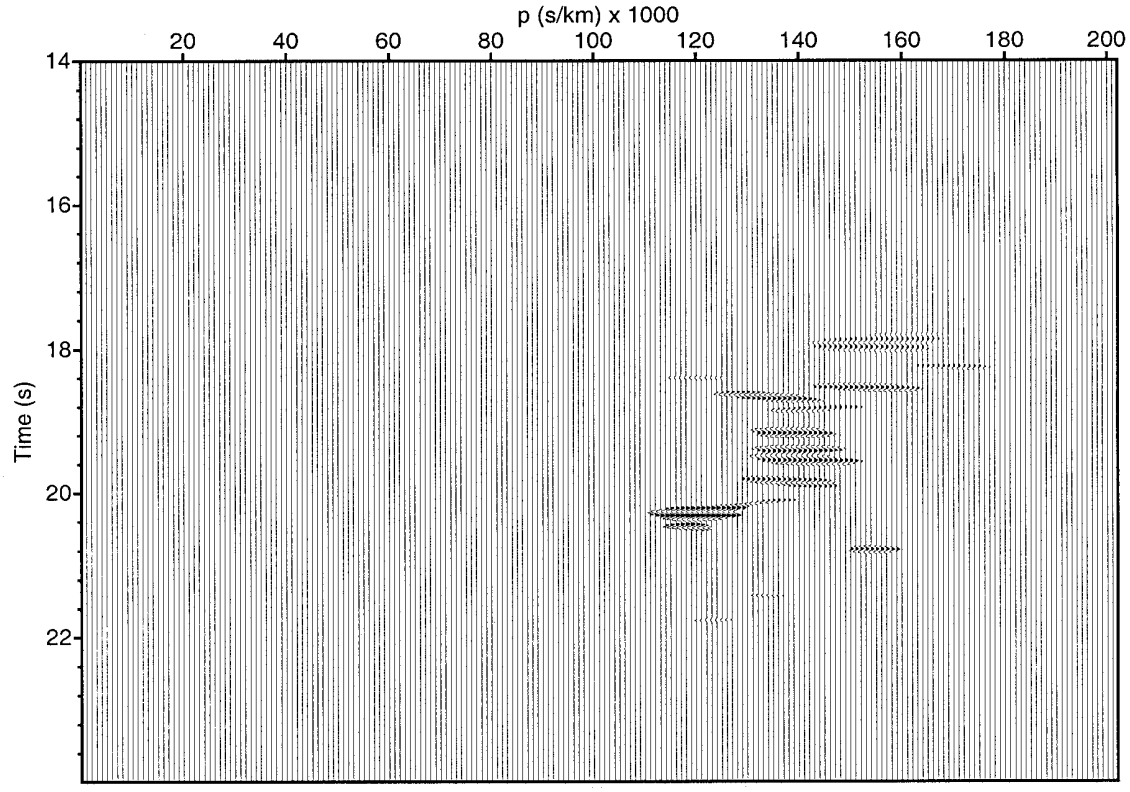
p (s/km) x 1000
20
40
60
80
100
120
140
160
180
200
14
16
18
20
22
Time (s)

(e)

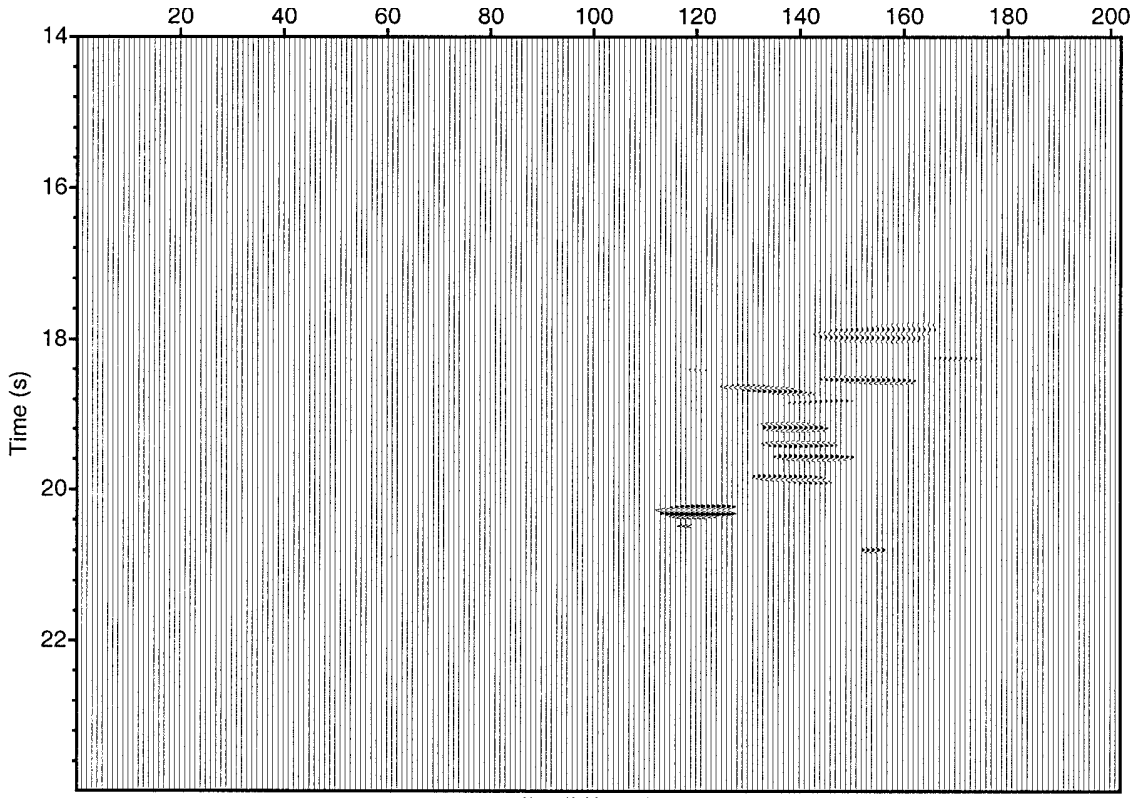
20
40
60
80
100
120
140
160
180
200
14
16
18
20
22
Time (s)

(f)

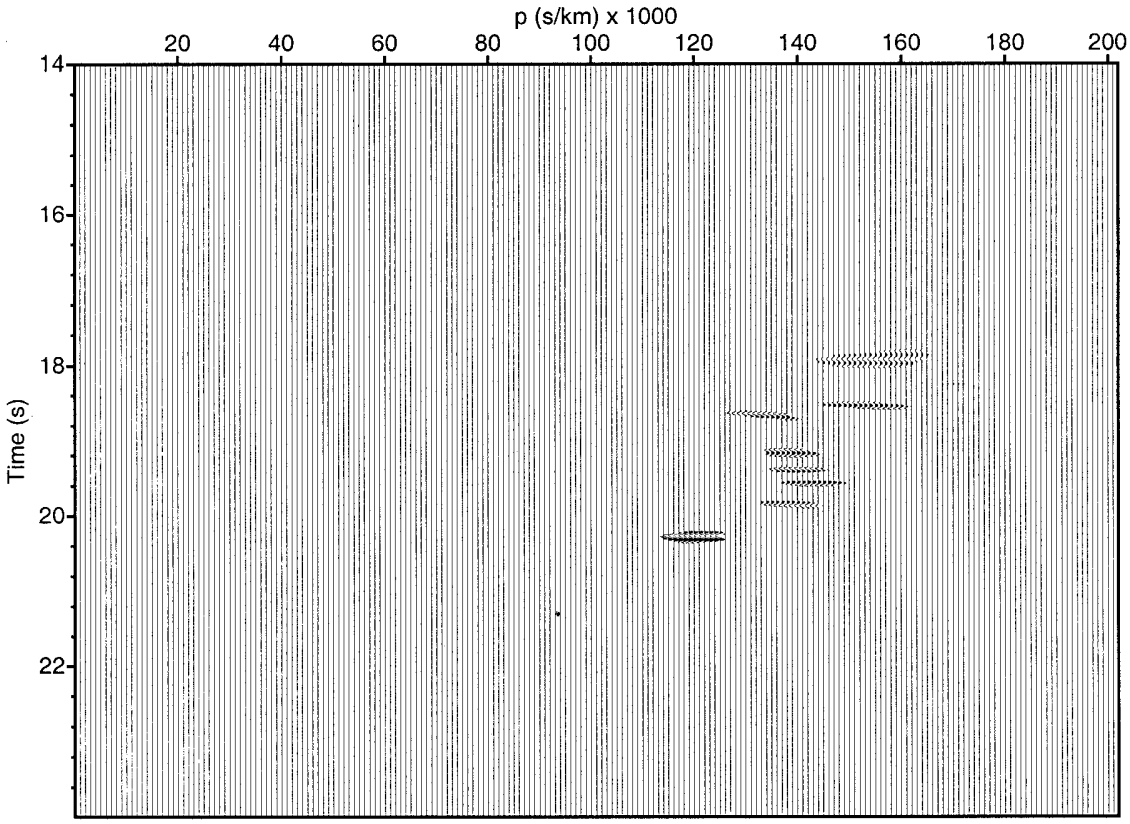
p (s/km) x 1000
20
40
60
80
100
120
140
160
180
200
14
16
18
20
22
Time (s)

(g)

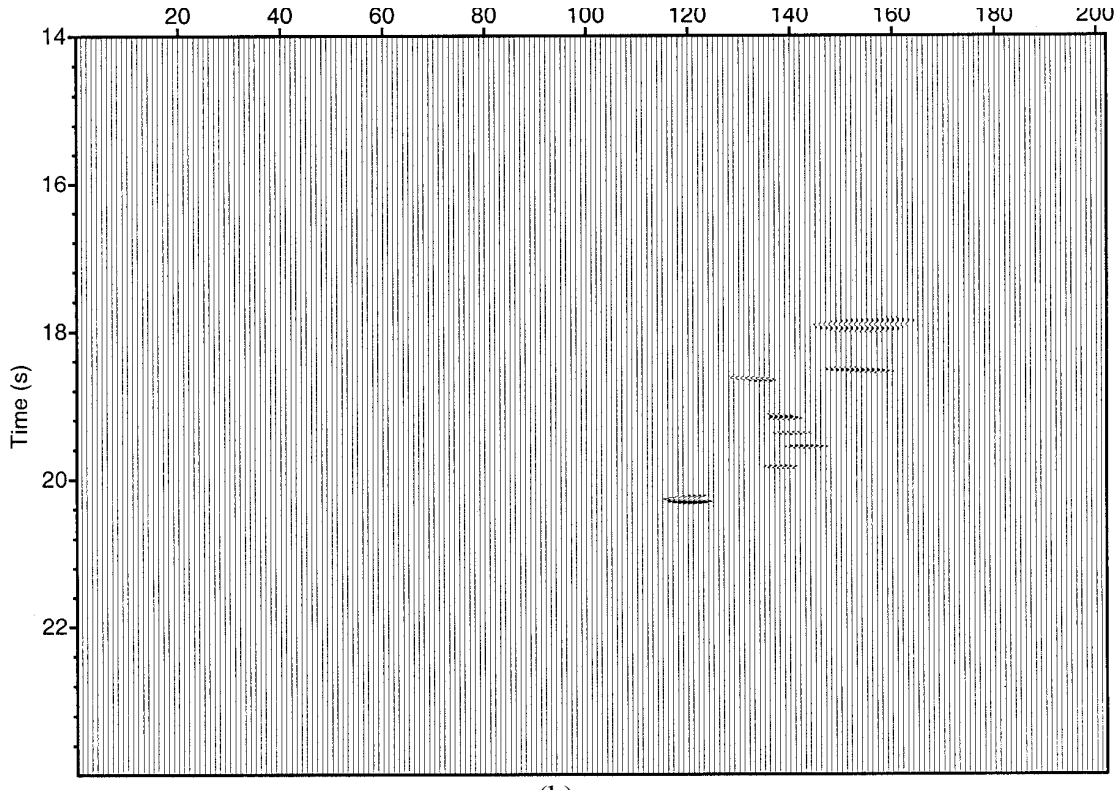
20
40
60
80
100
120
140
160
180
200
14
16
18
20
22
Time (s)

(h)

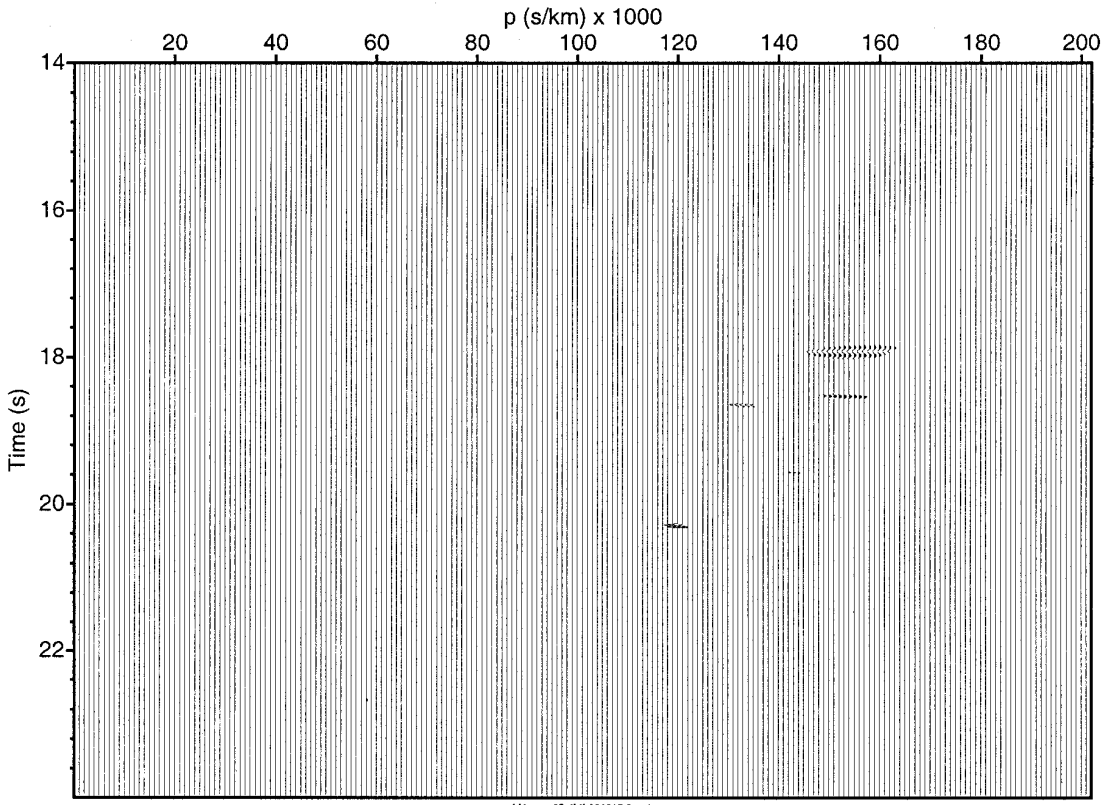
p (s/km) x 1000
20
40
60
80
100
120
140
160
180
200
14
16
18
20
22
Time (s)

(i)

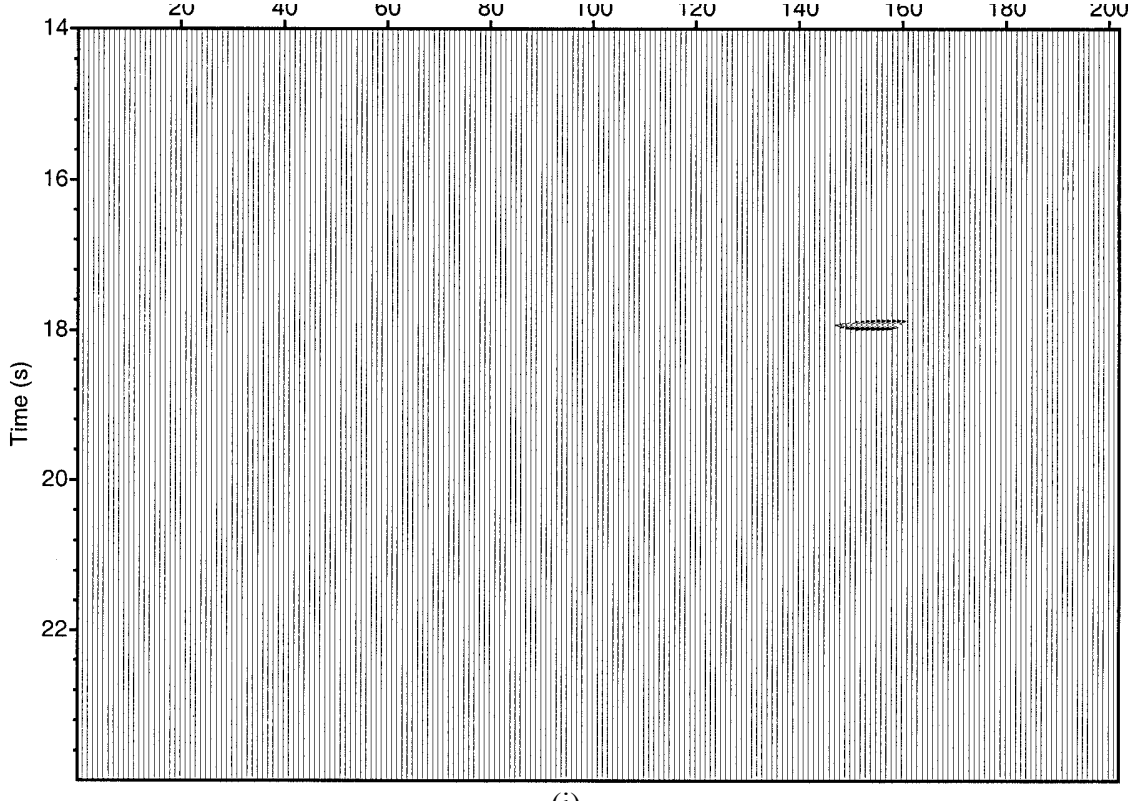
20
40
60
80
100
120
140
160
180
200
14
16
18
20
22
Time (s)

(j)

Figure 3.4: Hitchcock blast #2: a) Static-corrected shot gather. Distance range is 85.7-91.6 km. The gather was hi-cut filtered using a linear ramp from 10-15 Hz. The horizontal axis represents the distance in km from the shot while the vertical axis represents the reduced time. Static corrections were carried out after using a reduction velocity of 6.0 km/s to flatten the target event. (b) Semblance of the slant stack. Direct P wave shows an average ray parameter (p) of about 0.18 s/km. Several coherent arrivals immediately follow the direct P wave with smaller ray parameter. Some arrivals characterized by larger ray parameter than that of the direct P-wave are interpreted as converted P-SV waves. (c) Slant stack, time axis for the slant stack represents the travel times for the center offset trace. Events are concentrated in a time window of 14-16 s in an almost vertical panel bordered by 0.13 and 0.18 ray parameter values except for some deeper events that posses a smaller ray parameter. (d) Coherency filtered slant stacks that were used for migration. Threshold filters values are (d1) 0.55 (d2) and 0.7.

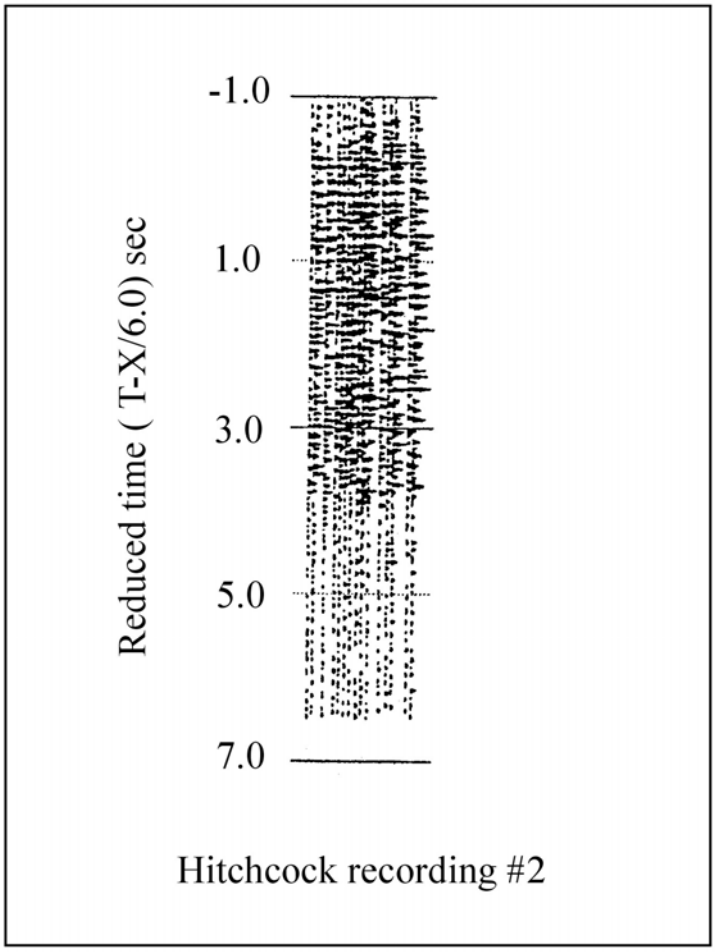

(Figure 3.4a)

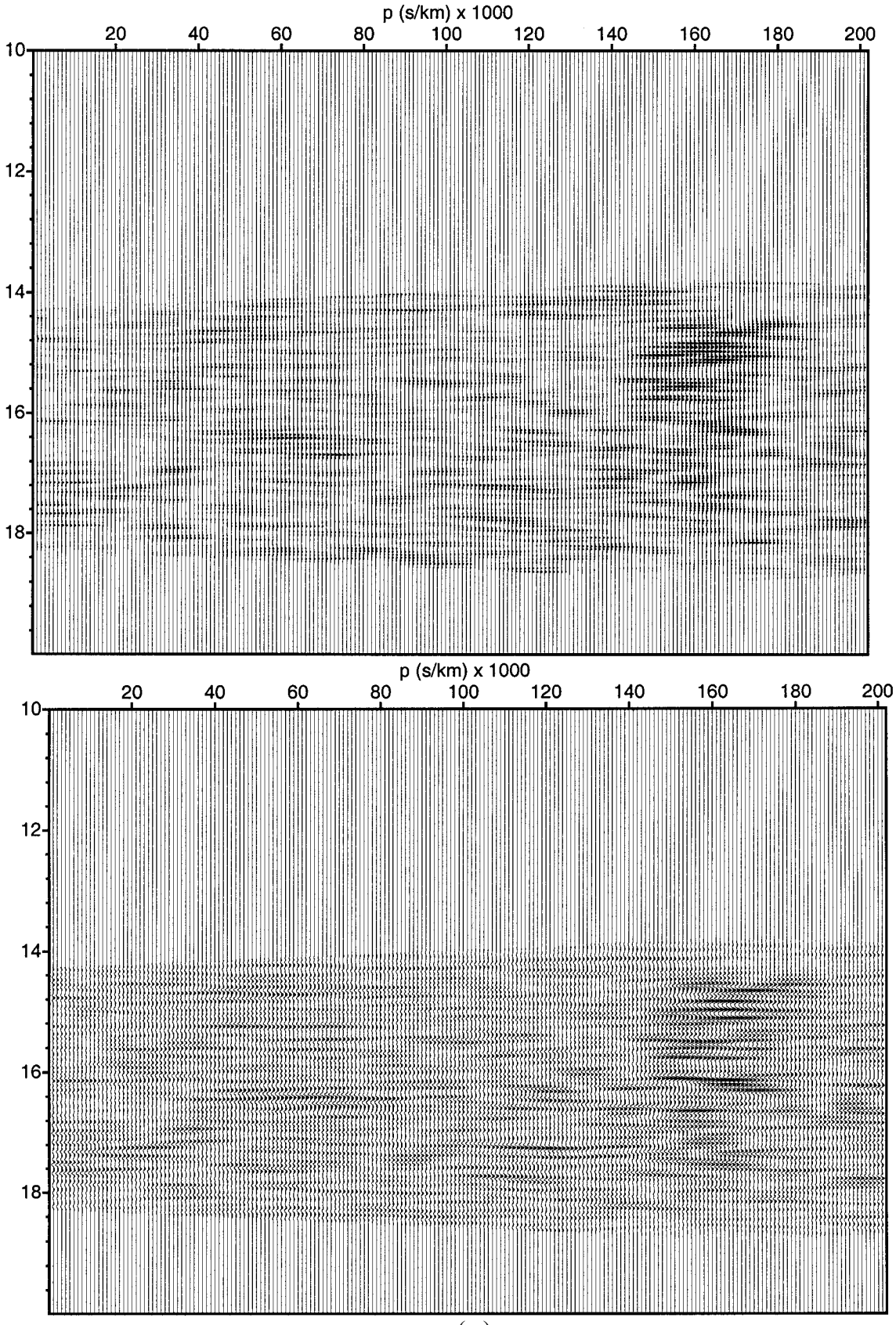
p (s/km) x 1000
20
40
60
80
100
120
140
160
180
200
10
12
14
16
18
p (s/km) x 1000
20
40
60
80
100
120
140
160
180
200
10
12
14
16
18

(c)

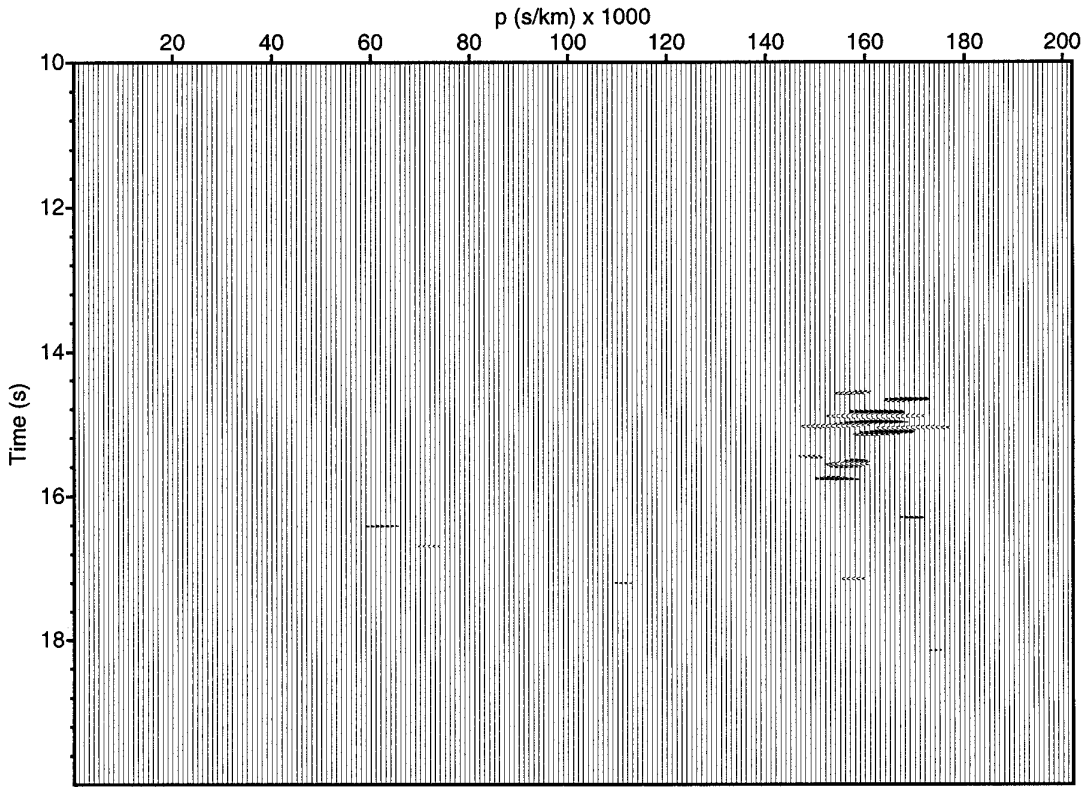
p (s/km) x 1000
20
40
60
80
100
120
140
160
180
200
10
12
14
16
18
Time (s)

(d1)

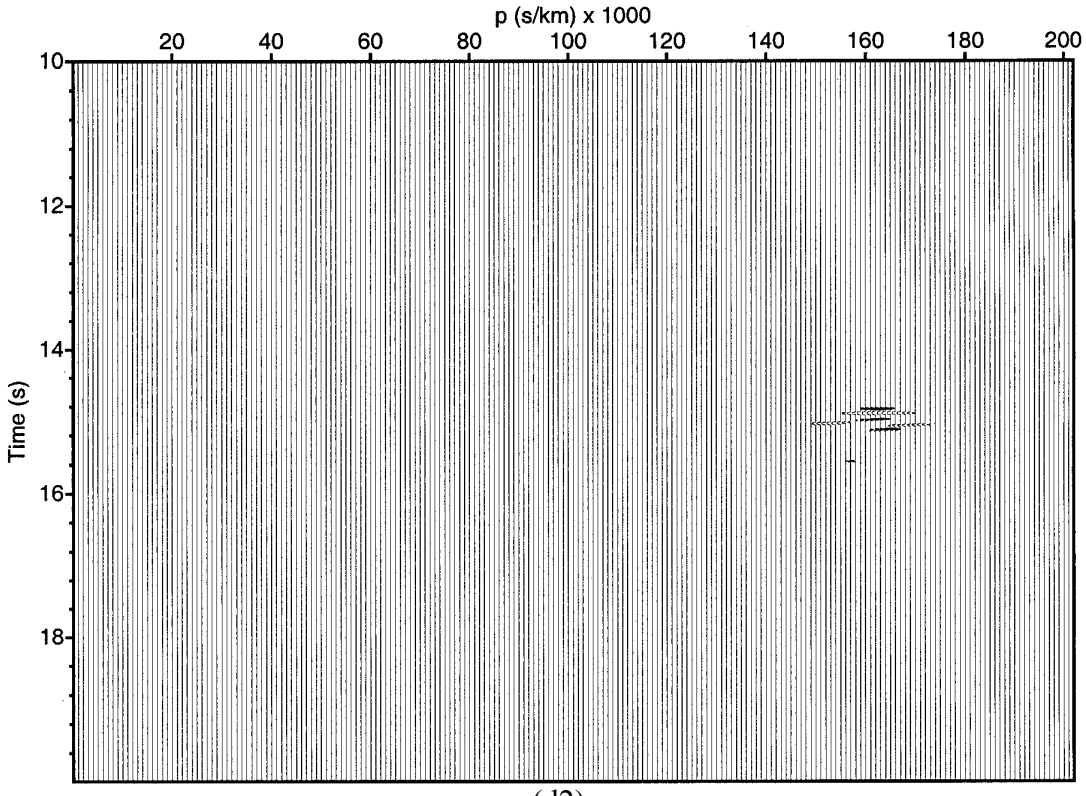
p (s/km) x 1000
20
40
60
80
100
120
140
160
180
200
10
12
14
16
18
Time (s)

(d2)

Figure 3.5: Hitchcock blast #3: Static-corrected shot gathers (vertical component) are shown in (a1) and (a2) with different static parameters. Distance range: 115-121.7 km. The gathers were high-cut filtered using a linear ramp from 10-15 Hz. Static corrections were carried out after using a reduction velocity of 6.6 and 8.3 km/s to flatten the target event. (b1,b2) semblance of slant stacks. Both sections similar events but deeper events are more focused in (b2) where higher velocity reduction used. (c1,c2) are the slant stacks of the same shot gather with two different velocity reduction. (d1,d2) are the coherency filtered slant stacks used in migration. PmP denotes an event interpreted as a reflection from Moho.

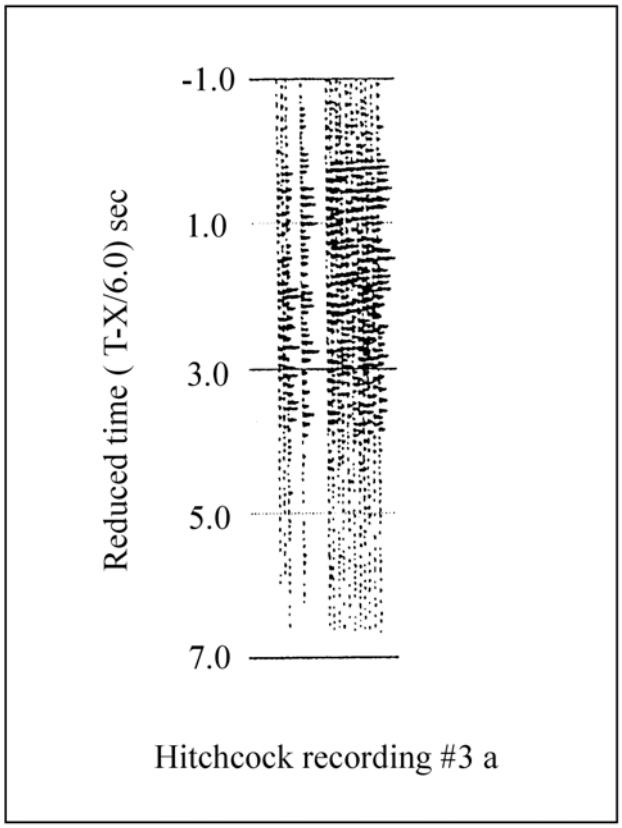

(Figure 3.5a1)

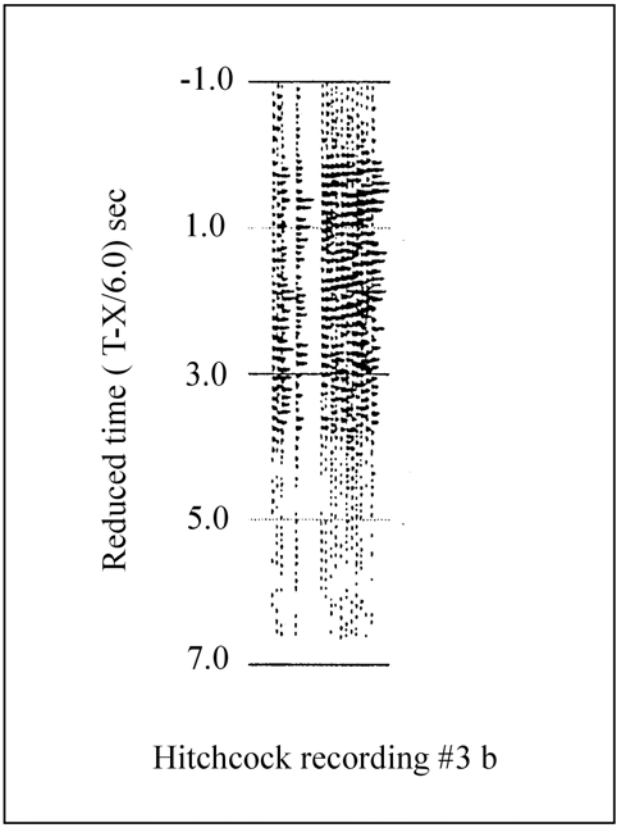

(Figure 3.5a2)

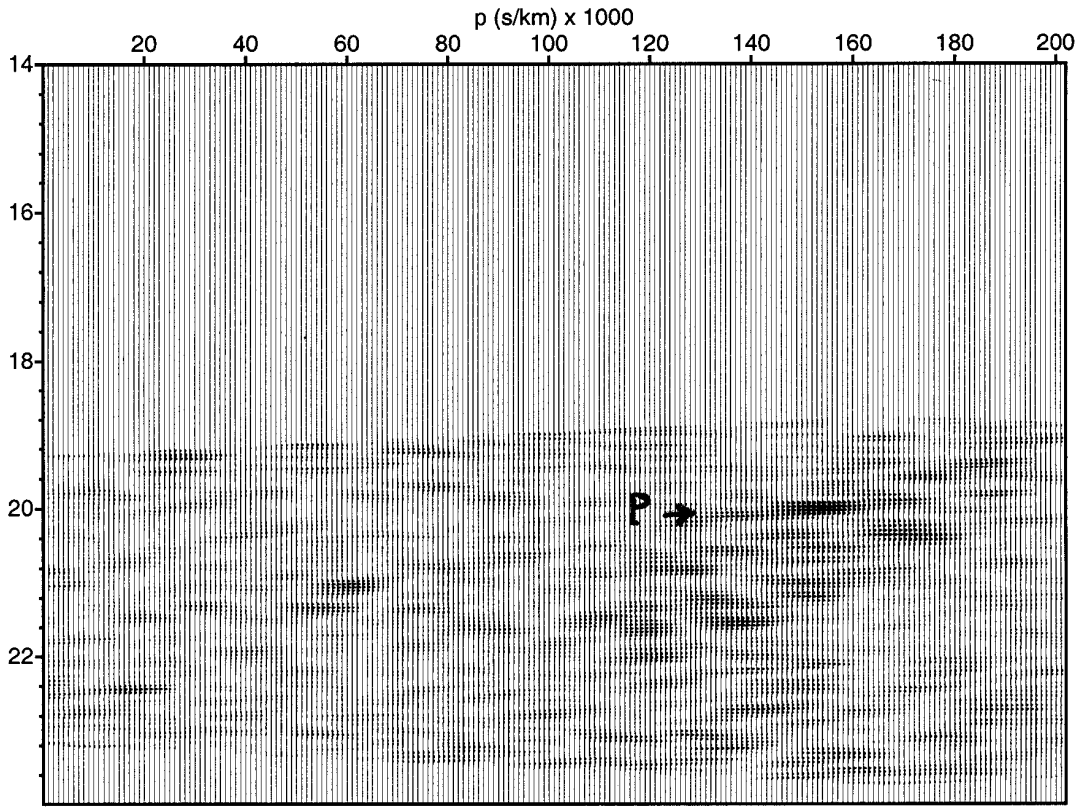
p (s/km) x 1000
20
40
60
80
100
120
140
160
180
200
14
16
18
20
22
P

(b1)

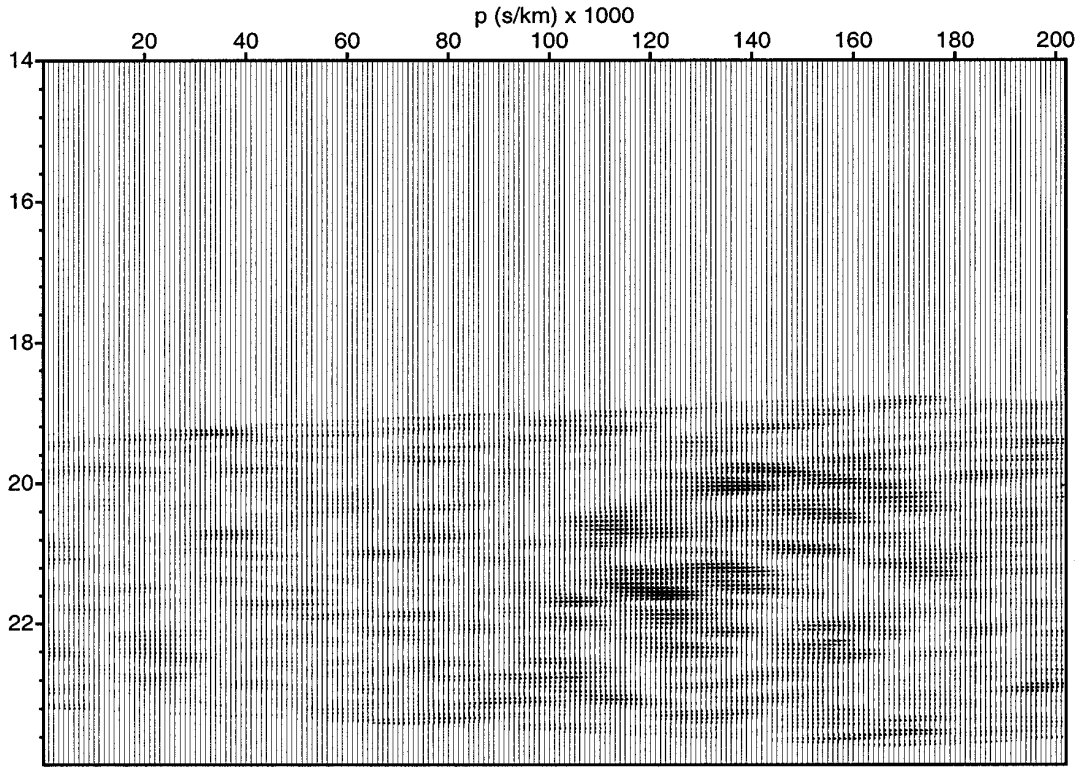
p (s/km) x 1000
20
40
60
80
100
120
140
160
180
200
14
16
18
20
22

(b2)

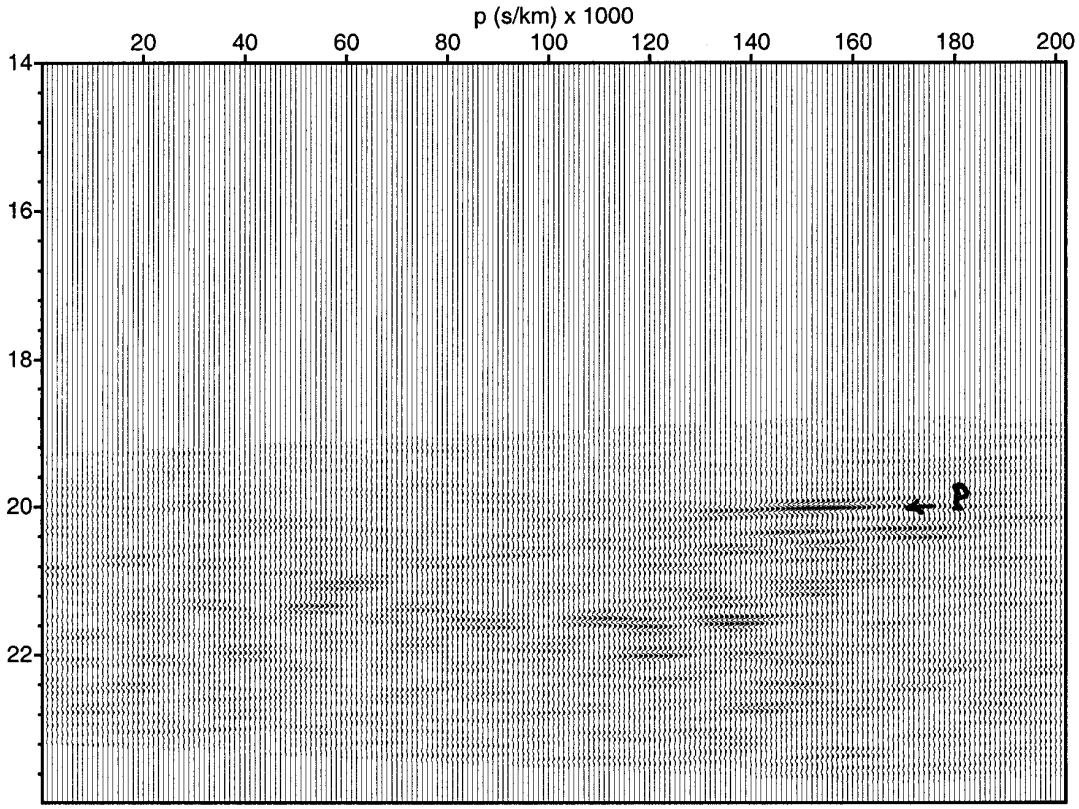
p (s/km) x 1000
20
40
60
80
100
120
140
160
180
200
14
16
18
20
22
P

(c1)

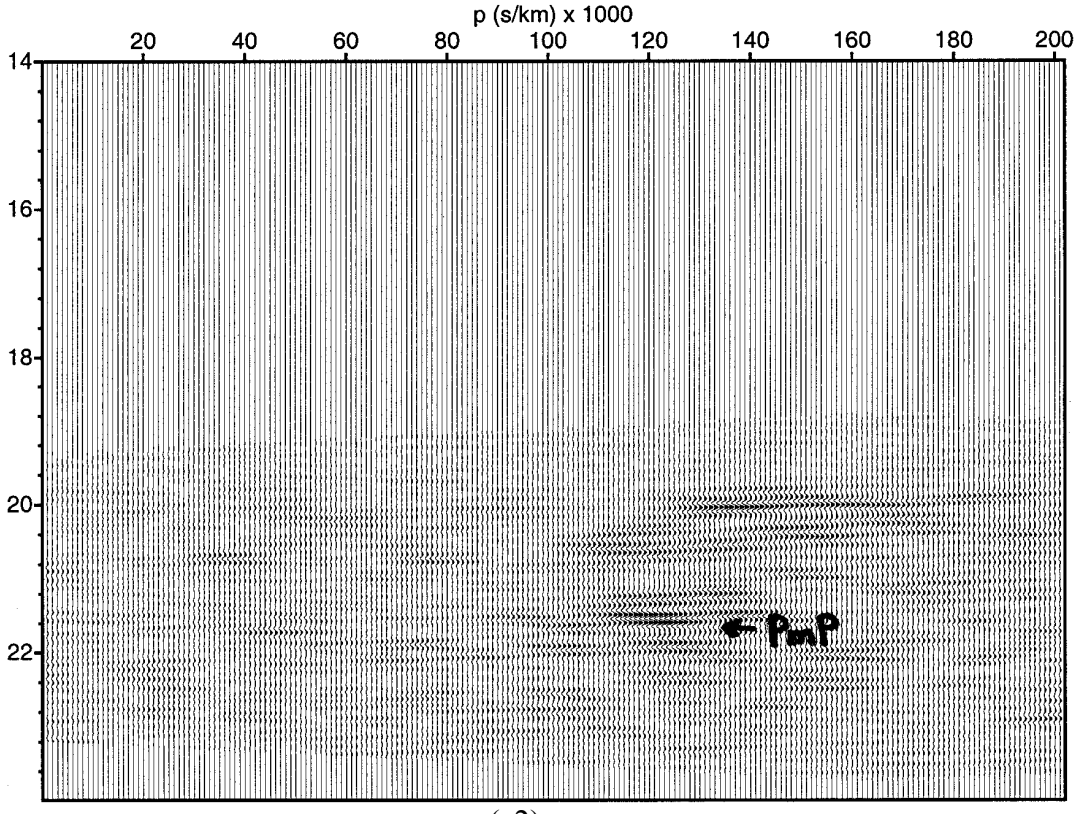
p (s/km) x 1000
20
40
60
80
100
120
140
160
180
200
14
16
18
20
22
PmP

(c2)

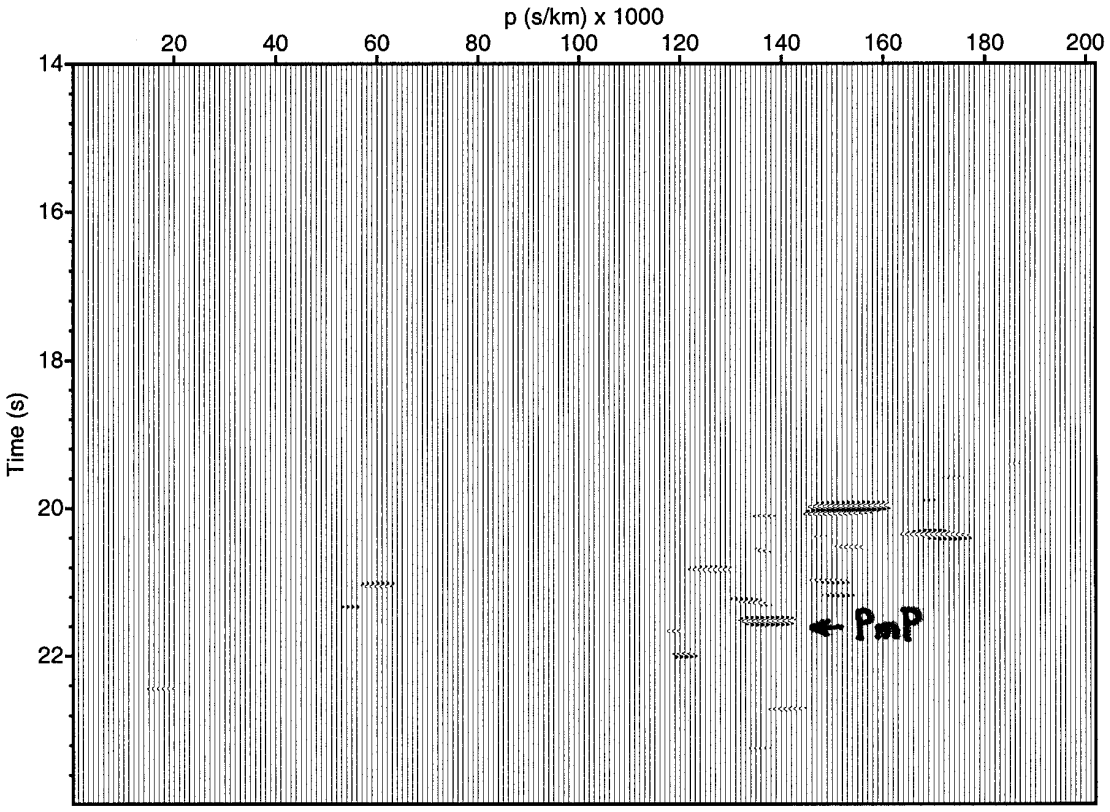
p (s/km) x 1000
20
40
60
80
100
120
140
160
180
200
14
16
18
20
22
Time (s)
PmP

(d1)

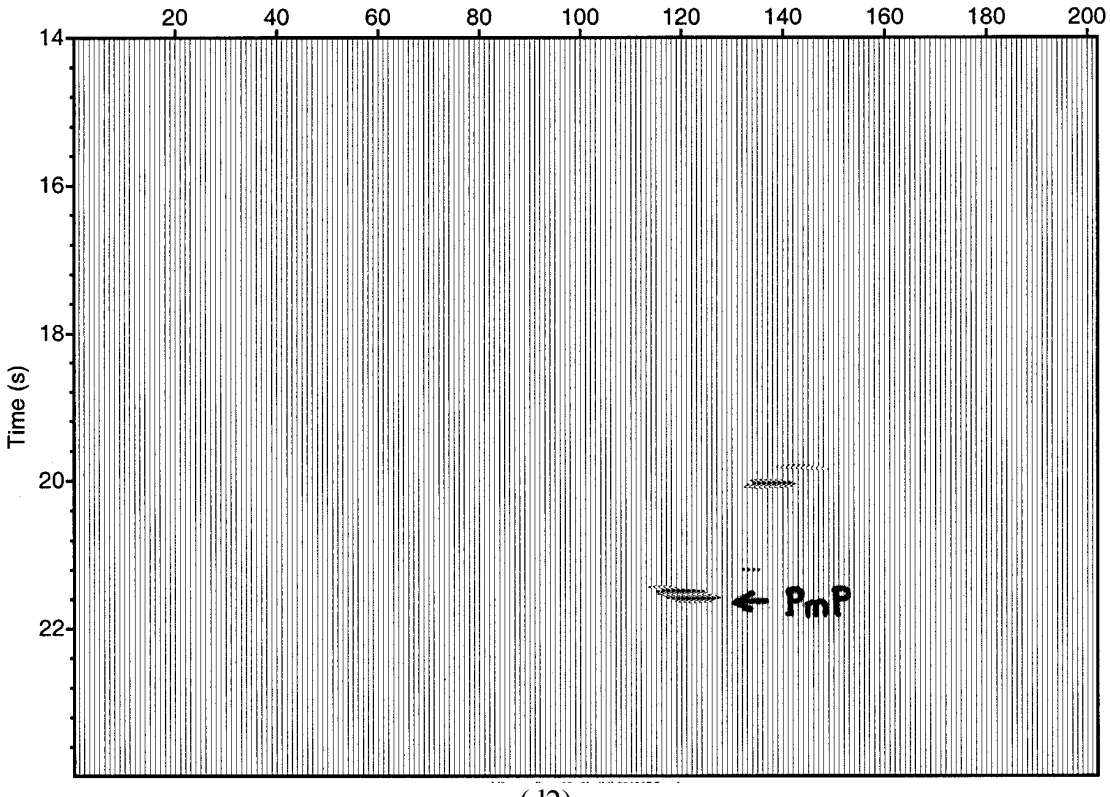
20
40
60
80
100
120
140
160
180
200
14
16
18
20
22
Time (s)
PmP

(d2)

Figure 3.6: Hitchcock blast #4: (a) static corrected shot gather. Distance range: 73.93-78.6 km. (b) semblance of the slant stack, (c) slant stack, and (d1,d2) coherency filtered slant stacks. The gather was high-cut filtered using a linear ramp from 10-15 Hz. The horizontal axis represents the distance in km from the shot while the vertical axis represents the reduced time. Static corrections were carried out after using a reduction velocity of 6.3 km/s to flatten the target event. The semblance and coherency filtered slant stacks show well resolved events that follow the direct P wave at times between 12.4 and 15.6 s. Threshold values used for migration are (d1) 0.5 and (d2) 0.55.

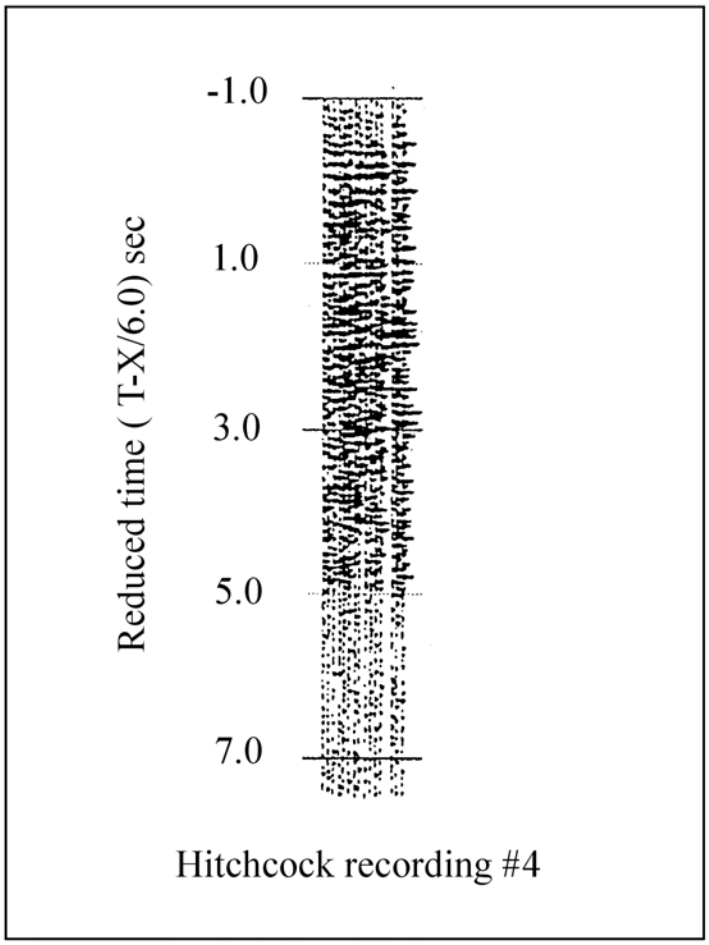

(Figure 3.6a)

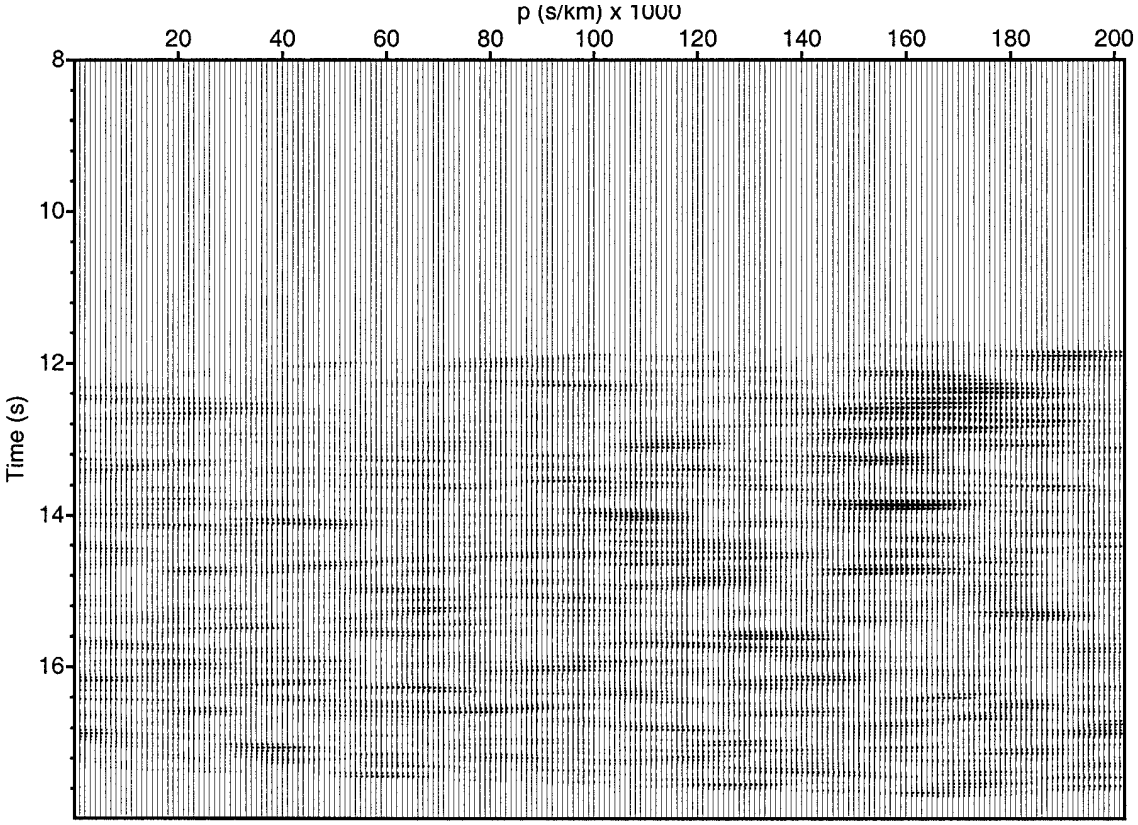
p (s/km) x 1000
20
40
60
80
100
120
140
160
180
200
8
10
12
14
16
Time (s)

(b)

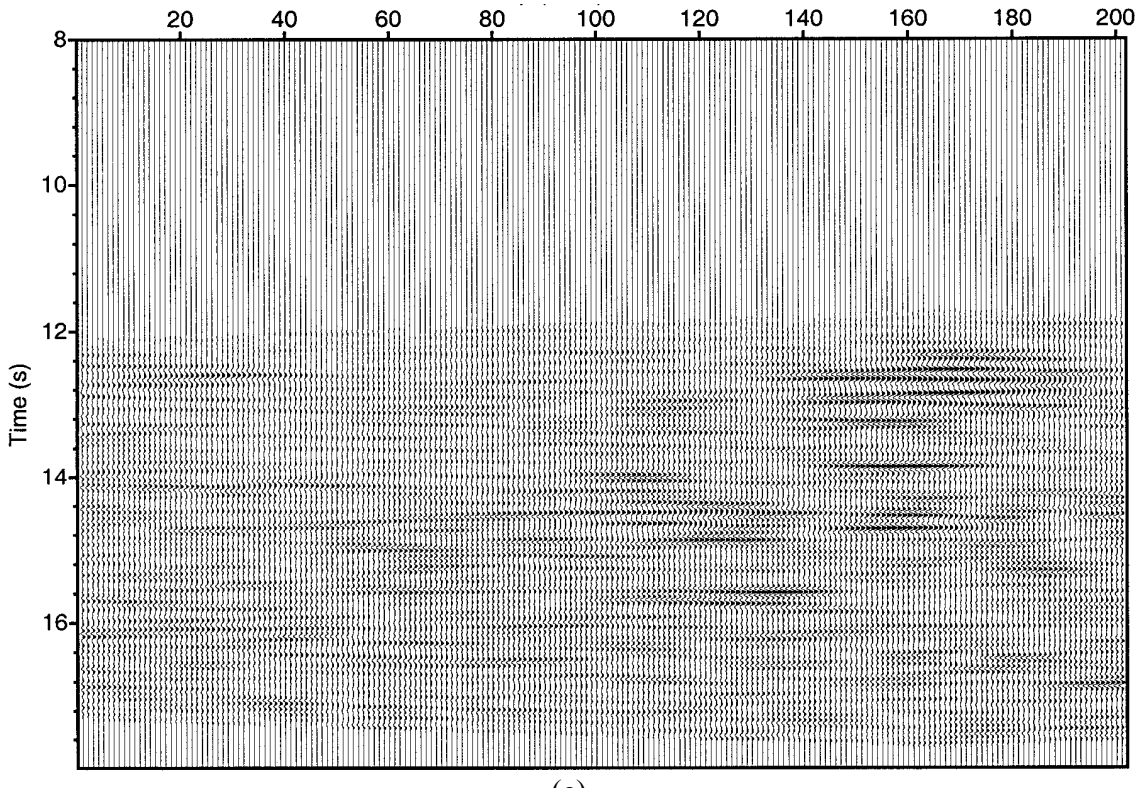
20
40
60
80
100
120
140
160
180
200
8
10
12
14
16
Time (s)

(c)

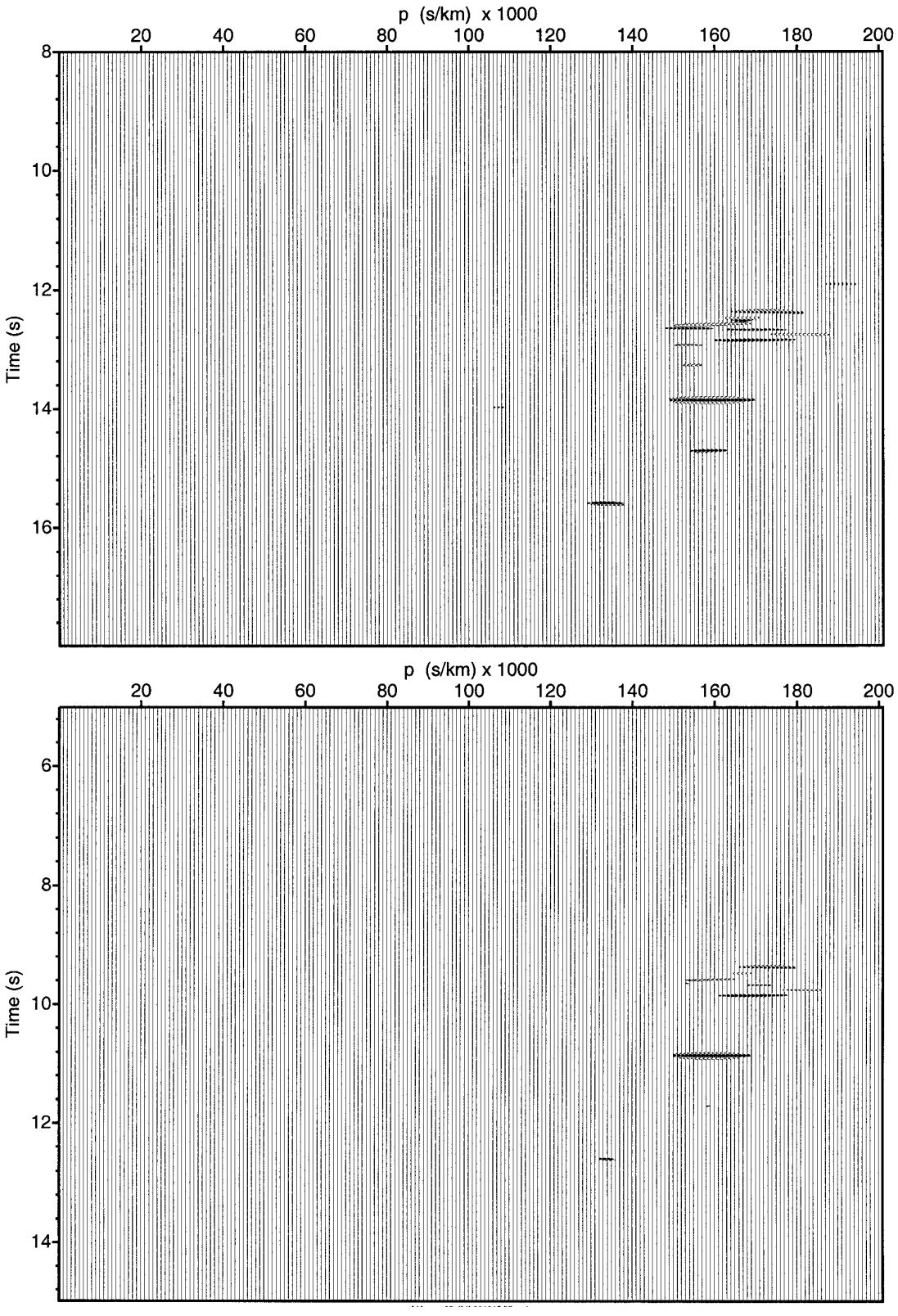
p (s/km) x 1000
20
40
60
80
100
120
140
160
180
200
Time (s)
8
10
12
14
16
p (s/km) x 1000
20
40
60
80
100
120
140
160
180
200
Time (s)
6
8
10
12
14

(d2)

Figure 3.7: Hitchcock blast #5: (a) Static corrected shot gather. Distance range: 78.9-84.6 km. The gather was high-cut filtered using a linear ramp from 10-15 Hz. The horizontal axis represents the distance in km from the shot while the vertical axis represents the reduced time. Static corrections were carried out after using a reduction velocity of 6.0 km/s to flatten the target event. (b) semblance of the slant stack, (c) slant stack, and (d) the coherency filtered slant stack used for migration. The semblance shows a low signal to noise ratio which is reflected in the coherency filtered slant stack (d) in which only a few events appear. Threshold used for migration: 0.7.

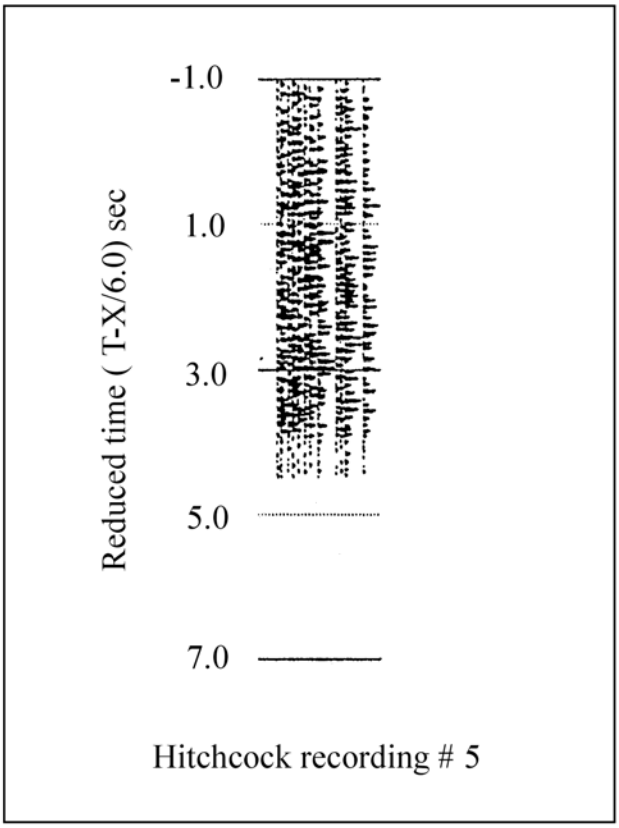

(Figure 3.7a)

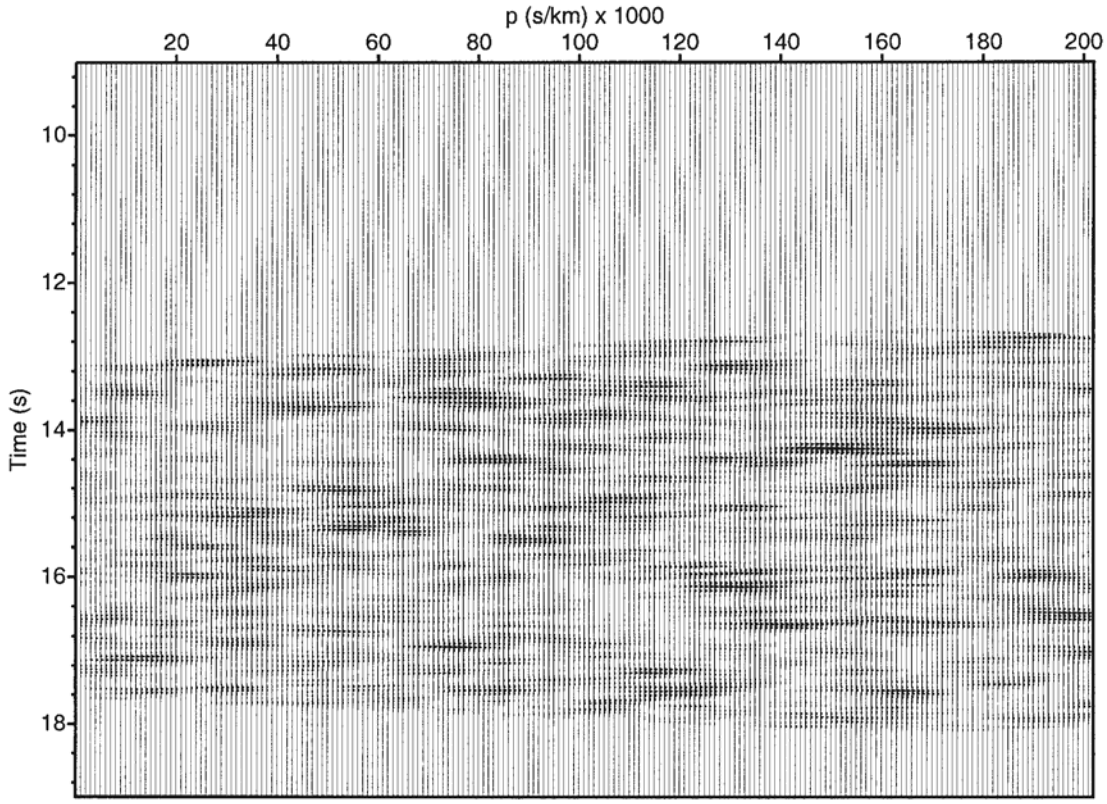
p (s/km) x 1000
20
40
60
80
100
120
140
160
180
200
Time (s)
10
12
14
16
18

(b)

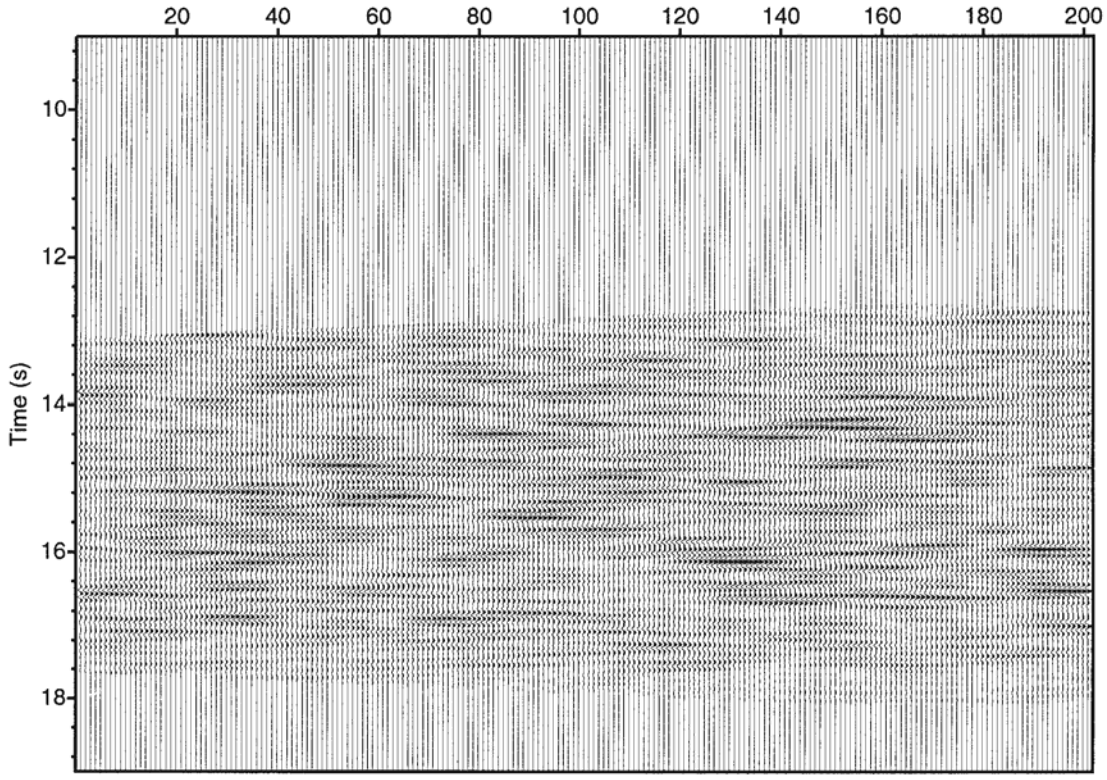
20
40
60
80
100
120
140
160
180
200
Time (s)
10
12
14
16
18

(c)

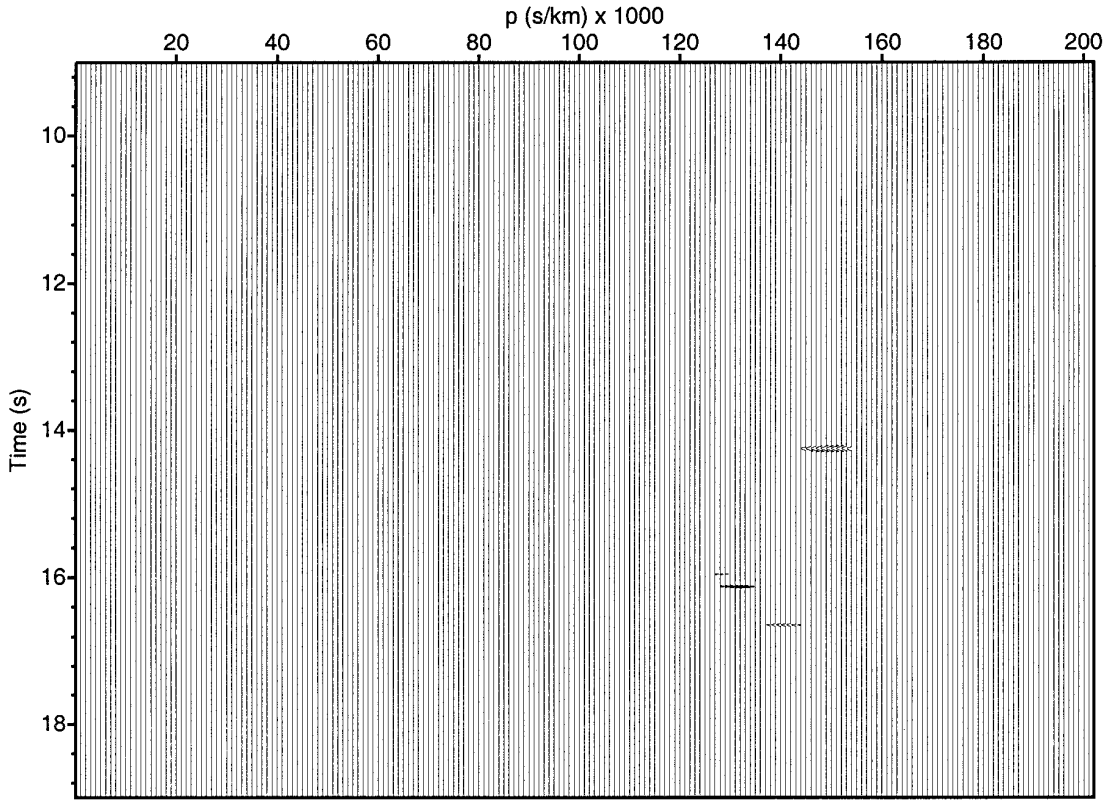
p (s/km) x 1000
20
40
60
80
100
120
140
160
180
200
Time (s)
10
12
14
16
18

(d)

Figure 3.8: Hitchcock blast #6: (a) Static corrected shot gather. Distance range: 48.3-55.3 km. The gather was high-cut filtered using a linear ramp from 10-15 Hz. The horizontal axis represents the distance in km from the shot while the vertical axis represents the reduced time. Static corrections were carried out after using a reduction velocity of 6.2 km/s to flatten the target event. (b) semblance of the slant stack, (c) slant stack, and (d) the coherency filtered slant stack used for migration. The semblance shows a well-focused direct P wave at 8 s followed by a well focused arrival at 8.6 s. The threshold value for the filtered slant stack is 0.55. In the filtered slant stack section (d) the deepest resolved event shows up at ~ 13.0 seconds. All other arrivals have ray parameters smaller than that of the direct P wave except for one that could be a converted P-Sv wave with ray parameter of about 0.19 s/km.

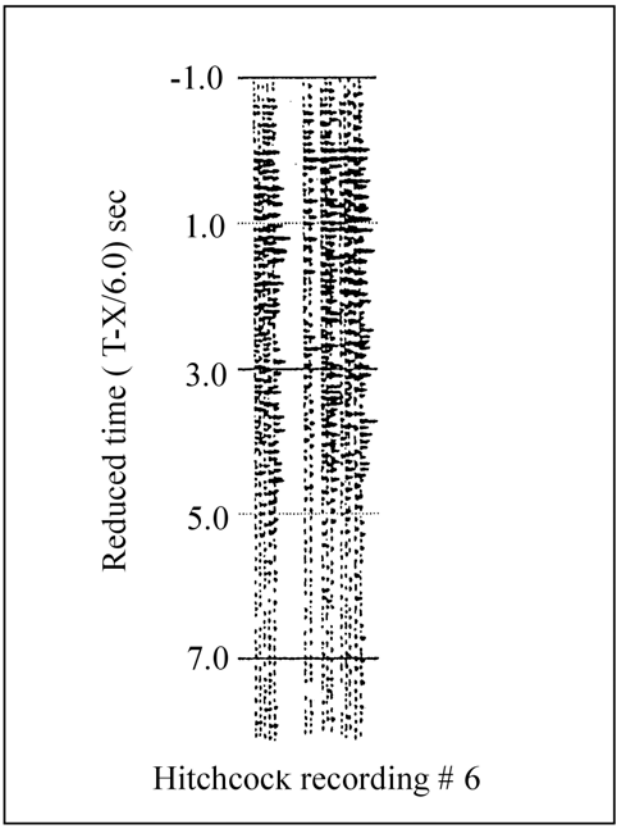

(Figure 3.8a)

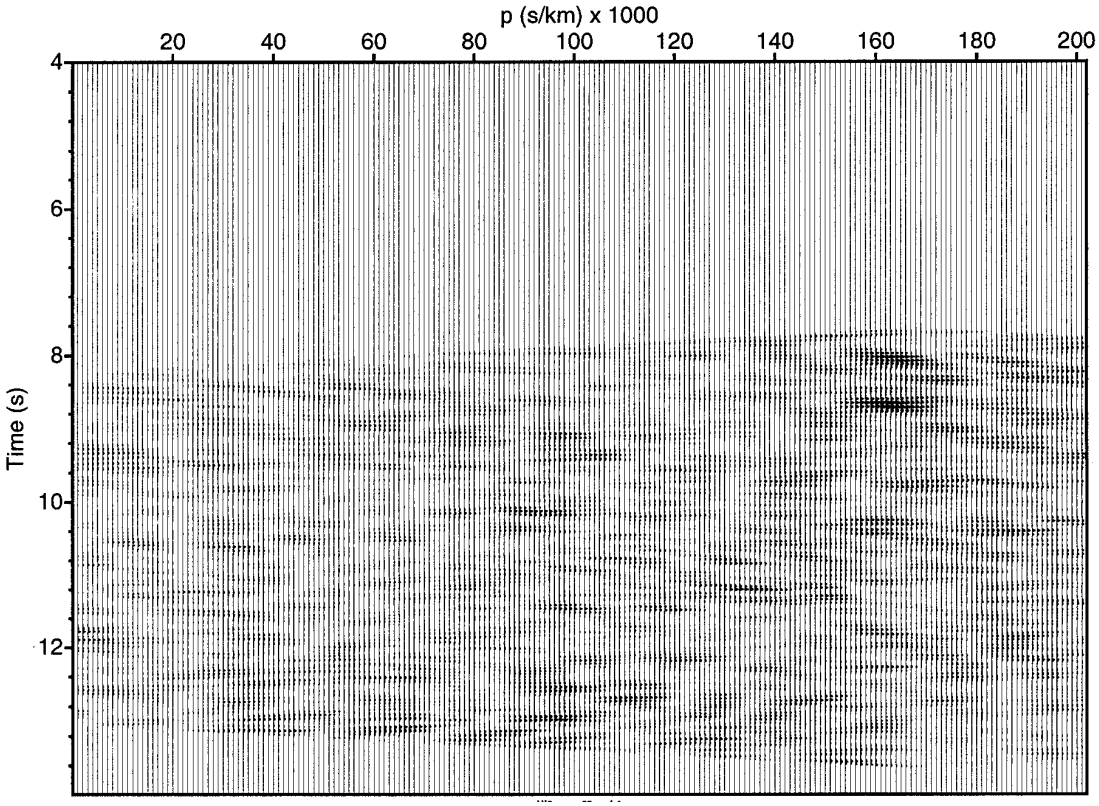
p (s/km) x 1000
20
40
60
80
100
120
140
160
180
200
4
6
8
10
12
Time (s)

(b)

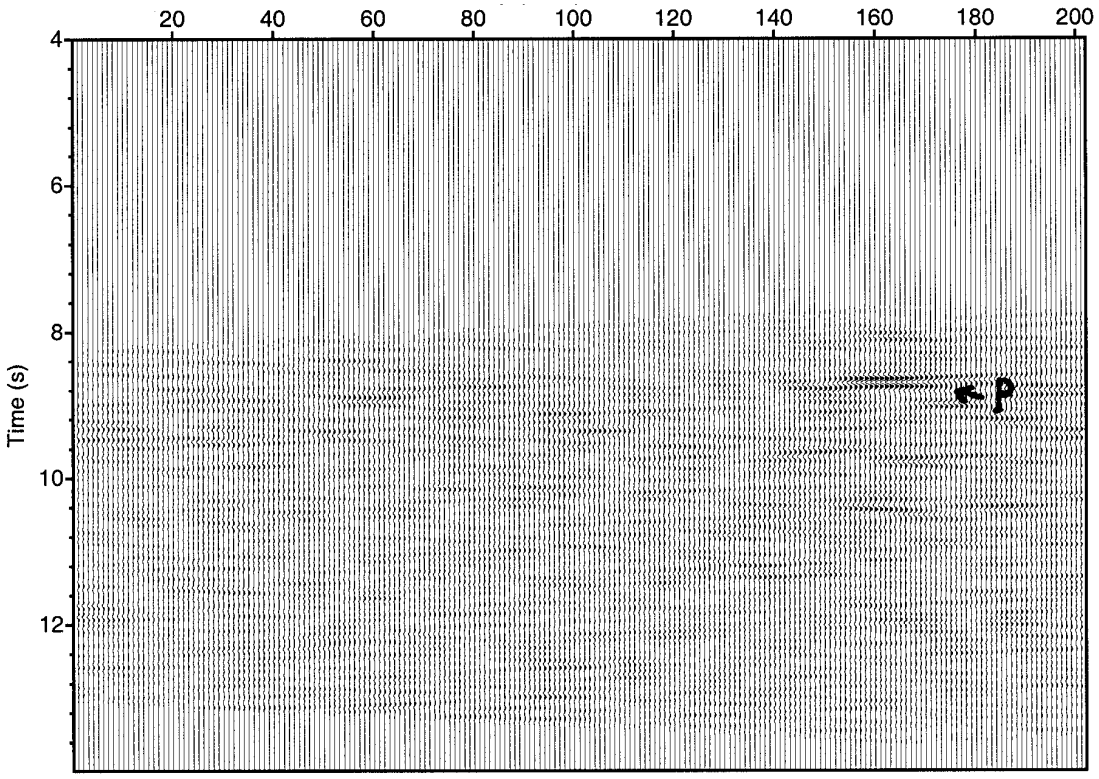
20
40
60
80
100
120
140
160
180
200
4
6
8
10
12
Time (s)
P

(c)

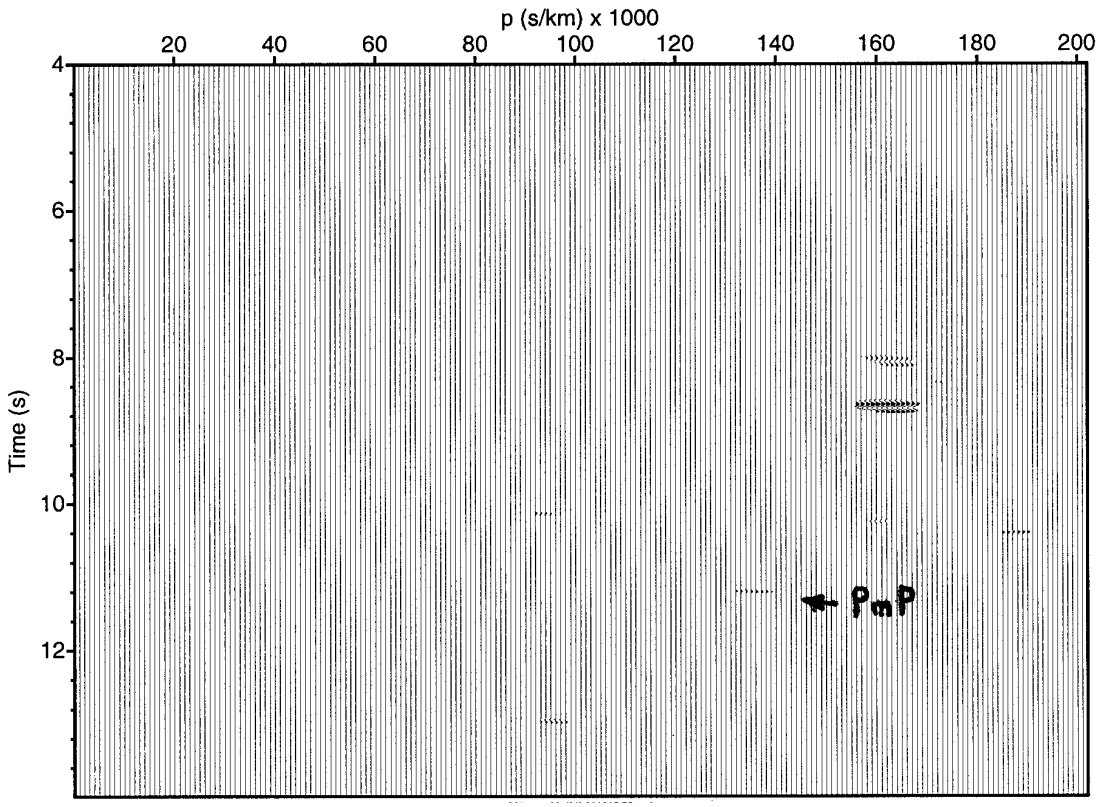
p (s/km) x 1000
20
40
60
80
100
120
140
160
180
200
Time (s)
4
6
8
10
12
PmP

(d)

Figure 3.9: Hitchcock blast #8, part A. (a) Static corrected shot gather. Distance range: 53.2-55.2 km. The gather was high-cut filtered using a linear ramp from 10-15 Hz. The horizontal axis represents the distance in km from the shot while the vertical axis represents the reduced time. Static corrections were carried out after using a reduction velocity of 6.2 km/s to flatten the target event. (b) semblance of the slant stack, (c) slant stack, and (d) the coherency filtered slant stack used for migration. The small array aperture results in poor resolution (smearing of events) in ray parameter. Although the slant stack was coherency filtered to a high threshold value of 0.7 (d) we still see events spanning the section almost without a particular pattern. The direct P wave can be recognized at about 9 seconds. The deepest event with a smaller ray parameter (0.095 s/km) appears at 14 seconds.

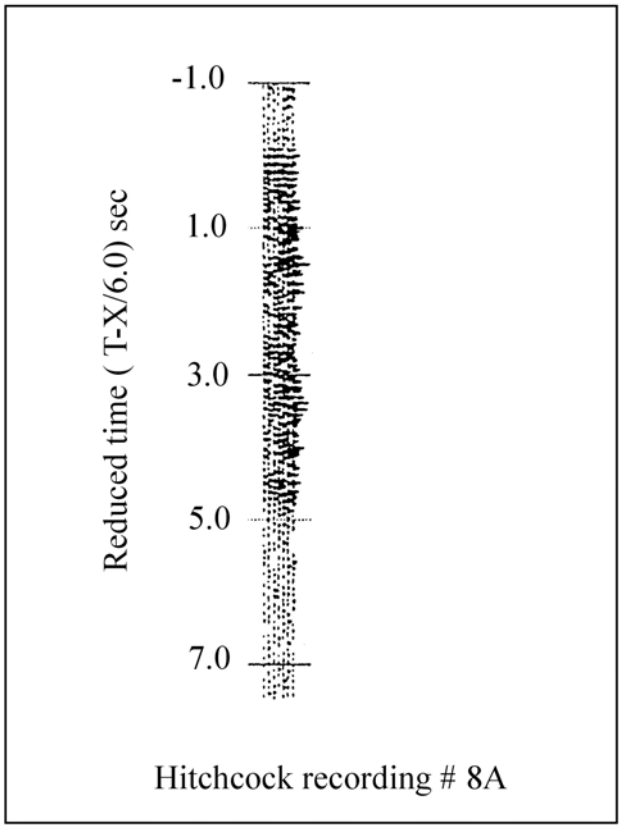

(Figure 3.9a)

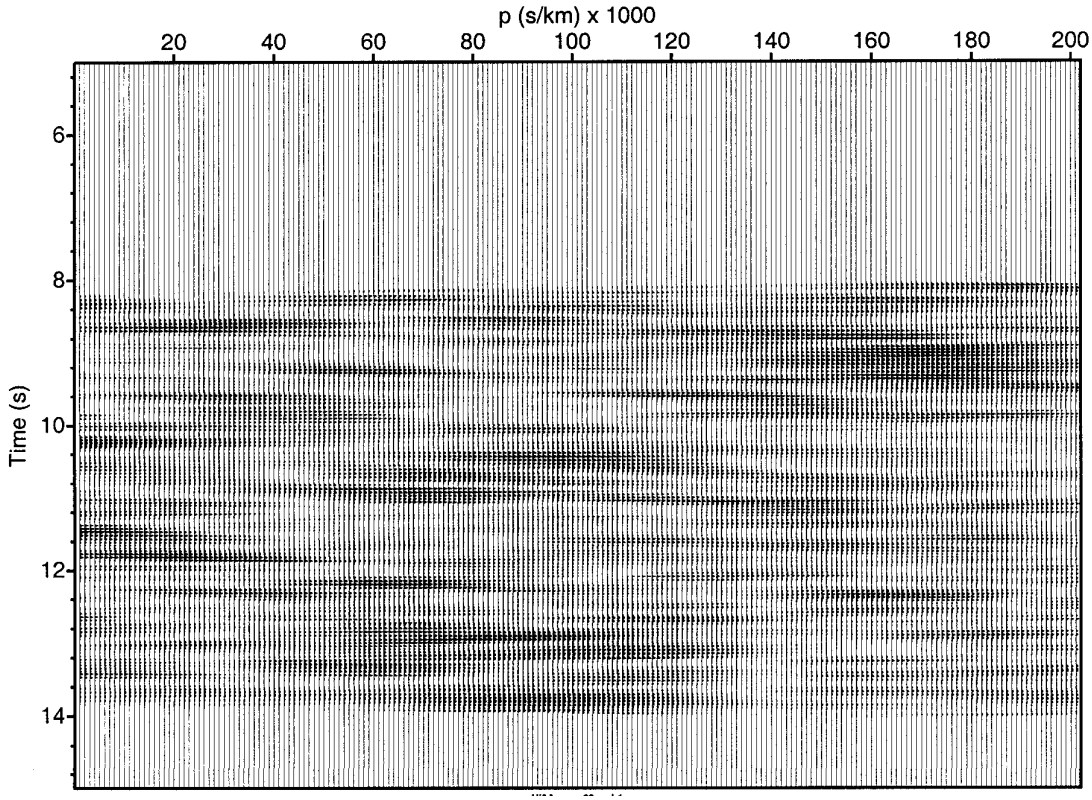
p (s/km) x 1000
20
40
60
80
100
120
140
160
180
200
Time (s)
6
8
10
12
14

(b)

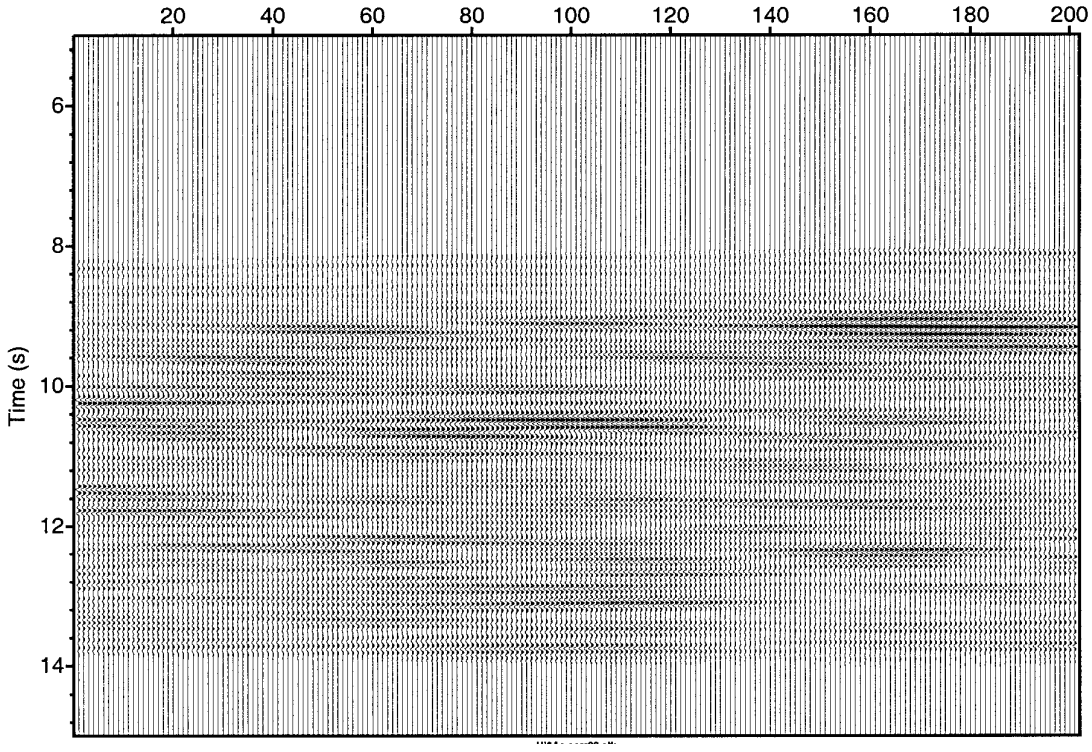
20
40
60
80
100
120
140
160
180
200
Time (s)
6
8
10
12
14

(c)

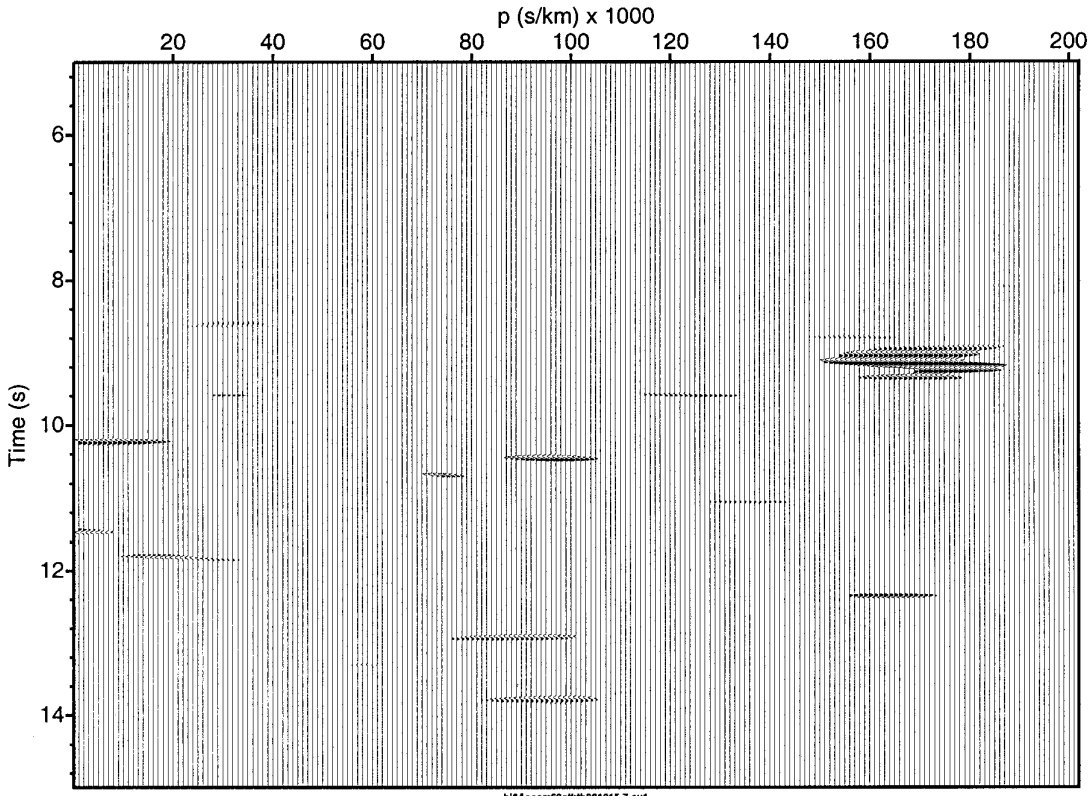

(d)

Figure 3.10: Hitchcock blast #8, part B: (a) Static corrected shot gather. Distance range: 56.9-59.7 km. The gather was high-cut filtered using a linear ramp from 10-15 Hz. The horizontal axis represents the distance in km from the shot while the vertical axis represents the reduced time. Static corrections were carried out after using a reduction velocity of 6.3 km/s to flatten the target event. (b) semblance of the slant stack, (c) slant stack, and (d) the coherency filtered slant stack used for migration. In contrast with part A of this array, both semblance and slant stack sections show a focused direct P wave followed by a series well-focused events with smaller ray parameter. The coherency filtered slant stack (d) shows the events that were migrated excluding the direct P wave. Threshold value used was 0.6.

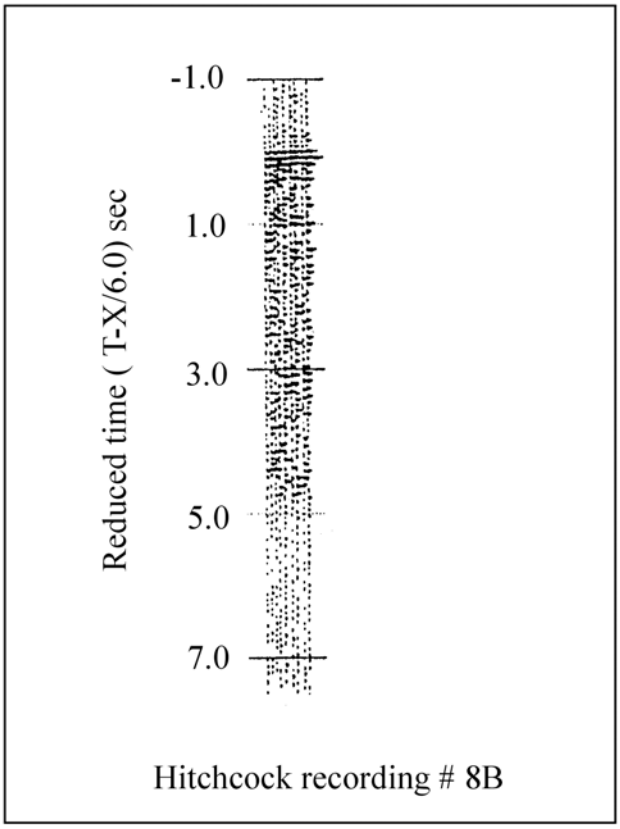

(Figure 3.10a)

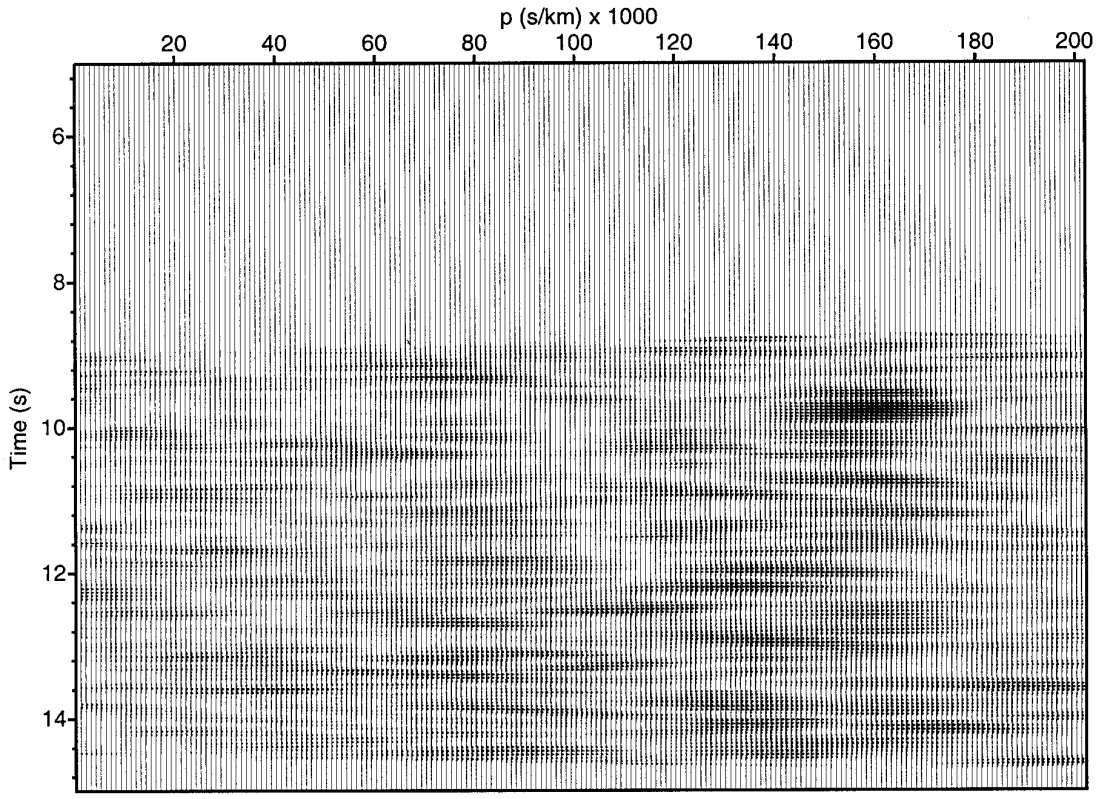
p (s/km) x 1000
20
40
60
80
100
120
140
160
180
200
Time (s)
6
8
10
12
14

(b)

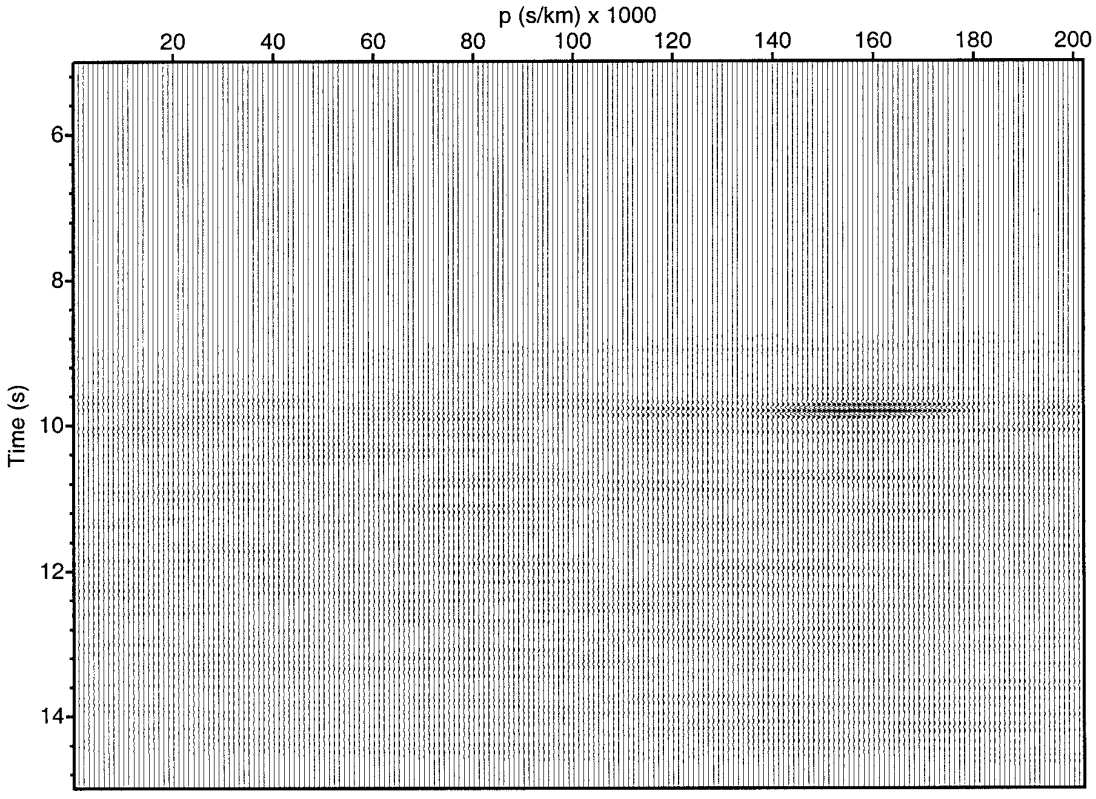
p (s/km) x 1000
20
40
60
80
100
120
140
160
180
200
Time (s)
6
8
10
12
14

(c)

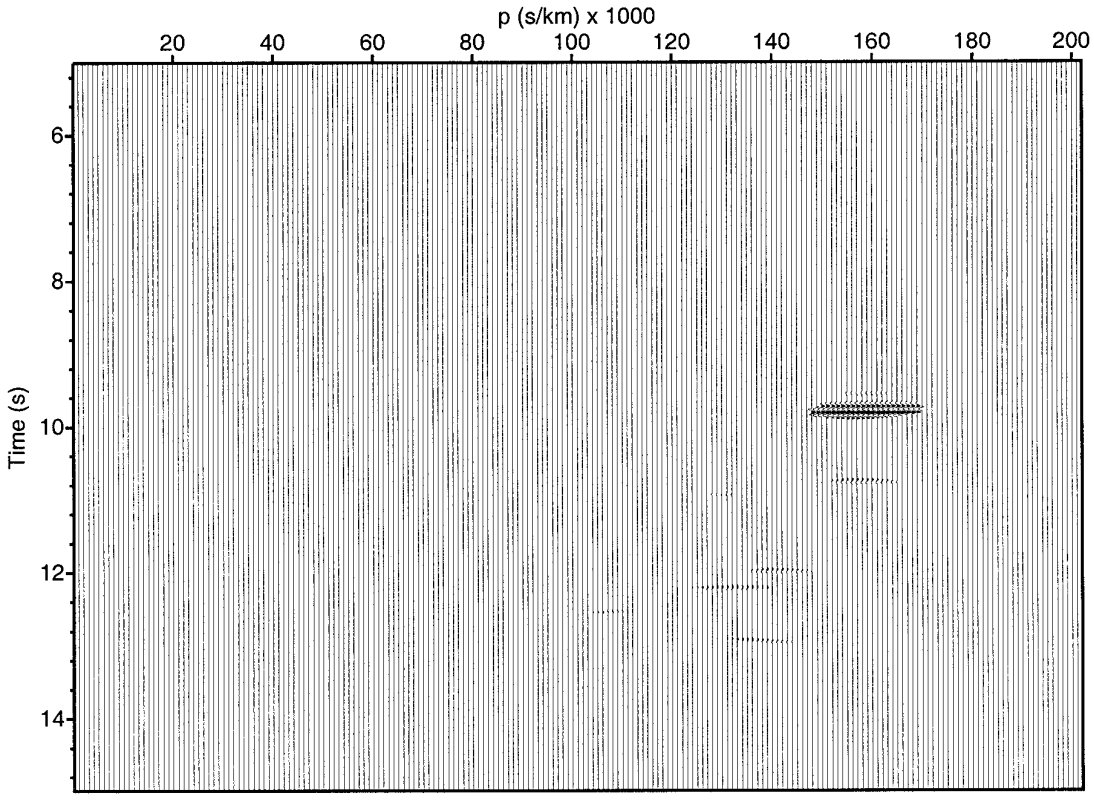

(d)

Figure 3.11: Hitchcock blast #9: (a) Static corrected shot gather. Distance range: 129.4-138.7 km. The gather was high-cut filtered using a linear ramp from 10-15 Hz. The horizontal axis represents the distance in km from the shot while the vertical axis represents the reduced time. Static corrections were carried out after using a reduction velocity of 8.1 km/s to flatten the target event. (b) semblance of the slant stack, (c) slant stack, and (d1,d2) the coherency filtered slant stacks used for migration. This is the longest array in this group of recordings (9.5 km). Two threshold values of 0.5 and 0.8 to produce the filtered slant stack sections that were migrated. PmP denotes event interpreted as a reflection from Moho.

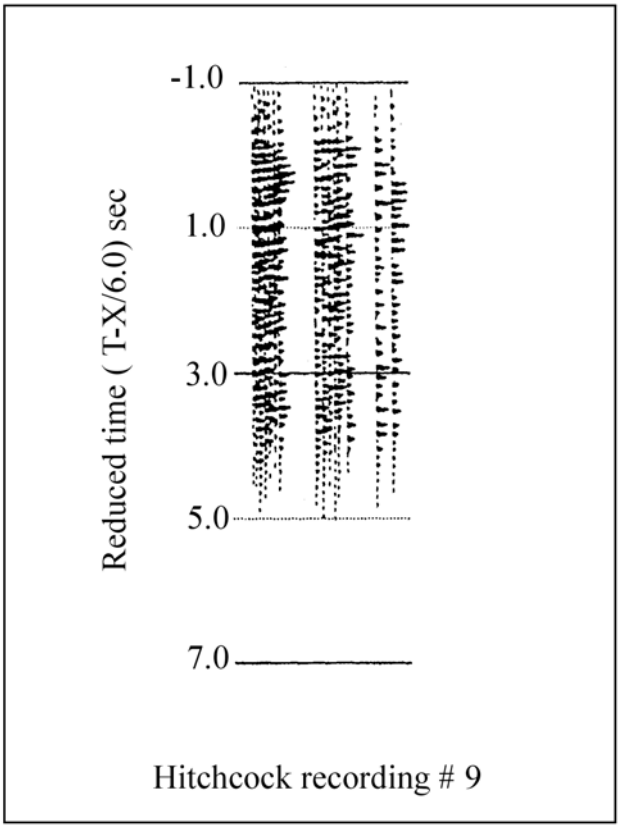

(Figure 3.11a)

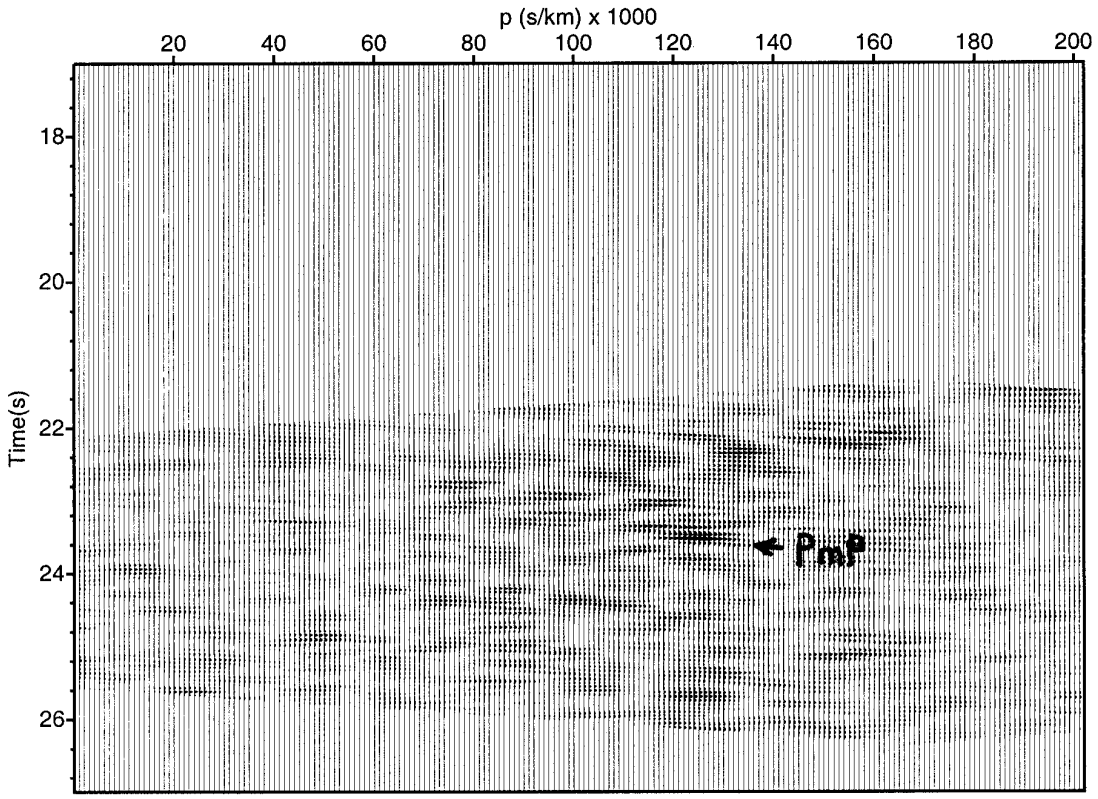
p (s/km) x 1000
20
40
60
80
100
120
140
160
180
200
18
20
22
24
26
Time(s)
PmP

(b)

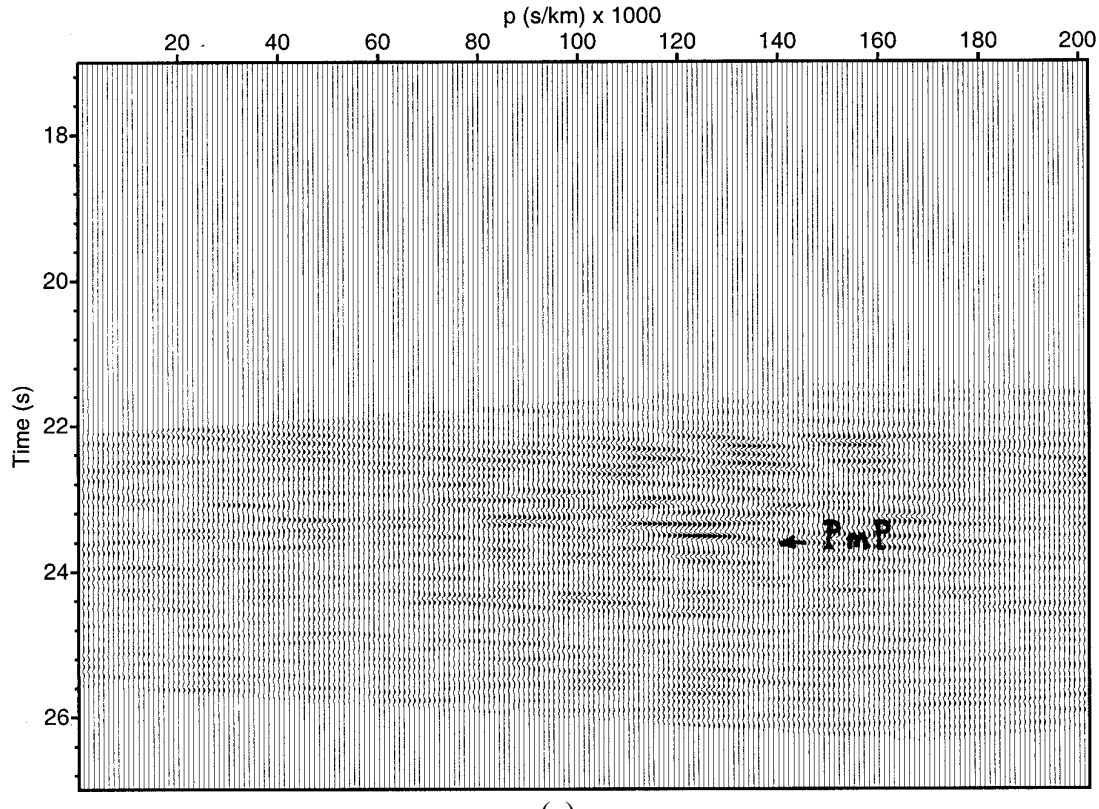
p (s/km) x 1000
20
40
60
80
100
120
140
160
180
200
18
20
22
24
26
Time (s)
PmP

(c)

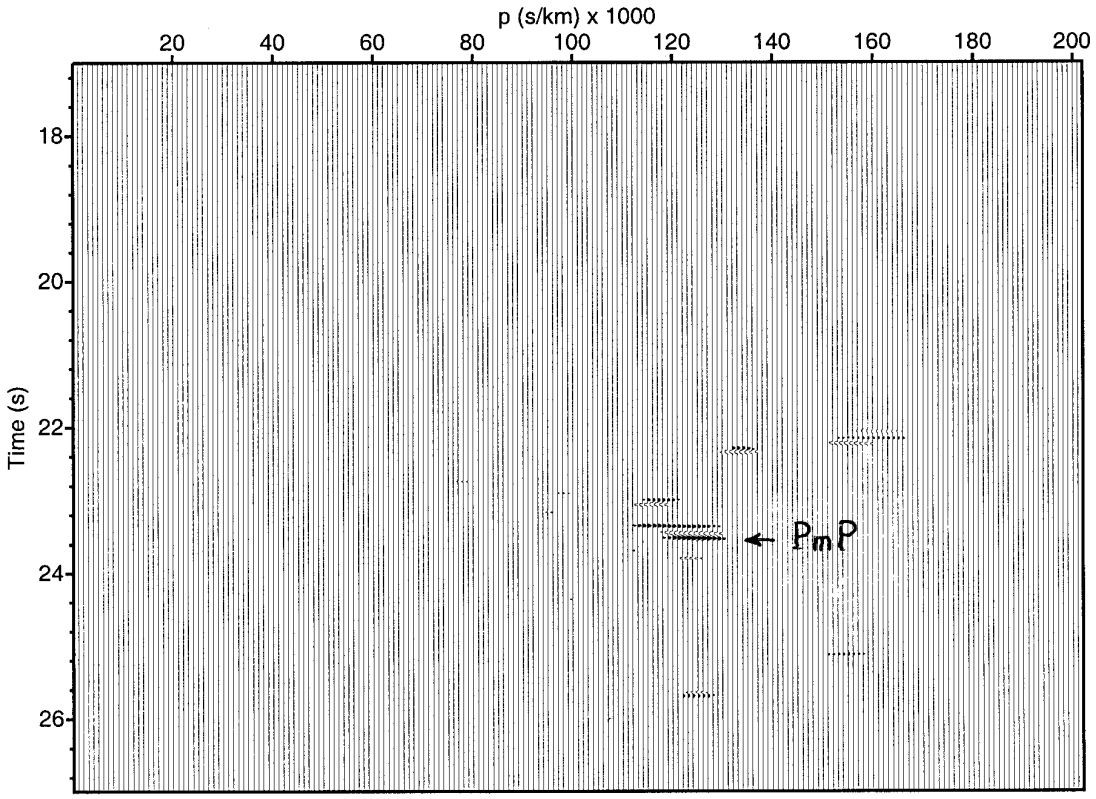
p (s/km) x 1000
20
40
60
80
100
120
140
160
180
200
Time (s)
18
20
22
24
26
PmP

(d1)

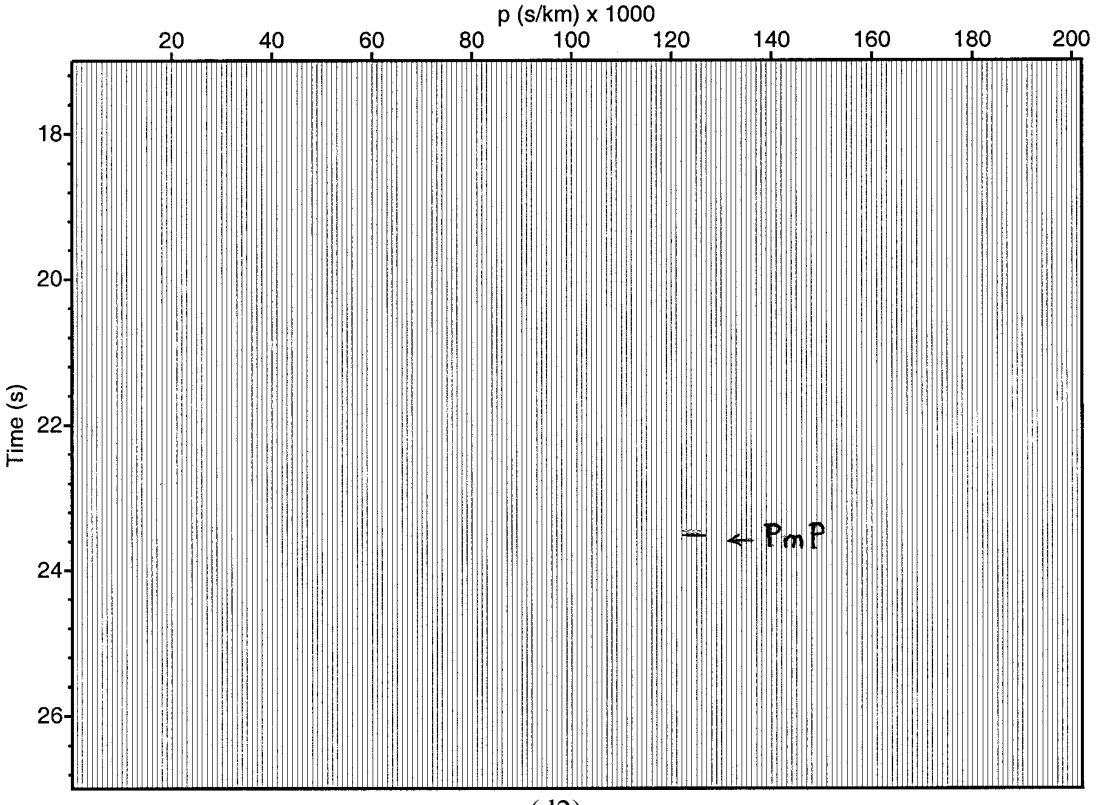
p (s/km) x 1000
20
40
60
80
100
120
140
160
180
200
Time (s)
18
20
22
24
26
PmP

(d2)

Figure 3.12: Hitchcock blast #10: (a) Static corrected shot gather. Distance range: 62.98-69.2 km. The gather was high-cut filtered using a linear ramp from 10-15 Hz. The horizontal axis represents the distance in km from the shot while the vertical axis represents the reduced time. Static corrections were carried out after using a reduction velocity of 6.3 km/s to flatten the target event. (b) semblance of the slant stack, (c) slant stack, and (d1,d2) the coherency filtered slant stacks used for migration. The semblance of this gather shows the direct P wave at 10.8 seconds followed by several events with ray parameters from 0.167 to 0.085 s/km in the time window 10.8-15 seconds. The threshold values used for migration were 0.5 and 0.7.

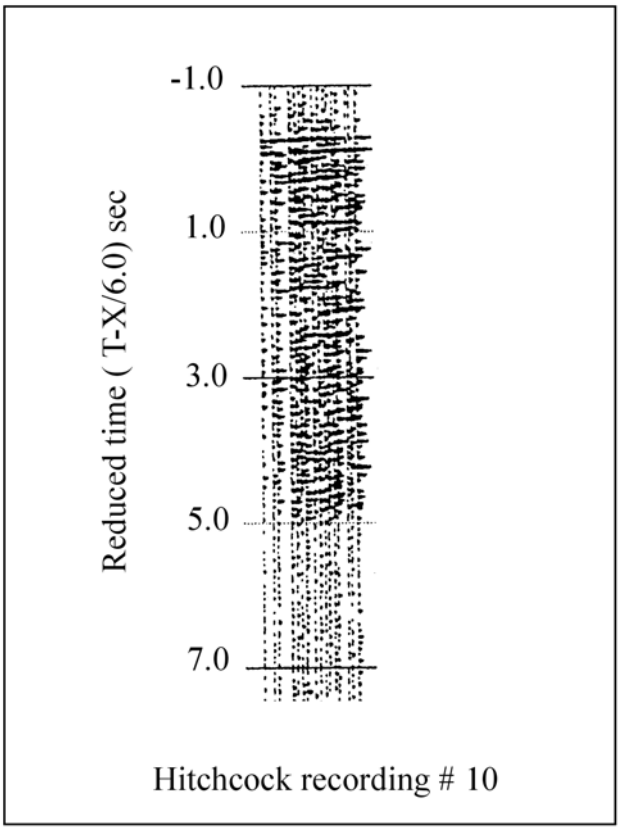

(Figure 3.12a)

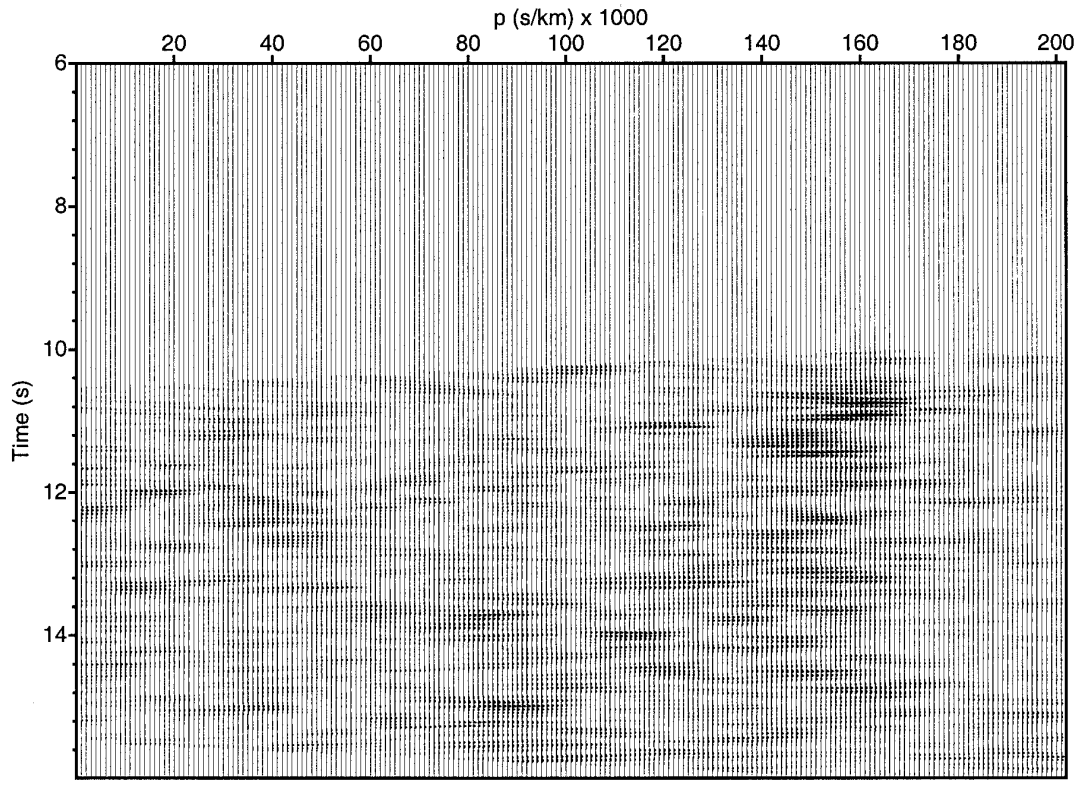
p (s/km) x 1000
20
40
60
80
100
120
140
160
180
200
6
8
10
12
14
Time (s)

(b)

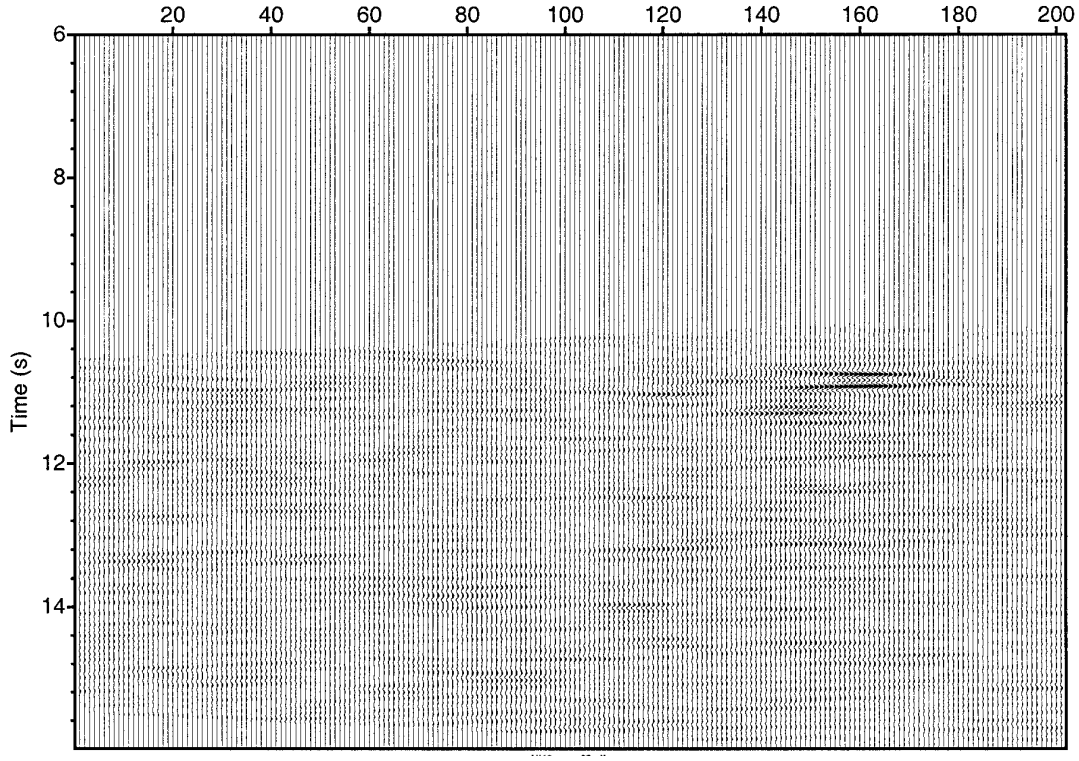
20
40
60
80
100
120
140
160
180
200
6
8
10
12
14
Time (s)

(c)

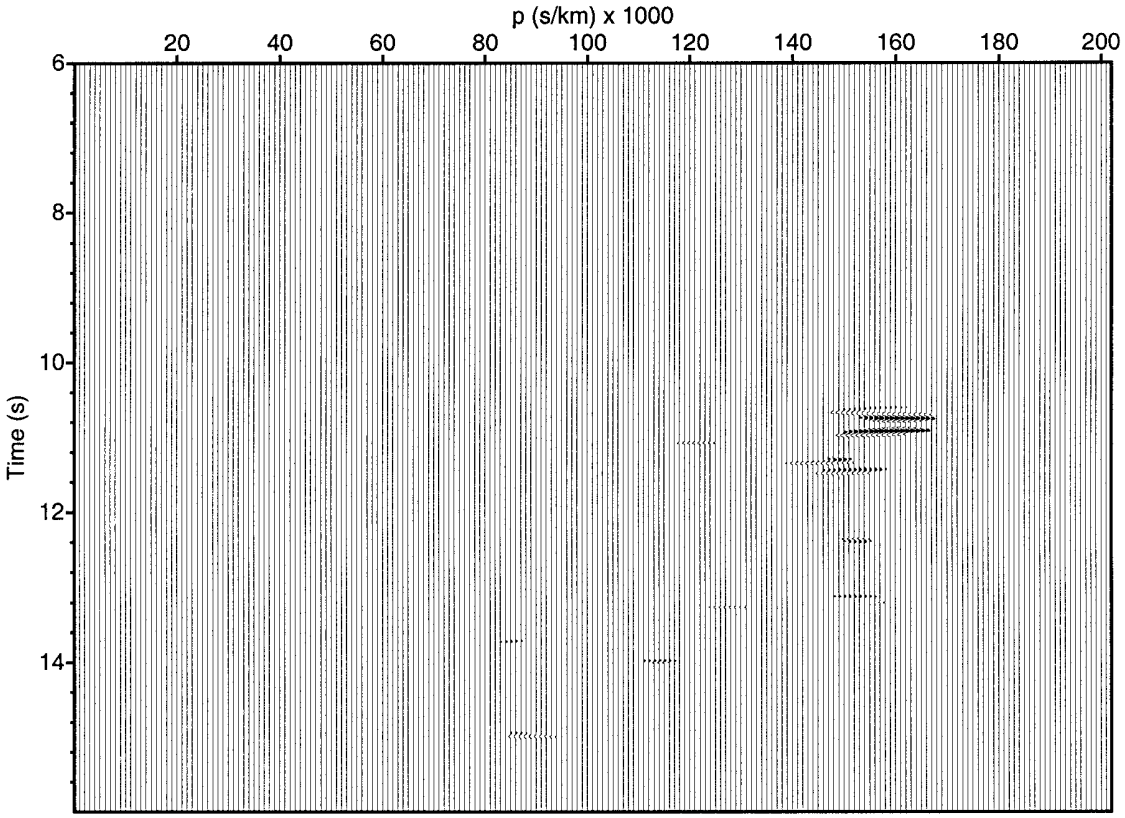
p (s/km) x 1000
20
40
60
80
100
120
140
160
180
200
6
8
10
12
14
Time (s)

(d1)

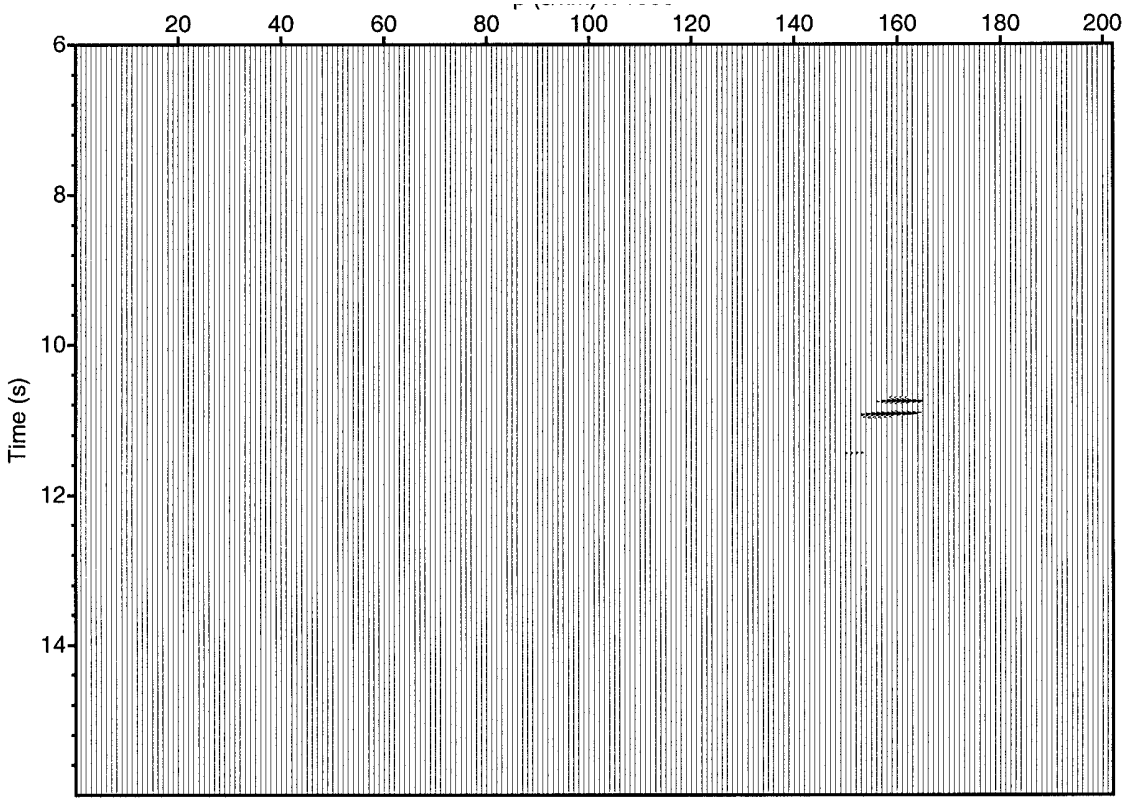
20
40
60
80
100
120
140
160
180
200
6
8
10
12
14
Time (s)

(d2)

Figure 3.13: Ruby blast #1: (a) Static corrected shot gather. Distance range 20.95 – 28.02 km. The gather was high-cut filtered using a linear ramp from 10-15 Hz. The horizontal axis represents the distance in km from the shot while the vertical axis represents the reduced time. Static corrections were carried out after using a reduction velocity of 6.1 km/s to flatten the target event. (b) semblance of the slant stack, (c) slant stack, and (d1,d2) the coherency filtered slant stacks used for migration. The coherency measure shows a strong event at about 4 s, which is interpreted as the direct P wave, followed by a strong reflection at 4.6 s with a ray parameter of 0.148 s/km. The threshold values used for migration were 0.3 and 0.4.

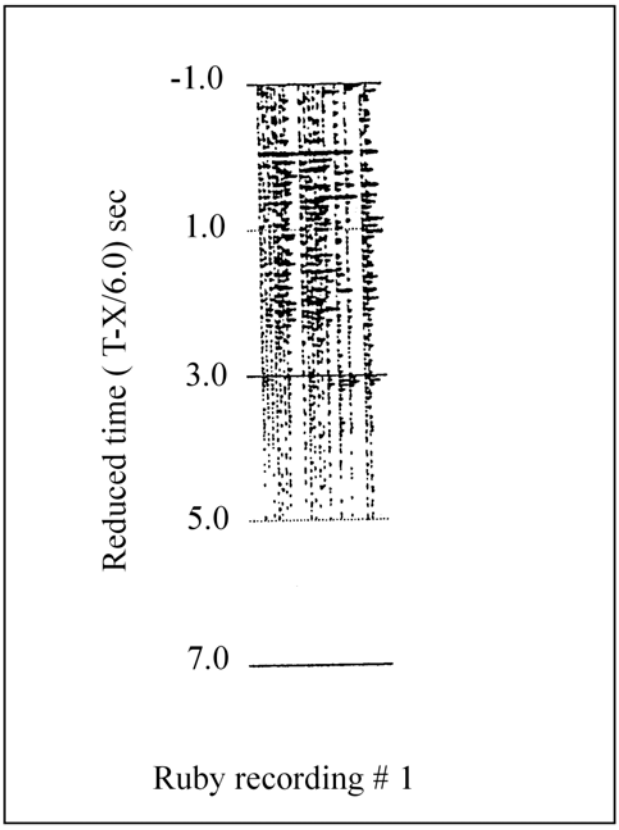

(Figure 3.13a)

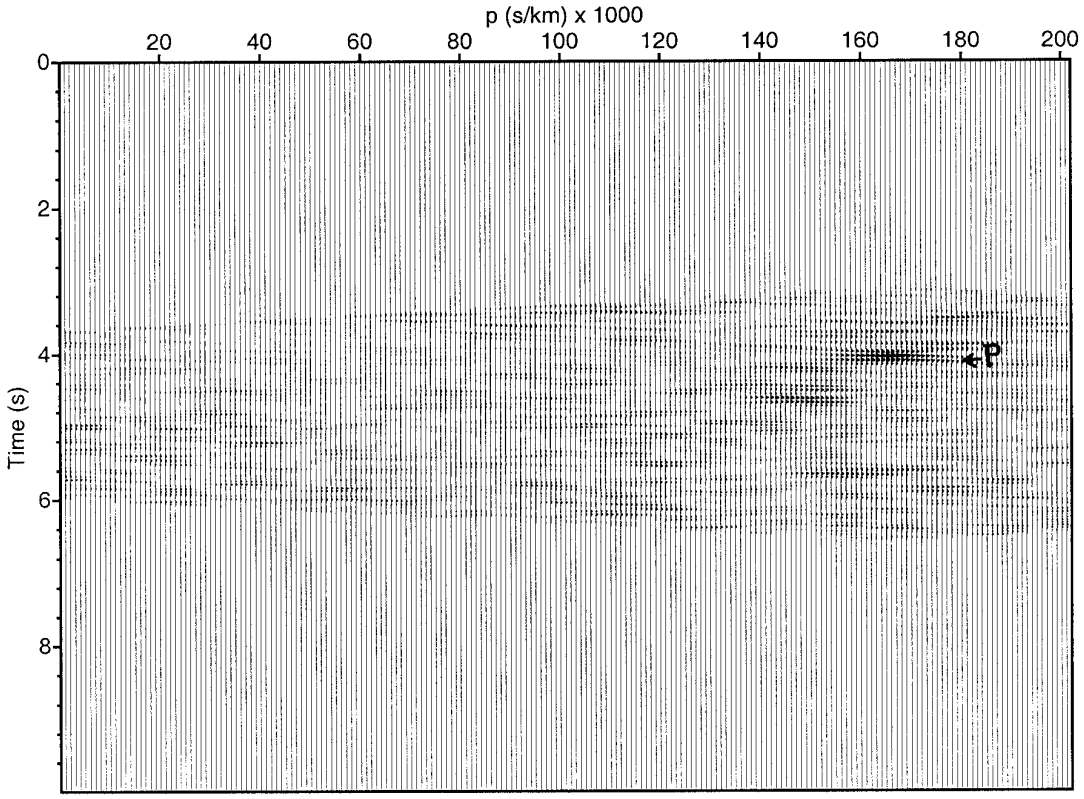
p (s/km) x 1000
20
40
60
80
100
120
140
160
180
200
0
2
4
6
8
Time (s)
P

(b)

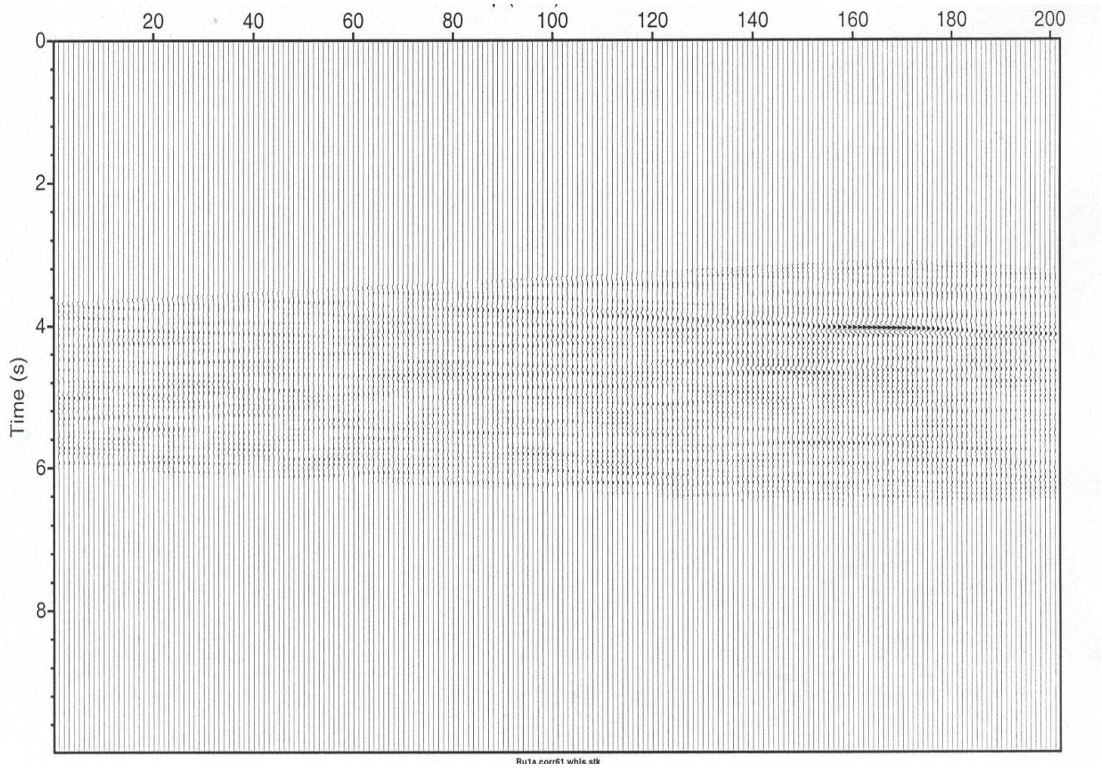
20
40
60
80
100
120
140
160
180
200
0
2
4
6
8
Time (s)

(c)

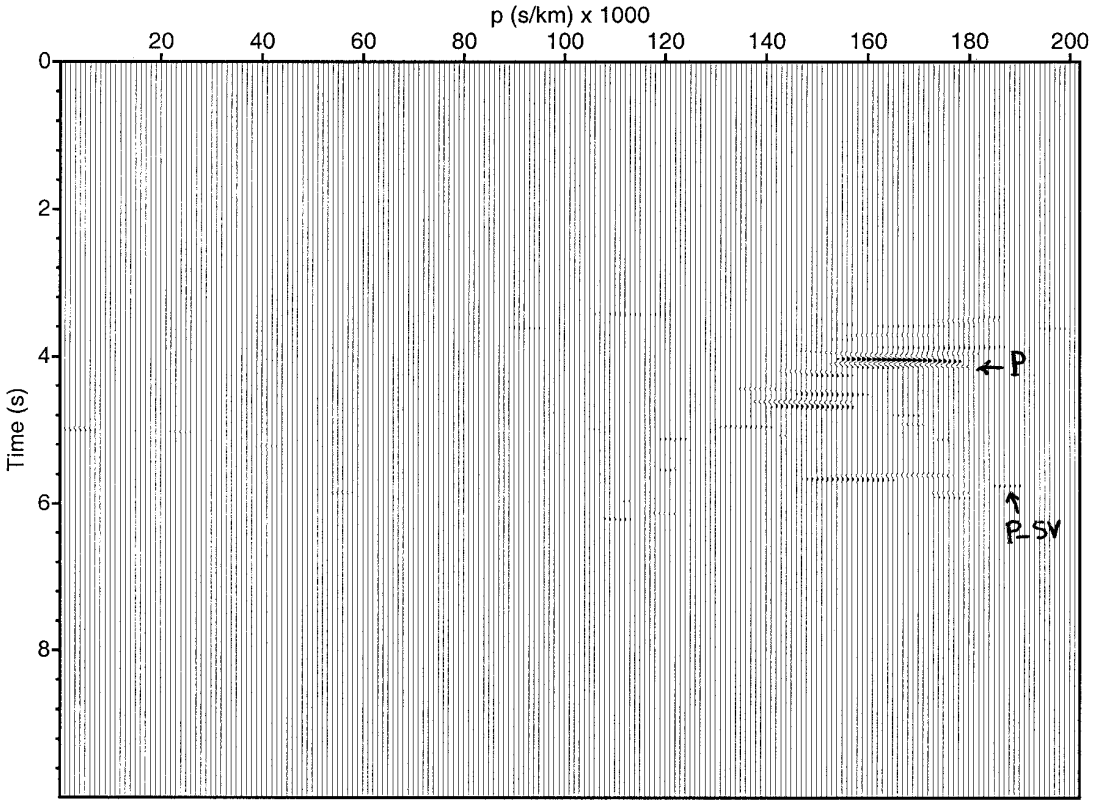
p (s/km) x 1000
20
40
60
80
100
120
140
160
180
200
0
2
4
6
8
Time (s)
P
P_SV

(d1)

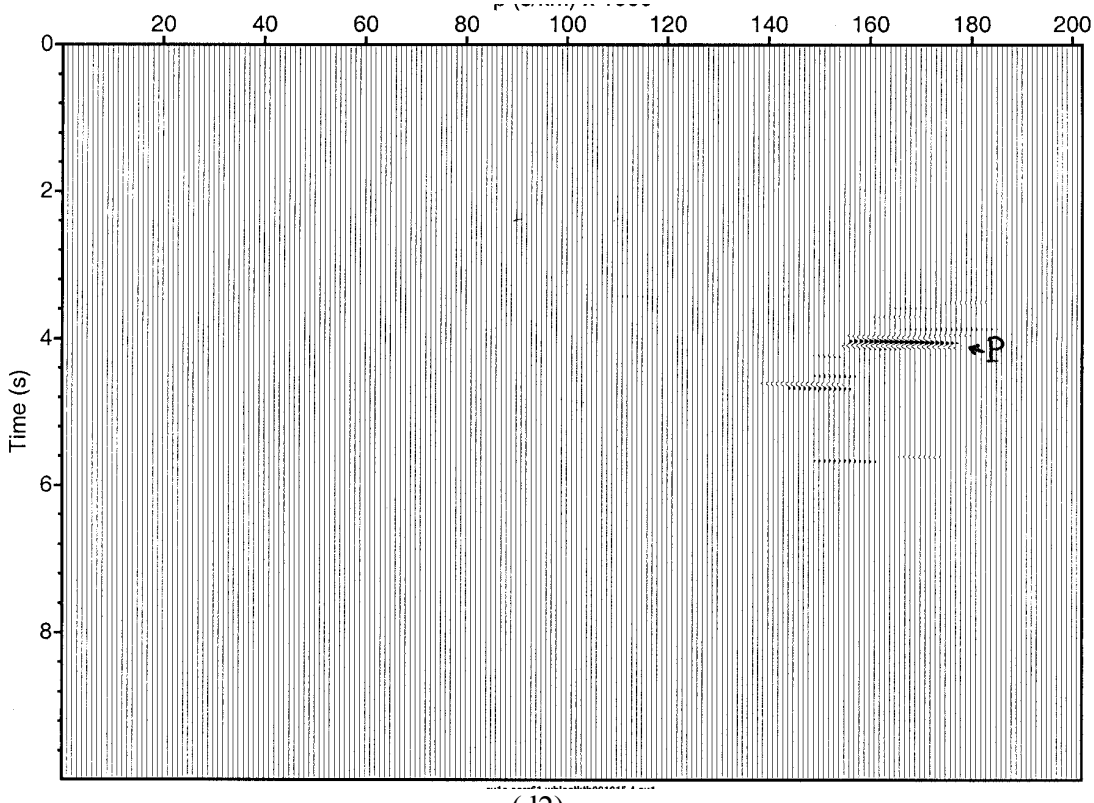
20
40
60
80
100
120
140
160
180
200
0
2
4
6
8
Time (s)
P

(d2)

Figure 3.14: Ruby blast #2, part A: (a) Static corrected shot gather. Distance range: 95.4-97.5 km. The gather was high-cut filtered using a linear ramp from 10-15 Hz. The horizontal axis represents the distance in km from the shot while the vertical axis represents the reduced time. Static corrections were carried out after using a reduction velocity of 6.2 km/s to flatten the target event. (b) semblance of the slant stack, (c) slant stack, and (d) the coherency filtered slant stack used for migration. The small array aperture produces considerable smearing (loss of resolution) in the slant stack. The direct P wave is strong and followed by reflections at smaller ray parameter. At 17-17.5 s an interesting series of events appears with a ray parameters of 0.122 and 0.145. A coherency filtered slant stack of 0.6 value was used for migration.

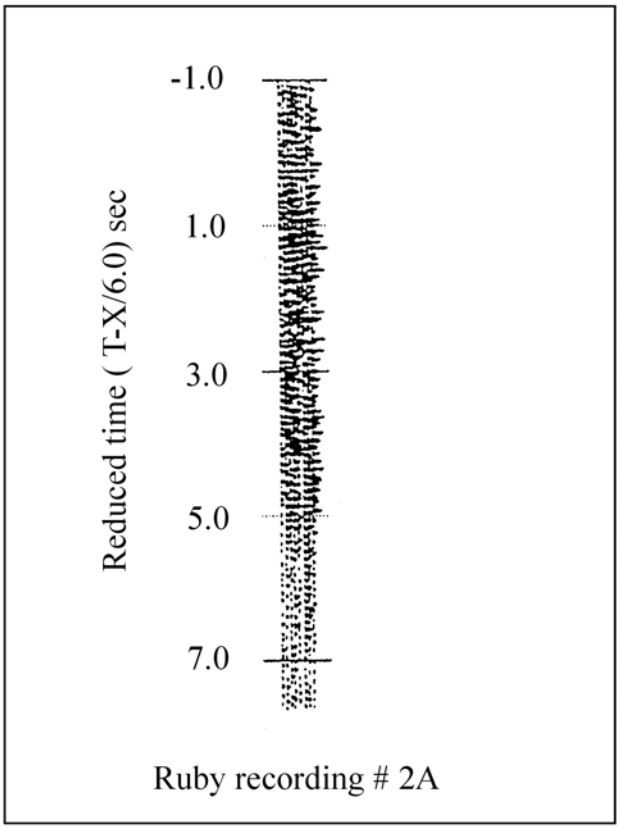

(Figure 3.14a)

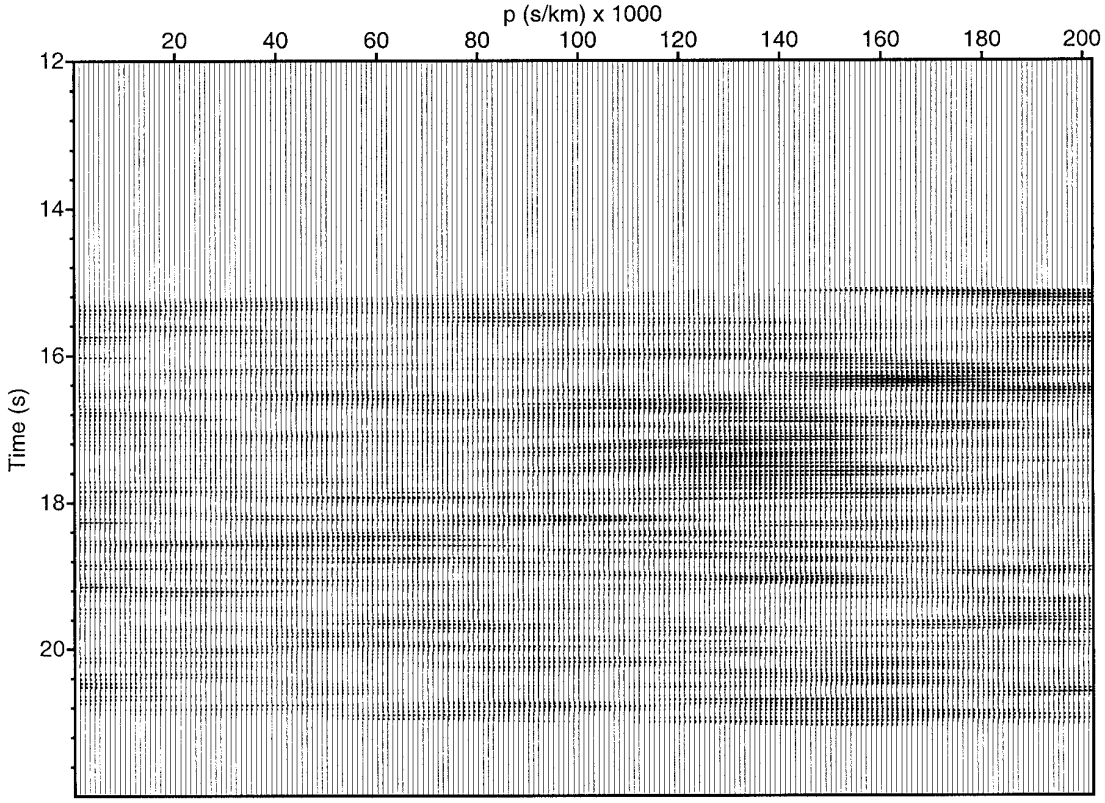
p (s/km) x 1000
20
40
60
80
100
120
140
160
180
200
12
14
16
18
20
Time (s)

(b)

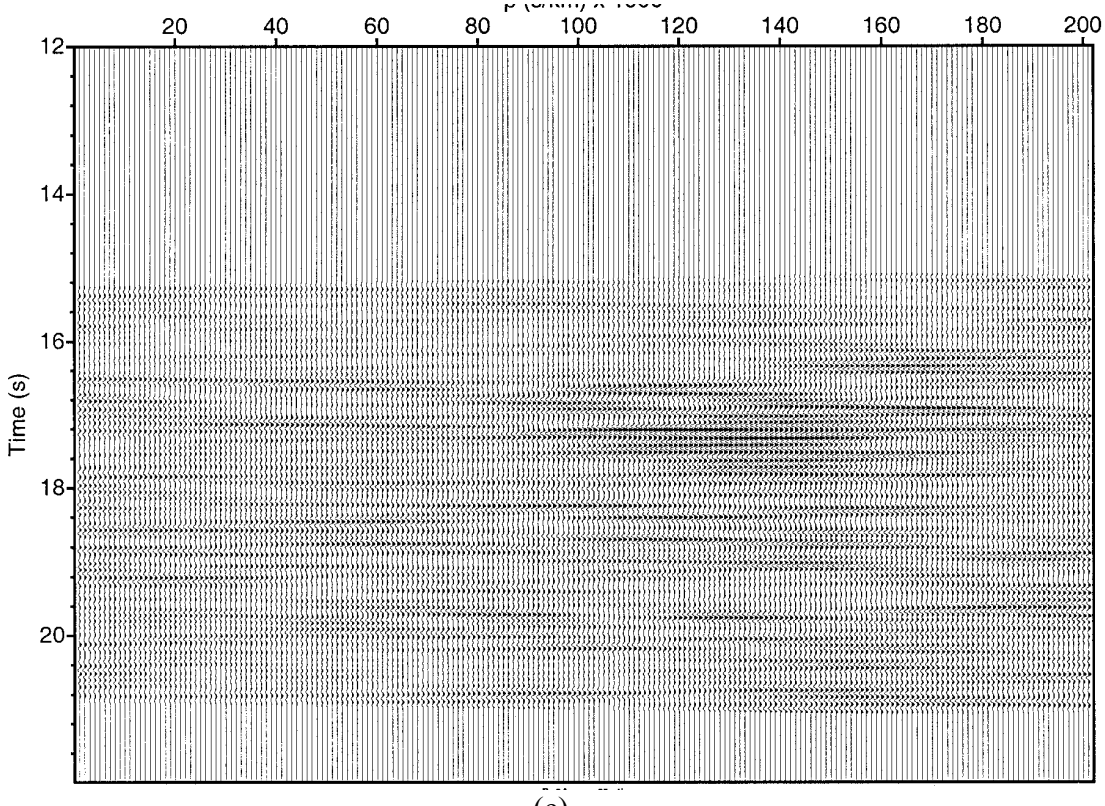
20
40
60
80
100
120
140
160
180
200
12
14
16
18
20
Time (s)

(c)

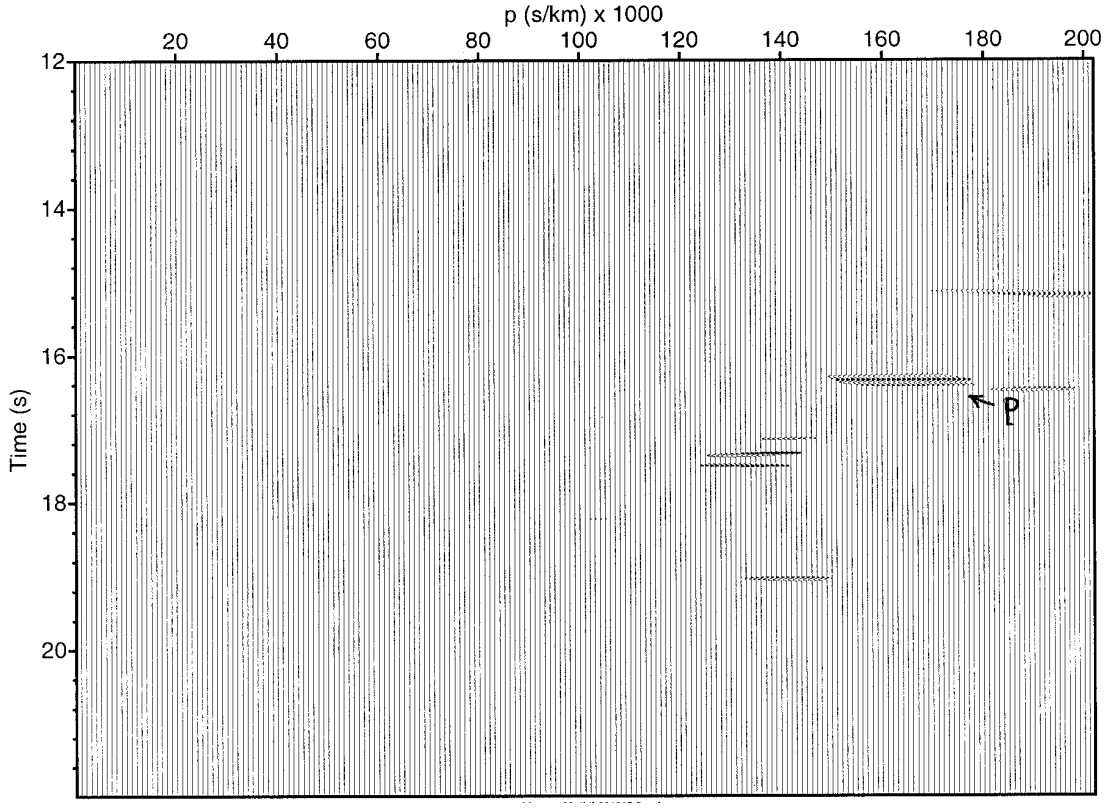
p (s/km) x 1000
20
40
60
80
100
120
140
160
180
200
12
14
16
18
20
Time (s)
P

(d)

Figure 3.15: Ruby blast #2, part B: (a) Static corrected shot gather. Distance range: 103.65-105.14 km. The gather was high-cut filtered using a linear ramp from 10-15 Hz. The horizontal axis represents the distance in km from the shot while the vertical axis represents the reduced time. Static corrections were carried out after using a reduction velocity of 7.3 km/s to flatten the target event. (b) semblance of the slant stack, (c) slant stack, and (d) the coherency filtered slant stack used for migration. The semblance and slant stack sections and consequently the coherency filtered slant stack sections show a high degree of smearing due to the small array aperture. Two sets of events can be identified; both of these sets lie in almost the same ray parameter range (0.120 – 0.150 s/km). The top set lies in time window of 17.2 – 18.6 seconds and the deep one in 20-21.6 s time window.

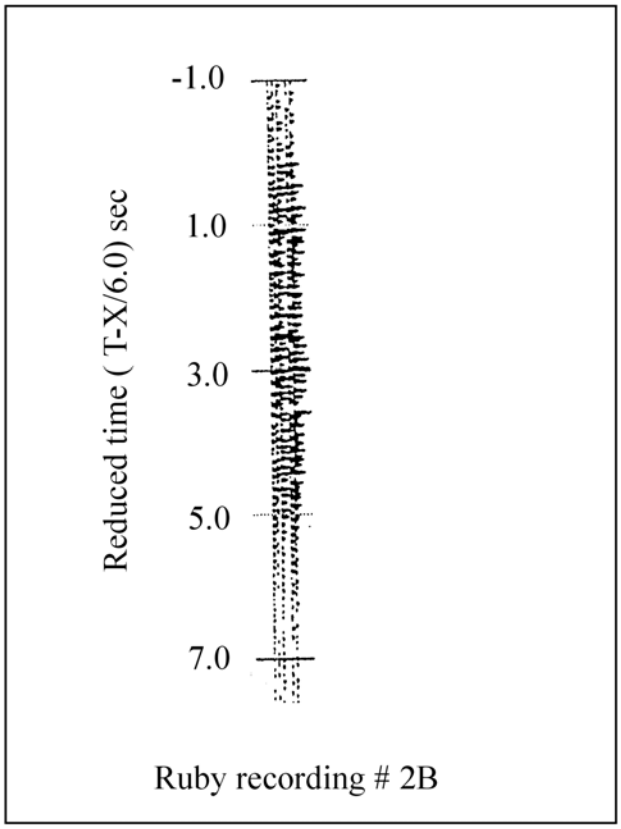

(Figure 3.15a)

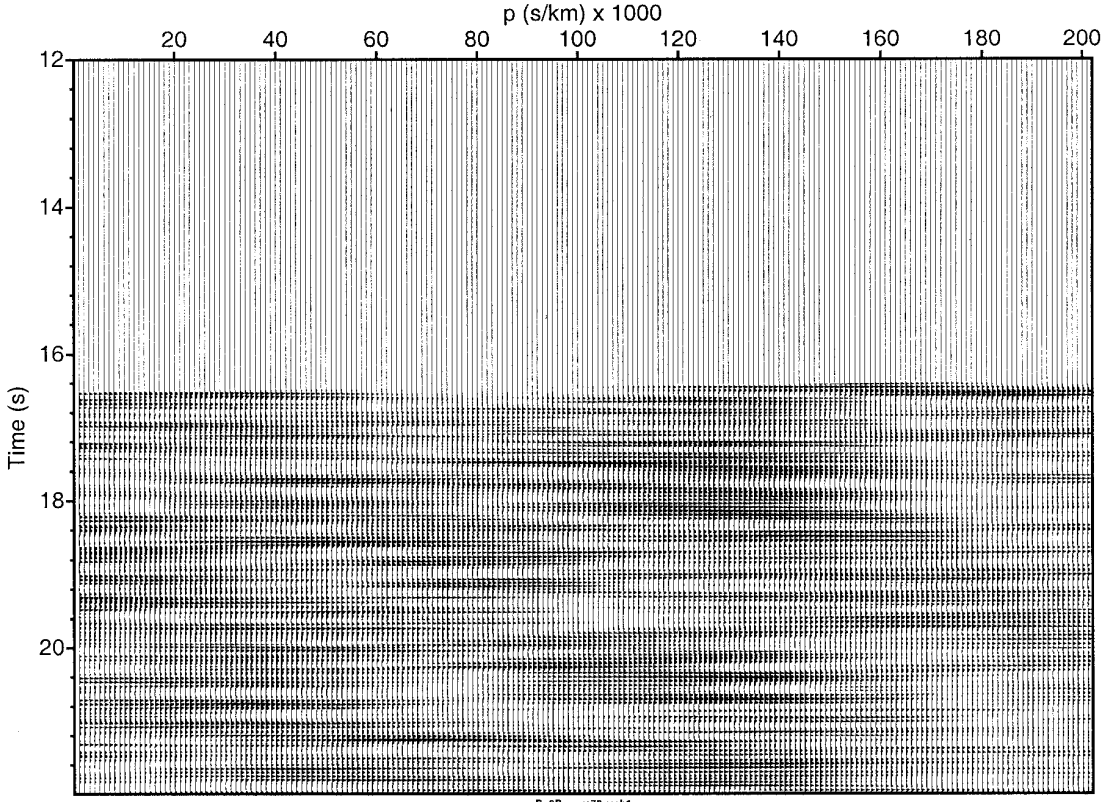
p (s/km) x 1000
20
40
60
80
100
120
140
160
180
200
12
14
16
18
20
Time (s)

(b)

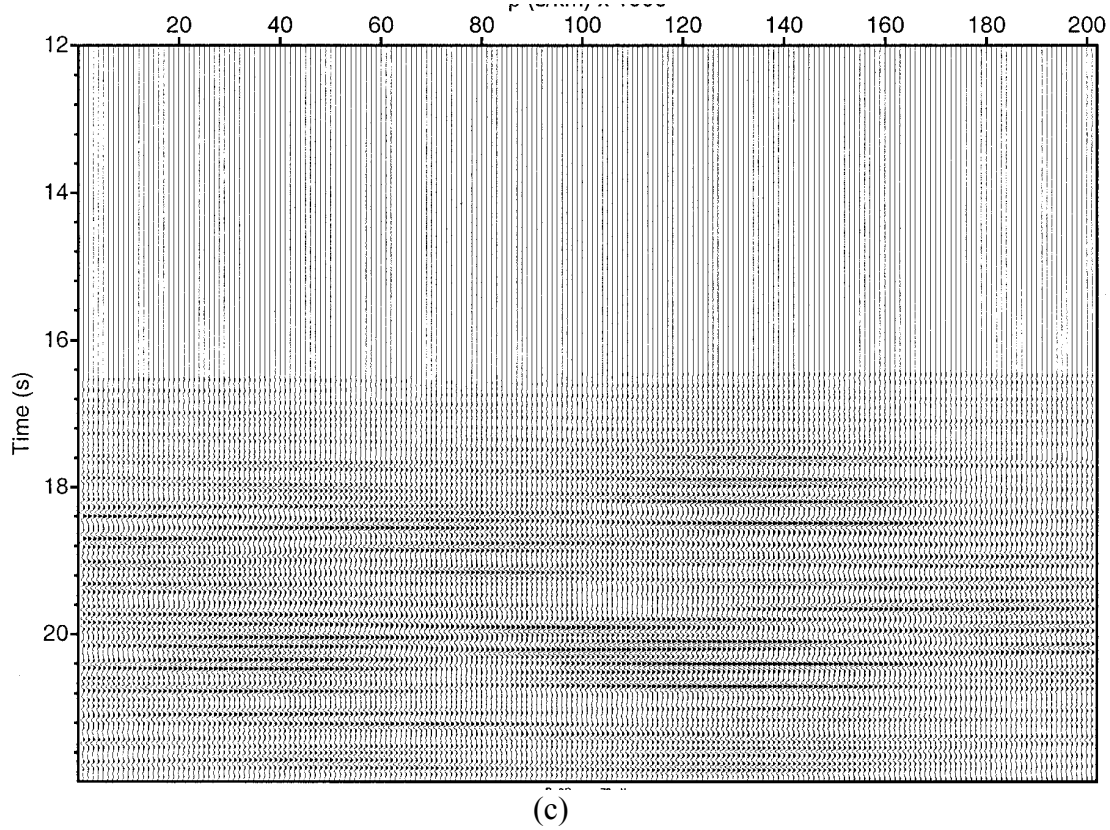
20
40
60
80
100
120
140
160
180
200
12
14
16
18
20
Time (s)

(c)

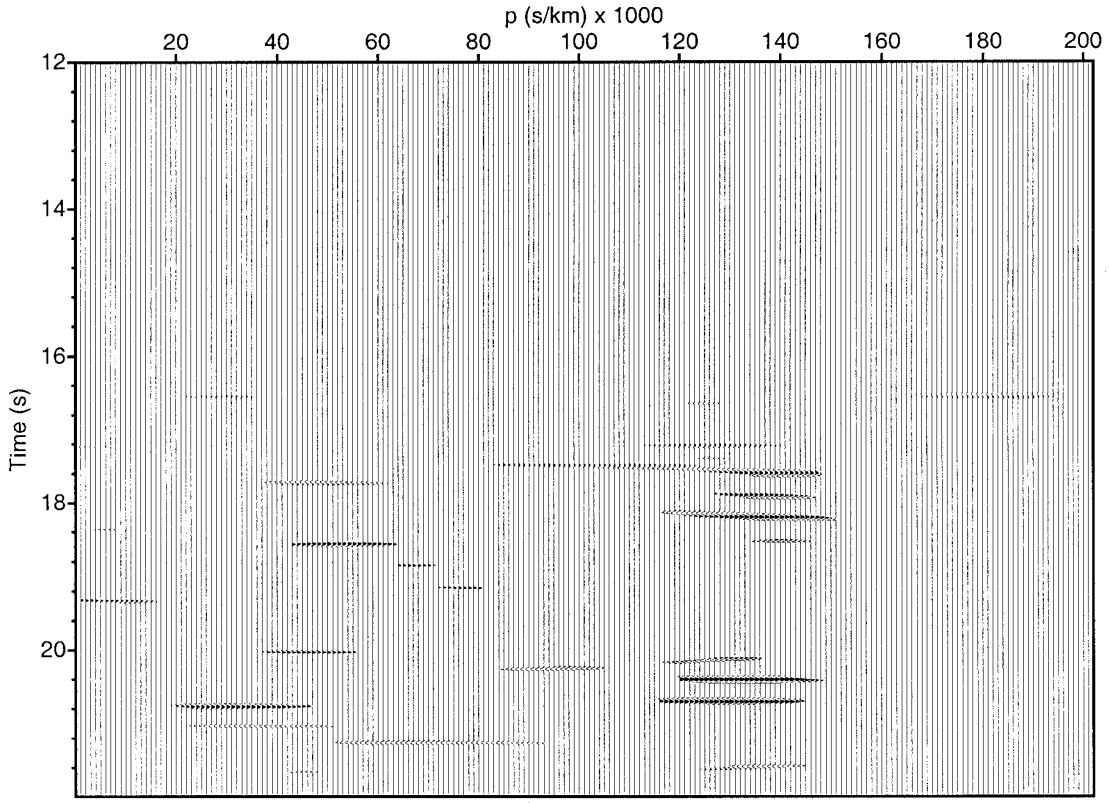
p (s/km) x 1000
20
40
60
80
100
120
140
160
180
200
12
14
16
18
20
Time (s)

(d)

Figure 3.16: Ruby blast #3: (a) Static corrected shot gather. Distance range: 60.1-65.65 km. The gather was high-cut filtered using a linear ramp from 10-15 Hz. The horizontal axis represents the distance in km from the shot while the vertical axis represents the reduced time. Static corrections were carried out after using a reduction velocity of 6.4 km/s to flatten the target event. (b) semblance of the slant stack, (c) slant stack, and (d1,d2) the coherency filtered slant stacks used for migration. Threshold values used for migration were 0.6 and 0.7.

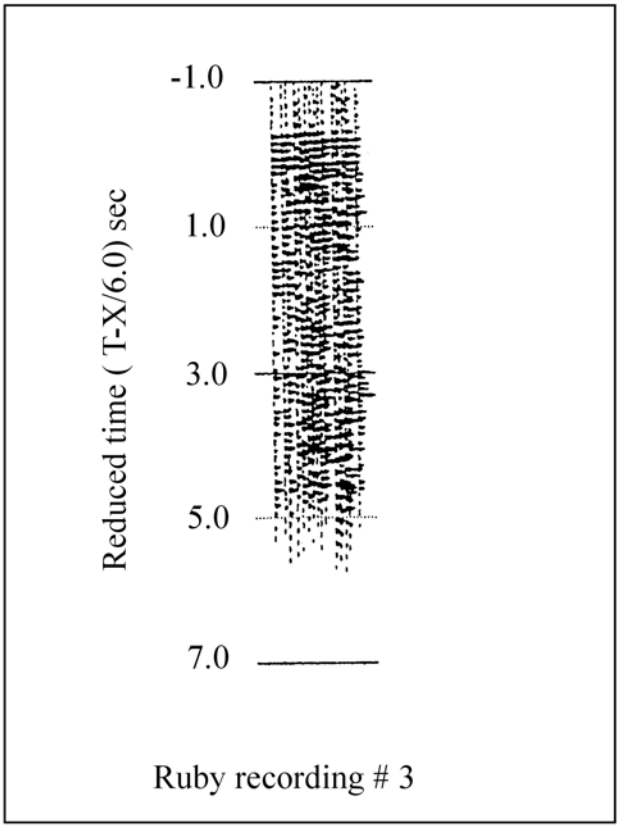

(Figure 3.16a)

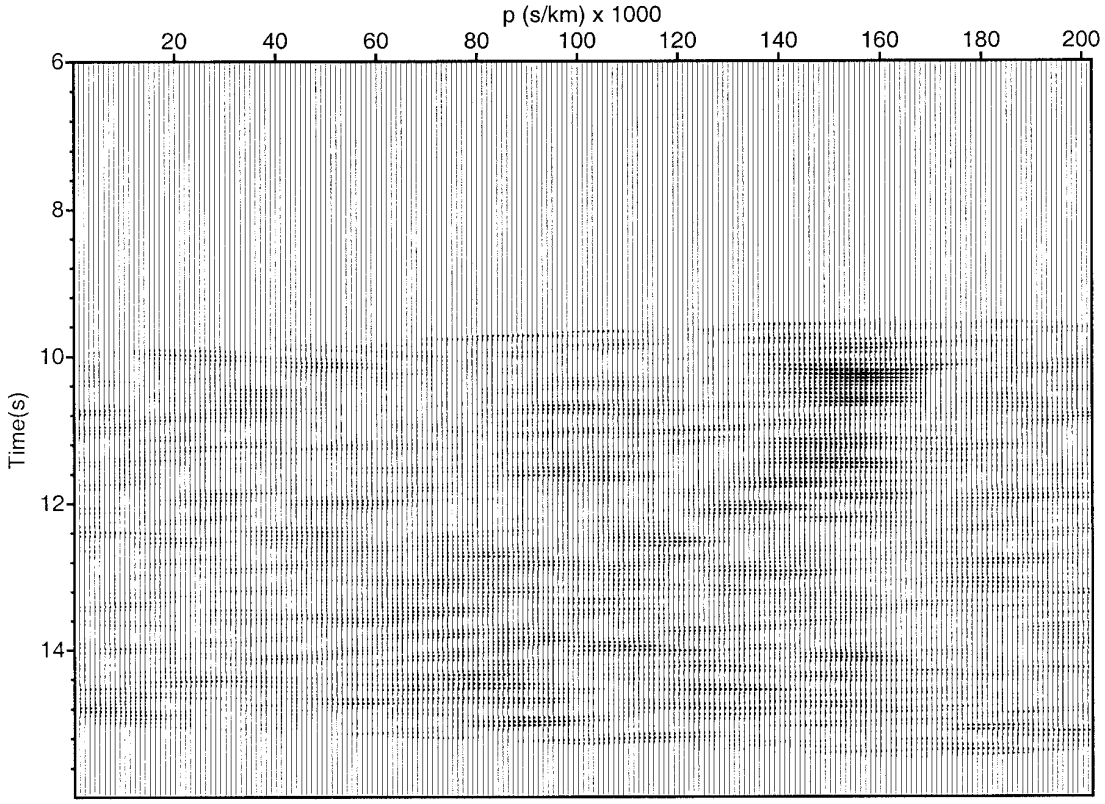
p (s/km) x 1000
20
40
60
80
100
120
140
160
180
200
6
8
10
12
14
Time(s)

(b)

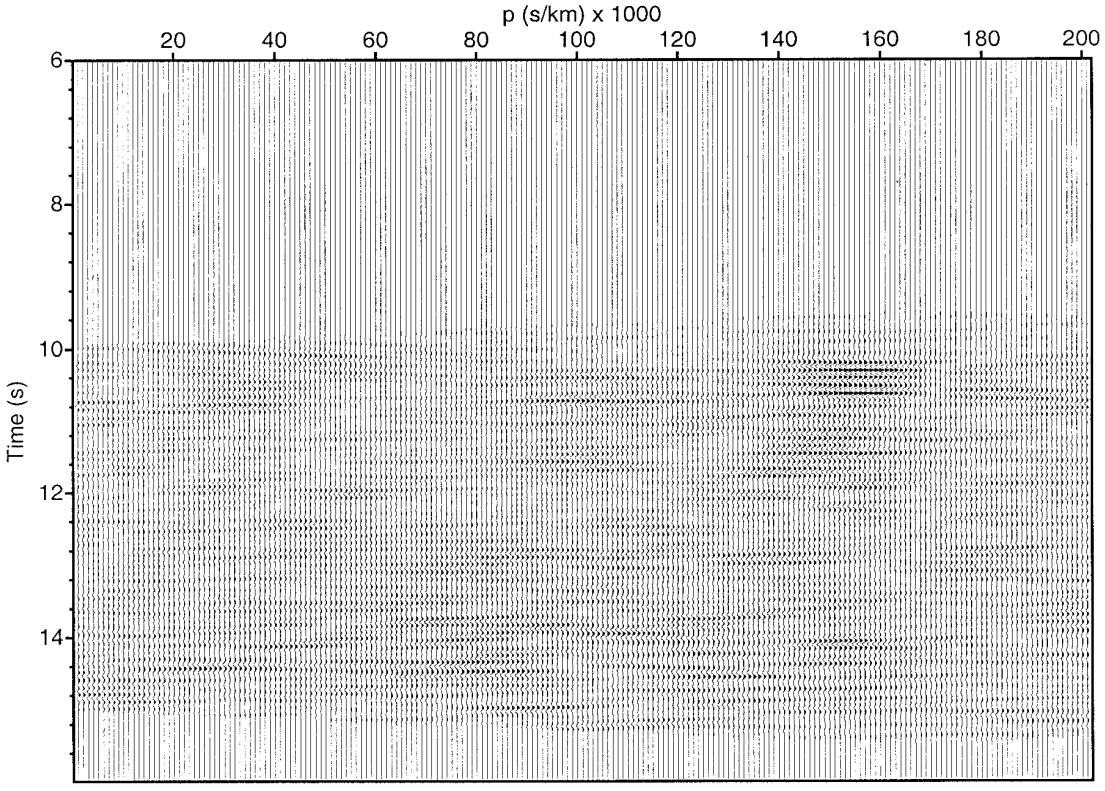
p (s/km) x 1000
20
40
60
80
100
120
140
160
180
200
6
8
10
12
14
Time (s)

(c)

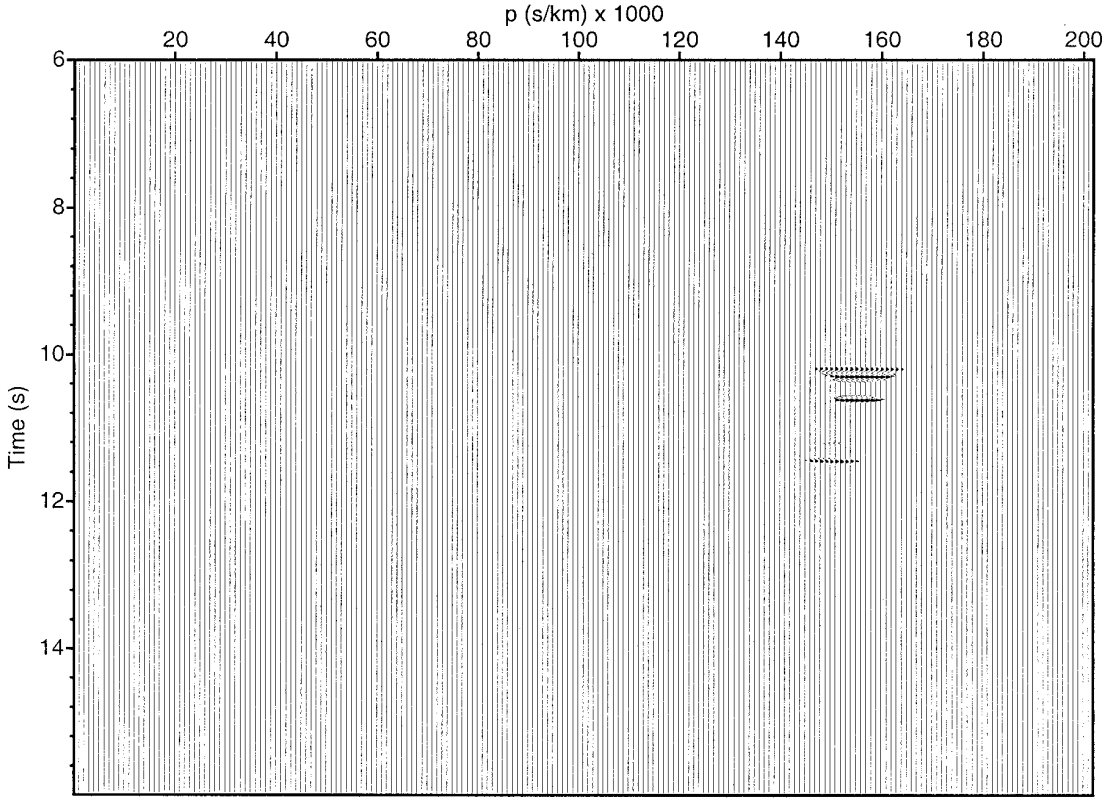
p (s/km) x 1000
20
40
60
80
100
120
140
160
180
200
6
8
10
12
14
Time (s)

(d1)

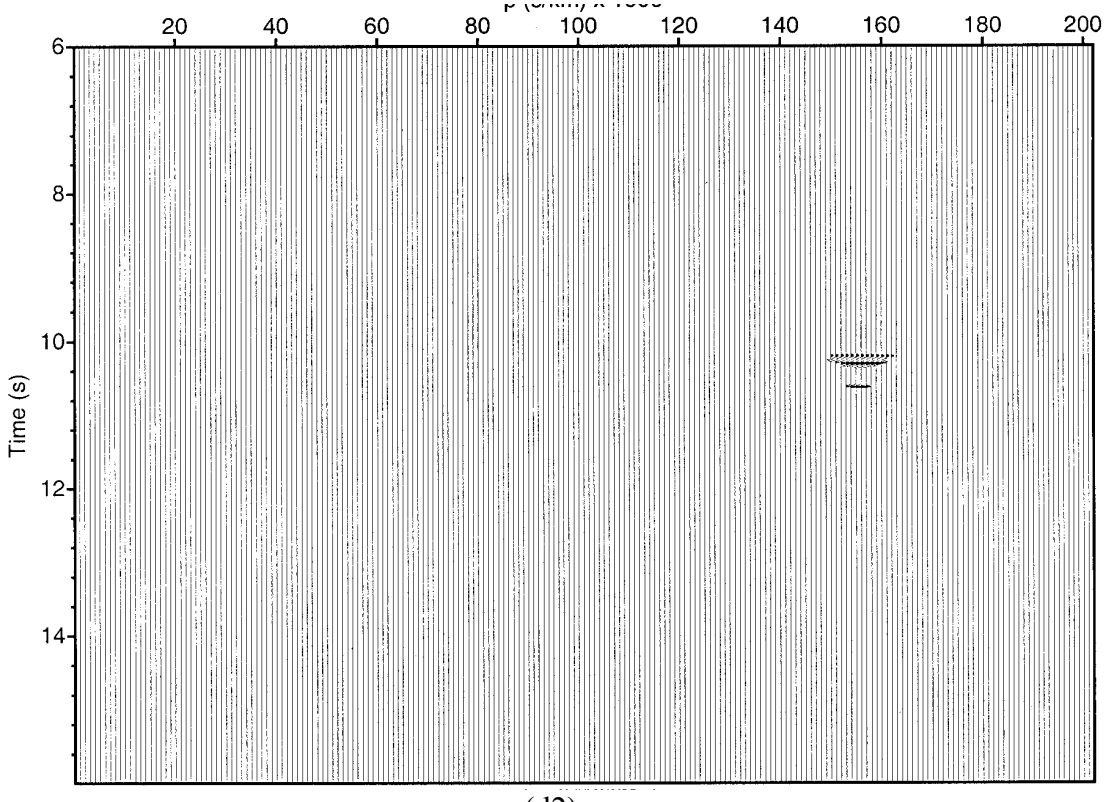
20
40
60
80
100
120
140
160
180
200
6
8
10
12
14
Time (s)

(d2)

Figure 3.17: Ruby blast #4: (a) Static corrected shot gather. Distance range: 75.8-82.5 km. The gather was high-cut filtered using a linear ramp from 10-15 Hz. The horizontal axis represents the distance in km from the shot while the vertical axis represents the reduced time. Static corrections were carried out after using a reduction velocity of 6.3 km/s to flatten the target event. (b) semblance of the slant stack, (c) slant stack, and (d) the coherency filtered slant stack used for migration. Threshold value was 0.4.

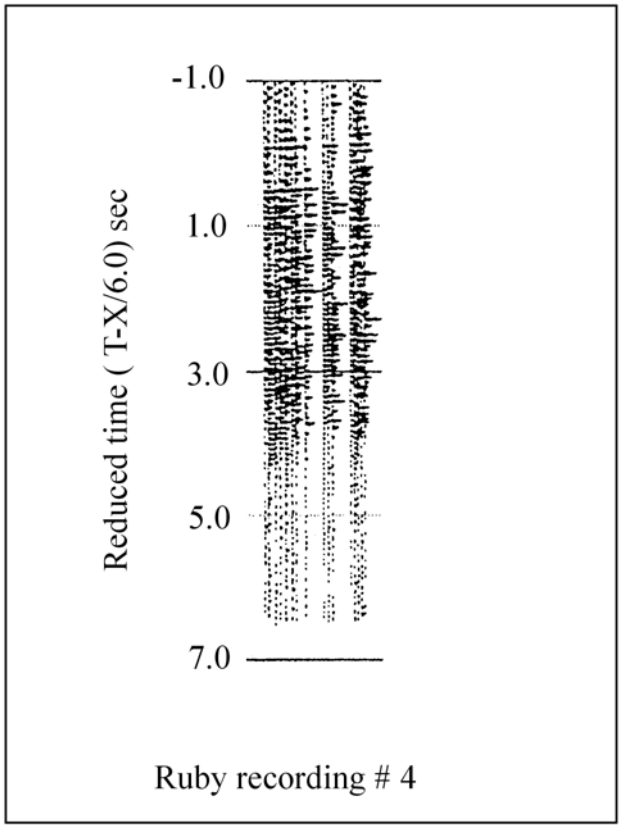

(Figure 3.17a)

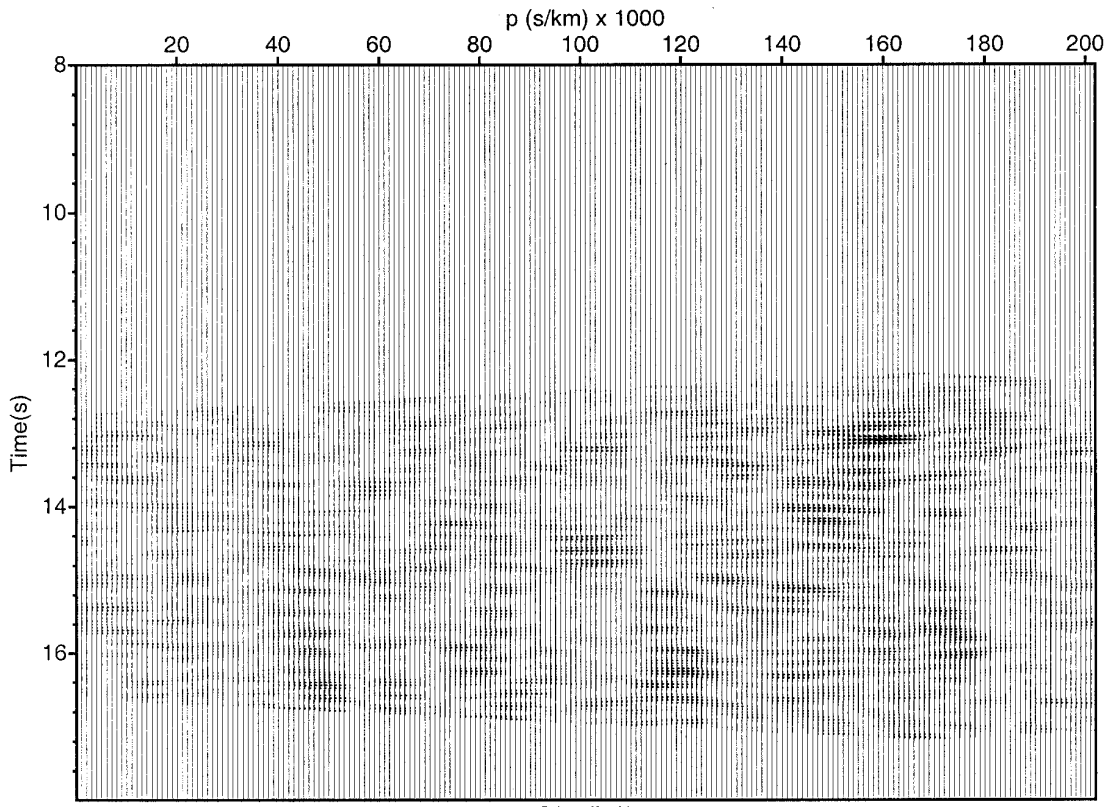
p (s/km) x 1000
20
40
60
80
100
120
140
160
180
200
8
10
12
14
16
Time(s)

(b)

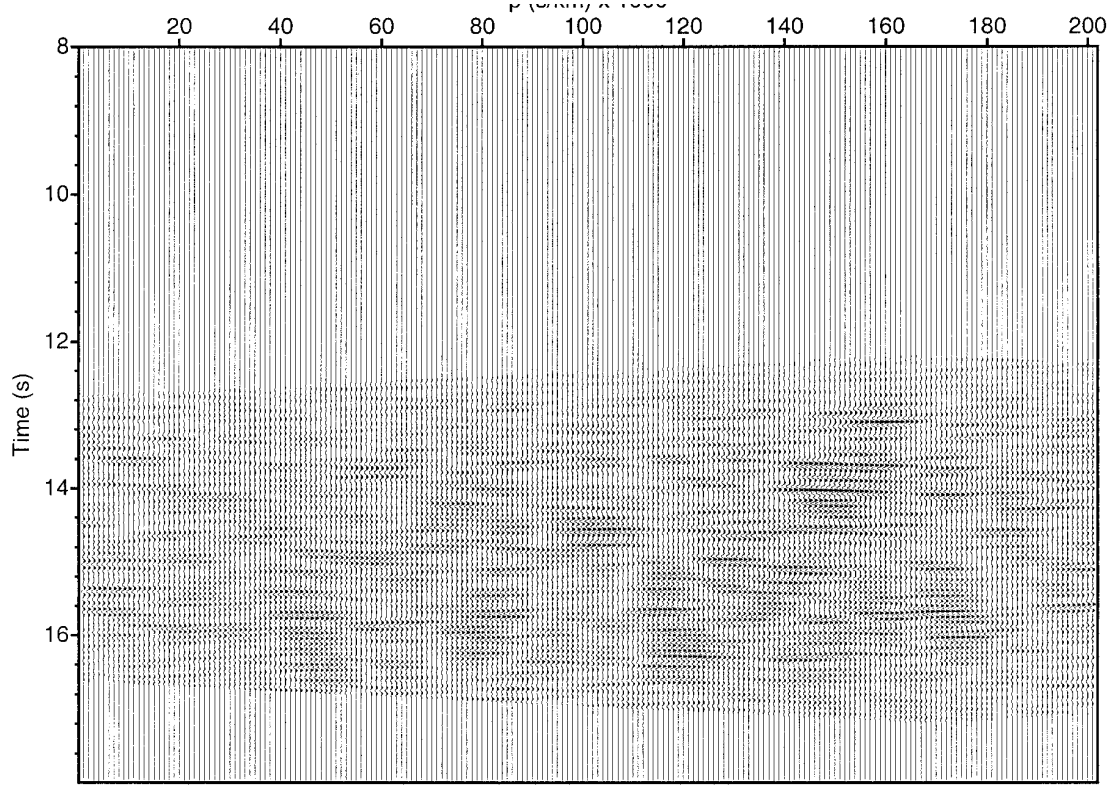
20
40
60
80
100
120
140
160
180
200
8
10
12
14
16
Time (s)

(c)

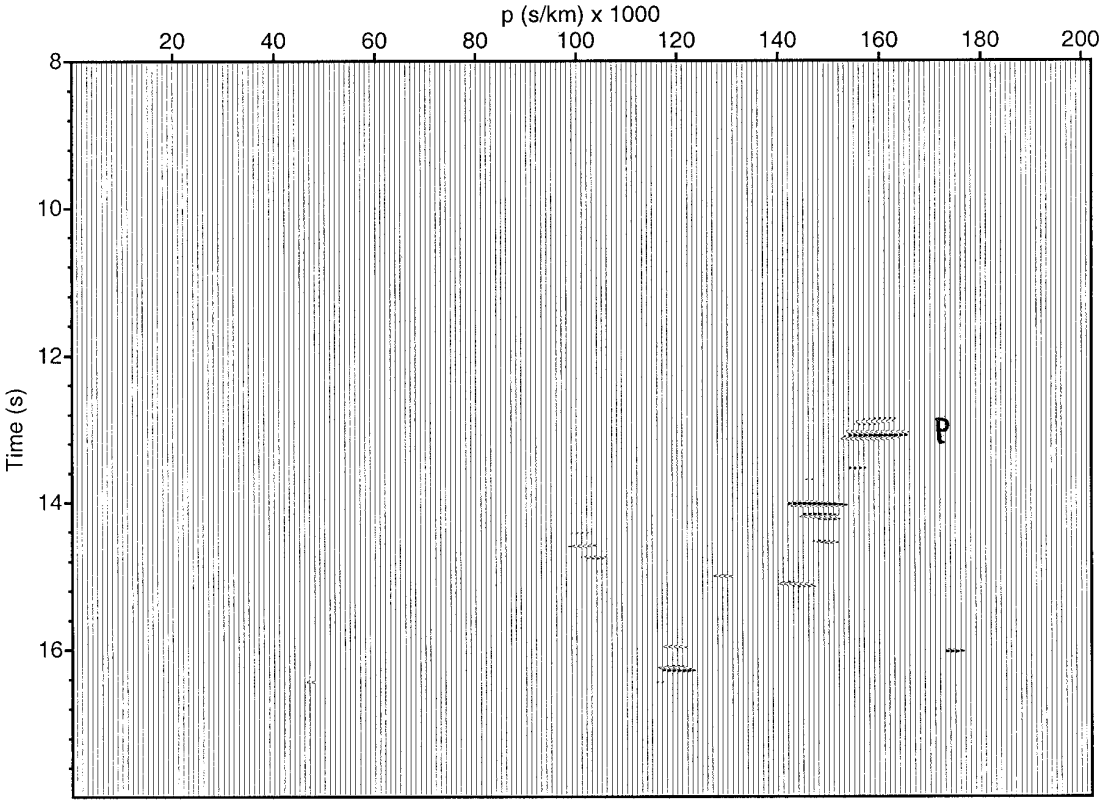
p (s/km) x 1000
20
40
60
80
100
120
140
160
180
200
8
10
12
14
16
Time (s)
P

(d)

Figure 3.18: Ruby blast #5, part B: (a) Static corrected shot gather. Distance range: 48.5-51.2 km. The gather was high-cut filtered using a linear ramp from 10-15 Hz. The horizontal axis represents the distance in km from the shot while the vertical axis represents the reduced time. Static corrections were carried out after using a reduction velocity of 6.5 km/s to flatten the target event. (b) semblance of the slant stack, (c) slant stack, and (d1,d2) the coherency filtered slant stacks used for migration. Threshold values used for migration are 0.6 and 0.7.

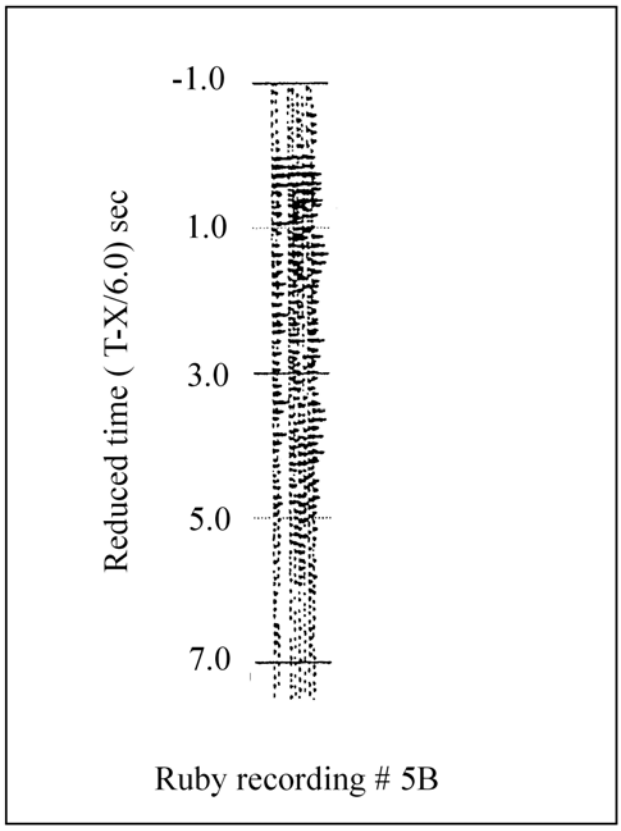

(Figure 3.18a)

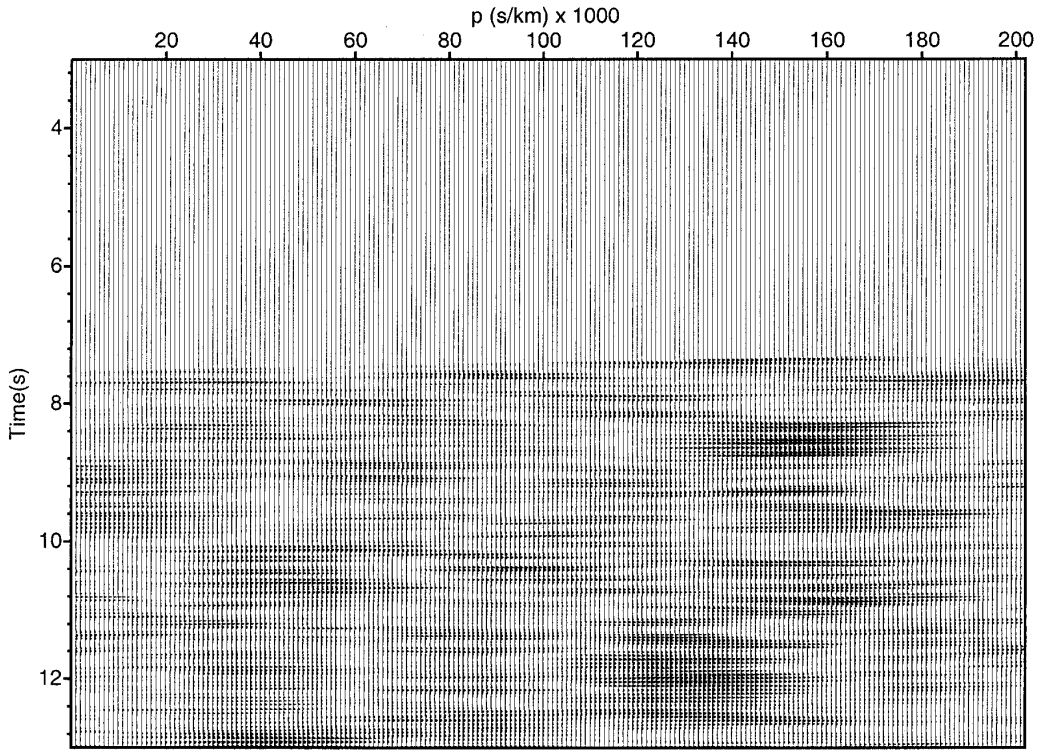
p (s/km) x 1000
20
40
60
80
100
120
140
160
180
200
Time(s)
4
6
8
10
12

(b)

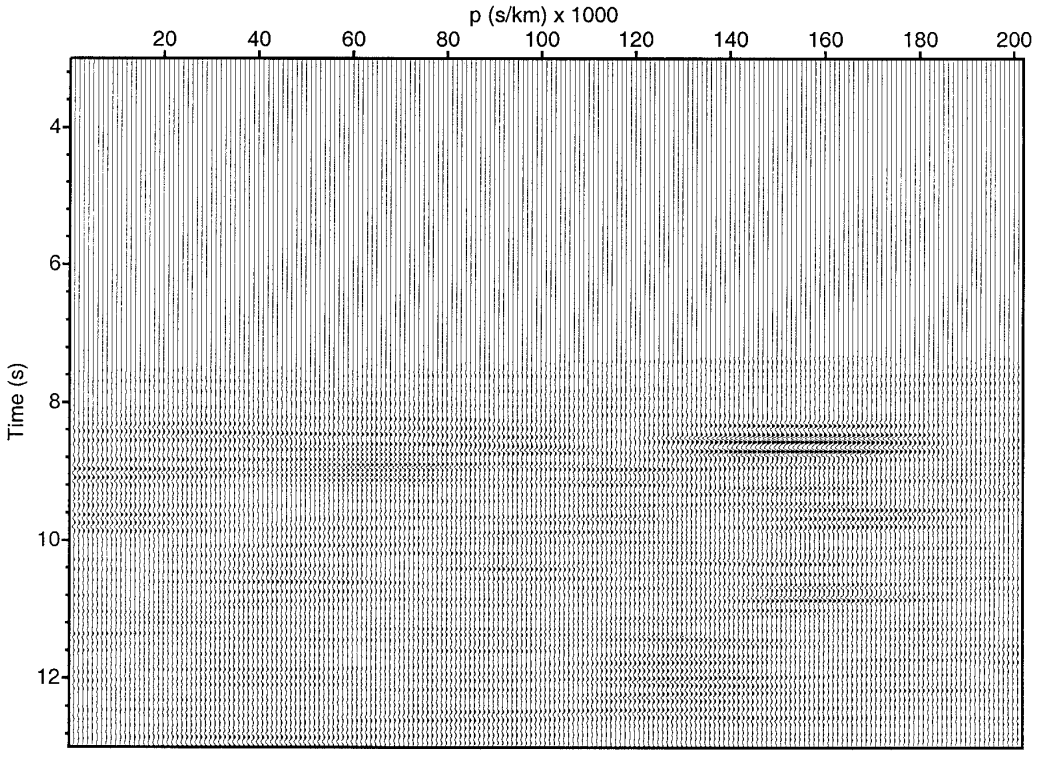
p (s/km) x 1000
20
40
60
80
100
120
140
160
180
200
Time (s)
4
6
8
10
12

(c)

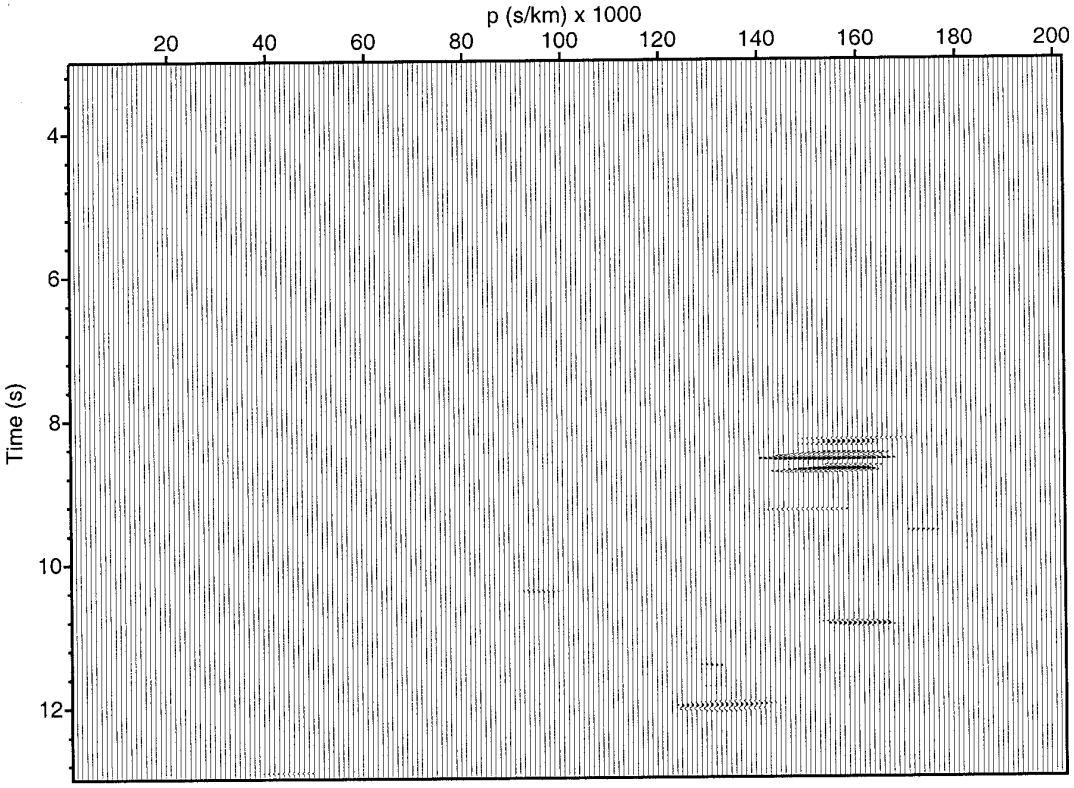
p (s/km) x 1000
20
40
60
80
100
120
140
160
180
200
Time (s)
4
6
8
10
12

(d1)

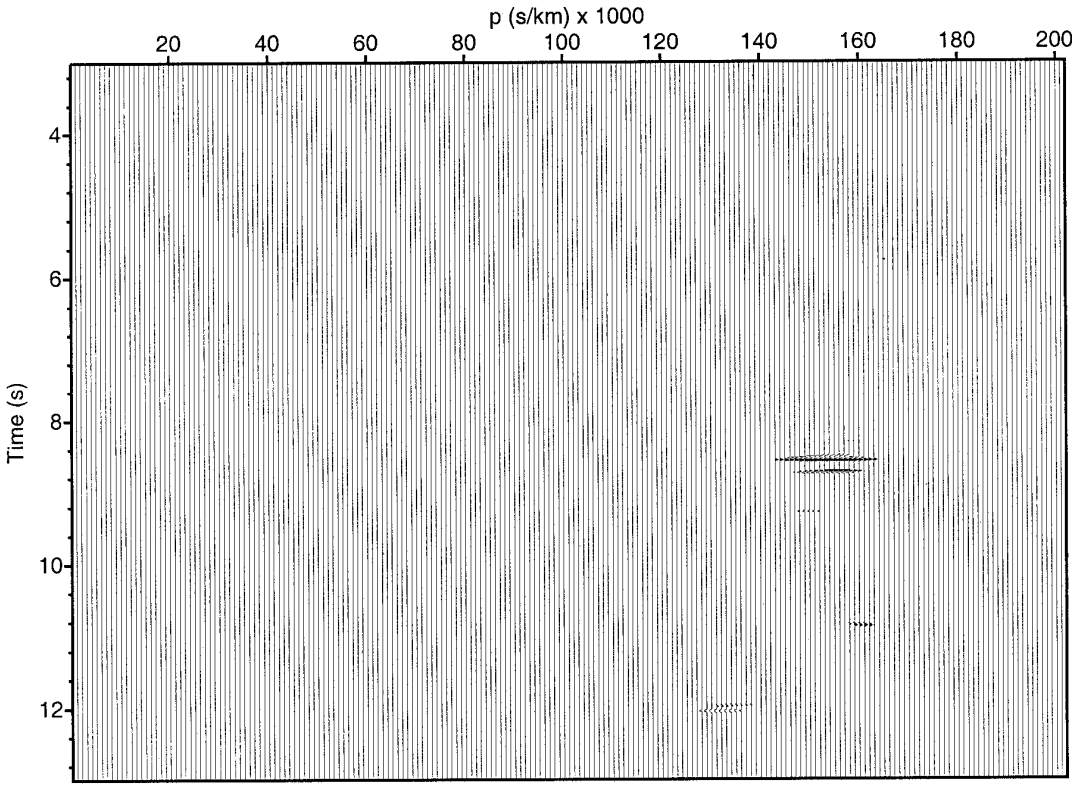
p (s/km) x 1000
20
40
60
80
100
120
140
160
180
200
Time (s)
4
6
8
10
12

(d2)

Figure 3.19: Ruby blast #6: (a) Static corrected shot gather. Distance range: 70.5-76.5 km. The gather was high-cut filtered using a linear ramp from 10-15 Hz. The horizontal axis represents the distance in km from the shot while the vertical axis represents the reduced time. Static corrections were carried out after using a reduction velocity of 6.5 km/s to flatten the target event. (b) semblance of the slant stack, (c) slant stack, and (d1,d2) the coherency filtered slant stacks used for migration. Thresholds of 0.35 and 0.5 were used.

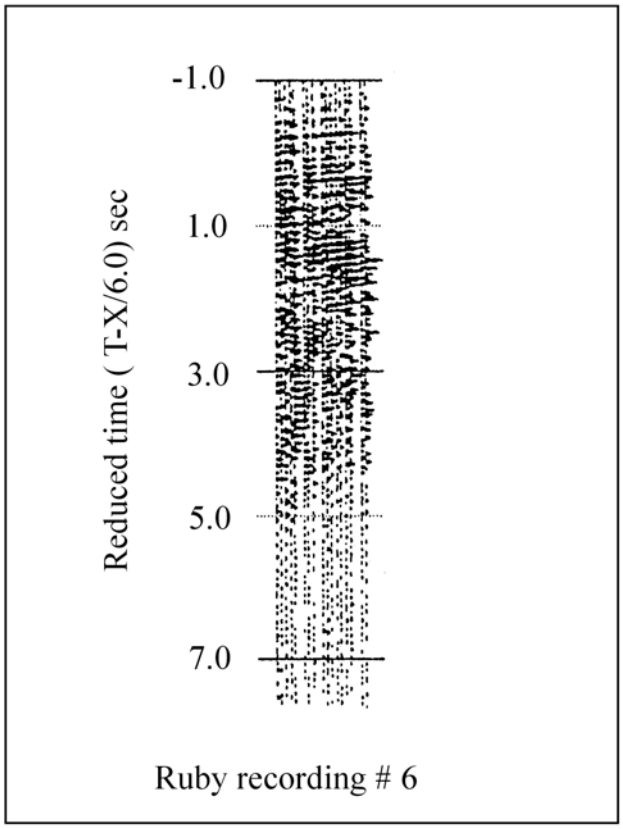

(Figure 3.19a)

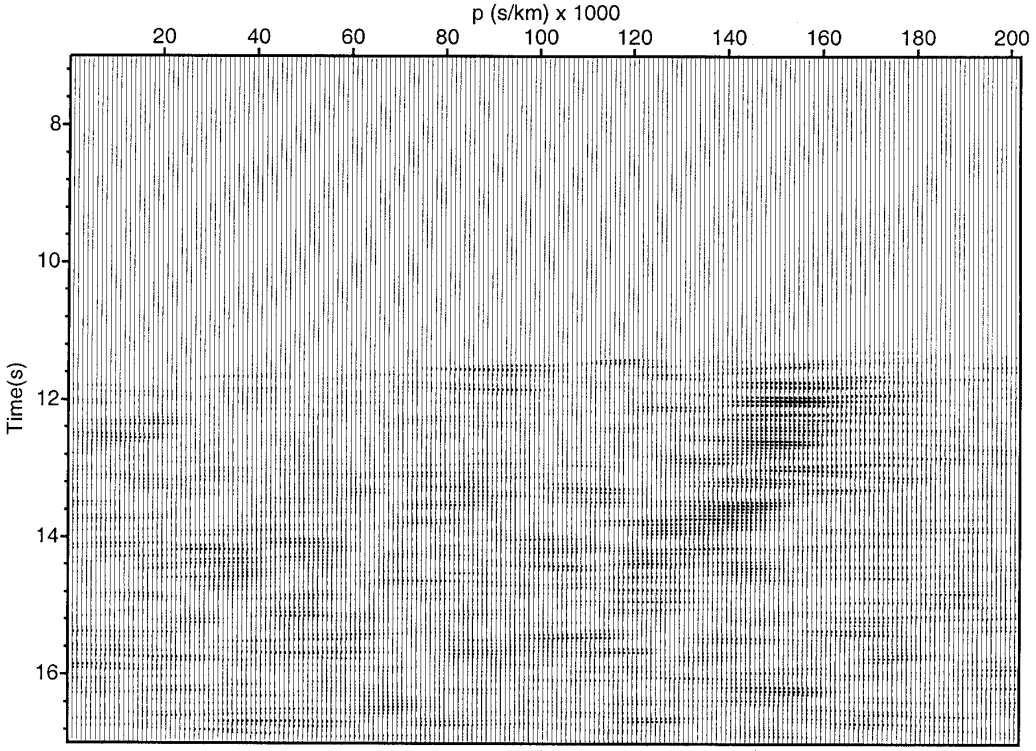
p (s/km) x 1000
20
40
60
80
100
120
140
160
180
200
8
10
12
14
16
Time(s)

(b)

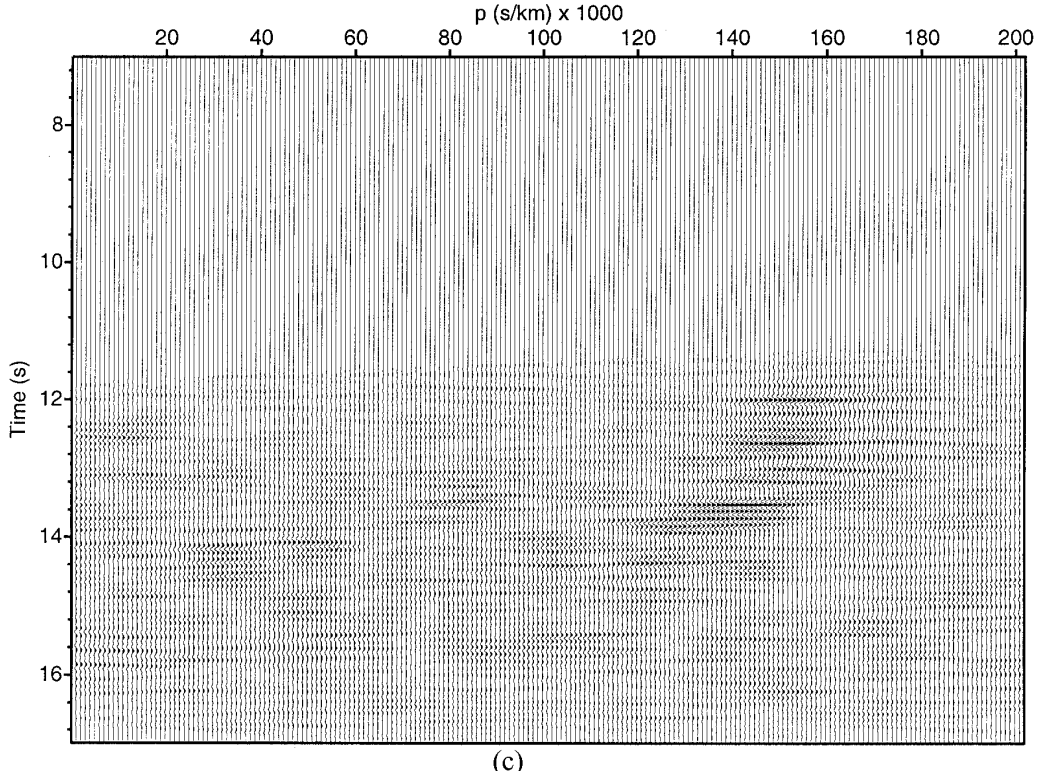
p (s/km) x 1000
20
40
60
80
100
120
140
160
180
200
8
10
12
14
16
Time (s)

(c)

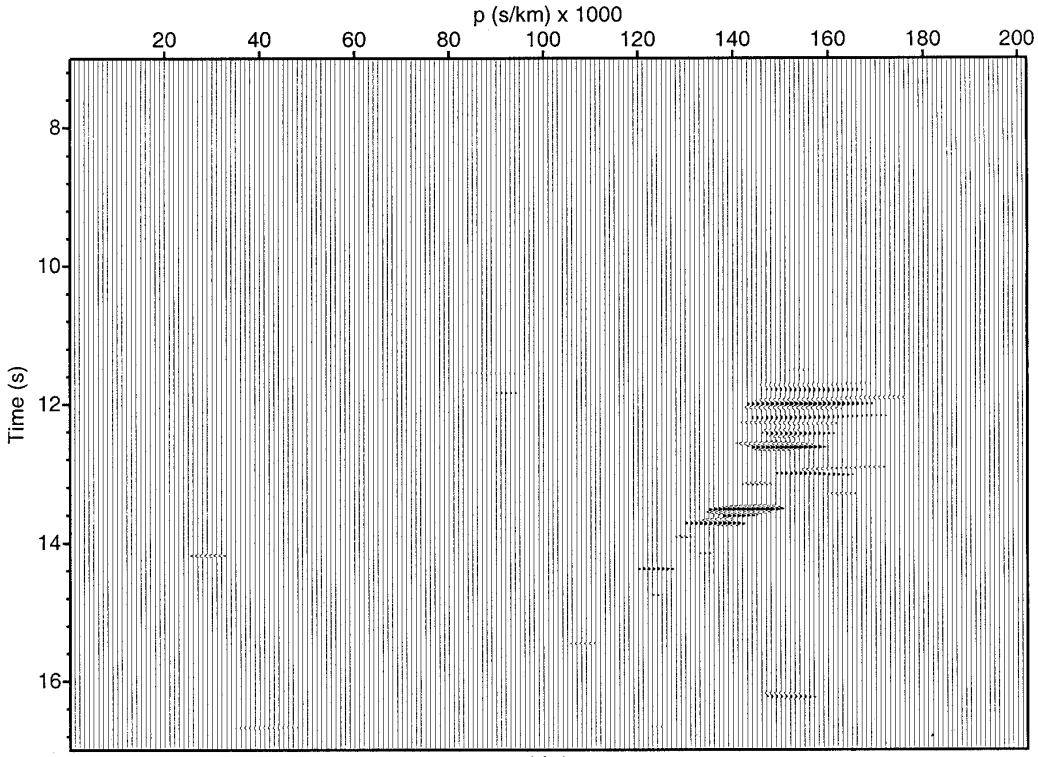
p (s/km) x 1000
20
40
60
80
100
120
140
160
180
200
Time (s)
8
10
12
14
16

(d1)

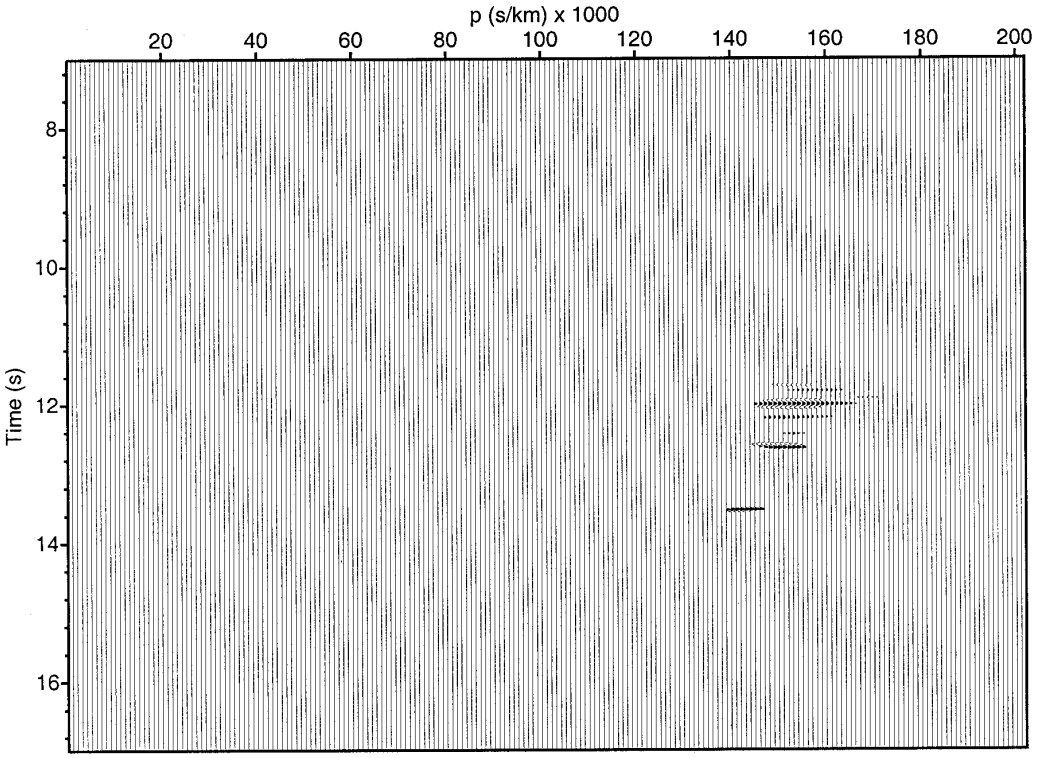
p (s/km) x 1000
20
40
60
80
100
120
140
160
180
200
Time (s)
8
10
12
14
16

(d2)

Figure 3.20: Migrated sections of recordings conducted at the Southern Aggregates Hitchcock quarry north of Macon, Georgia. The individual recordings are numbered a through i. For details refer to the text. In each section the star represents the shot location and the bar represents the array. The resolution width of each migrated event represents the confidence region of the reflector position. Resolution widths are controlled by the signal bandwidth and aperture of the recording array.

a. hi1

b. hi2

c. hi3

d. hi4

e. hi5

f. hi6

g. hi8A

h.hi8B

i. hi9

j. hi10

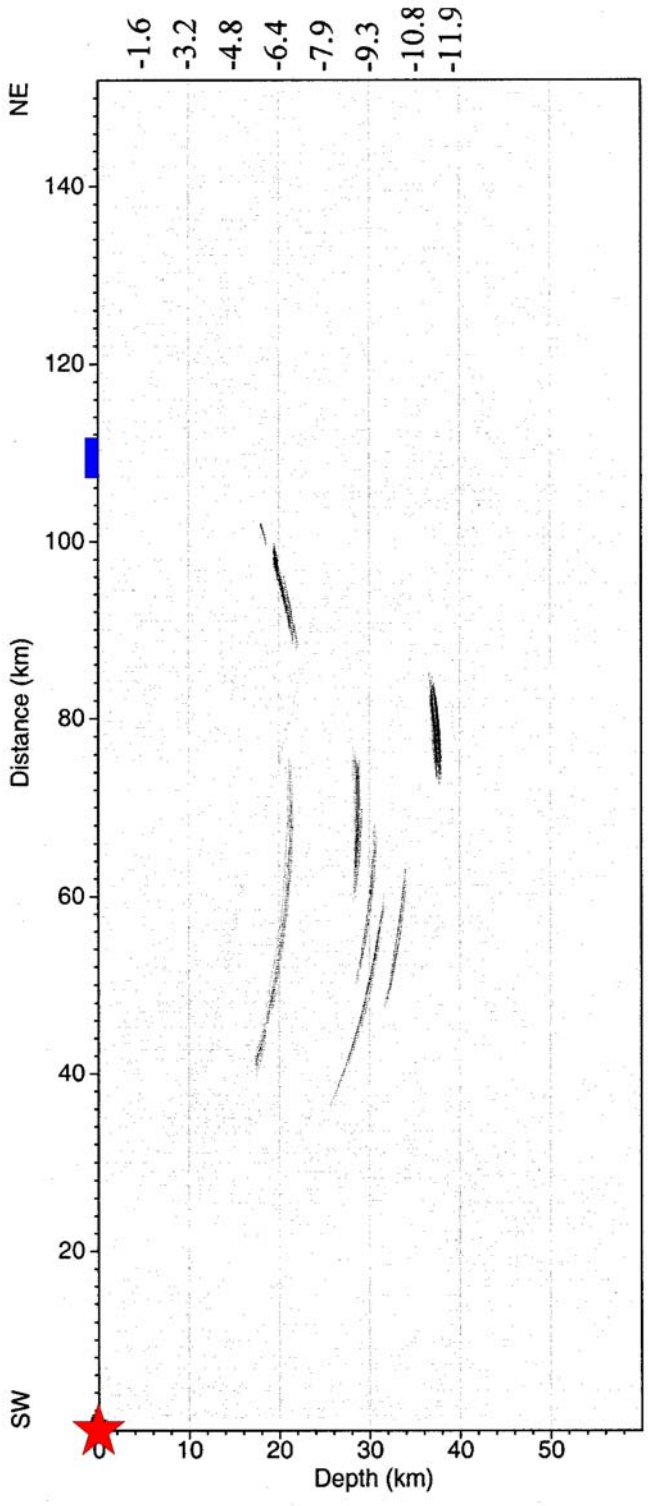
-1.6
-3.2
-4.8
-6.4
-7.9
-9.3
-10.8
-11.9
NE
SW
140
120
100
80
60
40
20
Distance (km)
0
10
20
30
40
50
Depth (km)

(a)

TWT (s)
-1.6
-3.2
-4.8
-6.4
-7.9
-9.3
-10.8
-11.9
NE
140
120
100
80
60
40
20
SW
Distance (km)
0
10
20
30
40
50
Depth (km)

(b)

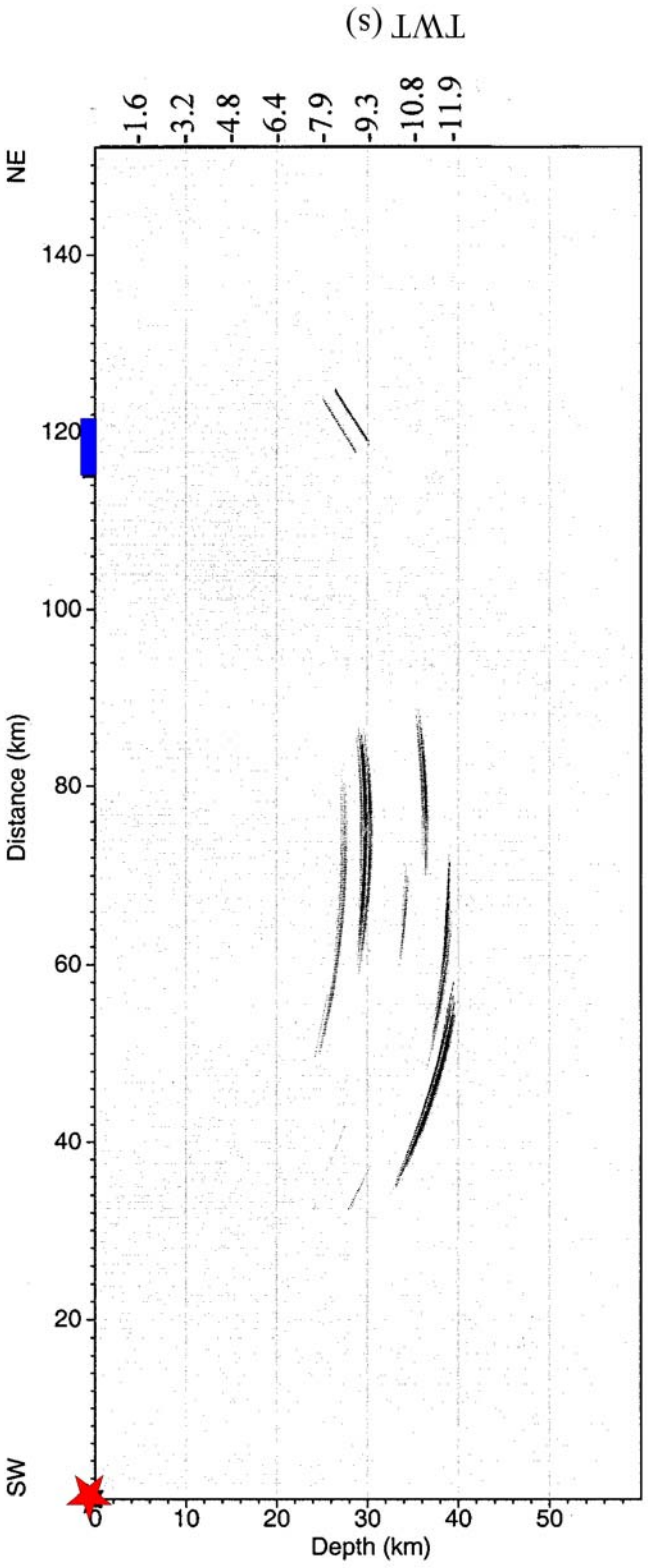
TWT (s)
-1.6
-3.2
-4.8
-6.4
-7.9
-9.3
-10.8
-11.9
NE
SW
Distance (km)
140
120
100
80
60
40
20
0
10
20
30
40
50
Depth (km)

(c)

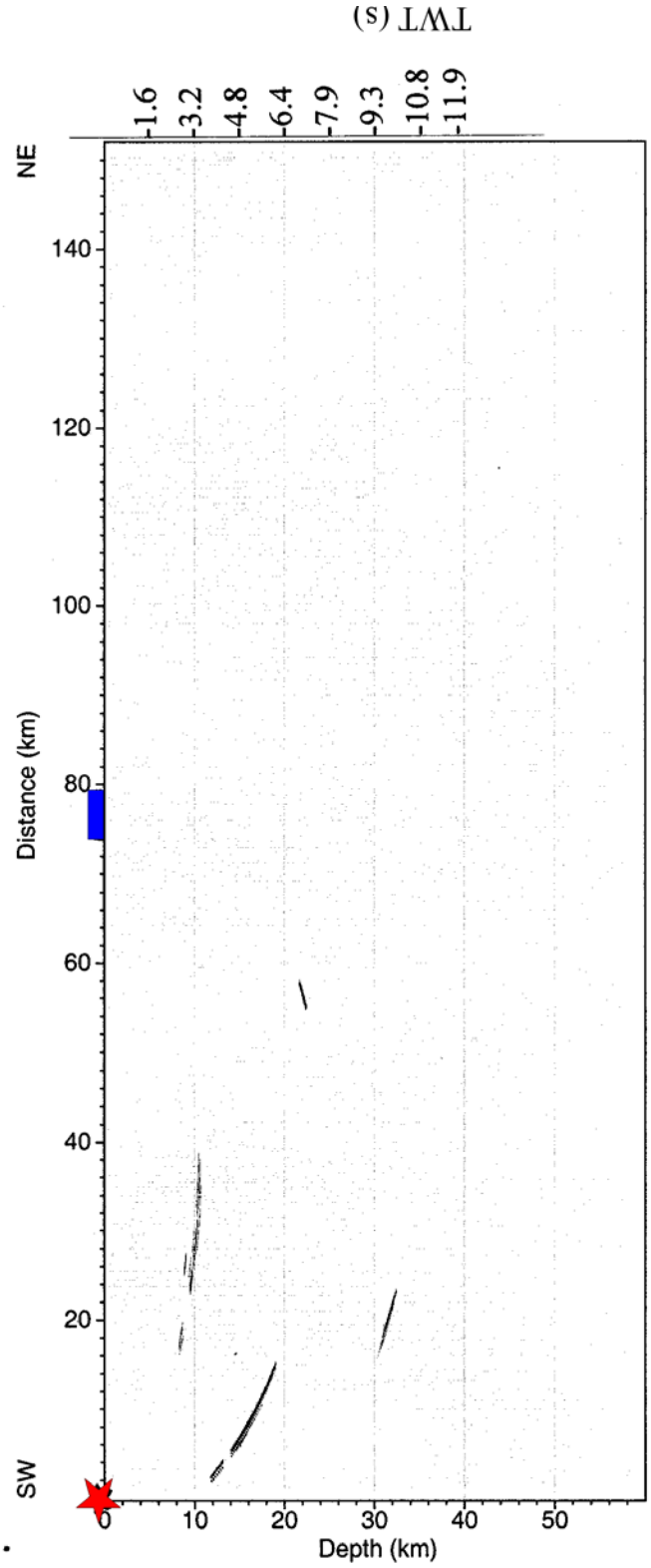
TWT (s)
1.6
3.2
4.8
6.4
7.9
9.3
10.8
11.9
NE
140
120
100
80
60
40
20
SW
Distance (km)
0
10
20
30
40
50
Depth (km)

(d)

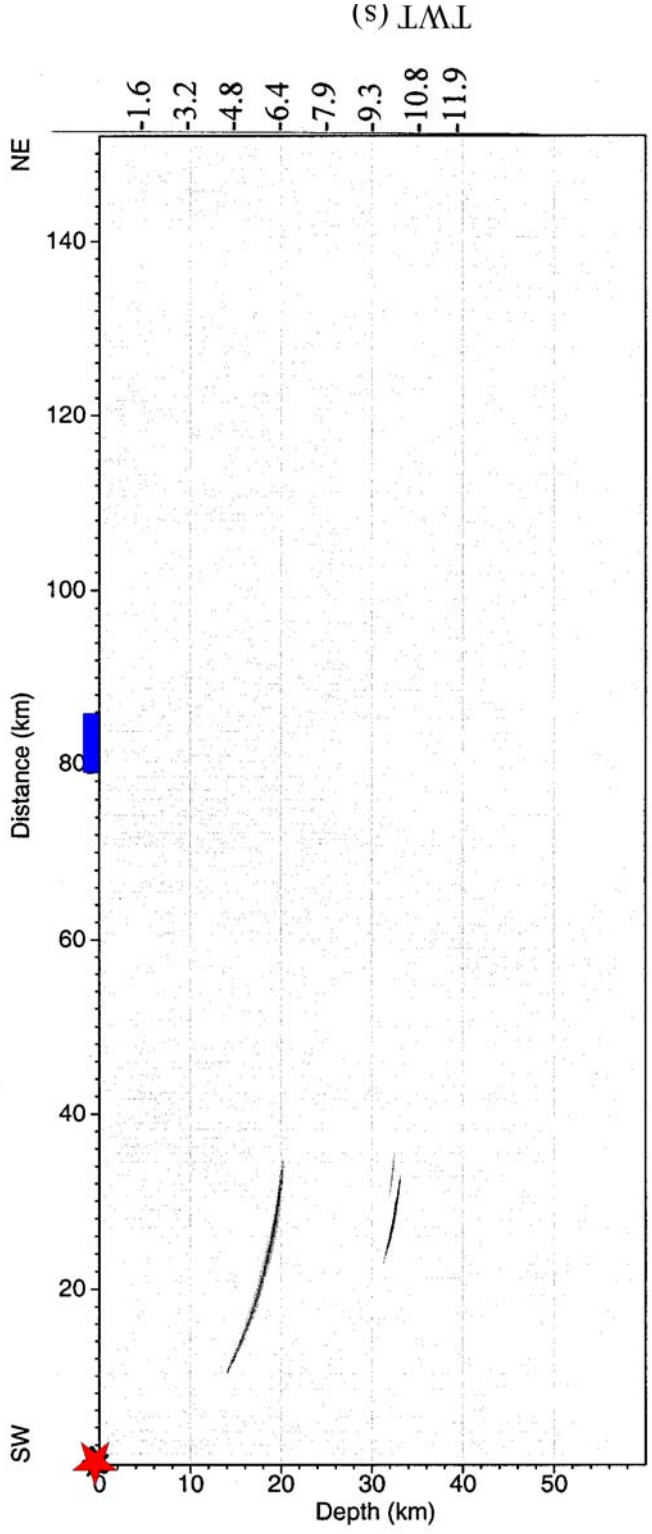
TWT (s)
-1.6
-3.2
-4.8
-6.4
-7.9
-9.3
-10.8
-11.9
NE
SW
Distance (km)
140
120
100
80
60
40
20
0
10
20
30
40
50
Depth (km)

(e)

TWT (s)
-1.6
-3.2
-4.8
-6.4
-7.9
-9.3
-10.8
-11.9
NE
SW
Distance (km)
140
120
100
80
60
40
20
0
10
20
30
40
50
Depth (km)

(f)

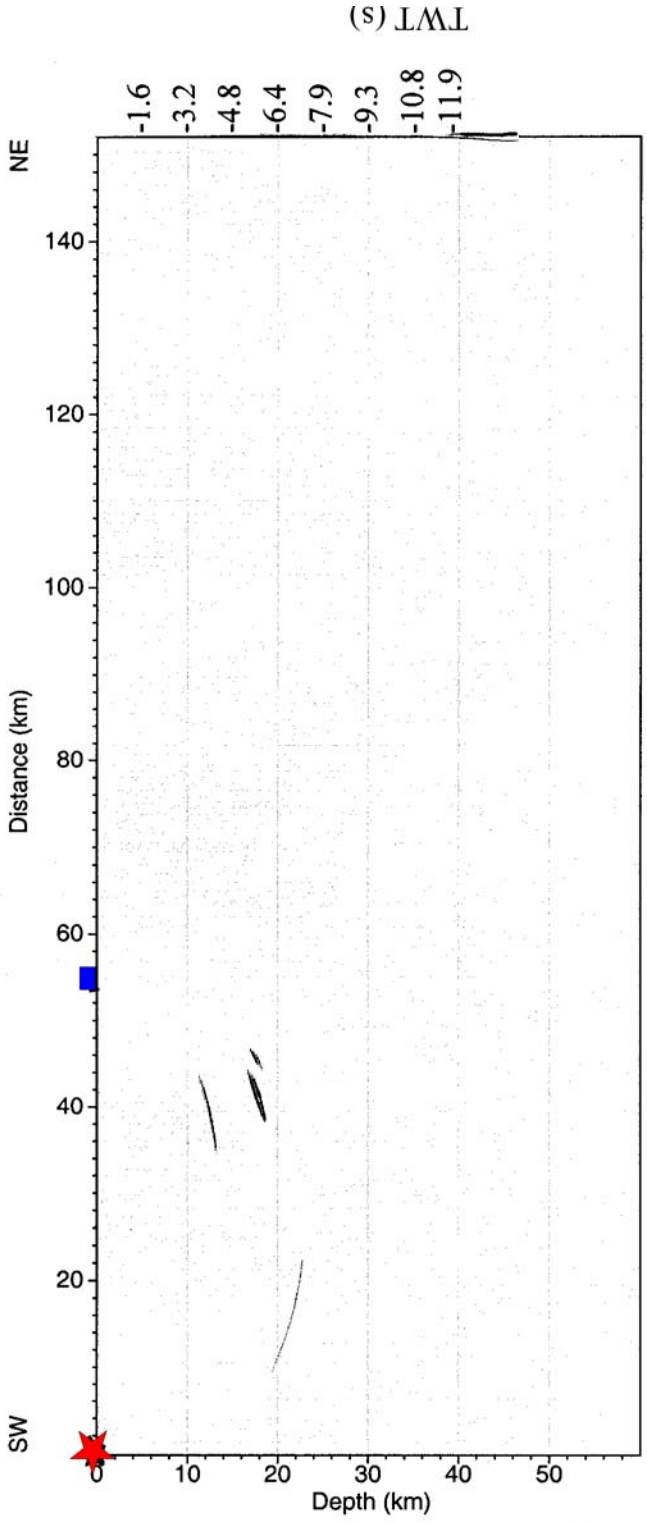
TWT (s)
-1.6
-3.2
-4.8
-6.4
-7.9
-9.3
-10.8
-11.9
NE
SW
Distance (km)
140
120
100
80
60
40
20
0
10
20
30
40
50
Depth (km)

(g)

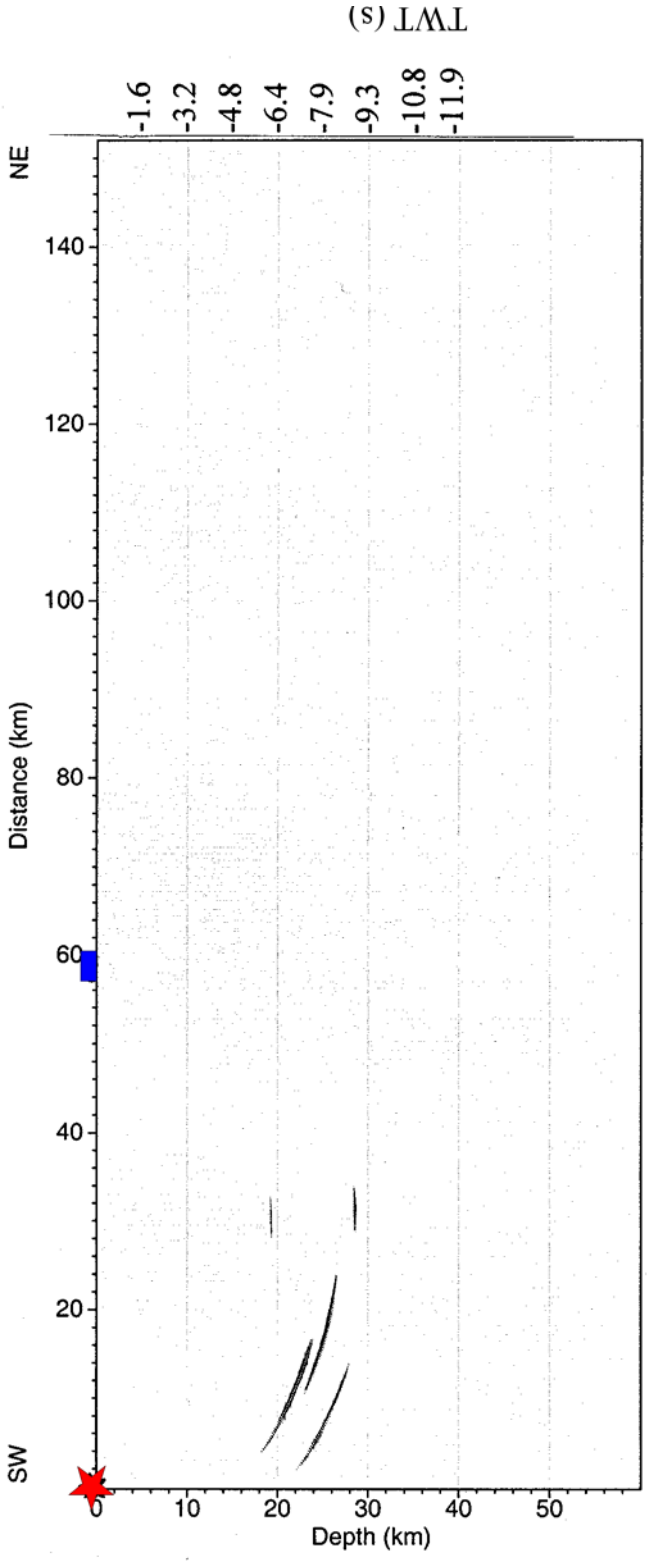
TWT (s)
-1.6
-3.2
-4.8
-6.4
-7.9
-9.3
-10.8
-11.9
NE
SW
Distance (km)
140
120
100
80
60
40
20
0
10
20
30
40
50
Depth (km)

(h)

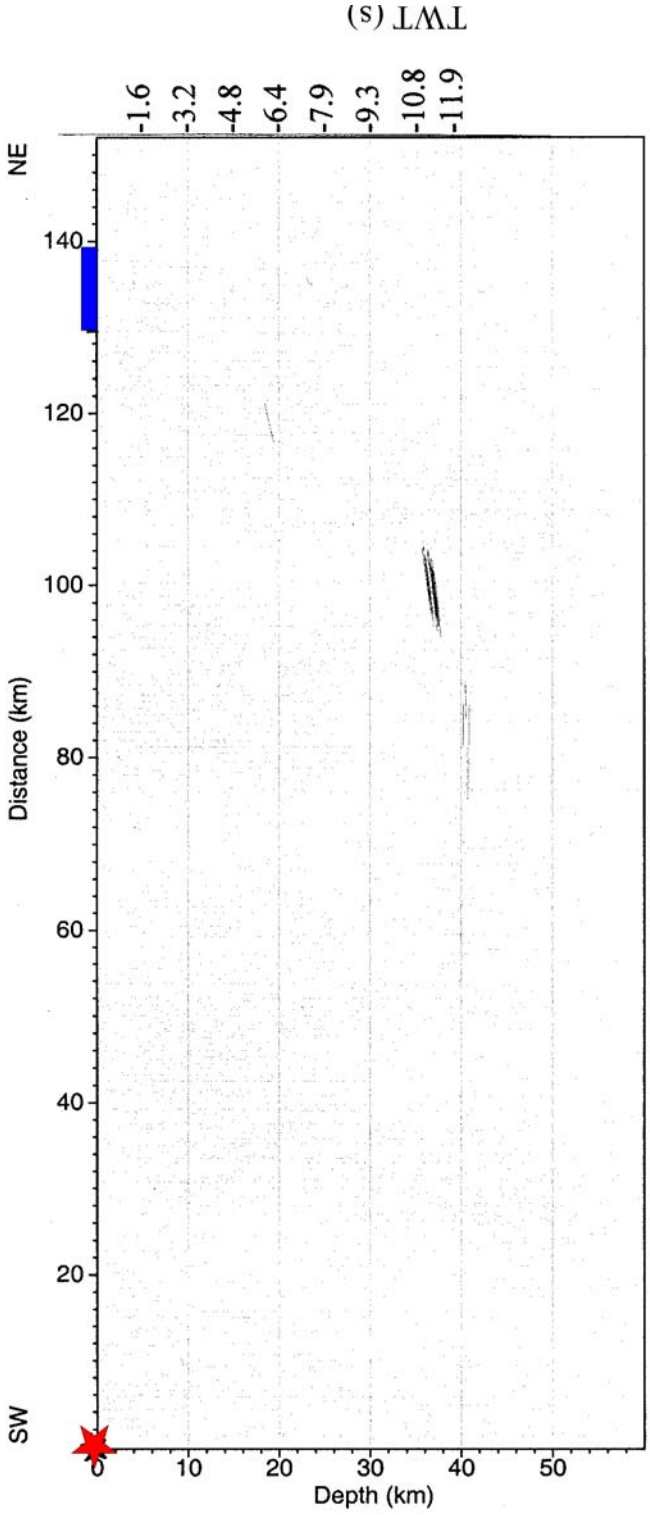
TWT (s)
-1.6
-3.2
-4.8
-6.4
-7.9
-9.3
-10.8
-11.9
NE
SW
Distance (km)
140
120
100
80
60
40
20
0
10
20
30
40
50
Depth (km)

(i)

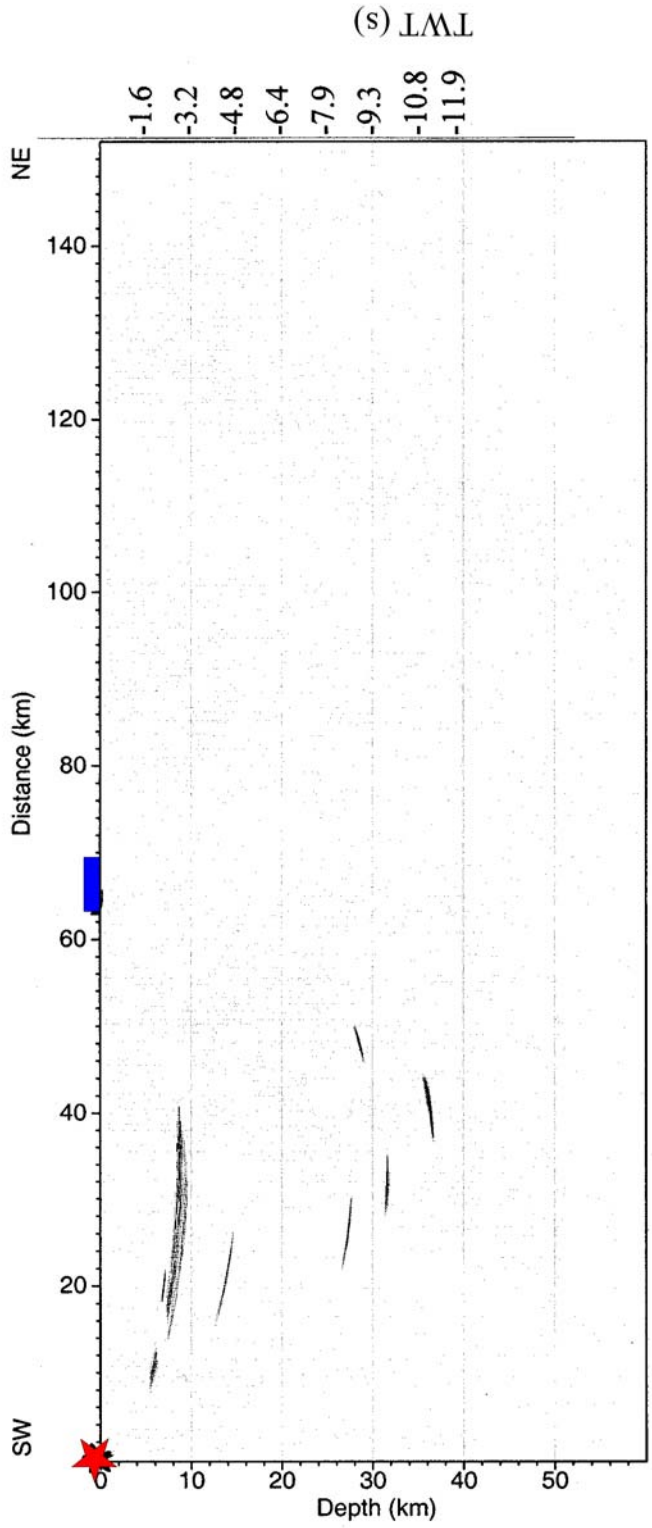
TWT (s)
-1.6
-3.2
-4.8
-6.4
-7.9
-9.3
-10.8
-11.9
NE
SW
Distance (km)
140
120
100
80
60
40
20
0
10
20
30
40
50
Depth (km)

(j)

Figure 3.21: Composite of migrated sections of Hitchcock recordings. (a) shows the composite of the recordings without normalization to the maximum amplitude. (b) shows the composite of the individually normalized migrated sections.

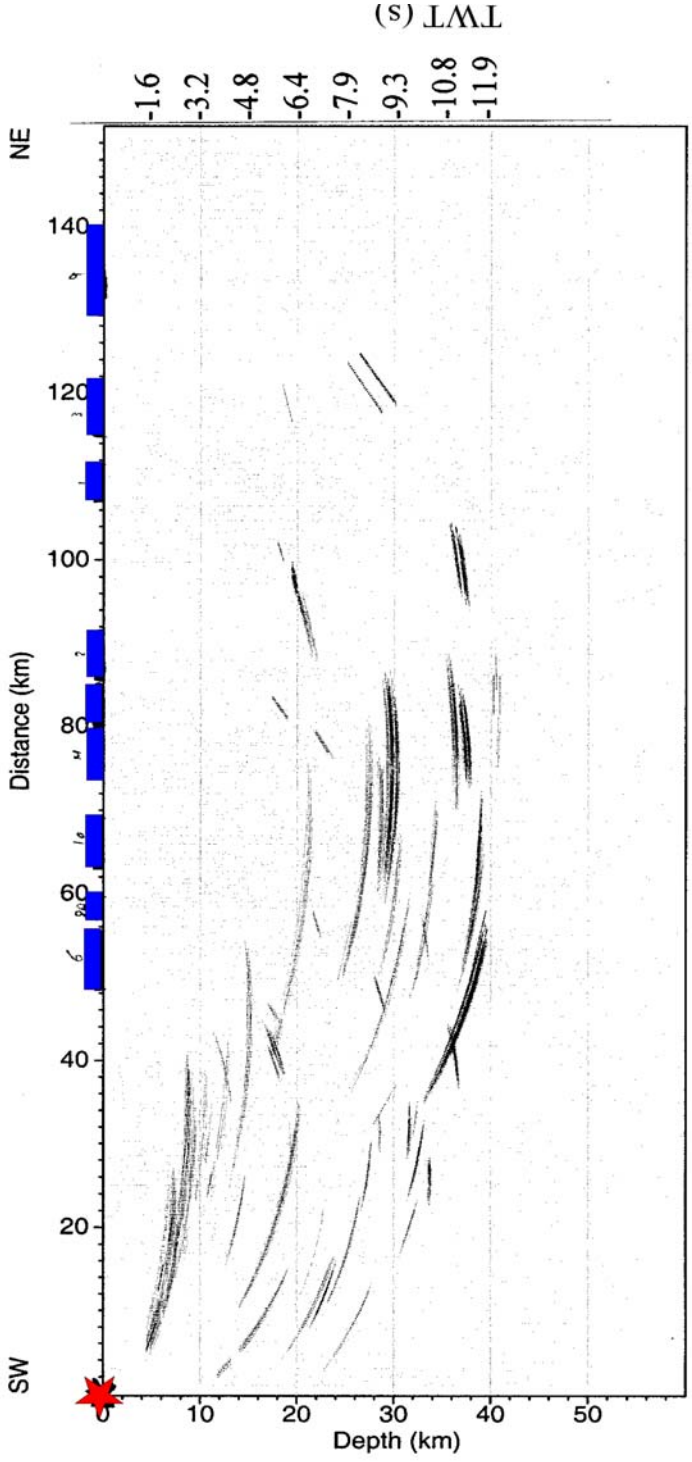
TWT (s)
-1.6
-3.2
-4.8
-6.4
-7.9
-9.3
-10.8
-11.9
NE
SW
Distance (km)
140
120
100
80
60
40
20
0
10
20
30
40
50
Depth (km)

(a)

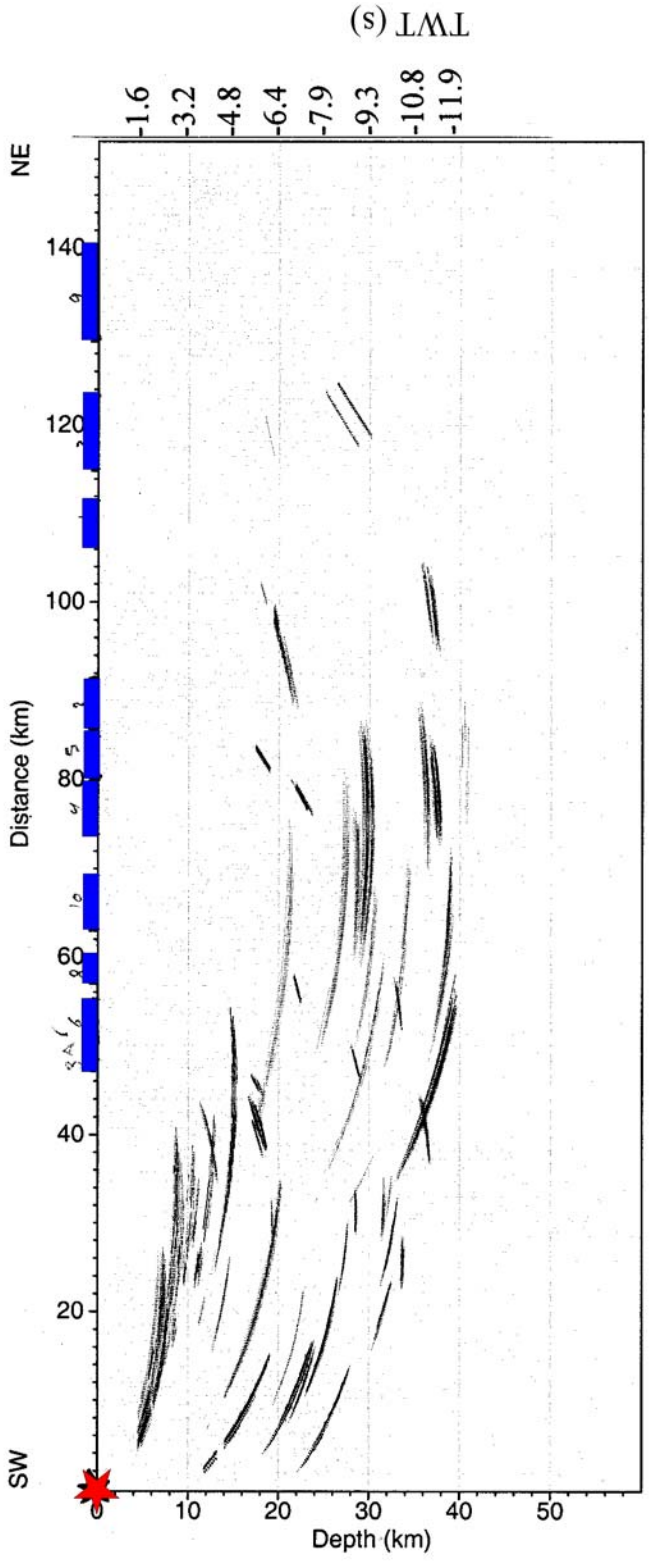
TWT (s)
-1.6
-3.2
-4.8
-6.4
-7.9
-9.3
-10.8
-11.9
NE
SW
Distance (km)
140
120
100
80
60
40
20
0
10
20
30
40
50
Depth (km)

(b)

Figure 3.22: Migrated sections for recordings of blasts at the Martin Marietta Ruby quarry, north of Macon, Georgia. The individual recordings are numbered a through g. For details refer to the text. In each section the star represents the shot location and the bar represents the array.

a. ru1 b. ru2A

c. ru2B d. ru3

e. ru4 f. ru5B

g. ru6

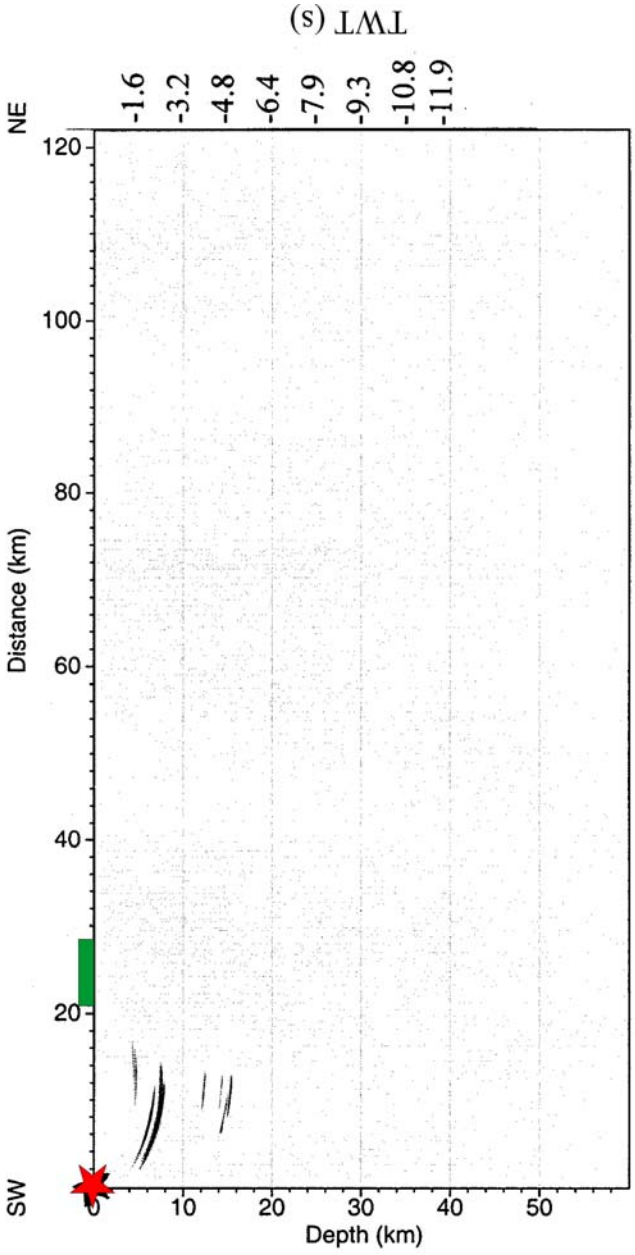
TWT (s)
-1.6
-3.2
-4.8
-6.4
-7.9
-9.3
-10.8
-11.9
NE
SW
Distance (km)
120
100
80
60
40
20
0
10
20
30
40
50
Depth (km)

(a)

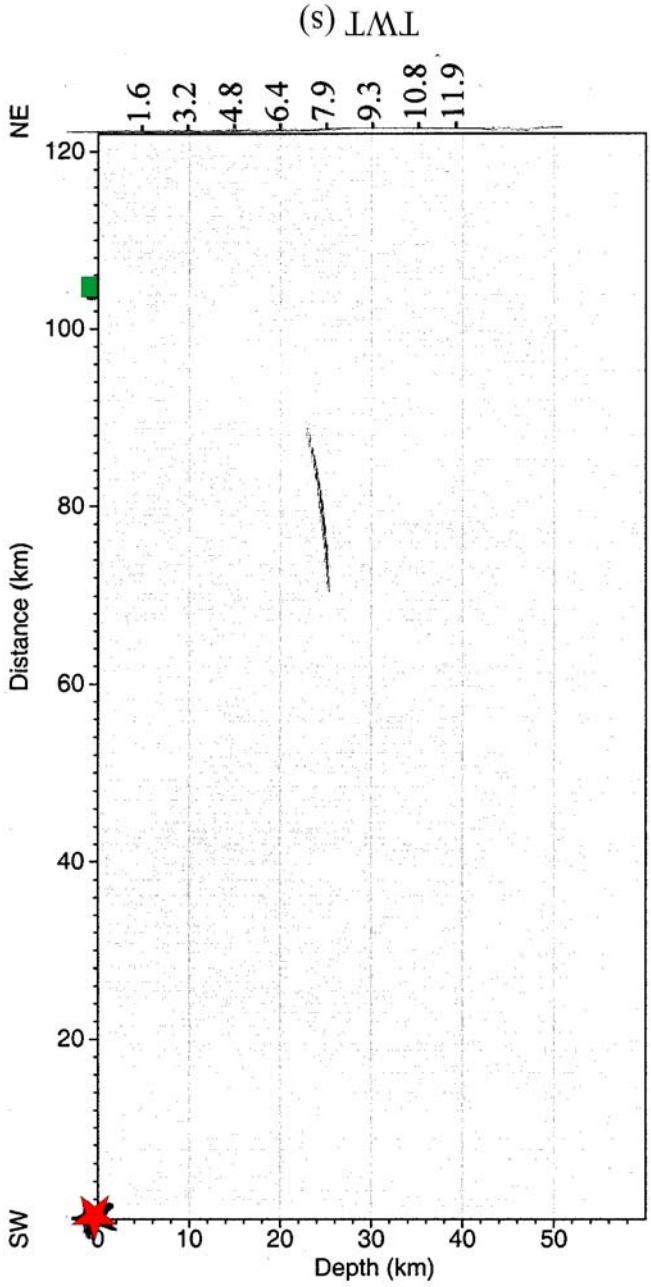
TWT (s)
1.6
3.2
4.8
6.4
7.9
9.3
10.8
11.9
NE
SW
120
100
80
60
40
20
Distance (km)
0
10
20
30
40
50
Depth (km)

(b)

TWT (s)
-1.6
-3.2
-4.8
-6.4
-7.9
-9.3
-10.8
-11.9
NE
SW
Distance (km)
120
100
80
60
40
20
0
10
20
30
40
50
Depth (km)

(c)

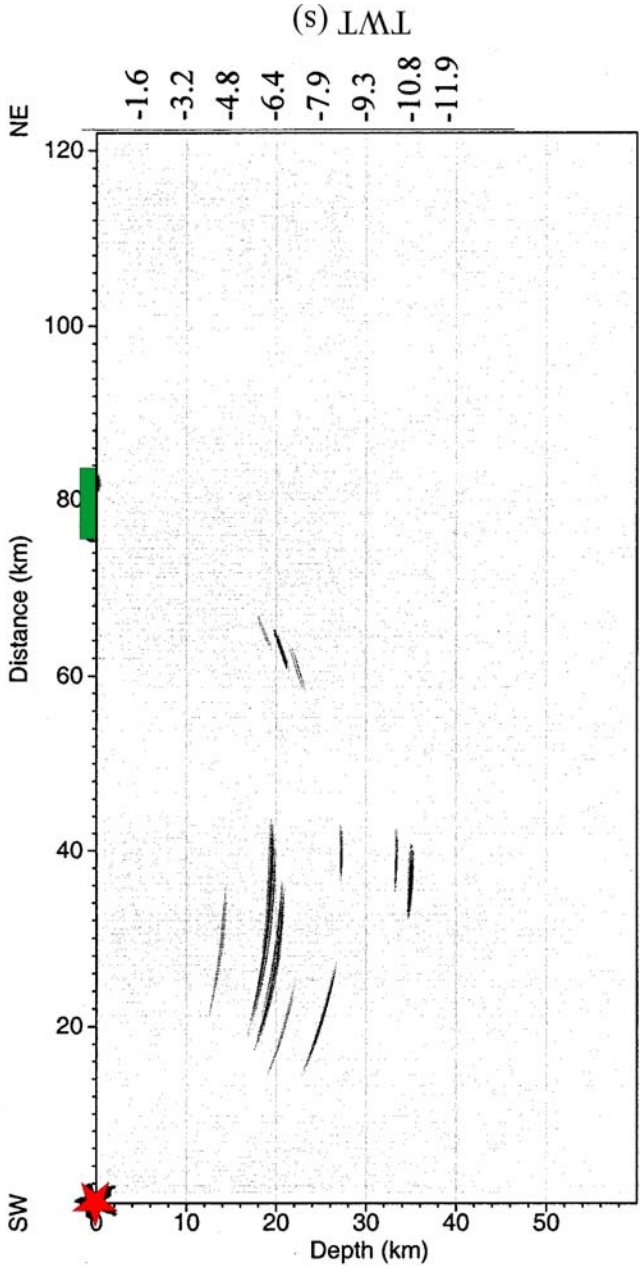
TWT (s)
-1.6
-3.2
-4.8
-6.4
-7.9
-9.3
-10.8
-11.9
NE
SW
Distance (km)
120
100
80
60
40
20
0
10
20
30
40
50
Depth (km)

(d)

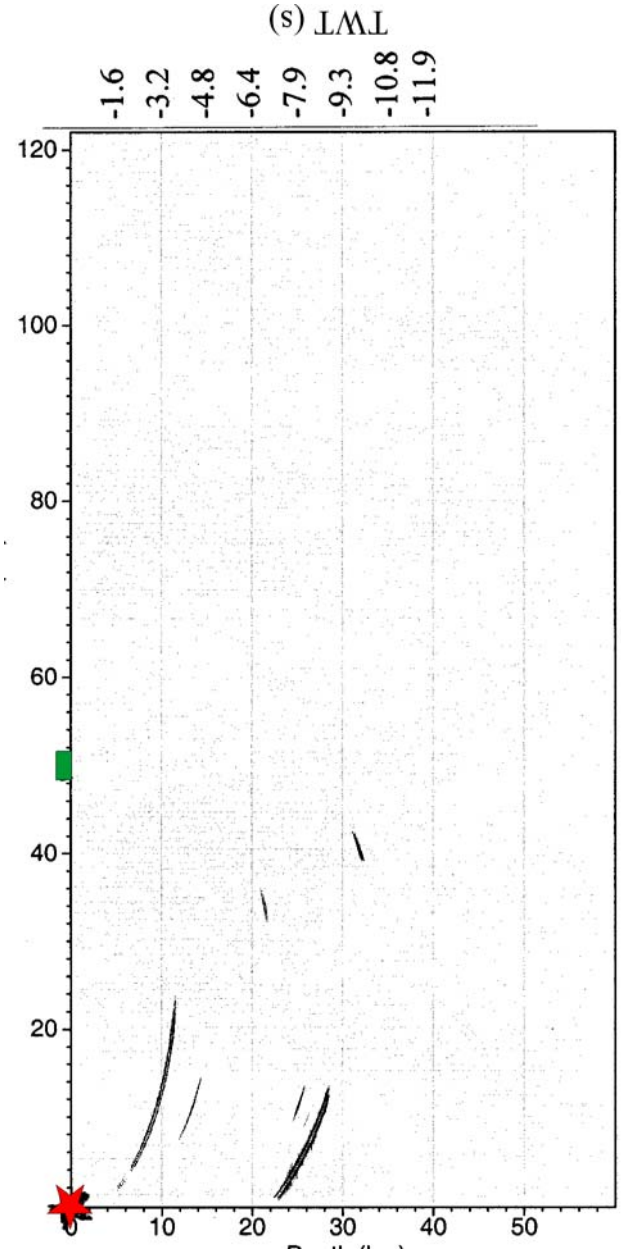

(e)

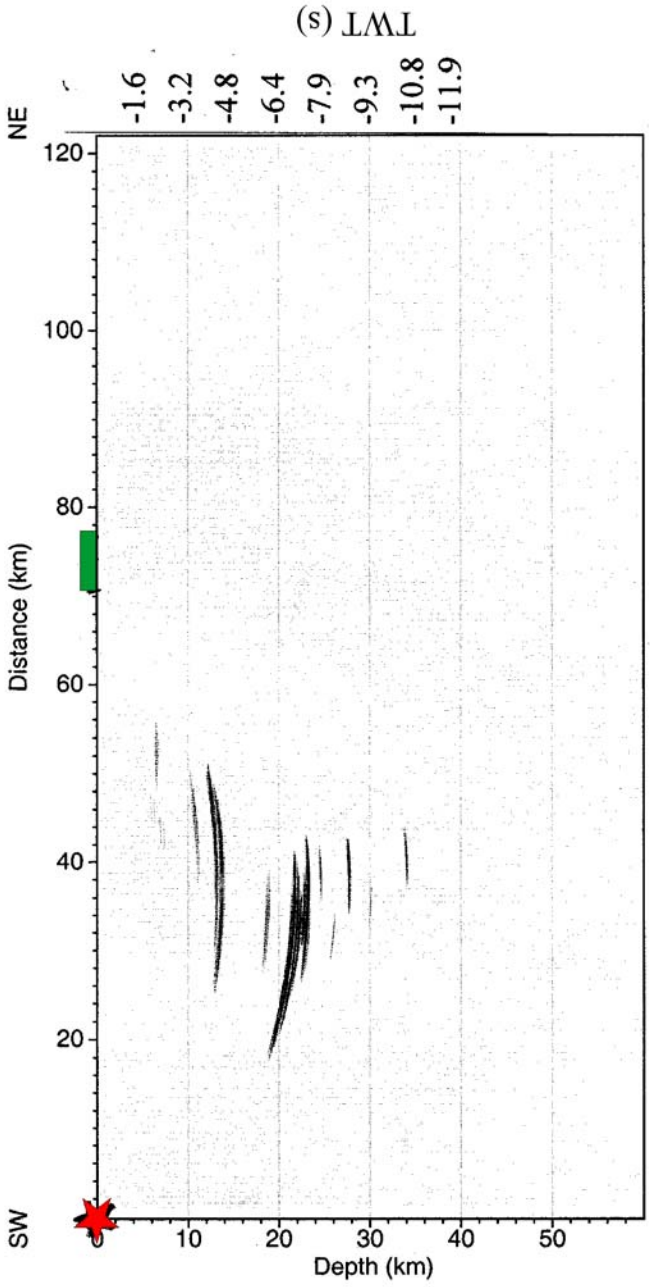
TWT (s)
-1.6
-3.2
-4.8
-6.4
-7.9
-9.3
-10.8
-11.9
NE
SW
120
100
80
60
40
20
Distance (km)
0
10
20
30
40
50
Depth (km)

(f)

Figure 3.23: Composite of migrated sections of Ruby recordings. (a) shows the composite of the recordings without normalization to the maximum amplitude. (b) shows the composite of the normalized individual migrated sections.

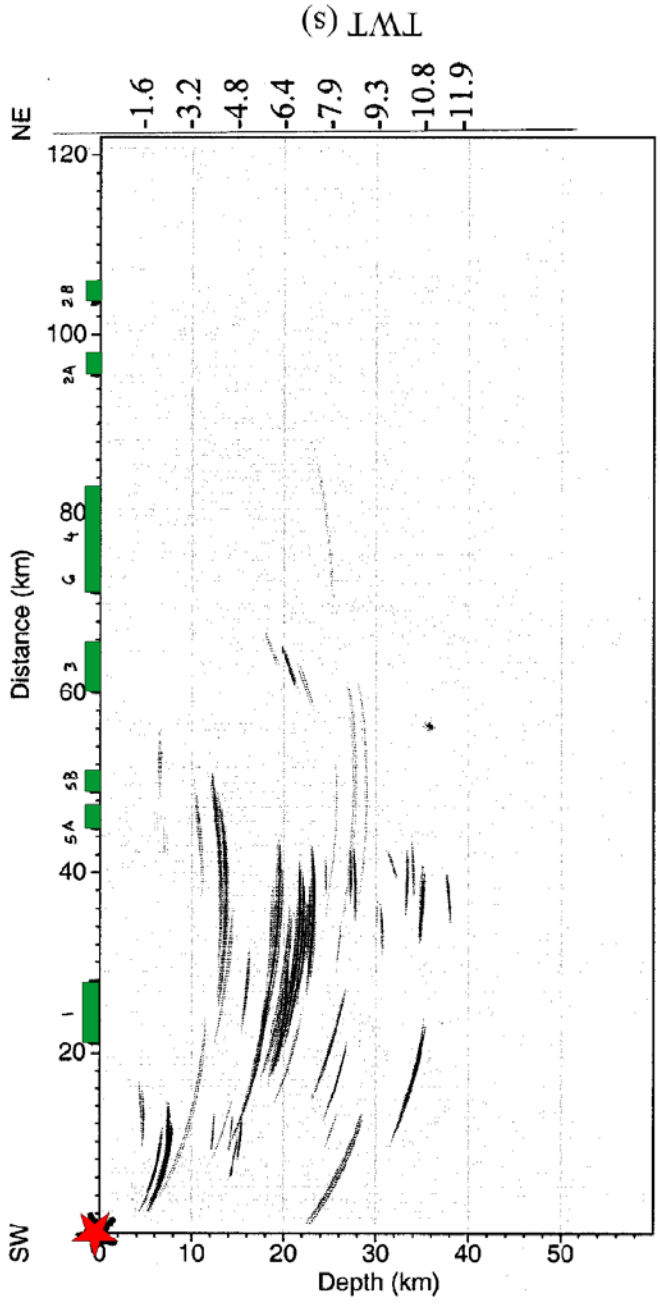
TWT (s)
-1.6
-3.2
-4.8
-6.4
-7.9
-9.3
-10.8
-11.9
NE
SW
Distance (km)
120
100
80
60
40
20
2B
2A
4
3
5B
5A
1
0
10
20
30
40
50
Depth (km)

(a)

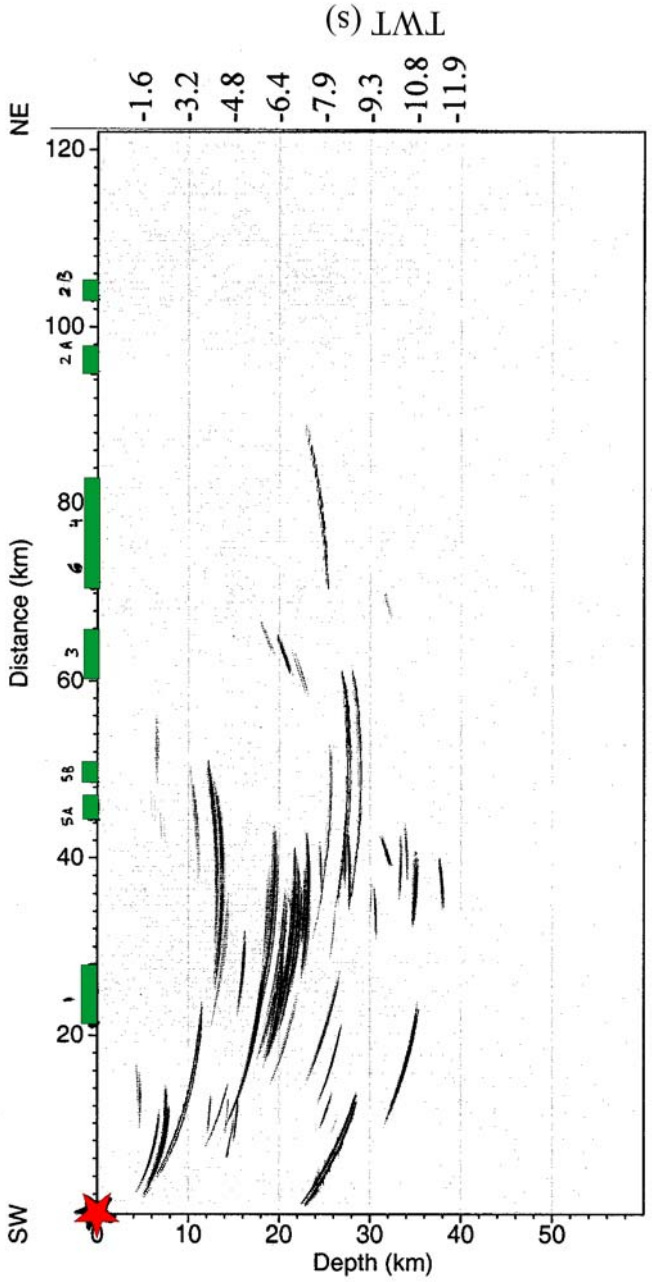
TWT (s)
-1.6
-3.2
-4.8
-6.4
-7.9
-9.3
-10.8
-11.9
NE
SW
Distance (km)
120
100
80
60
40
20
2B
2A
4
6
3
5B
5A
1
0
10
20
30
40
50
Depth (km)

(b)

Figure 3.24: Composite of migrated sections of all recordings from both Hitchcock and Ruby blasts. (a) shows the composite of the recordings without normalization to the maximum amplitude. (b) shows the composite of the normalized individual migrated sections.

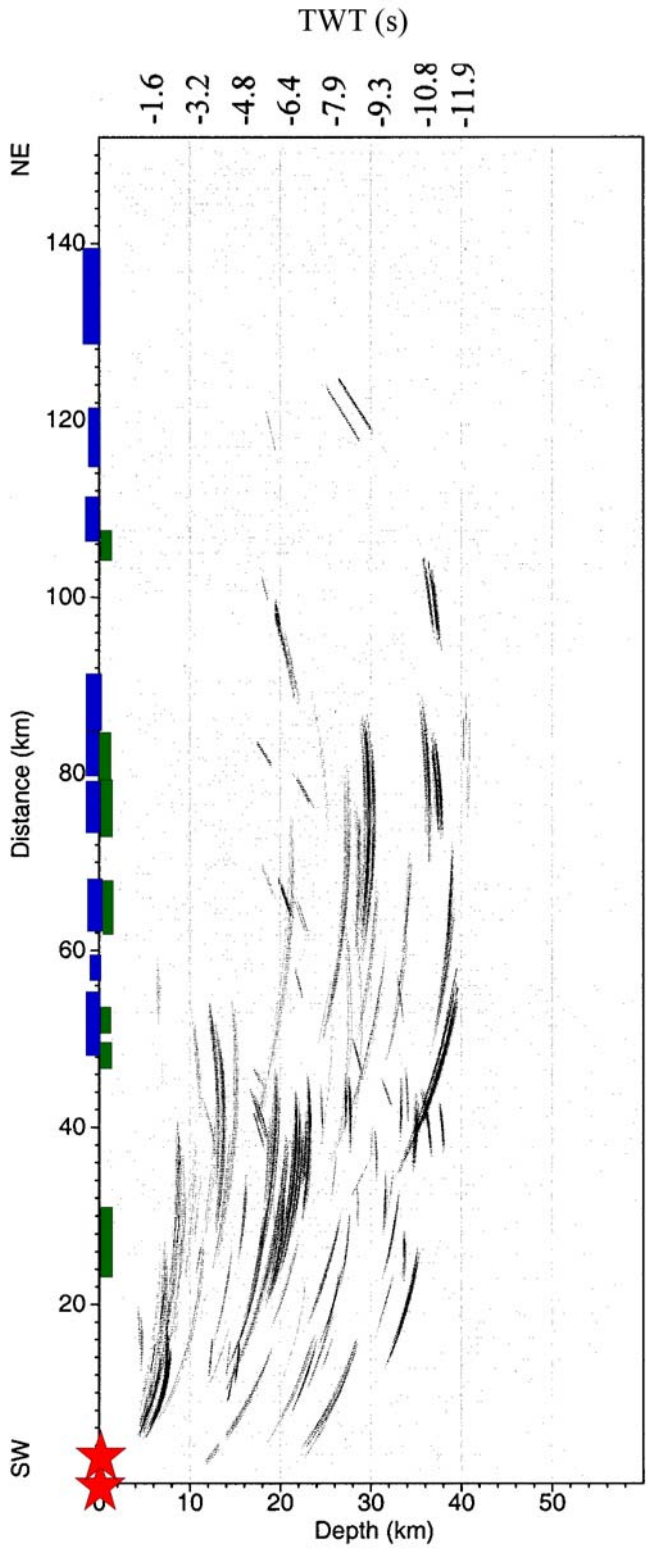
TWT (s)
-1.6
-3.2
-4.8
-6.4
-7.9
-9.3
-10.8
-11.9
NE
SW
Distance (km)
140
120
100
80
60
40
20
0
10
20
30
40
50
Depth (km)

(a)

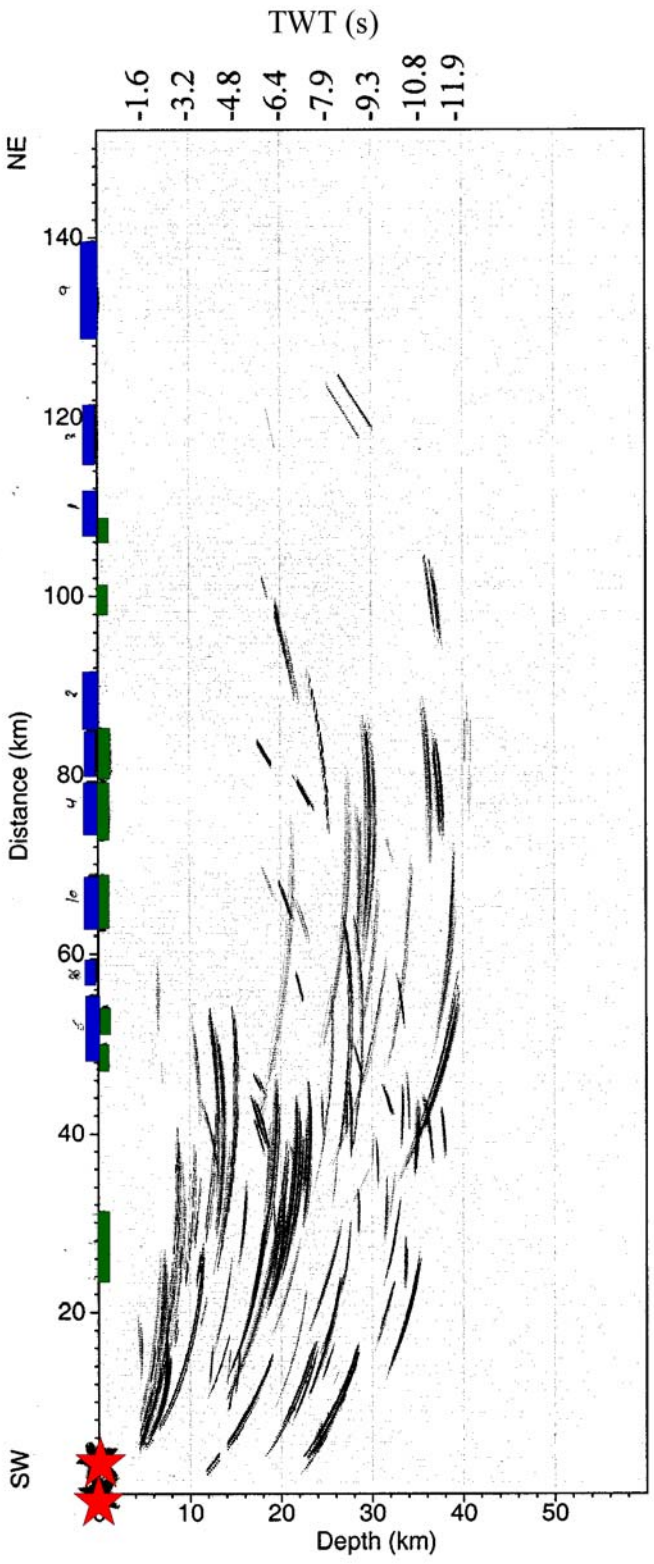
TWT (s)
-1.6
-3.2
-4.8
-6.4
-7.9
-9.3
-10.8
-11.9
NE
SW
Distance (km)
140
120
100
80
60
40
20
10
20
30
40
50
Depth (km)

(b)

Figure 3.25: COCORP Georgia line 1, coherency filtered and migrated at 4.5 km/s by Phinney and Roy-Chowdhury (1989). The solid lines are the interpretative lines discussed in text. The arrow at the top right corner shows the location where section intersects COCORP line 1. Approximate depths are computed assuming a constant crustal velocity of 6.0 km/s (inside scale) and velocity model A of Hawman (1996).

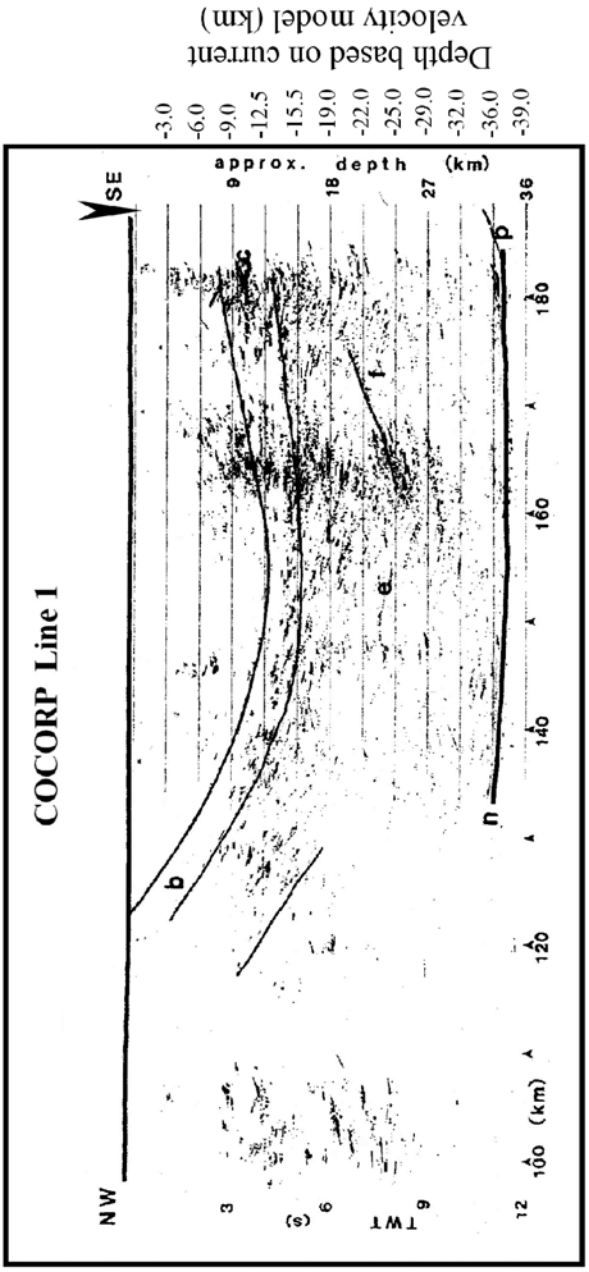
COCORP Line 1
NW
SE
TWT (s)
approx. depth (km)
Depth based on current velocity model (km)
-3.0
-6.0
-9.0
-12.5
-15.5
-19.0
-22.0
-25.0
-29.0
-32.0
-36.0
-39.0
9
18
27
36
100 (km)
120
140
160
180
a
b
c
d
e
f
n
p

(Figure 3.25)

Figure 3.26: COCORP Georgia line 5, coherency filtered and migrated at 4.5 km/s by Phinney and Roy-Chowdhury (1989). The solid lines are the interpretative lines. The arrow at the top right corner shows the location where our section intersects COCORP line 5. Approximate depths are computed assuming a constant crustal velocity of 6.0 km/s (inside scale) and velocity model A of Hawman (1996).

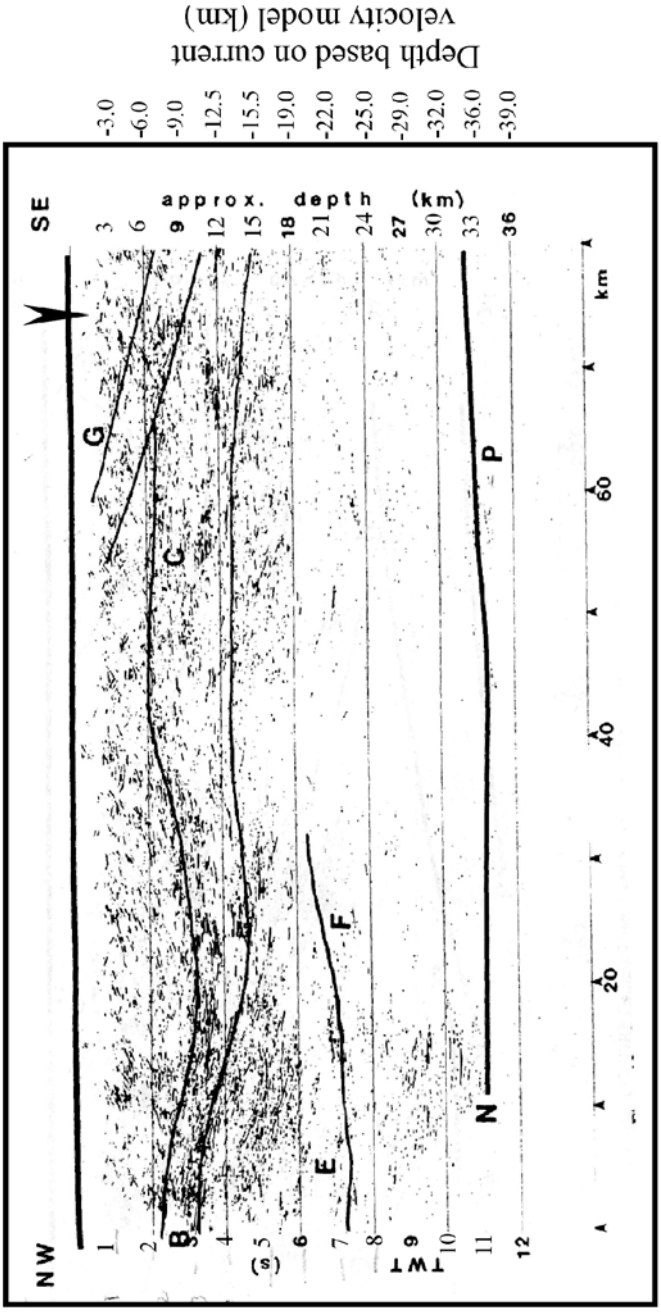
Depth based on current velocity model (km)
-3.0
-6.0
-9.0
-12.5
-15.5
-19.0
-22.0
-25.0
-29.0
-32.0
-36.0
-39.0
SE
NW
approx. depth (km)
3
6
9
12
15
18
21
24
27
30
33
36
G
C
B
E
F
N
P
(s)
TWT
1
2
4
5
6
7
8
9
10
11
12
20
40
60
km

(Figure 3.26)

Figure 3.27: Composite interpretation of reprocessed COCORP Georgia lines 1, 5, and 8 by Phinney and Roy-Chowdhury (1989). Rocks of the Kiokee Belt and Charlotte Belt are interpreted as stacks of thrust sheets that overlie a thinned and rifted Grenville crust. Dotted area marks the interior of Taconian orogen. "Eastern packages, east of G-H-Q: Avalonian continental collider. Western basement, west of a-B-D: Top of Grenville basement." (after Phinney and Roy-Chowdhury, 1989).

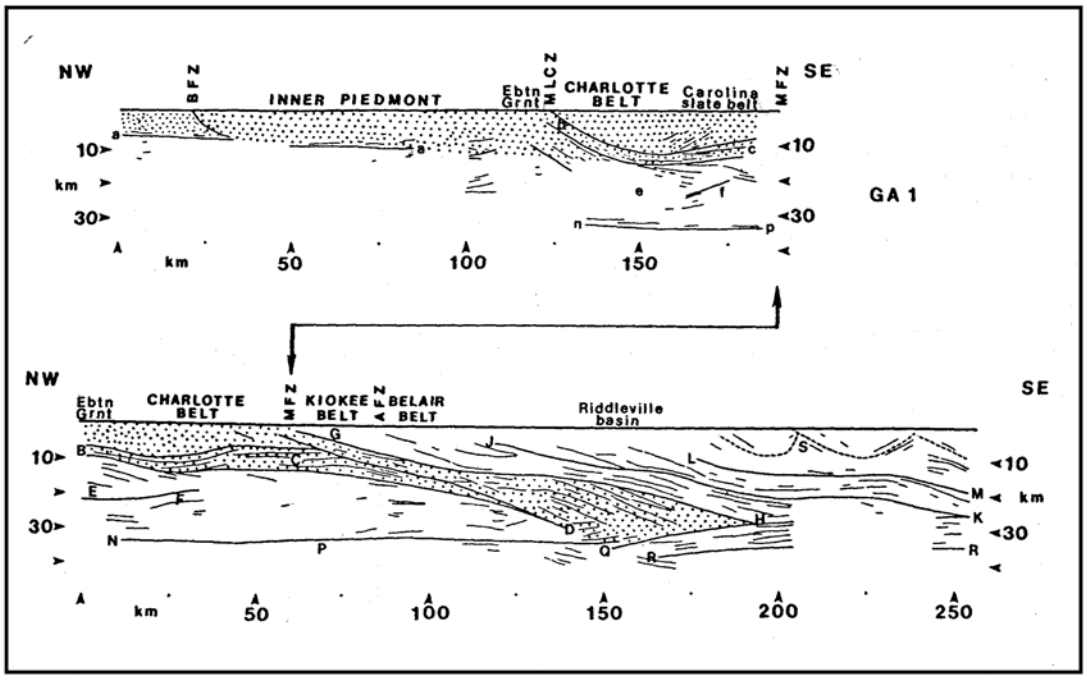
NW
BFZ
INNER PIEDMONT
Ebtn Grnt
MLCZ
CHARLOTTE BELT
Caroline slate belt
MFZ
SE
10
km
30
GA 1
km
50
100
150
NW
Ebtn Grnt
CHARLOTTE BELT
MFZ
KIOKEE BELT
MFZ
BELAIR BELT
Riddleville basin
SE
10
km
30
km
50
100
150
200
250

(Figure 3.27)

Figure 3.28: The migrated section for this study with solid lines showing interpreted boundaries between different interfaces. The two arrows at the top (C1 and C5) show the location of the intersection of COCORP lines 1 and 5 respectively with our section.

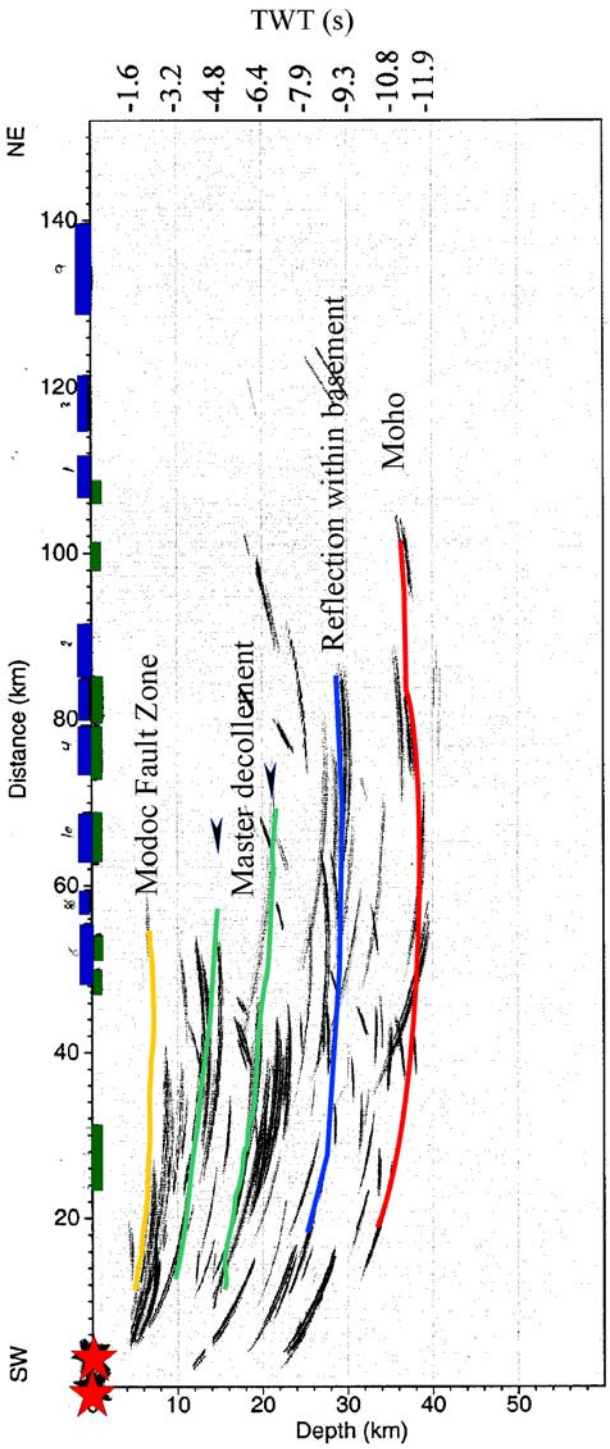
TWT (s)
-1.6
-3.2
-4.8
-6.4
-7.9
-9.3
-10.8
-11.9
NE
SW
Distance (km)
140
120
100
80
60
40
20
Modoc Fault Zone
Master decollement
Reflection within basement
Moho
10
20
30
40
50
Depth (km)

(Figure 3.28)

CHAPTER 4

SUMMARY AND CONCLUSIONS

The Elberton Granite study revealed that the instantaneous blasts fired at dimension-stone quarries generate usable seismic signals (frequency range: (4-50 Hz) to distances of at least 15 km. High-amplitude, multicyclic events arriving shortly after the direct P wave are interpreted as post-critical reflections from a layered complex at depths of 2 to 4 km. The events at 2 km are shallower than any previously recorded over the Elberton granite and the layered complex resembles reflection packages observed beneath other granitic plutons. Apparent dips are small (0-10 degrees to the southeast). The layered complex can be interpreted as a shear zone at the base of the granite, associated with late Alleghanian compression, or as compositional layering within the intrusive body itself, as originally emplaced. Other prominent features in the migrated image include subhorizontal reflections at a depth of roughly 6 km and a zone of reflections at depths between 5 and 10 km, with apparent dips ranging from 8^{o} to 20^{o} to the southeast. These reflections are similar to reflections seen in reprocessed COCORP Georgia line 1 and may be associated in part with the subsurface projection of the Towaliga-Hartwell fault zone. The Blue Ribbon blast produced the only migrated section that shows an event at 11 km; for the other blasts. This event is multicyclic, subhorizontal, relatively high in amplitude, and well resolved. Reflections with similar characteristics in profiles across

other crystalline terranes have been interpreted as mylonitic shear zones (Smithson et al., 1979; Hurich et al., 1985). We interpret this event as a package of reflections from the master decollement.

Improvement of the results in the upper 2-4 km has been achieved using the wide-angle technique where the reflections were poor in the COCORP work. The improvement resulted from the geometry of the experiments which employed the optimum offset method in recording to avoid the interference of the shear waves and the use of the wide-angle technique itself which took advantage of the increase in reflection coefficients near the critical angle to image relatively subtle contrasts in acoustic impedance between rock units of similar composition.

Wide-angle reflections generated by quarry blasts and recorded along the axis of the East Coast Gravity High within the Charlotte and Kiokee Belts have been used to image several interesting structures within the crust. This study concluded that several features in the upper 12 km are similar to those observed in overlapping portions of reprocessed COCORP data (Lines 1 and 5). Examples of these features are the Modoc fault zone and the master decollement. In the migrated sections, these features show a multicyclic character indicating a mylonitic nature. The migrated sections show that the interpreted top of the master decollement zone plunges ~5 degrees to the NE and extends for ~45 km, while the base plunges ~7 degrees to the NE and extends for ~75 km. Both the top and the bottom of the master decollement zone show a gradual decrease in dip from SW to NE and nearly flatten out at their NE borders. This implies that the Kiokee plunges to the northeast.

The wide-angle sections show strong reflections at roughly 30 km that do not appear in the COCORP profiles. These reflections are interpreted as layering at course scales that does not produce tuning at higher frequencies and therefore does not show up with appreciable amplitude in COCORP-style experiments.

Strong events at depths of 38-40 km show piecewise continuity over a distance of roughly 72 km. Based on their relative amplitude and apparent velocity; we interpret these events as near-critical and post-critical reflections from the Moho. Corresponding normal-incidence reflection times (11.6 - 11.9 s) computed using the velocity model of Hawman (1996) are slightly greater than times observed for reflection packages interpreted as Moho in the COCORP lines. The difference is attributed to differences in the wavelength of incident energy.

The elevated reflection coefficients at wide angles have proved quite useful for imaging subtle constrasts in acoustic impedance otherwise missed by near-vertical recording. Taken together, the different length-scales imaged by the higher-frequency COCORP and lower-frequency wide-angle reflection data provide complementary information on the structure of the crust for this portion of the southern Appalachians.